

Summer 2017

Stretching the limits of dynamic range, shielding effectiveness, and multiband frequency response

Matthew J. Hartmann
Louisiana Tech University

Follow this and additional works at: <https://digitalcommons.latech.edu/dissertations>



Part of the [Other Electrical and Computer Engineering Commons](#)

Recommended Citation

Hartmann, Matthew J., "" (2017). *Dissertation*. 55.
<https://digitalcommons.latech.edu/dissertations/55>

This Dissertation is brought to you for free and open access by the Graduate School at Louisiana Tech Digital Commons. It has been accepted for inclusion in Doctoral Dissertations by an authorized administrator of Louisiana Tech Digital Commons. For more information, please contact digitalcommons@latech.edu.

**STRETCHING THE LIMITS OF DYNAMIC RANGE,
SHIELDING EFFECTIVENESS, AND
MULTIBAND FREQUENCY RESPONSE**

by

Matthew J. Hartmann, B.S., M.S.

A Dissertation Presented in Partial Fulfillment
of the Requirements of the Degree
Doctor of Philosophy

COLLEGE OF ENGINEERING AND SCIENCE
LOUISIANA TECH UNIVERSITY

August 2017

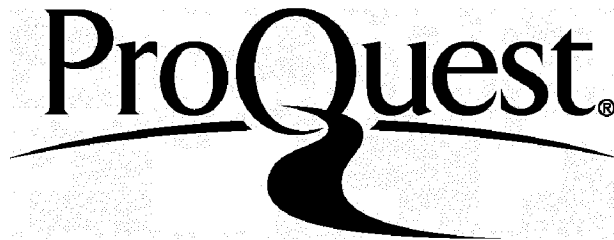
ProQuest Number: 10753662

All rights reserved

INFORMATION TO ALL USERS

The quality of this reproduction is dependent upon the quality of the copy submitted.

In the unlikely event that the author did not send a complete manuscript and there are missing pages, these will be noted. Also, if material had to be removed, a note will indicate the deletion.



ProQuest 10753662

Published by ProQuest LLC(2018). Copyright of the Dissertation is held by the Author.

All rights reserved.

This work is protected against unauthorized copying under Title 17, United States Code.
Microform Edition © ProQuest LLC.

ProQuest LLC
789 East Eisenhower Parkway
P.O. Box 1346
Ann Arbor, MI 48106-1346

LOUISIANA TECH UNIVERSITY

THE GRADUATE SCHOOL

June 28, 2017

Date

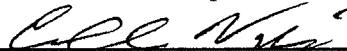
We hereby recommend that the dissertation prepared under our supervision by
Matthew J. Hartmann, B.S., M.S.

entitled **Stretching the Limits of Dynamic Range,
Shielding Effectiveness, and
Multiband Frequency Response**

be accepted in partial fulfillment of the requirements for the Degree of
Doctor of Philosophy in Engineering



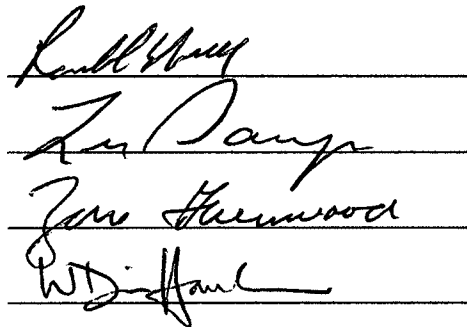
Supervisor of Dissertation Research



Head of Department
Engineering

Department

Recommendation concurred in:

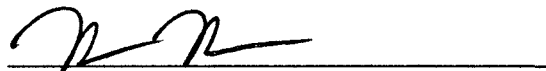


Advisory Committee

Approved:



Director of Graduate Studies



Dean of the College

Approved:



Dean of the Graduate School

ABSTRACT

In this dissertation, an RF MEMS variable capacitor suitable for applications requiring ultrawide capacitive tuning ranges is reported. The device uses an electrostatically tunable liquid dielectric interface to continuously vary the capacitance without the use of any moving parts. As compared to existing MEMS varactors in literature, this device has an extremely simple design that can be implemented using simple fabrication methods that do not necessitate the use of clean room equipment. In addition, this varactor is particularly suited for incorporating a wide range of liquid dielectric materials for specific tuning ratio requirements.

Additionally, the shielding effectiveness performance of graphene-doped ABS thin films is investigated. The use of graphene as a replacement for metal fillers in composite EMI shielding materials is quickly becoming a widely-investigated field in the electromagnetic compatibility community. By replacing conventional metal-based shielding methods with graphene-doped polymers, low-weight, field-use temporary shielding enclosures can be implemented that do not suffer from mechanical unreliability and corrosion/oxidation like a traditional metal enclosure. While the performance of composite EMI shielding materials has not yet surpassed metals, the advantages of polymer-based shielding methods could find usage in a variety of applications.

Finally, multiband pre-fractal antennas fabricated via 3D printing are reported. These devices are the first to incorporate the advantages of 3D printing (rapid

prototyping, fabrication of complex geometries otherwise unobtainable) with the advantages of self-similar antennas (increased gain and multiband performance) in a single device. The Sierpinski tetrahedron-based antenna design was both computationally modeled and physically realized to illustrate its potential as a solution to enable true multiband communication platforms.

APPROVAL FOR SCHOLARLY DISSEMINATION

The author grants to the Prescott Memorial Library of Louisiana Tech University the right to reproduce, by appropriate methods, upon request, any or all portions of this Dissertation. It is understood that "proper request" consists of the agreement, on the part of the requesting party, that said reproduction is for his personal use and that subsequent reproduction will not occur without written approval of the author of this Dissertation. Further, any portions of the Dissertation used in books, papers, and other works must be appropriately referenced to this Dissertation.

Finally, the author of this Dissertation reserves the right to publish freely, in the literature, at any time, any or all portions of this Dissertation.

Author _____

A handwritten signature in black ink, consisting of a large, stylized loop followed by a horizontal line and a short tail.

Date _____

7/22/2017

DEDICATION

For my late grandmother Evelyn Collins.

TABLE OF CONTENTS

ABSTRACT.....	iii
DEDICATION.....	vi
LIST OF TABLES.....	xi
LIST OF FIGURES.....	xiii
ACKNOWLEDGMENTS.....	1
CHAPTER 1 INTRODUCTION.....	1
1.1 Introduction.....	1
1.2 Scope of Research.....	3
1.3 Dissertation Organization.....	4
CHAPTER 2 MICROFLUIDIC VARIABLE CAPACITOR.....	5
2.1 Introduction.....	5
2.2 Variable Capacitors.....	8
2.2.1 Solid-State Varactors.....	9
2.2.2 MEMS Variable Capacitors.....	12
2.2.2.1 Gap-Tuned Variable Capacitors.....	16
2.2.2.1.1 Dual-Gap Varactors.....	23
2.2.2.1.2 Zipping Varactors.....	25
2.2.2.1.3 Interdigitated Gap-Tuned Varactors.....	31
2.2.2.1.4 Non-Electrostatically Actuated Gap-Tuned Varactors.....	34
2.2.2.2 Area-Tuned Variable Capacitors.....	40
2.2.2.2.1 Rotational Varactors.....	45

2.2.2.2.2	Non-Electrostatically Actuated Area-Tuned Varactors	47
2.2.2.3	Digital Variable Capacitors	51
2.2.2.4	Other MEMS Variable Capacitors	53
2.3	Microfluidic Variable Capacitor	60
2.3.1	Operational Theory	61
2.3.2	Modeling	64
2.3.3	Device Design and Fabrication	71
2.3.3.1	Electrodes and Alignment Marks	72
2.3.3.2	Microchannel and Microfluidic Reservoir	75
2.3.3.3	Inlet/Outlet Hole	78
2.3.3.4	Final Assembly	80
2.3.4	Testing and Measurement	81
2.3.5	Conclusions and Future Work	87
CHAPTER 3 GRAPHENE-DOPED POLYMER FILMS FOR ELECTROMAGNETIC INTERFERENCE SHIELDING APPLICATIONS		88
3.1	Introduction	88
3.2	Electromagnetic Shielding Theory	90
3.2.1	Reflection Loss	93
3.2.2	Absorption Loss	96
3.2.3	Losses Due to Multiple Internal Reflections	97
3.3	Methods for Measuring Far-Field Shielding Effectiveness	98
3.3.1	Open Field Method	98
3.3.2	Shielded Room Method	99
3.3.3	Shielded Box Methods	101
3.3.4	Coaxial Transmission Line Methods	102
3.3.4.1	ASTM ES7 Test Fixtures	102

3.3.4.2	ASTM D4935 Test Fixtures	104
3.3.4.3	TEM-t Cell Test Fixtures.....	105
3.4	A Brief Review of Composite Materials Used for EMI Shielding.....	106
3.5	Graphene-Doped Polymer Films for Electromagnetic Interference Shielding Applications.....	108
3.5.1	Measurement and Testing	109
3.5.1.1	Shielded Box Testing.....	109
3.5.1.2	DC 4-Point Probe Measurements	110
3.5.1.3	Coaxial Transmission Line Testing.....	116
3.5.2	Conclusions.....	123
CHAPTER 4 A 3D-PRINTED PRE-FRACTAL SIERPINSKI TETRAHEDRAL ANTENNA		124
4.1	Introduction.....	124
4.2	Application of Fractals in Antenna Engineering	126
4.2.1	Fractal Antenna Arrays	126
4.2.2	Fractal Shaped Antenna Elements	127
4.3	A 3D-Printed Pre-Fractal Sierpinski Tetrahedral Antenna.....	131
4.3.1	Antenna Design.....	132
4.3.2	Finite Element Modeling of the Antenna Structure	134
4.3.3	Antenna Fabrication.....	141
4.3.4	Antenna Measurement and Testing	145
4.3.5	Experimental Data	147
4.3.5.1	Sierpinski Gasket Antenna on Copper-Clad FR4.....	147
4.3.5.2	Electrolytically-Exfoliated Graphene Nanoflake-Doped Antennas ..	148
4.3.5.3	Graphene Nanoparticle-Doped Antennas	155
4.3.5.4	Conductive Filament Antennas	162

4.3.6 Comparative Analysis of the Collected Data..... 165

4.3.7 Conclusions and Future Work 169

BIBLIOGRAPHY..... 171

LIST OF TABLES

Table 2-1: Simulation Results: Finite-Element Modeling of Microfluidic Variable Capacitors.	70
Table 2-2: Microfluidic Varactor Capacitive Tuning Range Performance.	86
Table 3-1: Sheet Resistance [Ω/\square] Measurements for 1% Graphene-Nanoflake Doping.	111
Table 3-2: Sheet Resistance [Ω/\square] Measurements for 5% Graphene-Nanoflake Doping.	112
Table 3-3: Sheet Resistance [Ω/\square] Measurements for 10% Graphene-Nanoflake Doping.	112
Table 3-4: Sheet Resistance [Ω/\square] Measurements for 15% Graphene-Nanoflake Doping.	113
Table 3-5: Sheet Resistance [Ω/\square] Measurements for 20% Graphene-Nanoflake Doping.	113
Table 3-6: Sheet Resistance [Ω/\square] Measurements for 25% Graphene-Nanoflake Doping.	114
Table 3-7: Average Electrical Properties for Graphene Nanoflake-Doped ABS Films.	115
Table 3-8: Shielding Effectiveness [dB] Measurements for 1% Graphene-Nanoflake Doping.	119
Table 3-9: Shielding Effectiveness [dB] Measurements for 5% Graphene-Nanoflake Doping.	120
Table 3-10: Shielding Effectiveness [dB] Measurements for 10% Graphene-Nanoflake Doping.	120
Table 3-11: Shielding Effectiveness [dB] Measurements for 15% Graphene-Nanoflake Doping.	121

Table 3-12: Shielding Effectiveness [dB] Measurements for 20% Graphene-Nanoflake Doping.....	121
Table 4-1: Composite PLA filament volume resistivity specifications.	143

LIST OF FIGURES

Figure 2-1: A North American cell phone RF front-end with four GSM bands, four UMTS bands, three diversity UMTS bands, and a GPS band covering data channels from 800 to 2400 MHz [2].	6
Figure 2-2: Series <i>RLC</i> electronic resonator circuit.	7
Figure 2-3: Transfer function plot for a simple radio receiver with a resonant frequency of $f_0 = 89.1$ MHz for multiple Q_e values. Large Q_e values (> 50) are necessary to adequately reject signal transmissions on nearby channels.	8
Figure 2-4: Variation of depletion junction capacitance (C_j) with respect to unbiased junction capacitance (C_{j0}) with an applied electrical bias (V) for linearly graded, abrupt, and hyperabrupt <i>p-n</i> -junctions. A steeper dopant gradient (M) results in increased tunability at the expense of device linearity.	11
Figure 2-5: $N \times N$ solid-state varactor matrix for reducing nonlinearity in the tuning stage of a radio receiver.	12
Figure 2-6: A parallel plate capacitor with capacitance $C = Q/V $.	14
Figure 2-7: (a) A simple planar MEMS variable capacitor and (b) its equivalent mechanical model. The mechanical damping illustrated in (b) is typically attributed to viscous losses due to gas flow resistance at the micro-scale [40].	14
Figure 2-8: Coupled electromechanical model of a simple gap-tuned variable capacitor (a) without and (b) with an applied bias voltage. Adapted from [41].	17
Figure 2-9: Total system stiffness of a gap-tuned varactor as a function of electrode equilibrium displacement for arbitrary initial electrode spacing.	19
Figure 2-10: (a) Scanning electron microscope (SEM) image and (b) $C-V$ curve for Young and Boser's gap tuned varactor [10,11].	21
Figure 2-11: (a) SEM image and (b) cross-section schematic of Dec and Suyama's 3-plate gap-tuned varactor design [47].	22
Figure 2-12: (a) SEM image and (b) operational schematic of the uni-directionally actuated 3-plate variable capacitor [49].	23

Figure 2-13: (a) SEM picture and (b) cross-section schematic of a dual-gap varactor device [52].	24
Figure 2-14: (a) SEM image and (b) operational schematic of an inverted dual-gap MEMS variable capacitor [59].	25
Figure 2-15: A zipping actuator/varactor at (a) initial beam displacement, (b) cantilever pull-in, and (c) zipping regime [64].	26
Figure 2-16: Tunable capacitor device developed by Hung and Senturia. (a) Top view showing a shaped bottom electrode underneath a rectangular cantilever beam. (b) Lengthwise cross-section of beam under actuation in the zipping regime. The air gap under the end of the beam is defined by dimple spacers. (c) Width cross-section illustrating the dimple spacers [66].	27
Figure 2-17: Zipping varactors using (a) transverse interdigitated electrodes [74], and (b) longitudinal interdigitated electrodes with a tethered suspension to increase local stiffness [75].	28
Figure 2-18: (a) Schematic illustration and (b) $C-V$ response of corrugated-cantilever zipping varactor [76].	29
Figure 2-19: SEM image of tapered bimorph zipping varactor mounted on a coplanar waveguide [77].	30
Figure 2-20: (a) Device schematic, (b) SEM image, and (c) model and prototype $C-V$ characteristics for the dual-zipping variable capacitor [81].	31
Figure 2-21: (a) Micrograph of the interdigitated gap-tuned variable capacitor; (b) Close-up view of the actuator and variable capacitor microstructure; (c) $C-V$ response for the device [90].	32
Figure 2-22: (a) HARPSS varactor reported in [92]; (b) HARPSS varactor reported in [93]; Silver varactor reported in [94].	33
Figure 2-23: (a) SEM image and (b) $C-V$ response for the high-precision, capacitive-switch actuated interdigitated gap-tuned variable capacitor [96].	34
Figure 2-24: (a) Finite element simulated deformation of vertically deflecting electrothermal actuators (scaled 100x); (b) SEM image and (c) $C-V$ response of electrothermally actuated gap-tuned variable capacitor [98].	35
Figure 2-25: (a) Photograph and (b) capacitive response vs. frequency for the device reported in [101].	36
Figure 2-26: SEM images of (a) the completed device, (b) thermal isolation scheme, and (c) latching mechanism for the device described in [102].	37

Figure 2-27: (a) SEM image of piezoelectrically-actuated gap-tuned varactor and (b) C - V response and device schematic [103].	38
Figure 2-28: (a) SEM image and (b) C - V response of piezoelectric cantilever-tuned varactor [104].	39
Figure 2-29: (a) SEM image and (b) C - V response of gap-tuned varactor using a AlN bimorph actuator [107, 108].	40
Figure 2-30: Schematic for a section of an interdigitated comb-drive system representative of both an area-tuned variable capacitor and actuator. Adapted from [41].	40
Figure 2-31: (a) Optical image illustrating device operation with varying bias voltages and (b) C - V characteristics of a comb-drive-actuated area-tuned varactor device [5].	43
Figure 2-32: (a) Schematic representation and (b) SEM image of the fabricated area-tuned variable capacitor using vertical actuation [115].	44
Figure 2-33: (a) Schematic and (b) SEM image of the comb-drive actuated area tuned parallel plate varactor device.	44
Figure 2-34: (a) Schematic, (b) SEM image, and (c) C - V characteristics of the rotational area-tuned varactor device with different finger lengths [118].	45
Figure 2-35: SEM image of gear-driven varactor with a bow-tie electrode turned to approximately 10° off of perpendicular where C_{\min} occurs at 0° and C_{\max} occurs at 90° of rotation [121].	46
Figure 2-36: (a) SEM image of rotational comb-drive variable capacitor with insets depicting folded-beam suspension and variable capacitor structure; (b) C - V response and (c) Q_e vs. frequency plots [122].	47
Figure 2-37: Electrothermally actuated area-tuned comb-drives [125].	48
Figure 2-38: (a) Device schematic and (b) SEM image of laterally-actuated area-tuned capacitor [126].	49
Figure 2-39: (a) SEM image of rotational electrothermally-actuated varactor, (b) close-up view of fragmented electrodes, (c) C - V characteristics of the device, and (d) capacitance vs. frequency plot for varying control voltages [128].	50
Figure 2-40: (a) SEM image and (b) device schematic of a piezoelectrically-actuated varactor device [129].	50

Figure 2-41: A 6-bit RF-MEMS digital variable capacitor utilizing weighted capacitance selection of bits composed of bistable MEMS capacitive switches. Adapted from [130].....	51
Figure 2-42: MEMS capacitive switch mounted in a shunt configuration over a coplanar waveguide [130].....	52
Figure 2-43: Schematic of an RF MEMS ohmic switch [142].....	53
Figure 2-44: (a) Operational diagram and (b) SEM image of a scratch-drive-actuated variable capacitor [147].	54
Figure 2-45: (a) Conceptual schematic, (b) operational schematic, and (c) SEM image of a dielectrically-tuned MEMS varactor device [148].....	54
Figure 2-46: (a) SEM image and (b) $C-V$ characteristics of a torsion beam MEMS varactor [149].....	55
Figure 2-47: (a) Perspective view and (b) side view of operational schematic of MEMS toggle varactor. (c) Photograph of a completed device [150].....	56
Figure 2-48: (a) Operational schematic and (b) SEM image of a V-shaped area-tuned varactor [153].....	56
Figure 2-49: (a) SEM image and (b) $C-V$ characteristic curve of vertically-oriented gap-tuned varactor [154].....	57
Figure 2-50: (a) Operational schematic, (b) SEM image, and (c) $C-V$ characteristic curve of a gap-tuned varactor with an electrically floating plate [158].....	58
Figure 2-51: (a) CAD drawing of liquid-metal varactor, (b) pictures illustrating thermal expansion of mercury within the microchannel, and (c) $C-V$ response of the device [161].	59
Figure 2-52: Vertically-aligned carbon nanofibers forming a parallel-plate capacitor [162].....	59
Figure 2-53: (a) Schematic view of the variable capacitor and its switching components, (b) $C-V$ relationship as a function of switch position and voltage, and (c) continuous tuning capabilities of the device [163].	60
Figure 2-54: Conceptual illustration of microfluidic variable capacitor operation. The fringing electric field at the capacitor edge generates a polarization force that pushes the molecular dipoles of the liquid dielectric material further into the area of electrode overlap.....	61

Figure 2-55: Schematic representation of a parallel plate capacitor filled with partially inserted dielectric materials. This configuration yields parallel capacitances with differing permittivities.	62
Figure 2-56: Simulations for device capacitance as a function of fill percentage for a microfluidic variable capacitor with a 20 mm x 2 mm x 25 μm microchannel.	67
Figure 2-57: Simulations for device capacitance as a function of fill percentage for a microfluidic variable capacitor with a 20 mm x 4 mm x 25 μm microchannel.	68
Figure 2-58: Simulations for device capacitance as a function of fill percentage for a microfluidic variable capacitor with a 40 mm x 2 mm x 25 μm microchannel.	69
Figure 2-59: Simulations for device capacitance as a function of fill percentage for a microfluidic variable capacitor with a 40 mm x 4 mm x 25 μm microchannel.	70
Figure 2-60: 3D plots of electric field lines and distribution for a biased microfluidic varactor over (a) the entire varactor length and (b) focused on the electrode edge. The arrows are normalized to illustrate field direction and their length is not indicative of field strength. Surface plots of transverse electric field distributions (c) at the electrode edge and (d) at the electrode feed point.	71
Figure 2-61: Exploded view of a microfluidic variable capacitor device detailing each portion of the assembly.	72
Figure 2-62: Photolithography mask design for patterning microfluidic varactor electrodes. The hourglass shapes on each side are alignment marks to ensure a maximum area of electrode overlap.	73
Figure 2-63: Process flow diagram for patterning electrodes and alignment marks. (a) Substrate is coated with 50 nm of chromium. (b) A 1 μm layer of S1811 photoresist is deposited on top of the chromium and exposed to UV radiation. (c) The photoresist layer is developed, removing unwanted photoresist features. (d) The exposed chromium is etched, leaving behind the patterned features topped with photoresist. (e) The photoresist is moved, revealing the patterned chromium layer underneath.	74
Figure 2-64: Glass substrates with photolithographically-patterned alignment marks and electrodes designed for microfluidic varactors with microchannel dimensions (a) 2 mm x 20 mm x 25 μm , (b) 4 mm x 20 mm x 25 μm , (c) 2 mm x 40 mm x 25 μm , and (d) 4 mm x 40 mm x 25 μm	75
Figure 2-65: A top-down view of a microfluidic stop valve including angle definitions. Adapted from [171].	76
Figure 2-66: Microchannel pattern used to define the microchannel, stop valves, and microfluidic reservoirs for microfluidic variable capacitor devices.	77

Figure 2-67: Xurographically-patterned microchannel layer for a 4 mm x 40 mm x 25 μm microfluidic variable capacitor device.	78
Figure 2-68: Photograph of a patterned microchannel layer affixed to a prepared substrate with key features illustrated.....	78
Figure 2-69: A 4 mm x 40 mm x 25 μm microfluidic variable capacitor electrode substrate with etched/drilled through-holes.....	79
Figure 2-70: The components of an Upchurch Scientific Nanoport Assembly to be affixed to a glass substrate using thermal-set epoxy rings.....	79
Figure 2-71: A 2 mm x 20 mm x 25 μm microfluidic variable capacitor electrode substrate with completed inlet/outlet hole assemblies.....	80
Figure 2-72: Completed microfluidic variable capacitors with varying microchannel dimensions.....	80
Figure 2-73: Device capacitance as a function of fill percentage and actuation voltage for a microfluidic varactor with 2 mm x 20 mm x 25 μm microchannel dimensions.	82
Figure 2-74: Device capacitance as a function of fill percentage and actuation voltage for a microfluidic varactor with 4 mm x 20 mm x 25 μm microchannel dimensions.	83
Figure 2-75: Device capacitance as a function of fill percentage and actuation voltage for a microfluidic varactor with 2 mm x 40 mm x 25 μm microchannel dimensions.	84
Figure 2-76: Device capacitance as a function of fill percentage and actuation voltage for a microfluidic varactor with 4 mm x 40 mm x 25 μm microchannel dimensions.	85
Figure 2-77: Capacitance vs. fill percentage data for different microchannel dimensions.....	86
Figure 3-1: Classification of EM radiation as a portion of the electromagnetic spectrum [172].	88
Figure 3-2: Characterization of electromagnetic waves as a function of distance from source [174].	91
Figure 3-3: As distance between the radiating antenna and surface of incidence increases, the wavefront becomes increasingly planar.	91
Figure 3-4: Behavior of normally-incident plane waves on a shielding medium. Adapted from [174].	92
Figure 3-5: A block diagram describing the open field shielding effectiveness measurement [176].	99

Figure 3-6: Schematic diagram of shielded room shielding effectiveness measurements. Adapted from [178].....	100
Figure 3-7: Block diagram of shielded box shielding effectiveness measurement. Adapted from [176].....	101
Figure 3-8: (a) Cross-sectional view (adapted from [176]) and (b) picture of ASTM ES7 test fixture [193].....	103
Figure 3-9: (a) Cross-sectional view (adapted from [176]) and (b) picture of ASTM D4395 test fixture [193].....	104
Figure 3-10: (a) Load and (b) reference samples for ASTM D4395-based test fixtures.	105
Figure 3-11: (a) Cross-sectional view (adapted from [176]) and (b) schematic diagram of the TEM-t cell (adapted from [200]).	106
Figure 3-12: (a) Graphene-doped resin coated shielded box and (b) collected signal attenuation data.	110
Figure 3-13: (a) Experimental set-up and (b) samples used to determine electrical properties of graphene nanoflake-doped ABS films.....	111
Figure 3-14: Sheet resistance as a function of doping concentration for graphene-doped ABS thin films. The error bars represent the standard deviation of each dopant concentration.	116
Figure 3-15: Custom coaxial transmission line test fixture for measuring shielding effectiveness based on the ASTM D4395 method.....	117
Figure 3-16: Shielding effectiveness measurement being made using the custom coaxial transmission line test fixture.....	118
Figure 3-17: Shielding effectiveness of ABS/graphene samples as a function of dopant concentration and frequency. The error bars represent the standard deviation of the measured shielding effectiveness for a particular dopant concentration and frequency.....	122
Figure 4-1: Fractal patterns used in antenna radiating elements. (a) Sierpinski gasket; (b) Sierpinski carpet; (c) Koch curve; (d) Hilbert curve, (e) Peano curve, (f) Minkowski island.....	127
Figure 4-2: A computer-generated rendering of a 5 th -order Sierpinski tetrahedron.....	129
Figure 4-3: (a) Perturbed Sierpinski gasket monopole antenna with truncated central gaps and (b) a diagram of the three-dimensional conical monopole antenna [245].	129

Figure 4-4: Pyramidal antenna utilizing four perturbed planar Sierpinski gasket antennas [246].	130
Figure 4-5: Brass Sierpinski tetrahedral antenna fabricated by Alaydrus [247].	131
Figure 4-6: Sierpinski gasket pre-fractal structure illustrating 3 rd -order self-similarity with a scaling factor of $\delta = 2$.	132
Figure 4-7: Three-dimensional model of the proposed 3 rd -order Sierpinski tetrahedral antenna.	133
Figure 4-8: Simulated input return loss as a function of material and pre-fractal iteration over a frequency range of 0.1–3.0 GHz for a Sierpinski tetrahedral antenna.	135
Figure 4-9: Simulated input return loss for 3 rd -order tetrahedral (3D) and planar (2D) Sierpinski pre-fractal antennas. The 3D antenna exhibits increased power dissipation at higher-order resonant frequencies as well as increased bandwidth at lower-order resonant frequencies.	136
Figure 4-10: Spatial variance of the simulated electric field distribution over a 3 rd -order Sierpinski tetrahedral antenna's surface at (a) 1.55 GHz, (b) 3.00 GHz, (c) 3.70 GHz, and (d) 6.25 GHz. As the excitation frequency increases, the electric field intensifies over an increasingly smaller surface area of the radiating element.	138
Figure 4-11: Simulated radiation characteristics of a 3 rd -order Sierpinski tetrahedral pre-fractal antenna. As the frequency increases, the directivity of the antenna changes with more omnidirectional behavior observed at higher frequency resonances.	139
Figure 4-12: Simulated 3D radiation pattern data for a 3 rd -order Sierpinski tetrahedral antenna at (a) 1.55 GHz, (b) 3.00 GHz, (c) 3.70 GHz, and (d) 6.25 GHz.	139
Figure 4-13: Simulated input return loss of pre-fractal Sierpinski tetrahedral antennas on a finite ground plane. The numbers in parentheses represent the order of the pre-fractal iteration.	140
Figure 4-14: Third-order Sierpinski tetrahedron substrates fabricated by FLD 3D-printing ABS filament. These substrates are to be coated with conductive carbon films and will serve as the radiating element for a monopole antenna.	142
Figure 4-15: A 3D-printed Sierpinski antenna coated with (a) an electrolytically-exfoliated-graphene-doped acetone-ABS solution and (b) a carbon nanoparticle-doped acetone-ABS solution.	143
Figure 4-16: SEM images of printed samples of (a) graphite-doped-PLA filament and (b) graphene-doped-PLA filament. The additional carbon-content of the graphene-doped-PLA filament resulted in decreased bonding between subsequent layers of the printed material.	144

- Figure 4-17:** A 3D-printed Sierpinski tetrahedral antenna with radiating element made from (a) graphite-doped-PLA filament and (b) graphene-doped-PLA filament... 145
- Figure 4-18:** Photograph of the VNA and Reflection/Transmission test module during an antenna transmission parameter measurement. 146
- Figure 4-19:** Photographs of (a) a lithographically-patterned Sierpinski gasket antenna radiating element and (b) an assembled gasket antenna. (c) Measured S_{21} data taken for the antenna shown in (b)..... 147
- Figure 4-20:** (a, b) Photographs of a 3D-printed ABS substrate coated with a 1%-by-weight doped solution of 80:20 acetone/ABS. (c) Measured S_{21} data taken for the antenna shown in (a) and (b)..... 148
- Figure 4-21:** (a, b) Photographs of a 3D-printed ABS substrate coated with a 5%-by-weight doped solution of 80:20 acetone/ABS. (c) Measured S_{21} data taken for the antenna shown in (a) and (b)..... 149
- Figure 4-22:** (a, b) Photographs of a 3D-printed ABS substrate coated with a 10%-by-weight doped solution of 80:20 acetone/ABS. (c) Measured S_{21} data taken for the antenna shown in (a) and (b)..... 150
- Figure 4-23:** (a, b) Photographs of a 3D-printed ABS substrate coated with a 15%-by-weight doped solution of 80:20 acetone/ABS. (c) Measured S_{21} data taken for the antenna shown in (a) and (b)..... 151
- Figure 4-24:** (a, b) Photographs of a 3D-printed ABS substrate coated with a 20%-by-weight doped solution of 80:20 acetone/ABS. (c) Measured S_{21} data taken for the antenna shown in (a) and (b)..... 152
- Figure 4-25:** (a, b) Photographs of a 3D-printed ABS substrate coated with a 25%-by-weight doped solution of 80:20 acetone/ABS. (c) Measured S_{21} data taken for the antenna shown in (a) and (b)..... 153
- Figure 4-26:** S_{21} response of the copper reference antenna and electrolytically-exfoliated graphene-nanoparticle-doped antennas (a) over the measurement bandwidth of the test set-up and (b) over a frequency range of 0.8–1.8 GHz to eliminate noise contributions. 154
- Figure 4-27:** (a, b) Photographs of a 3D-printed ABS substrate coated with a 1%-by-weight doped solution of 80:20 acetone/ABS. (c) Measured S_{21} data taken for the antenna shown in (a) and (b)..... 155
- Figure 4-28:** (a, b) Photographs of a 3D-printed ABS substrate coated with a 5%-by-weight doped solution of 80:20 acetone/ABS. (c) Measured S_{21} data taken for the antenna shown in (a) and (b)..... 156

- Figure 4-29:** (a, b) Photographs of a 3D-printed ABS substrate coated with a 10%-by-weight doped solution of 80:20 acetone/ABS. (c) Measured S_{21} data taken for the antenna shown in (a) and (b)..... 157
- Figure 4-30:** (a, b) Photographs of a 3D-printed ABS substrate coated with a 15%-by-weight doped solution of 80:20 acetone/ABS. (c) Measured S_{21} data taken for the antenna shown in (a) and (b)..... 158
- Figure 4-31:** (a, b) Photographs of a 3D-printed ABS substrate coated with a 20%-by-weight doped solution of 80:20 acetone/ABS. (c) Measured S_{21} data taken for the antenna shown in (a) and (b)..... 159
- Figure 4-32:** (a, b) Photographs of a 3D-printed ABS substrate coated with a 25%-by-weight doped solution of 80:20 acetone/ABS. (c) Measured S_{21} data taken for the antenna shown in (a) and (b)..... 160
- Figure 4-33:** S_{21} response of the copper reference antenna and electrolytically-exfoliated graphene-nanoparticle-doped antennas (a) over the measurement bandwidth of the test set-up and (b) over a frequency range of 0.8–1.8 GHz to eliminate noise contributions. 161
- Figure 4-34:** (a, b) Photographs of a 3D-printed carbon-doped PLA tetrahedral antenna radiating element. (c) Measured S_{21} data taken for the antenna shown in (a) and (b). 163
- Figure 4-35:** (a, b) Photographs of a 3D-printed graphene-doped PLA tetrahedral antenna radiating element. (c) Measured S_{21} data taken for the antenna shown in (a) and (b). 164
- Figure 4-36:** S_{21} response of the copper reference antenna and 3D-printed antennas utilizing conductive PLA filaments (a) over the measurement bandwidth of the test set-up and (b) over a frequency range of 0.8–1.8 GHz to eliminate low-frequency noise contributions. 165
- Figure 4-37:** Normalized transmission coefficient data for antenna radiating elements which received an electrolytically-exfoliated graphene-nanoflake-doped conductive coating. 167
- Figure 4-38:** Normalized transmission coefficient data for antenna radiating elements which received a graphene-nanoparticle-doped conductive coating. 168
- Figure 4-39:** Normalized transmission coefficient data for the best-performing coated antennas, conductive filament antennas, and copper antenna..... 169

ACKNOWLEDGMENTS

I would like to express profound gratitude towards all of my family, friends, and colleagues who have helped and supported me throughout the arduous task of completing this dissertation.

CHAPTER 1

INTRODUCTION

1.1 Introduction

The ever-increasing demand for connectivity and the transfer of information has yielded amazing technological advances in recent years. The field of telephony has evolved from the old rotary phone on the wall at my grandmother's general store to modern smart phones capable of sending and receiving calls from across the globe wirelessly while also functioning as a jukebox, portable movie theatre, and video game system that fits in one's pocket. Satellite communication, once reserved for strategic military assets, is now standard on most automobiles manufactured in the United States. The ability to store data for machine processing has evolved from punch cards to magnetic media to the logic state of an anti-fuse. The rate at which technology is created and replaced is seen by many as overwhelming.

The push towards smaller, multi-function communication platforms has been at the forefront of modern radio frequency hardware engineering. Advancements in personal hand-held communications systems, wireless local area networks, and satellite communications applications have necessitated the development and use of components with enhanced functionality and a small physical footprint, and as ground and satellite communications advance the demand for these features will become even more stringent.

At the current state-of-the-art, the miniaturization of a communications system can no longer proceed through integration alone as the fundamental limits of IC scaling and monolithically-integrated passive component performance are approached. Instead, future miniaturization must occur through a reduction in component count which is only achievable by increasing the functionality of radio frequency systems and their individual components, an area where novel microelectromechanical system designs have vast potential through the use of non-traditional materials, processing, and architectures. The implementation of individual microdevices designed to perform the operation of an entire functional block within a radio transceiver not only decreases the system size and cost, but increases reliability and performance.

As the usage of wireless communication technology has become the norm throughout the world, the ubiquity of the wireless signals generated by the multitude of different radios and transceivers has led towards a renewed interest in novel electromagnetic shielding and compatibility methods. Add to this electromagnetic interference the ever-present threat of electrical infrastructure attacks via electromagnetic pulse attacks and the need for low-cost, easily-implementable electromagnetic shielding becomes paramount to protect not only consumer electronic devices and their users but SCADA-controlled areas of infrastructure and industry utilized by our modern technological society. While metal has been the traditional choice for electromagnetic shielding materials, the use of composite materials is becoming an attractive alternative due to their low cost, weight, and ease of production. The investigation of conductive nanoparticles—particularly those which are constituent of abundant materials—in

composite electromagnetic shielding materials is at the forefront of versatile, cost-effective shielding methods for a variety of applications.

As more portions of the electromagnetic spectrum become utilized for modern communications technologies, multifrequency antennas are quickly becoming an attractive solution when different communications systems require similar electromagnetic performance from their radiating elements. Spearheading the field of multifrequency antenna research is the concept of fractal antennas: radiative devices that exhibit self-similarity within their physical architecture to enable multiband response while also yielding a reduction in size. These modifications to classic antenna architectures generate high-performance devices with increased bandwidth and reduced size which can be used in the miniaturization of space vehicles, drones, and UAVs as well as wireless energy harvesting and cellular telephony systems applications, however the practical realization of some geometries has been limited by fabrication technologies. By using additive manufacturing techniques in combination with nanotechnology, the realization of electrically-conductive complex geometric structures is now possible—fractal antennas are no longer limited to planar geometries due to their difficulty in fabricating.

1.2 Scope of Research

Interest in the frequent innovations seen in the field of radio frequency engineering have directed my academic research for the duration of my graduate career. Whether conducting experiments for the Cyber Innovation Center, the Louisiana Space Consortium, Army Missile Command, or the Air Force Research labs, the focus of my research has always been on the various aspects of wireless communication, from

increasing the dynamic range of receivers (as seen in Chapter 2), to minimizing or eliminating the effects of electromagnetic interference (as seen in Chapter 3), to the development of multiband antennas to enable wideband communications systems (as seen in Chapter 4). These topics illustrate the potential of micro- and nanotechnology applications as a supplement to the established field of radio frequency engineering.

1.3 Dissertation Organization

The remainder of this dissertation is divided into three chapters. Chapter 2 focuses on the design and development of a microfluidic variable capacitor and includes a review of the state-of-the-art regarding RF MEMS variable capacitors, classifying the various devices based on their design features. Additionally, a new design capable of achieving extremely wide continuous tuning is introduced, and simulations and experimental data collected for the microfluidic RF MEMS device are presented. Chapter 3 focuses on the development of graphene-doped polymer films for EMI shielding applications, with a review of electromagnetic shielding theory and test methods as well as experimental data supporting the use of non-metallic fillers in composite EMI shielding materials. Finally, Chapter 4 focuses on the design and development of 3D printed Sierpinski tetrahedral fractal antennas. The chapter includes a review of fractal-based antennas and antenna arrays, the first reported computer modeling of a 3rd-order Sierpinski tetrahedral antenna using the finite element method, and the radiation characteristics of the realized antenna design using a variety of conductive coatings and conductive filaments.

CHAPTER 2

MICROFLUIDIC VARIABLE CAPACITOR

2.1 Introduction

Wireless communication technology is the backbone of the modern digital age. From cellular telephony to portable computing to satellite communications, the wireless transmission of electromagnetic signals of varying frequencies has enabled ubiquitous connectivity and access to information across our entire planet. The rapid rise in usage of wireless communication technology has led to explosive growth in consumer, industrial, and military applications of radio frequency (RF), microwave, and millimeter wave systems and circuits and created a significant demand for novel high-performance components to simplify and scale down the various radio transceiver architectures used within the industry [1]. As an example, consider a sample multiband cell phone transceiver used in the North American market space, shown **Figure 2-1**. Such a device requires sixteen different discretely-implemented fixed filters which occupy up to 80% of the RF board area [2, 3]. The development of tunable filters, reconfigurable matching networks, and adaptive antennas could significantly reduce the size, cost, and power consumption while increasing overall performance.

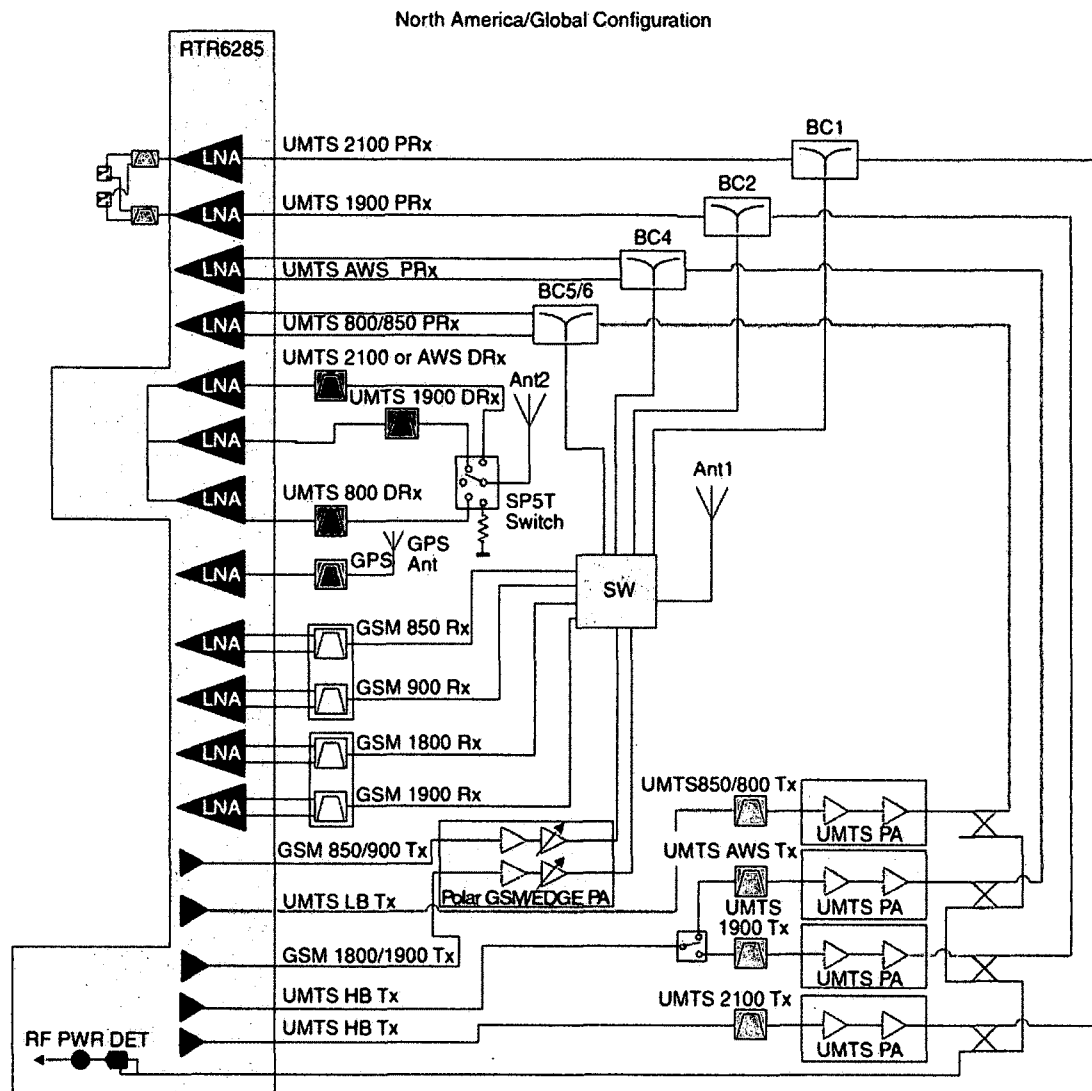


Figure 2-1: A North American cell phone RF front-end with four GSM bands, four UMTS bands, three diversity UMTS bands, and a GPS band covering data channels from 800 to 2400 MHz [2].

Passive electronic components like inductors, capacitors, and resonators are the building blocks of wireless communication networks and are required to transmit, filter, and receive high frequency electromagnetic signals. An electronic resonator (or resonant circuit) in its most basic form consists of a series *RLC* circuit containing a resistor, inductor, and capacitor as shown in **Figure 2-2**.

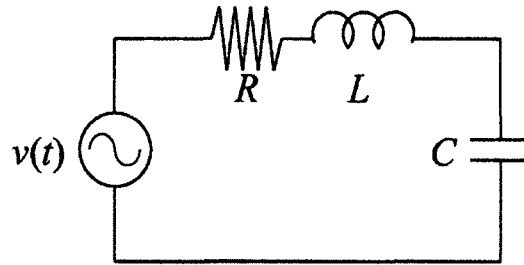


Figure 2-2: Series RLC electronic resonator circuit.

Two important parameters that characterize an electronic resonator are its resonant frequency, expressed in Hertz, given by

$$f_0 = \frac{1}{2\pi\sqrt{LC}}, \quad \text{Eq. 2-1}$$

and its electronic quality factor, given by

$$Q_e = \frac{1}{R}\sqrt{\frac{L}{C}}, \quad \text{Eq. 2-2}$$

where R , L , and C are the circuit's effective resistance, inductance, and capacitance, respectively. The use of variable capacitors and/or inductors in the resonator circuit results in a tunable resonator with a variable resonant frequency, allowing the operating point of the system to change depending on the instantaneous values of L and C . The tunability of the electronic resonator enables a radio to receive signals over a range of frequencies while the electronic quality factor determines the selectivity of the radio. For example, consider a radio receiver designed for the FM frequency band (88–108 MHz). To listen to the Louisiana Tech radio station KLPI, the receiver must be tuned to the center frequency of 89.1 MHz and have a quality factor large enough to filter signals beyond the 200 kHz channel bandwidth, as shown in **Figure 2-3**. The low Q_e values seen in **Figure 2-3** are indicative of poor selectivity as the receiver bandwidth is too large to

filter incident signals from outside the operating band with any degree of efficacy. As a result, high- Q_e components are a fundamental requirement of all wireless receiver systems.

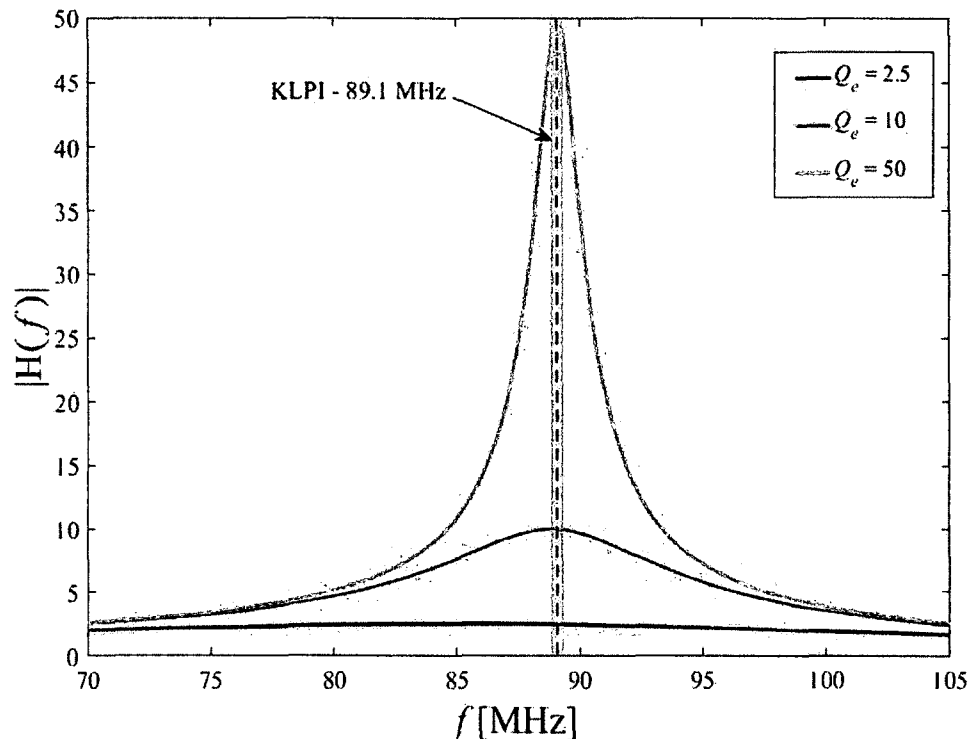


Figure 2-3: Transfer function plot for a simple radio receiver with a resonant frequency of $f_0 = 89.1$ MHz for multiple Q_e values. Large Q_e values (> 50) are necessary to adequately reject signal transmissions on nearby channels.

2.2 Variable Capacitors

The variable capacitor, or varactor as it is commonly known, is an integral passive component in RF systems which require tuning over all or a portion of a frequency band. The performance of a variable capacitor is typically defined by two figures of merit: the capacitive tuning ratio (CTR) of the device and the electronic quality factor (Q_e) of the device at the frequency of interest. The CTR of a variable capacitor is defined as

$$CTR = \frac{C_{\max} - C_{\min}}{C_{\min}} \times 100\% \quad \text{Eq. 2-3}$$

where C_{\max} is the maximum capacitance and C_{\min} is the minimum capacitance of the device. CTR is a measure of the absolute capacitance range of a device; however, this figure does not distinguish between continuous and discontinuous ranges within the capacitance-voltage ($C-V$) characteristics of the device. The Q_e of a varactor device is defined as

$$Q_e = \frac{1}{2\pi f C R_s} \quad \text{Eq. 2-4}$$

where f is the operational frequency of the device, C is the instantaneous device capacitance, and R_s is the equivalent series resistance of the device which represents power losses occurring during each cycle of RF excitation. Analysis of **Eq. 2-4** shows that maximizing Q_e for a varactor design requires minimizing resistive losses.

2.2.1 Solid-State Varactors

Modern radio frequency circuits utilize varactor diodes which operate by reverse-biasing a semiconductor $p-n$ -junction to control the width of the depletion region of the device. Under reverse-bias conditions for an abrupt junction, minority carrier extraction removes charge carriers from the depletion region, resulting in more dopant atoms being ionized and thus a voltage-variable charge on both sides of the junction interface is established, given by

$$|Q| = A \left[2q \epsilon_0 \epsilon_r (V_0 - V) \frac{N_d N_a}{N_d + N_a} \right]^{\frac{1}{2}}, \quad \text{Eq. 2-5}$$

where Q is the charge stored on one side of the depletion region, A is the cross-sectional area of the junction, q is the elementary charge constant, ϵ_0 is the permittivity of free

space, ϵ_r is the relative permittivity of the semiconductor material, V_0 is the electric potential barrier height of the unbiased junction, V is the applied voltage, and N_a and N_d are the dopant concentrations of the n - and p -sides of the junction, respectively.

Taking the derivative of **Eq. 2-5** with respect to the total barrier potential ($V_0 - V$) yields the junction capacitance of the device:

$$C_j = \left| \frac{dQ}{d(V_0 - V)} \right| = \frac{A}{2} \left[\frac{2q\epsilon_0\epsilon_r N_d N_a}{(V_0 - V) N_d + N_a} \right]^{\frac{1}{2}}. \quad \text{Eq. 2-6}$$

Eq. 2-6 shows that a biased p - n -junction has a nonlinear capacitive response to an applied electrical bias. **Figure 2-4** depicts the C - V characteristics of linearly graded, abrupt, and hyperabrupt p - n -junctions with an arbitrary unbiased barrier potential. The observed nonlinear behavior is one of the principal drawbacks of solid-state varactors: the device capacitance has an inherent dependence on the applied signal power such that superposition of an RF signal onto a DC bias voltage can result in a significant capacitance change around the operating point, introducing distortion and aliasing of the RF signal [4].

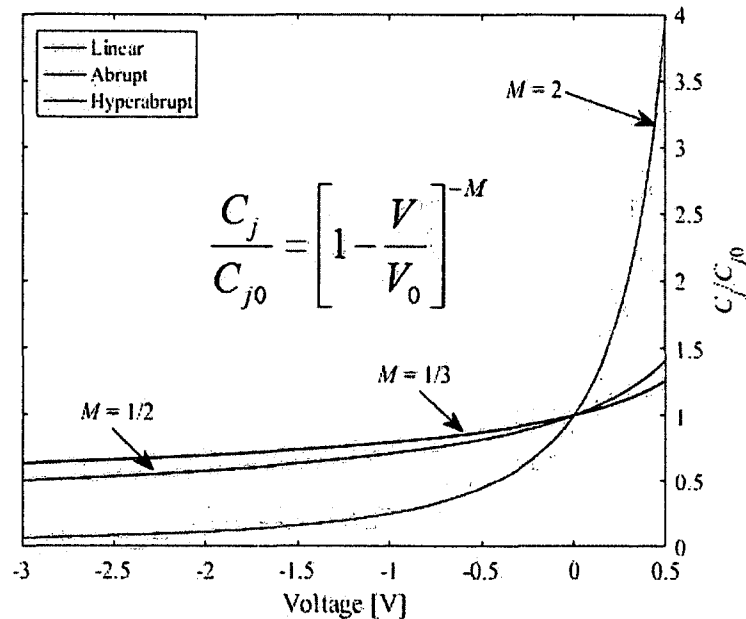


Figure 2-4: Variation of depletion junction capacitance (C_j) with respect to unbiased junction capacitance (C_{j0}) with an applied electrical bias (V) for linearly graded, abrupt, and hyperabrupt p - n -junctions. A steeper dopant gradient (M) results in increased tunability at the expense of device linearity.

To avoid the power handling limitations of a single varactor, many designers chose to implement them in a parallel-series matrix configuration like the one shown in **Figure 2-5**. This configuration divides the signal power among the series stages to prevent accidental forward biasing of the tuning section while the parallel implementation brings the total capacitance back to that of a single device. This practice significantly reduces nonlinear effects; however, the increased component count raises the size, cost, and power consumption of the tuning area [5]. Monolithic (on-chip) integration of tuning varactor diodes has the potential to negate these drawbacks, but numerous investigations into BiCMOS, SiGe, and GaAs RFIC varactors have yielded devices with Q_e values too low to function within a wireless communication system. The low quality factor values can be attributed principally to the use of semiconductor

substrates which have inherently high resistive losses [1]. Solid-state varactors also suffer from limited *CTR* values—**Figure 2-4** shows that an ideal hyperabrupt varactor diode can achieve a maximum *CTR* of approximately 1000% under reverse bias, however commercially available varactor diodes peak at 250–500% [6, 7].

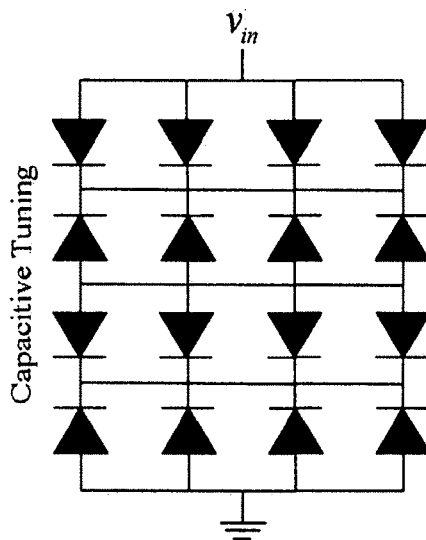


Figure 2-5: $N \times N$ solid-state varactor matrix for reducing nonlinearity in the tuning stage of a radio receiver.

2.2.2 MEMS Variable Capacitors

Increased usage of hand-held and satellite-based applications within scientific, industrial, and military systems has initiated a shift towards smaller, low-power devices that require both increased functionality and reduced power consumption without introducing signal degradation or sacrificing performance. To achieve these stringent requirements, electronics design engineers are moving away from off-chip passive components and are instead monolithically integrating IC-compatible microelectromechanical systems (MEMS)-based devices into RF systems where a

smaller device footprint and lower power consumption are among the paramount criteria for implementation.

RF MEMS technology developed specifically to meet the needs of modern communication platforms requiring high dynamic range components with low integration losses on a size-scale equal to or smaller than semiconductor junction-based devices. Since the field's inception in the early 1990s for defense-related systems [8, 9], RF MEMS have been implemented as a replacement for solid-state components in voltage-controlled oscillators [10–16], phase shifters [17–24], tunable filter systems [25–29], tunable antennas [30–34], and reconfigurable matching networks [35–39]. In some instances, a single RF MEMS device may perform the role of an entire solid-state circuit [2, 5]. The rapid growth of the field is due predominately to the exceptional performance characteristics of micromachined components like high isolation, low insertion losses, and low power consumption as compared to solid-state components and devices in the same role [4].

One area of significant research within the field of RF MEMS is the development of different high- Q_e varactor designs. MEMS variable capacitors are based principally on the classic parallel plate capacitor (shown in **Figure 2-6**) due to difficulties in the manufacture of non-planar structures using conventional microfabrication techniques.

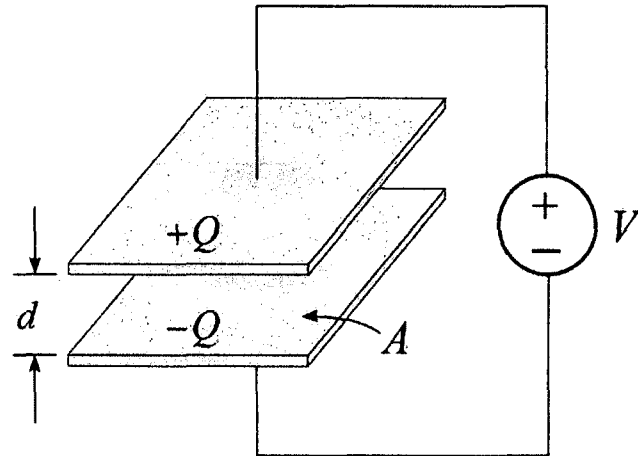


Figure 2-6: A parallel plate capacitor with capacitance $C = |Q/V|$.

MEMS variable capacitors are typically comprised of two planar electrodes separated by a suspension of micromechanical springs. In these devices, one electrode remains stationary and acts as a reference frame while the second electrode is allowed to move and serves as the proof mass of a harmonic oscillator system, as shown in **Figure 2-7**.

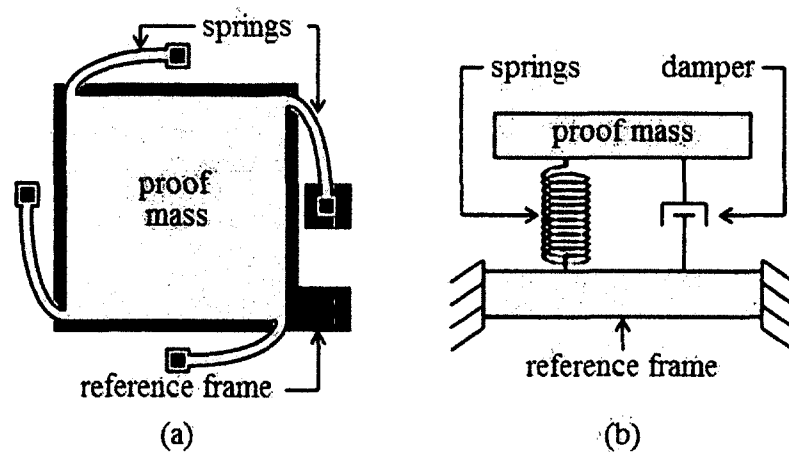


Figure 2-7: (a) A simple planar MEMS variable capacitor and (b) its equivalent mechanical model. The mechanical damping illustrated in (b) is typically attributed to viscous losses due to gas flow resistance at the micro-scale [40].

The varactor functionality of the device shown in **Figure 2-7** is achieved by inducing proof mass displacement through electrostatic, magnetostatic, piezoelectric, or thermal actuation with electrostatic actuation being the most prevalent method. As the displacement between the reference frame (stationary electrode) and proof mass (dynamic electrode) changes, the device capacitance also changes. If an RF signal is applied across the capacitor electrodes, electrostatic attraction between the charged plates should induce electrode movement (assuming a pliant suspension), however in most cases no such displacement can be observed due to the low mechanical bandwidth of the system. This phenomenon can most easily be explained by reviewing the equation for the relative displacement of the proof mass of a simple harmonic oscillator as a function of excitation frequency, ω ,

$$x_m - x_f = \frac{-\omega^2 x_f}{-\omega^2 + j\omega\gamma/m + k_m/m} = \frac{-\omega^2 x_f}{-\omega^2 + j\omega\omega_0/Q_m + \omega_0^2} \quad \text{Eq. 2-7}$$

where x_m is the proof mass position; x_f is the reference frame position; ω_0 is the resonant frequency of the mechanical oscillator which depends on the mass, m , and stiffness, k_m , of the suspension, and Q_m is the mechanical quality factor for the system which depends on the damping coefficient γ , of the system. If the device is excited significantly beyond its resonant frequency ($\omega \gg \omega_0$), **Eq. 2-7** simplifies to

$$x_f - x_m \approx \frac{-\omega^2 x_f}{-\omega^2} \approx x_f. \quad \text{Eq. 2-8}$$

Solving **Eq. 2-8** for x_m yields $x_m = 0$, which shows that the proof mass is effectively stationary under high frequency excitation where $\omega \gg \omega_0$ and thus any AC bias implemented with RF signals will not modulate the device capacitance around its DC operating point as is the case with solid-state varactors.

The capacitance, C , of a parallel plate device can be expressed as a function of its dimensions as

$$C = \epsilon_r \epsilon_0 \frac{A}{d} \quad \text{Eq. 2-9}$$

where ϵ_r is the relative permittivity of the dielectric material between the capacitor plates, ϵ_0 is the permittivity of free space, A is the area of overlap between the capacitor electrodes, and d is the distance separating the capacitor electrodes as shown previously in **Figure 2-6**. Examination of **Eq. 2-9** reveals that there are three parameters which can be changed to vary the capacitance of a parallel plate capacitor-based device—electrode separation, d , electrode area, A , and relative permittivity, ϵ_r . The most prevalent method of creating tunability in a MEMS capacitor is by manipulating the geometric properties of the device, resulting in gap-tuned and area-tuned devices, while varying capacitance by changing the dielectric material between the electrodes has received significantly less scientific exploration.

2.2.2.1 Gap-Tuned Variable Capacitors

A gap-tuned variable capacitor consists of a movable electrode separated from an anchored (stationary) electrode by a mechanical suspension with stiffness k_m . **Figure 2-8** depicts the basic operational principle of an electrostatically actuated gap-tuned varactor.

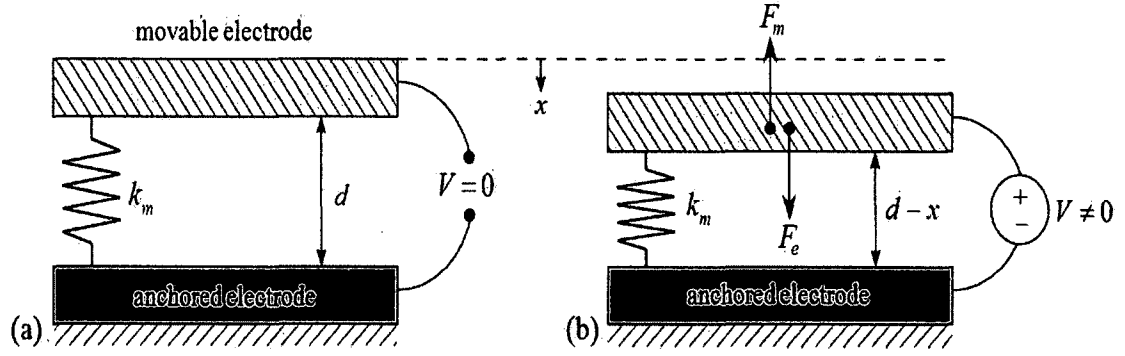


Figure 2-8: Coupled electromechanical model of a simple gap-tuned variable capacitor (a) without and (b) with an applied bias voltage. Adapted from [41].

If a low frequency electric potential is present across the parallel capacitor electrodes, Coulombic attraction between the charged electrodes generates an electrostatic force, F_e , which causes an out-of-plane displacement, x , of the movable electrode towards the anchored electrode. This displacement causes the capacitance of the device to vary with x as

$$C = \epsilon_r \epsilon_0 \frac{A}{d-x}. \quad \text{Eq. 2-10}$$

The energy, W , stored by a capacitor is given by

$$W = \frac{1}{2} CV^2 \quad \text{Eq. 2-11}$$

and from this the electrostatic force generated by the applied voltage is

$$F_e = \left| \frac{\partial W}{\partial x} \right| = \frac{1}{2} \left| \frac{\partial C}{\partial x} \right| V^2 = \frac{1}{2} \epsilon_r \epsilon_0 \frac{A}{(d-x)^2} V^2. \quad \text{Eq. 2-12}$$

The electrostatic force generated by an applied bias is countered by a restorative spring force, F_m , supplied by the mechanical suspension such that the total force acting on the system, F_{tot} , is given by

$$F_{tot} = F_e + F_m = \frac{1}{2} \epsilon_r \epsilon_0 \frac{A}{(d-x)^2} V^2 - k_m x. \quad \text{Eq. 2-13}$$

Examination of **Eq. 2-13** reveals a fundamental limitation of the cap-tuned capacitor tuning scheme: since the restorative force depends linearly on x while the actuating force depends on the square of x , at a sufficiently large induced displacement the electrostatic force will overcome the restorative spring force and the plates will snap together. This phenomenon is known as the pull-in effect and provides the basis for MEMS capacitive switch operation [4]. Without precautionary measures to prevent the plates from snapping together, the pull-in effect can cause permanent damage to a device from stiction, arcing, and mechanical deformation of the electrodes [41, 42].

By treating the pull-in effect as an electrostatic spring force, the total stiffness of the system, k_{tot} , can be analyzed to determine the maximum continuous tuning range of a simple gap-tuned device:

$$k_{tot} = \frac{\partial F}{\partial x} = \frac{\epsilon_r \epsilon_0 A}{(d-x)^3} V^2 - k_m = k_e - k_m. \quad \text{Eq. 2-14}$$

At the pull-in point, the electrostatic and mechanical spring forces cancel. Rearranging **Eq. 2-13** under the condition that $F_{tot} = 0$ and solving for V^2 yields

$$V^2 = \frac{2k_m x (d-x)^2}{\epsilon_r \epsilon_0 A}. \quad \text{Eq. 2-15}$$

Substituting **Eq. 2-15** into **Eq. 2-14** yields

$$k_{tot} = \frac{2k_m x}{d-x} - k_m \quad \text{Eq. 2-16}$$

which expresses the system stiffness as a function of electrode displacement. A plot of **Eq. 2-16** is shown in **Figure 2-9**.

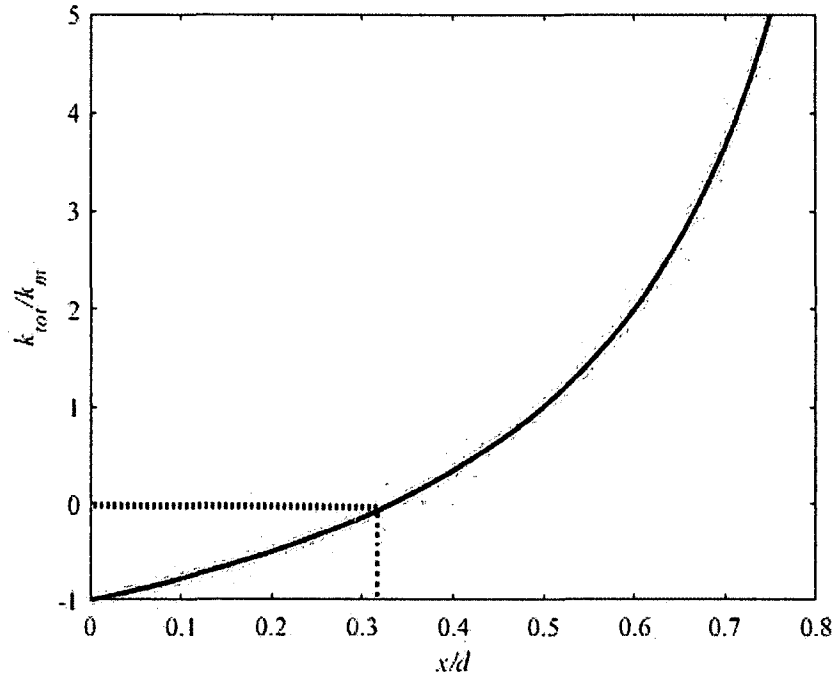


Figure 2-9: Total system stiffness of a gap-tuned varactor as a function of electrode equilibrium displacement for arbitrary initial electrode spacing.

Figure 2-9 illustrates that any displacement greater than $x = d/3$ results in an unstable system ($k_{tot} > 0$) wherein any increase in x causes a force which further increases x as the electrostatic force is then greater than the restoring spring force. Substituting $x = d/3$ into **Eq. 2-17** yields the maximum capacitance that can be achieved before pull-in occurs:

$$C_{\max} = \epsilon_r \epsilon_0 \frac{A}{d - \frac{d}{3}} = \frac{3}{2} \frac{\epsilon_r \epsilon_0 A}{d} = 1.5C_0 \quad \text{Eq. 2-17}$$

where C_0 is the unbiased capacitance of the parallel plate device. From **Eq. 2-17**, the theoretical limit for the capacitive tuning range of a gap-tuned varactor is 150%, however the presence of fringing fields and variances in electrode alignment due to manufacturing errors often limit the tuning ratio of these devices to significantly lower values.

The first gap-tuned MEMS varactor device was fabricated in 1996 by Young and Boser. The device was created via surface micromachining of multiple 1 μm thick layers of aluminum on a silicon substrate [10, 11]. The varactor uses suspensions of four folded-beam springs in a parallel configuration to enable vertical movement of the 200 μm \times 200 μm electrodes over a 1.5 μm electrode gap. Aluminum was used for the device layer to limit resistive losses and thereby achieve a high electrical quality factor at RF frequencies, while a bottom layer of aluminum serves as a ground plane and shields the device structure from the lossy silicon substrate. A thick oxide layer isolates the device layer from the electrical ground, reducing parasitic effects which could influence the capacitive tuning range of the device. The electrode perforations seen in the SEM image of **Figure 2-10** reduce the effects of squeeze film damping between the capacitor electrodes, enabling an increased response time of the device to a changing electrical bias.

The device achieved a continuous variable capacitance from 2.11 pF at 0 V bias to 2.46 pF at 5.5 V bias, corresponding to a *CTR* of 16.6%—significantly less than the theoretical maximum of 50% due to parasitic coupling between the aluminum suspension and stationary electrodes as well as deformation of the dynamic electrode structures. A Q_e of 62 at 1 GHz was achieved from the use of a conductive device structure, exceeding the electronic quality factors reported by then state-of-the-art varactor diodes at similar frequencies. Subsequent iterations of the design were able to lower the tuning voltage to 3 V while achieving similar *CTR* and Q_e [12], while similar designs developed by other researchers achieved *CTR* values of 35.7% with a Q_e of 23 at 1 GHz [16] and *CTR* values of 50%, the theoretical maximum, with Q_e of 20 at 1 GHz [43]. The two-plate varactor

design was later enhanced by introducing mechanical restraints which increase local spring-stiffness, thereby preventing or limiting pull-in effects as the dynamic electrode displacement increases [44–46].

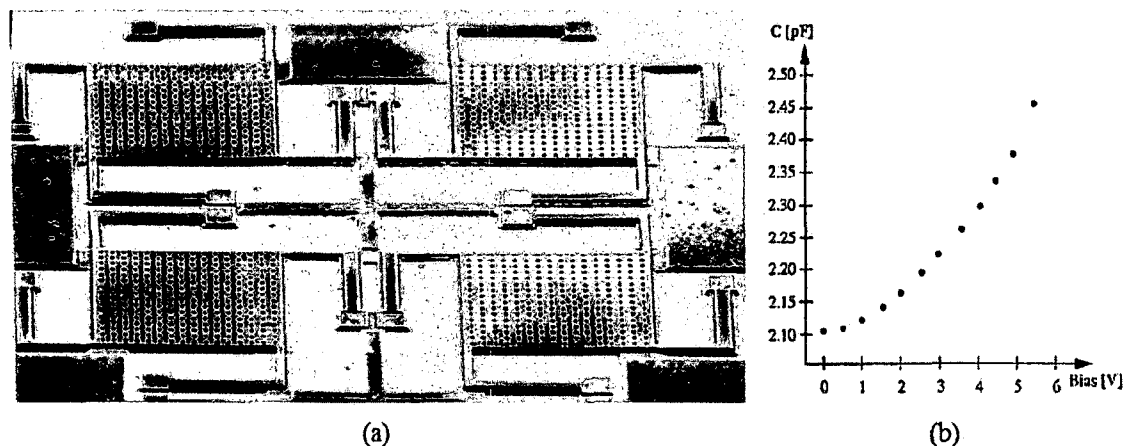


Figure 2-10: (a) Scanning electron microscope (SEM) image and (b) C - V curve for Young and Boser’s gap tuned varactor [10,11].

Dec and Suyama expanded on the work of Young and Boser by developing a three-plate gap-tuned system, shown in **Figure 2-11**, to increase the maximum theoretical tuning ratio of gap-tuned devices [47]. The 3-plate scheme utilizes two control voltages to electrostatically actuate the movable center electrode in both the up direction (increasing device capacitance) and down direction (decreasing device capacitance). The extended range of movement for the center plate allow the device capacitance to change by $\pm 0.5C_0$, thereby achieving a maximum theoretical CTR of 100%. The device was fabricated using a multi-user MEMS polysilicon (MUMPs) process [48]. The polysilicon electrodes are $426 \mu\text{m} \times 426 \mu\text{m}$, with a nominal separation of $0.75 \mu\text{m}$. The capacitance of the signal capacitor (formed between the top stationary electrode and the movable plate) varied from 3.5 pF with $V_1 = 0 \text{ V}$ and $V_2 = 1.8 \text{ V}$ to 4.39 pF with $V_1 = 0.7 \text{ V}$ and $V_2 = 0 \text{ V}$, corresponding to a CTR of 25.4%, again significantly lower than the maximum

theoretical value. This is ascribed principally to residual stresses in the movable electrode layer which cause deformation of the plate and the parasitic capacitances formed by the RF-signal pads on the die. An electronic quality factor of 9.6 at 1 GHz was measured for the device. Further refinement of the 3-plate tuning scheme by Dec and Suyama achieved a CTR of 87% however the Q_e of the device was only measured to be 15.4 at 1 GHz, attributed to the use of lossy polysilicon device structures required in the MUMPS process [43].

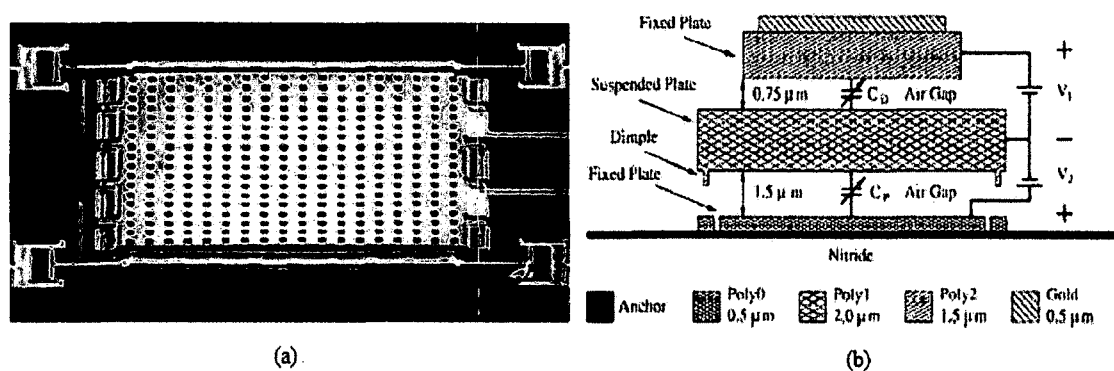


Figure 2-11: (a) SEM image and (b) cross-section schematic of Dec and Suyama's 3-plate gap-tuned varactor design [47].

In 2007, Konishi *et al.* added physical spacers to the 3-plate tuning system which enabled the formation of a signal capacitance with a very small electrode separation (0.3 μm) [49]. Unlike the device described in [47], actuation is no longer bi-directional; instead the actuation voltage serves to increase the gap of the signal capacitor which causes the device capacitance to decrease with applied voltage. The design, shown in **Figure 2-12**, demonstrated a remarkable CTR of 1200% by utilizing a large initial separation between the movable plate and bottom-most electrode, however no electronic quality factor data was included in the paper. Barrière *et al.* developed a similar design capable of increased power handling at the cost of limited (292%) CTR [50].

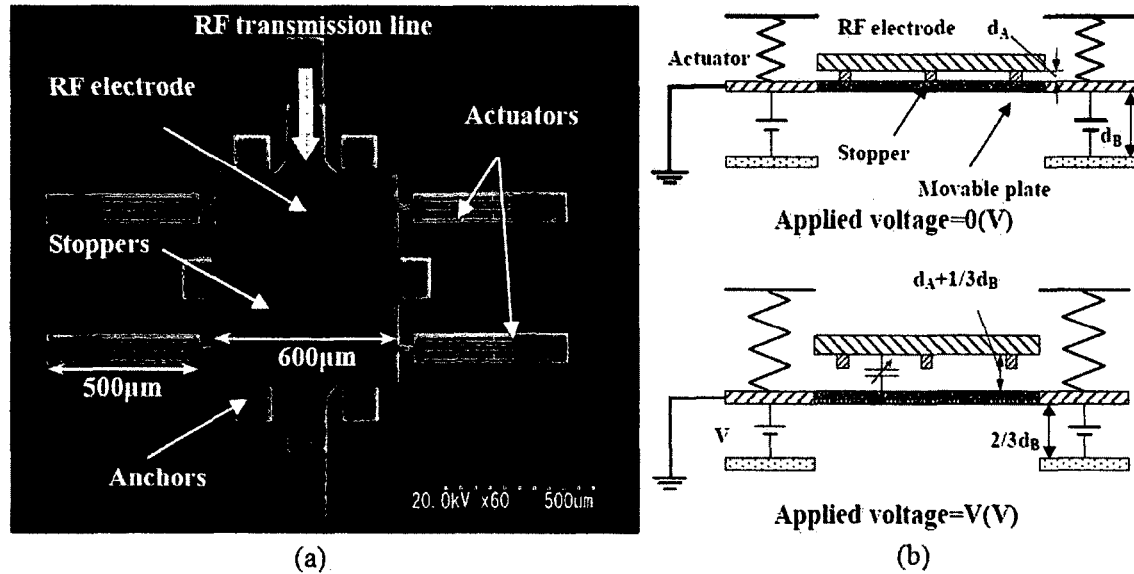


Figure 2-12: (a) SEM image and (b) operational schematic of the uni-directionally actuated 3-plate variable capacitor [49].

2.2.2.1.1 Dual-Gap Varactors

A significant advancement in the performance of parallel-plate gap-tuned varactors was achieved by Zou *et al.* wherein their research group developed a stepped dynamic electrode which isolates the signal capacitance from the electrostatic actuation capacitors [51, 52], shown in **Figure 2-13**. By using a gap between the actuation electrodes of more than three-times that of the gap used to define the signal capacitance, pull-in instability is no longer a factor and the travel range of the signal electrode is greatly increased. Thermally evaporated gold thin film is used as the material of the fixed bottom plates while the suspended top plate is made of electroplated Permalloy (nickel-iron alloy) to limit resistive losses. Surface roughness and stress induced warping of the signal electrode, as well as the presence of an insulation layer to prevent stiction, limited the CTR of the device to 69.8%, however a Q_e of 30 at 5 GHz was reported [52]. The benefit of isolating the actuation and signal electrodes has been exploited by numerous

other dual-gap varactor designs [53–58], with tuning ranges exceeding 500% [56, 57] and Q_e values between 50 and 100 at K_a -band frequencies [53, 54, 56].

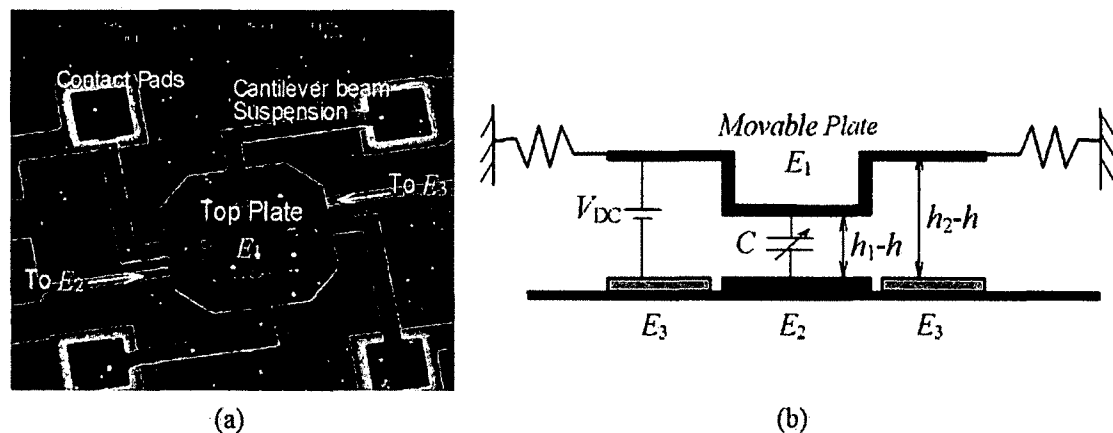


Figure 2-13: (a) SEM picture and (b) cross-section schematic of a dual-gap varactor device [52].

Nieminen *et al.* developed a dual gap varactor that utilizes a planar dynamic electrode and stationary electrodes of varying heights [59], the opposite of the isolated tuning scheme developed in [51]. The device, shown in **Figure 2-14**, was fabricated using a novel surface micromachining process on gold structural layers patterned on top of a low resistivity silicon substrate. The lossy substrate was then removed via etching to prevent resistive losses at RF frequencies. The inverted dual-gap device achieved a CTR of 125% and Q_e of 66 at 1 GHz. Similar designs by other researchers [60–63] achieved CTR s of up to 367% [60] however significantly high Q_e values were not reported.

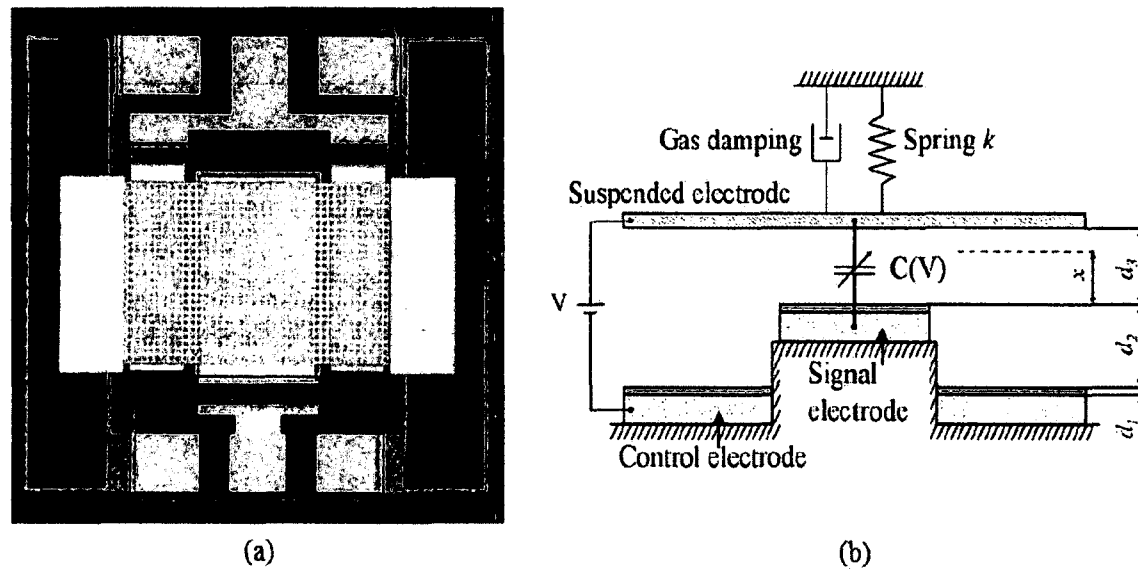


Figure 2-14: (a) SEM image and (b) operational schematic of an inverted dual-gap MEMS variable capacitor [59].

2.2.2.1.2 Zipping Varactors

Electrostatically-actuated zipping varactors are an adaptation of “touch-mode” actuators in which a pliant electrically conductive cantilever (or membrane) and planar electrode are electrically biased such that the beam deflects to contact the planar electrode. Subsequent biasing creates a “zipping” motion which increases the contact area between the conductive cantilever and planar electrode, as seen in **Figure 2-15**. In a zipping varactor, the restorative mechanical spring force increases as the effective beam length becomes shorter due to the zipping action. To counteract this increase in mechanical spring force and continue zipping towards the anchor, the electrostatic spring force must also be increased by applying more electrical bias. A linear C - V response can be achieved by optimizing the shape of the bottom electrode such that the electrostatic force increases towards the cantilever anchor. Because the region of beam deflection within the device results in non-parallel plates, there is no closed-form solution for the

total device capacitance although approximations can be made under specific circumstances [65].

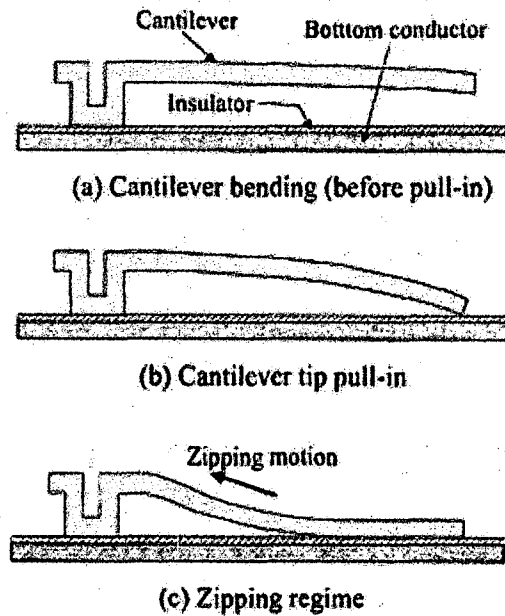


Figure 2-15: A zipping actuator/varactor at (a) initial beam displacement, (b) cantilever pull-in, and (c) zipping regime [64].

The first zipping varactor was developed by Hung and Senturia in 1998 [64]. In this design (shown in **Figure 2-16**), a rectangular cantilever is pulled down towards the patterned bottom electrode via electrostatic actuation. After the cantilever collapses onto the bottom electrode because of pull-in effects, the device geometry becomes a clamped-clamped beam in which there is a vertical offset between the anchor points, yielding an ‘S’-shaped beam structure. Further biasing causes the ‘S’ to move towards the anchor, resulting in the zipping motion depicted in **Figure 2-15**. The device utilizes dimples to maintain a small air gap between the cantilever beam and bottom electrode during actuation. This practice serves to prevent stiction, shorting, and dielectric charging during

operation. The device achieved a CTR of 76.8%, however no Q_e values could be obtained since only DC characterization was performed.

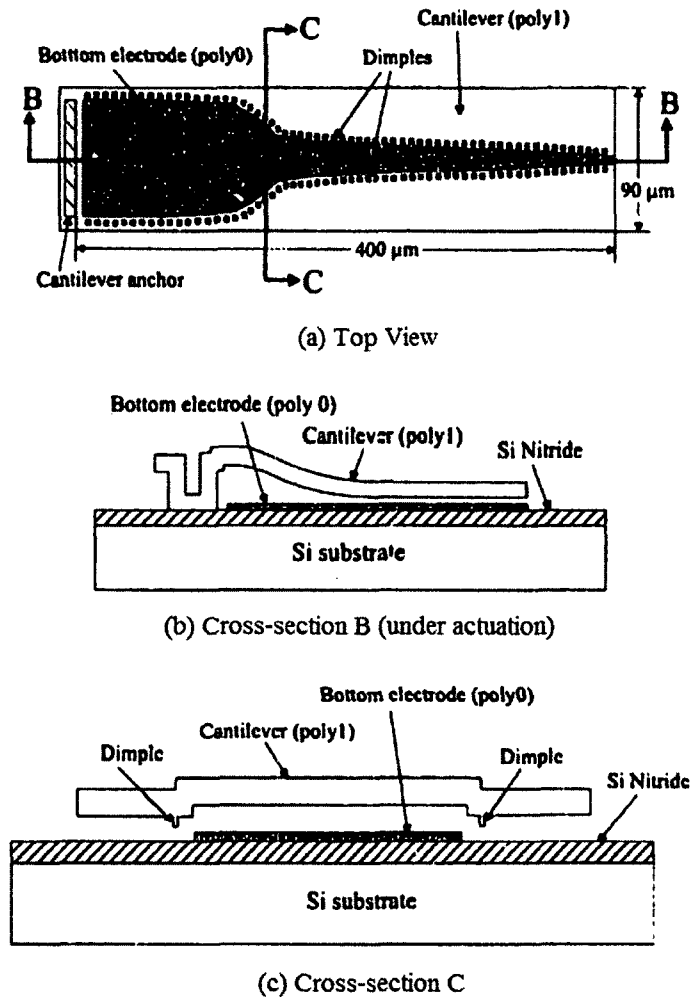


Figure 2-16: Tunable capacitor device developed by Hung and Senturia. (a) Top view showing a shaped bottom electrode underneath a rectangular cantilever beam. (b) Lengthwise cross-section of beam under actuation in the zippering regime. The air gap under the end of the beam is defined by dimple spacers. (c) Width cross-section illustrating the dimple spacers [66].

Similar zippering varactors to [64] have been fabricated by other researchers [67–75]. Ionis *et al.* fabricated their device using the MUMPs process as used by Hung and Senturia and achieved a CTR of 48.4% [68, 69]. They improved upon the previous design

by depositing a gold layer on top of the cantilever to improve Q_e measurements, however a value of only 6.5 at 1.5 GHz was reported, significantly lower than expected. Luo *et al.* explored the use of multiple cantilevers of varying lengths connected in parallel to extend tunability via multiple pull-in characteristics, however the use of a high-permittivity dielectric material created significant issues with dielectric charging and stiction [71]. Mahameed *et al.* developed multiple zipping varactors with separated actuation and RF electrodes [74, 75], as shown in **Figure 2-17**. These devices exhibited significantly better performance than other cantilever-based zipping varactor designs, achieving *CTRs* of 180% and 230% and Q_e of greater than 100 at 3 and 5 GHz, respectively.

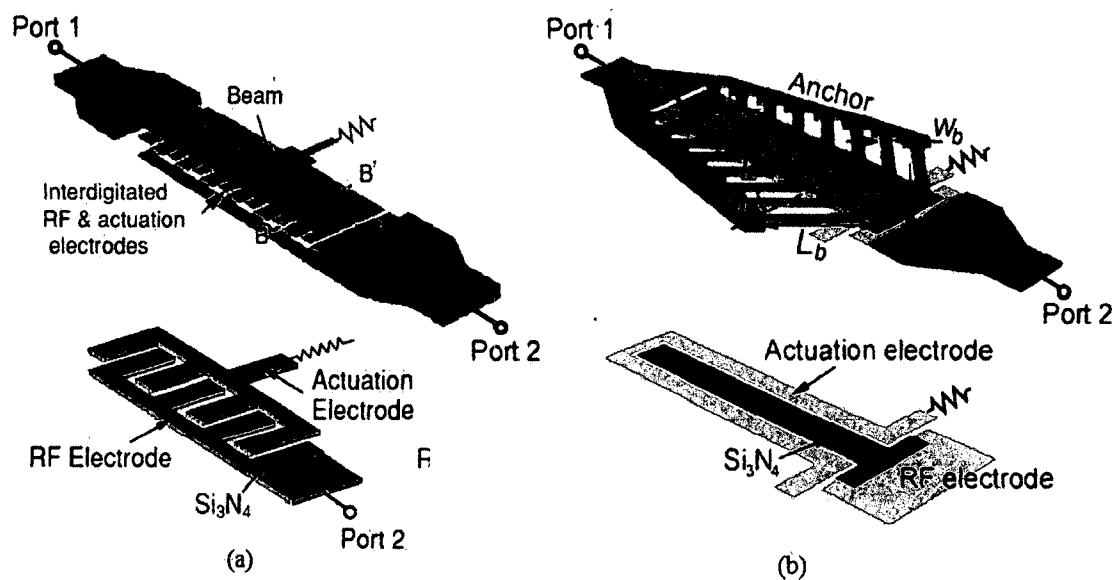


Figure 2-17: Zipping varactors using (a) transverse interdigitated electrodes [74], and (b) longitudinal interdigitated electrodes with a tethered suspension to increase local stiffness [75].

Muldavin *et al.* developed a zipping varactor that utilizes a corrugated tri-layer ($\text{SiO}_2/\text{Al}/\text{SiO}_2$) cantilever with a stress-induced deflection which causes zipping to be directed away from the anchor point [76], as shown in **Figure 2-18**. The device utilized

separate actuation and RF electrodes which were biased using bipolar square-wave signals. By adjusting the potentials seen across each electrode pair, the amount of overlap capacitance could be varied, resulting in a CTR of nearly 1600%, however no Q_e values were reported.

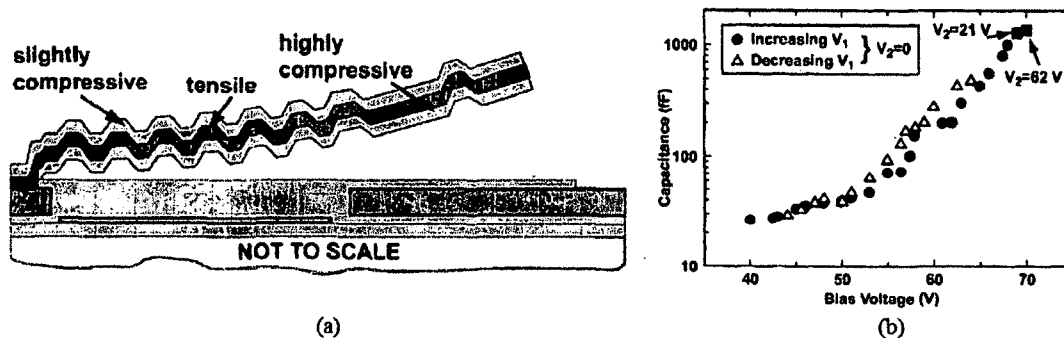


Figure 2-18: (a) Schematic illustration and (b) C - V response of corrugated-cantilever zipping varactor [76].

Pu *et al.* expanded on the work of Muldavin by developed curved cantilever-based zipping varactors that utilize a tapered cantilever for extended tuning range [77–79], shown in **Figure 2-19**. The devices are made of gold and the tapered cantilevers have a Cr/Cu layer on top to create a residual stress which causes the initial curved profile seen above. The linear tapering of the cantilever increases the local mechanical stiffness of the beam along its length towards the free end which makes the pull-in voltage change as a function of length, thereby preventing switch-like operation which would occur if the cantilever and actuation electrode had the same dimensions. The tapered beam design resulted in a CTR of 1545% with a Q_e of 176 at 2 GHz [77] while a subsequent iteration of the design achieved a CTR of 2700% with a Q_e of 317 at 1 GHz [79].

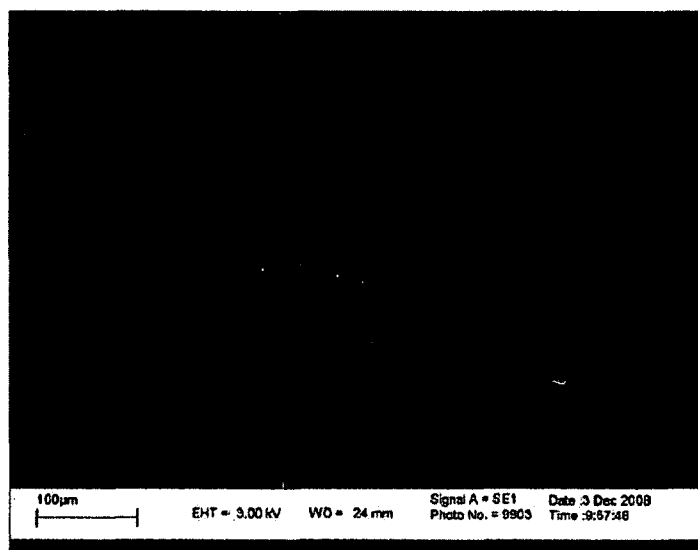


Figure 2-19: SEM image of tapered bimorph zipping varactor mounted on a coplanar waveguide [77].

Bakri-Kassem and Mansour expanded on the zipping varactor concept by developing devices which use flexible metal planar membranes to achieve zipping motion [80]. In this design, both the top electrode (a rigid metal plate) and bottom electrode (a flexible polysilicon membrane coated with a nitride insulation layer) are allowed to move under electrical biasing, resulting in a small tuning range before pull-in effects occur. After the pull-in voltage is exceeded, the plates collapse together and then zip further as the bias voltage is increased, achieving a discontinuous CTR of 280% and a Q_e of 8.8 at 1 GHz. To achieve continuous tunability, Bakri-Kassem *et al.* revised the design of [80] by removing the initial gap between the varactor plates [81], as seen in **Figure 2-20**. The varactor is made of two plates with different curvatures suspended over an etched cavity in the silicon substrate, where the differing curvatures are the features that enable zipping operation which resulted in a CTR of 115% and a Q_e greater than 300

at 1.5 GHz. A third design was implemented which placed stiff carrier beams at the corners of the upper flexible electrode for the purpose of maintaining separation at the edges of the device for a linear C - V response [82]. The addition of the unanchored cantilever beams increased rigidity before total collapse of the plates, resulting in a nearly linear CTR of nearly 500% and a Q_e of 29 at 1 GHz. Other researchers explored membrane-based zipping varactors [83–89] with design innovations including a circular tethered membrane and fulcrum to expand tunability [84], a segmented dynamic electrode based on micromechanical hinges which provide tailorable stiffness at specific nodes to increase linearity [86, 87], and suspensions of differing lengths which create a spatially-varying pull-in effect that smooths the device C - V response [89].

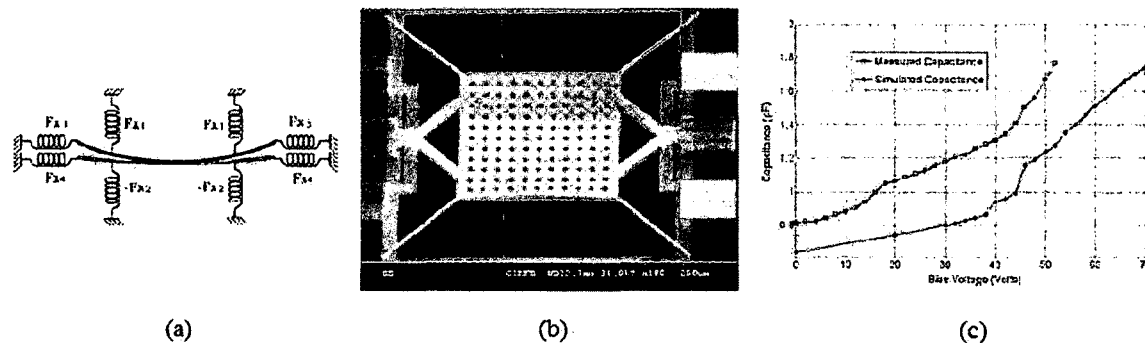


Figure 2-20: (a) Device schematic, (b) SEM image, and (c) model and prototype C - V characteristics for the dual-zipping variable capacitor [81].

2.2.2.1.3 Interdigitated Gap-Tuned Varactors

As an alternative to vertical (out-of-plane) electrostatic actuation schemes, some researchers have developed gap-tuned varactors that rely on in-plane actuation via capacitive comb-drives. The use of comb-drive actuators negates the possibility of pull-in instability however the overall size of the varactor device is typically larger than out-of-plane electrostatic actuation-based designs with a similar nominal capacitance due to

the requirement of multiple (often hundreds) of overlapping fingers to achieve said capacitance.

The first interdigitated gap-tuned varactor was developed by Li and Tien and was created using a bulk micromachining method: deep reactive ion etching (DRIE) of a silicon wafer (acting as the device layer) bonded to a glass wafer (acting as the substrate) [90]. The DRIE micromachining process allows for complex device architectures to be fabricated using only a few processing steps as opposed to the surface micromachining techniques used to manufacture the devices previously described. The device, shown in **Figure 2-21**, achieved a CTR of 311% with no Q_e value reported. Xiao *et al.* developed a similar design which achieved a CTR of 595% and a low Q_e value of 120 at 100 MHz, limiting the device's use to low frequency systems [91].

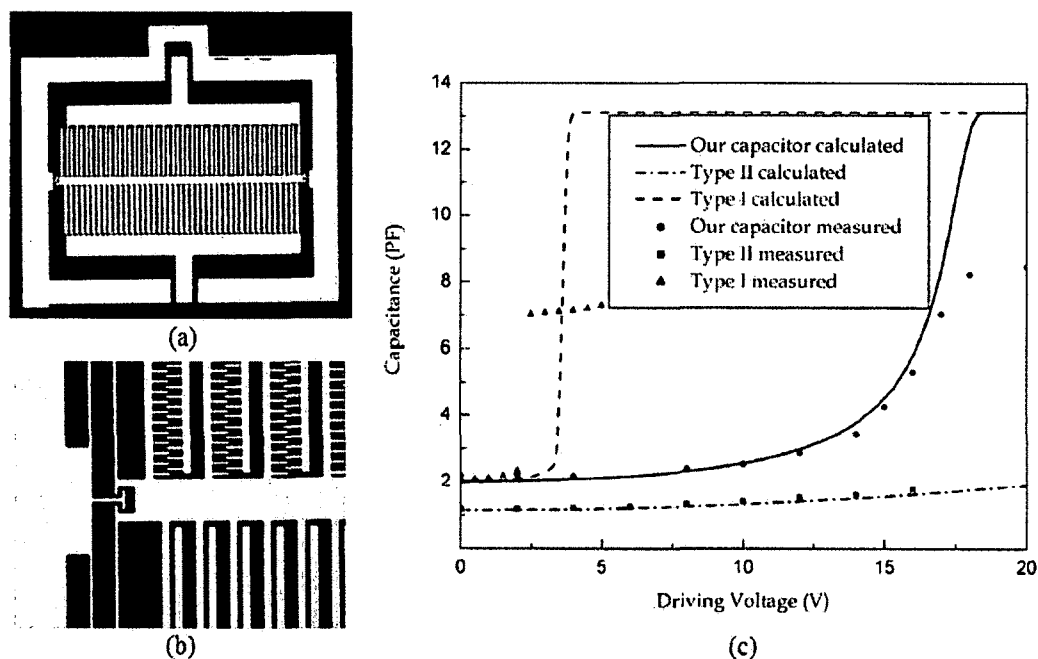


Figure 2-21: (a) Micrograph of the interdigitated gap-tuned variable capacitor; (b) Close-up view of the actuator and variable capacitor microstructure; (c) C - V response for the device [90].

Monajemi and Ayazi developed an interdigitated gap-tuned varactor suitable for higher frequency applications by using high aspect-ratio combined poly- and single-crystal silicon (HARPSS) technology [92]. The HARPSS fabrication technology enables extremely small electrode gaps to be achieved, resulting in an DC actuation voltage of only 2 V to be used to tune the device capacitance. The design included a low-inductance suspension and a thin gold coating over the interdigitated fingers which yielded a CTR of 100% and a Q_e of 49 at 1 GHz. A subsequent design iteration increased the CTR to 240%, however only simulated quality factor data was presented [93]. Rais-Zadeh and Ayazi also developed an interdigitated gap-tuned varactor using an electroplated silver device layer on an insulating polymer substrate. The high conductivity silver structure greatly increased the Q_e to 200 at 1 GHz, however the tuning ratio was only 129% [94]. The HARPSS and silver devices are shown in **Figure 2-22**.

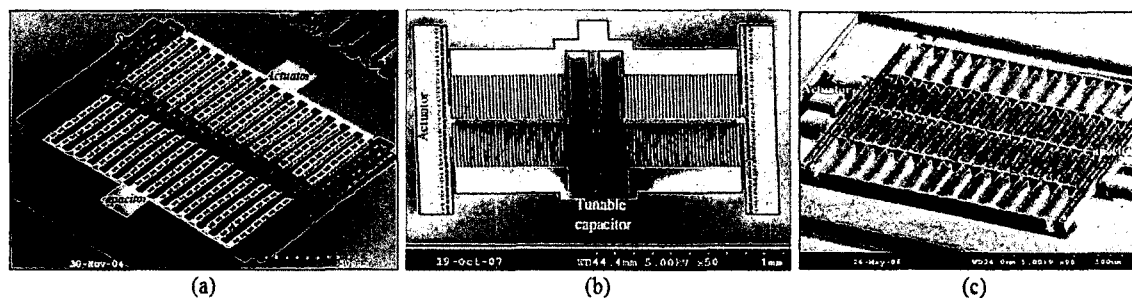


Figure 2-22: (a) HARPSS varactor reported in [92]; (b) HARPSS varactor reported in [93]; Silver varactor reported in [94].

Han and Cho developed an interdigitated gap-tuned varactor that uses parallel-interconnected capacitive switches as actuators [95, 96]. The device, shown in **Figure 2-23**, utilizes capacitive switches with varying electrode displacements to control the overall displacement (and thus tuning) with a high degree of precision. By using an array of parallel-connected capacitive switch actuators, a CTR of 76% with a Q_e of 24 at 1 GHz

was reported. Additionally, the unique tuning scheme allowed for the device capacitance to be varied with ~ 10 fF precision, a tenfold increase in precision versus other gap-tuned devices.

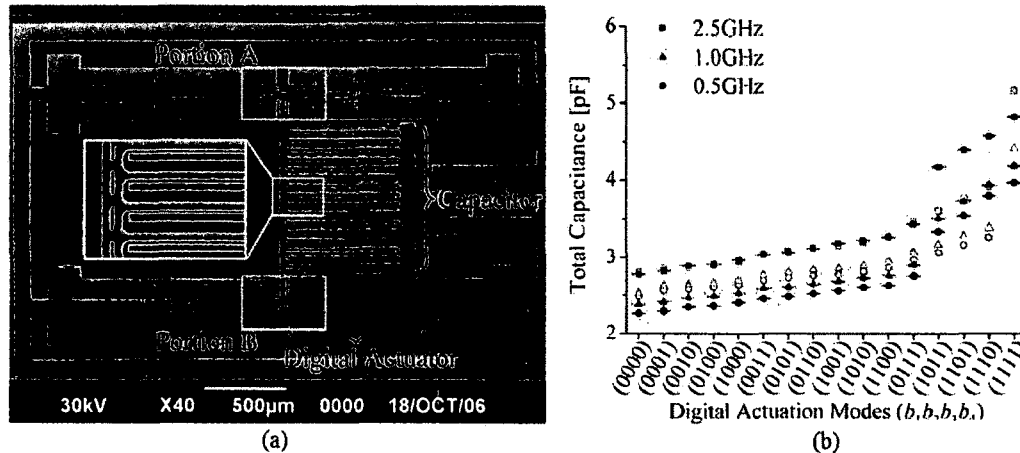


Figure 2-23: (a) SEM image and (b) C - V response for the high-precision, capacitive-switch actuated interdigitated gap-tuned variable capacitor [96].

2.2.2.1.4 Non-Electrostatically Actuated Gap-Tuned Varactors

In addition to electrostatic actuation, many researchers have explored alternative actuation schemes like electrothermal and piezoelectric actuation. Electrothermal actuation is based on the thermal expansion of the actuator microstructure, usually caused by resistive heating of the structure by applying a current. Electrothermal actuators are capable of generating large forces using low operational voltages, however they typically suffer from high DC power consumption and slow response, limited by the time it takes to heat or cool the structural material.

The first electrothermally actuated gap-tuned varactor was demonstrated by Wu *et al.* and utilized flip-chip integration of a polysilicon device structure onto an insulating substrate [97, 98]. Thermal expansion of the actuator arms causes the vertical displacement of the upper electrode to increase, as shown in **Figure 2-24**. This geometric

amplification tuning scheme yielded a CTR of 600%, and the device's transfer to a ceramic substrate yielded a measured Q_e of 1050 at 1 GHz. Designs using similar electrothermal actuators were demonstrated by Feng *et al.* [99] and Mireles *et al.* [100].

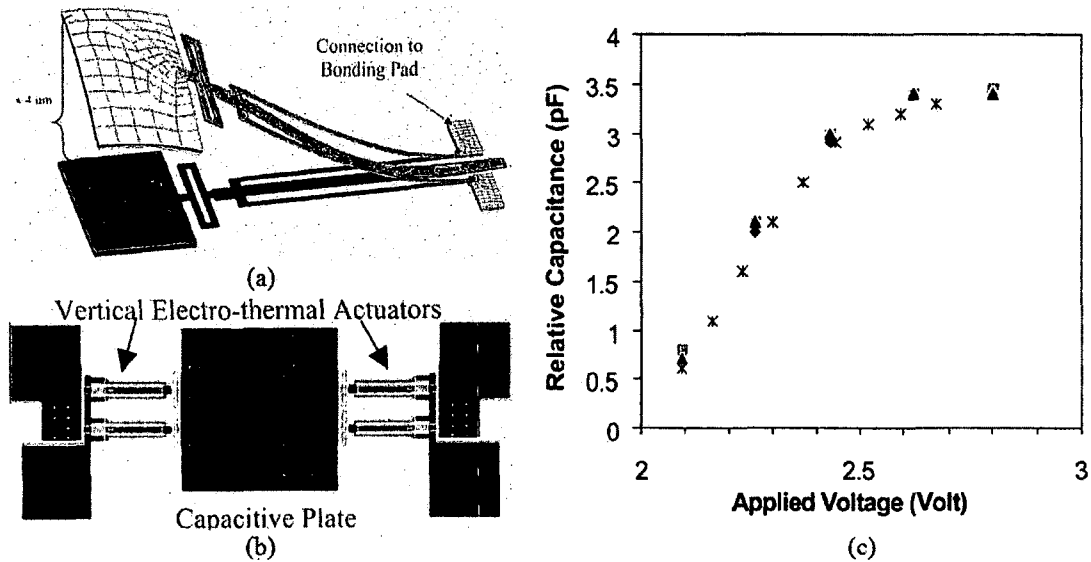


Figure 2-24: (a) Finite element simulated deformation of vertically deflecting electrothermal actuators (scaled 100x); (b) SEM image and (c) C - V response of electrothermally actuated gap-tuned variable capacitor [98].

Jackson and Saavedra developed an electrothermally actuated interdigital gap-tuned varactor [101], shown in **Figure 2-25**. The device utilizes a chevron-shaped electrothermal actuator that uses geometric amplification to increase the relative displacement generated by the actuator, enabling in-plane movement of the dynamic electrode fingers. The device achieved a CTR of 88.2%; no Q_e data was available.

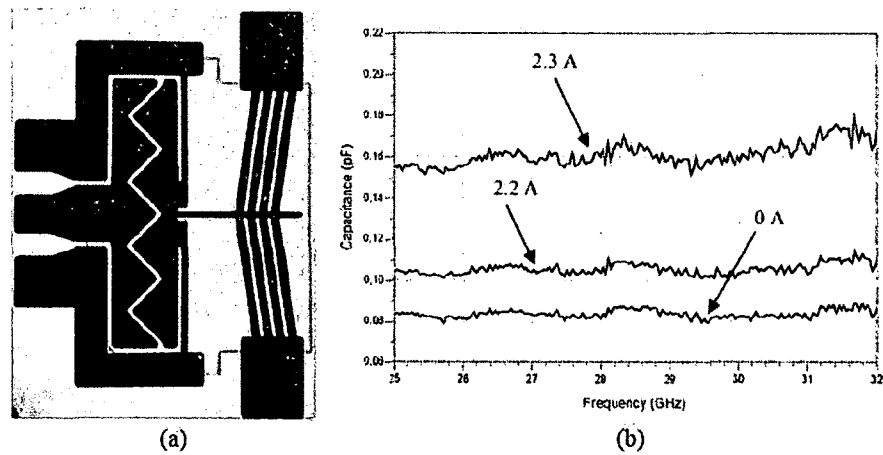


Figure 2-25: (a) Photograph and (b) capacitive response vs. frequency for the device reported in [101].

Reinke *et al.* developed an electrothermally-actuated interdigitated gap-tuned varactor with a secondary electrothermally-actuated latching mechanism (shown in **Figure 2-26**), allowing the device to maintain discrete capacitance values without expending additional power [102]. The device's varactor area is thermally isolated from the actuators which limits unwanted heat-induced deflection of the cantilever electrodes. Additionally, this practice isolates the actuator from the RF signal path, lowering the parasitic capacitances which could restrict tunability. A *CTR* of 590% was reported with a Q_e of 95 at 1 GHz using a tuning voltage of only 3 V.

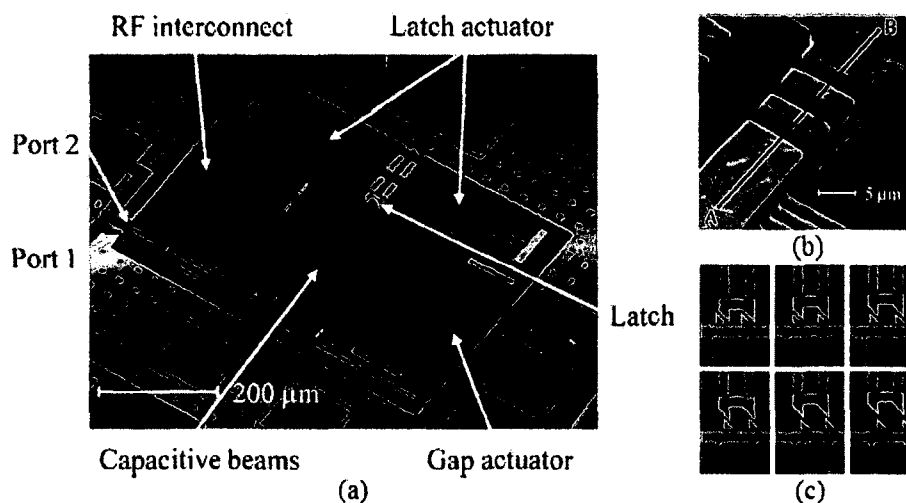


Figure 2-26: SEM images of (a) the completed device, (b) thermal isolation scheme, and (c) latching mechanism for the device described in [102].

Piezoelectric actuation requires the use of specialized materials which mechanically deform in the presence of electric fields. Such actuators are capable of bi-directional displacements using low operational voltages, however the displacements generated are typically small but can be amplified by using multiple transducers in parallel.

The first gap-tuned varactor utilizing piezoelectric actuation was developed by Park *et al.* in 2001 [103]. Shown in **Figure 2-27**, the device utilizes PZT actuators whose height increases under the application of a biasing electric field. The device achieved a *CTR* of 210% and a *Q_e* of 210 at 1 GHz, however the processing temperatures required to fabricate the device (650 °C) were too high to enable integration with standard IC electronics.

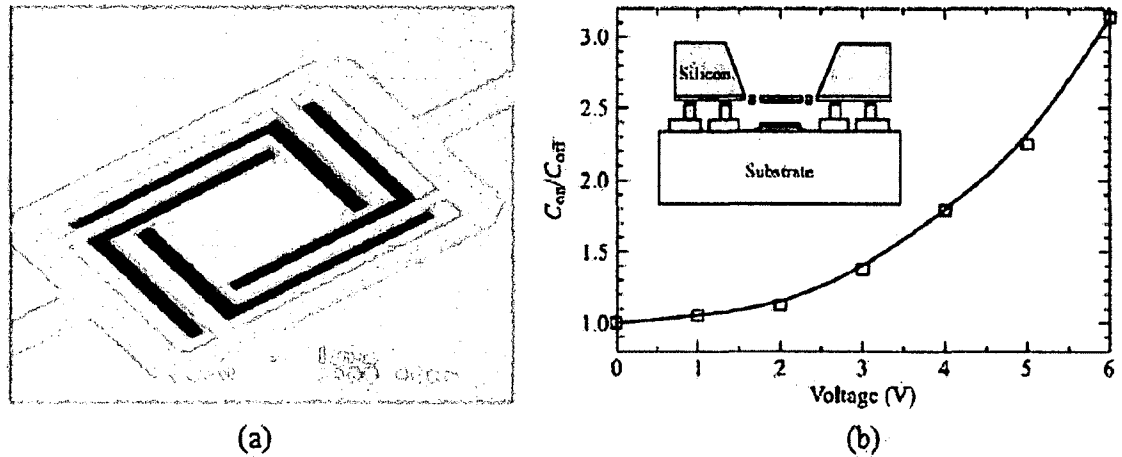


Figure 2-27: (a) SEM image of piezoelectrically-actuated gap-tuned varactor and (b) C - V response and device schematic [103].

Lee and Kim developed a gap-tuned variable capacitor that uses ZnO unimorph actuators to induce electrode separation [104]. Zinc oxide was chosen as the piezoelectric material as processing occurs at 300 °C, a temperature compatible with IC fabrication and processing. Shown in **Figure 2-28**, the device works by using bi-directional deflection of the actuator beam to raise or lower the mass structure, thereby changing the device capacitance. The device achieved a large CTR of 2000%, however the Q_e was measured to be 10 at 2 GHz, too low for implementation into many RF systems. Future work developing a modified piezoelectrically-actuated varactor yielded a CTR of 1300% with a Q_e of 20 at 2 GHz [105, 106].

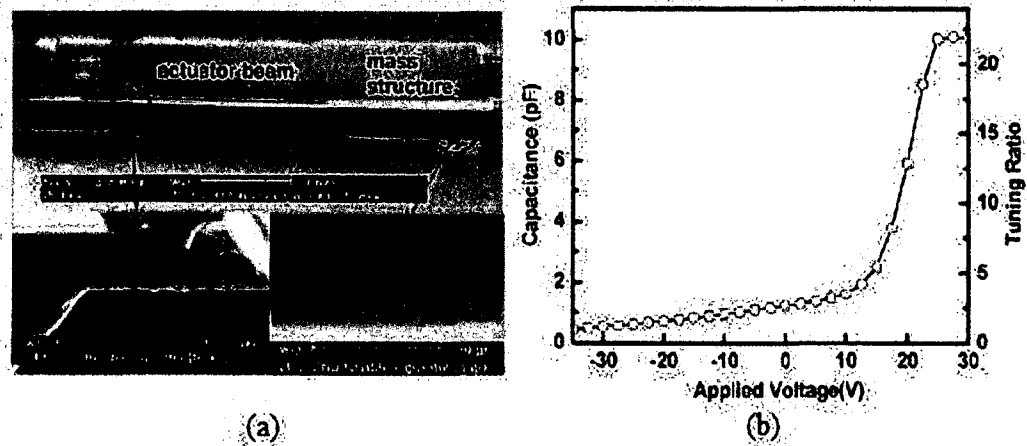


Figure 2-28: (a) SEM image and (b) C - V response of piezoelectric cantilever-tuned varactor [104].

Nagano *et al.* developed a piezoelectrically-actuated gap-tuned variable capacitor that utilizes a stacked AlN bimorph structure to enable simultaneous contraction and expansion of individual piezoelectric structures [107, 108], shown in **Figure 2-29**. By systemically inducing compression in some regions and expansion in others through the use of differing polarity voltages, cantilever deflection is achieved which causes the unanchored electrode to move vertically. The resulting CTR of the device was 400% with no quality-factor information available.

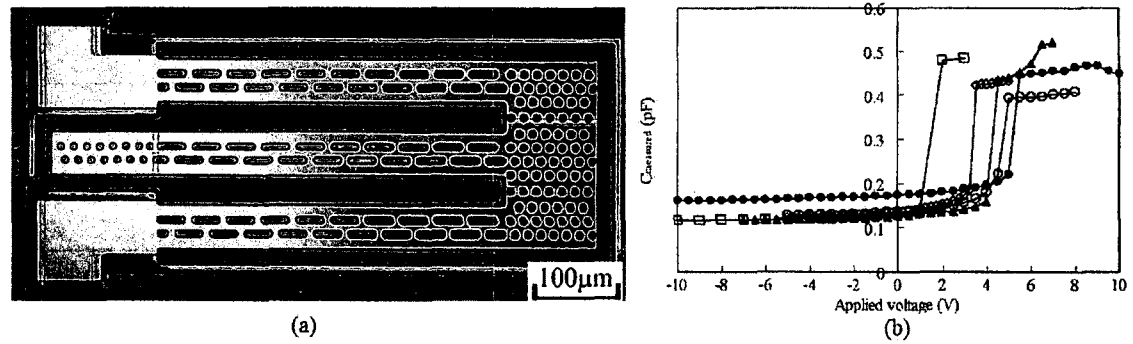


Figure 2-29: (a) SEM image and (b) C - V response of gap-tuned varactor using an AlN bimorph actuator [107, 108].

2.2.2.2 Area-Tuned Variable Capacitors

Area-tuned variable capacitors operate by changing the area of the overlap between parallel capacitor electrodes, with the most common implementation being interdigitated comb-drive devices, as shown in **Figure 2-30**.

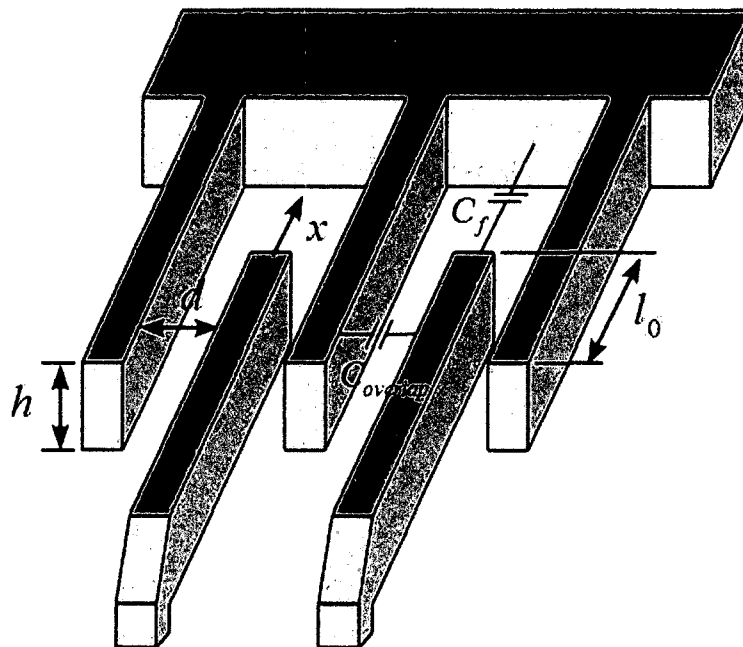


Figure 2-30: Schematic for a section of an interdigitated comb-drive system representative of both an area-tuned variable capacitor and actuator. Adapted from [41].

In an area-tuned comb-drive device, the variable capacitance is formed by the parallel electrical connection of multiple finger sidewalls. When a finger of the comb-drive moves by a distance x , the capacitance formed by a single finger-to-finger overlap is given by

$$C_{overlap} = \epsilon_r \epsilon_0 \frac{h(l_0 + x)}{d} + C_f, \quad \text{Eq. 2-18}$$

where again ϵ_r is the relative permittivity of the dielectric material between the capacitor plates, ϵ_0 is the permittivity of free space, and d is the distance separating the sidewalls of the finger electrodes. The parameters h and l_0 represent the height and initial overlap length of the fingers, and C_f represents the fringing capacitance formed with the substrate, as shown previously in **Figure 2-30**. The fringing capacitance C_f is usually orders of magnitude smaller than the capacitance formed by the overlapping of the interdigitated fingers and is usually neglected. From this, the total capacitance of a device consisting of N overlapped fingers can be approximated as

$$C_{tot} \approx \epsilon_r \epsilon_0 \frac{Nh(l_0 + x)}{d}. \quad \text{Eq. 2-19}$$

Comb-drive devices are actuated using a separate interdigitated structure wherein electrostatic attraction through DC bias results in an electrostatic force,

$$F_e = \left| \frac{\partial W}{\partial x} \right| = \frac{1}{2} \left| \frac{\partial C}{\partial x} \right| V^2 = \epsilon_r \epsilon_0 \frac{Nh}{2d} V^2, \quad \text{Eq. 2-20}$$

that increases the overlap of the actuation electrodes. As this actuation electrode overlap increases, the entire device structure is moved which changes the overlap of the signal electrodes, yielding a variable device capacitance which depends on the lateral electrode displacement as seen in **Eq. 2-20**.

Comb-drive-based area-tuned varactors offer many advantages over traditional vertically-actuated gap-tuned capacitors: fabrication is usually achieved via simple bulk micromachining processes as opposed to complex surface micromachining, there is an inherent isolation between the actuation and signal electrodes, and the designs are easily scalable to meet specific nominal capacitance requirements. The principal drawback of comb-drive-based devices is the large device footprint necessary to realize the device.

Larson *et al.* developed a “proof-of-concept” area-tuned varactor in 1991 [8, 9]. Using interdigitated electrodes, a variable capacitance was demonstrated by manually manipulating the electrodes to vary the area of overlap. The first electrostatically-actuated area-tuned MEMS varactors were realized by Yao *et al.* in 1998 [5, 109]. The device featured a suspended array of interdigitated comb fingers linked to a comb-drive actuator, shown in **Figure 2-31**. The device was fabricated using DRIE surface micromachining and coated with a thin aluminum layer to lower resistive losses to the semiconductor substrate, achieving a CTR of 200% and Q_e of 34 at 500 MHz. Subsequent iterations of the design tripled the RF performance, yielding a CTR of 740% with a Q_e greater than 100 at a frequency of 500 MHz by utilizing thicker device layers, low resistivity substrates, and an enhanced mechanical suspension [26, 110–113]. A similar design developed by Yalçinkaya *et al.* had a CTR of 100% with a Q_e of 100 at 100 MHz [114].

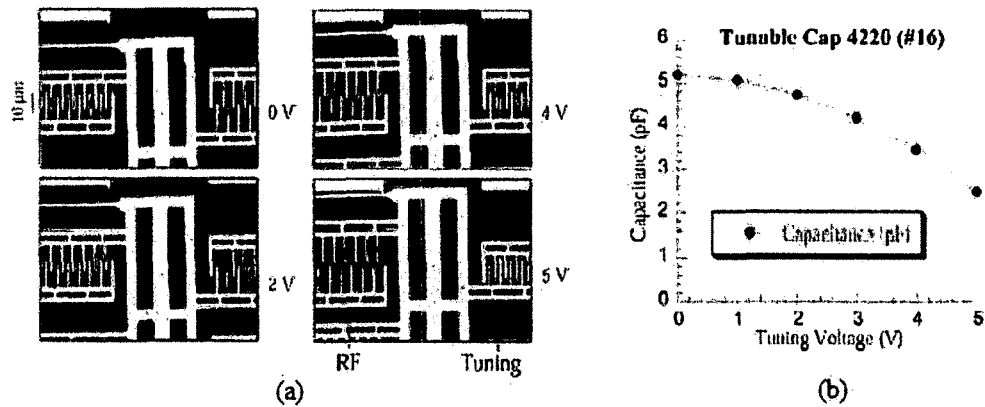


Figure 2-31: (a) Optical image illustrating device operation with varying bias voltages and (b) C - V characteristics of a comb-drive-actuated area-tuned varactor device [5].

Seok *et al.* developed an area-tuned variable capacitor that uses the vertical displacement of the overall device structure to change the relative height of the overlap between fingers in its interior comb-drive varactor structure [115], shown in **Figure 2-32**. The device employs the same actuation scheme as seen in numerous parallel-plate gap-tuned devices, however the displacement range is limited to the height of the comb fingers, negating any possibility of pull-in effects over the voltage tuning range of the device. A CTR of 10.2% and a Q_e of 4 at 2 GHz were reported, with the unusually low values attributed to the fringing electric fields and thin device structure respectively.

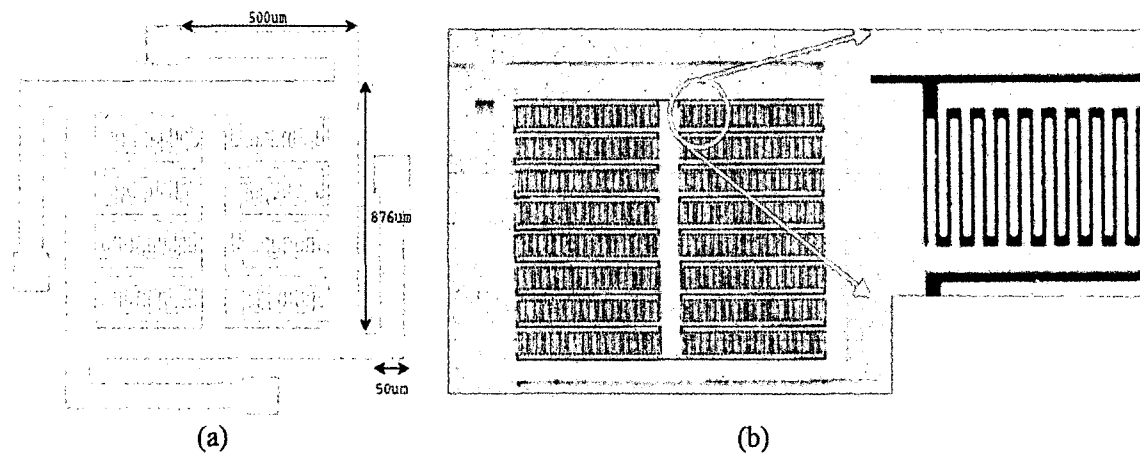


Figure 2-32: (a) Schematic representation and (b) SEM image of the fabricated area-tuned variable capacitor using vertical actuation [115].

Dai *et al.* developed an area-tuned varactor that uses a comb-drive actuator to induce in-plane displacement of a large planar electrode [116]. The in-plane movement of the large electrode causes a change in overlap area between the dynamic and stationary electrodes, yielding a variable capacitance. The device, shown in **Figure 2-33**, was fabricated using a commercial 0.35 μm CMOS process, making it compatible with most standard IC technologies. The design yielded a CTR of 47.1% with no available Q_e data.

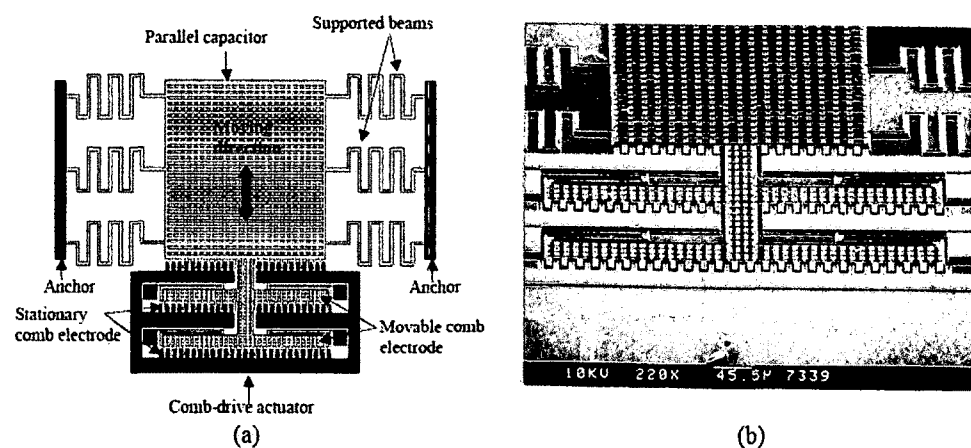


Figure 2-33: (a) Schematic and (b) SEM image of the comb-drive actuated area tuned parallel plate varactor device.

2.2.2.2.1 Rotational Varactors

In order to minimize the footprint of area-tuned devices, Nguyen *et al.* developed an area-tuned device based on macro-scale varactors which utilize out-of-plane rotation to obtain a large tuning range while keeping the device compact [117, 118]. The device, shown in **Figure 2-34**, was fabricated using a DRIE process on a silicon device layer which was anodically bonded to a Borofloat glass substrate. Photoresist polymer hinges are used to connect the two sets of comb fingers, and the surface tension of the hinges creates the initial diagonal offset of the actuator comb-fingers shown above. This microscale adaptation of a mechanical variable capacitor device achieved a *CTR* of 3085% and a Q_e of 273 at a frequency of 1 GHz. While the device outperforms nearly all other MEMS varactor designs, the fabrication process is extremely complex and would likely prohibit monolithic integration with most ICs. Kim and Lin developed a varactor using a similar angular comb-drive actuator affixed to a torsional spring and achieved a *CTR* of 393% [119].

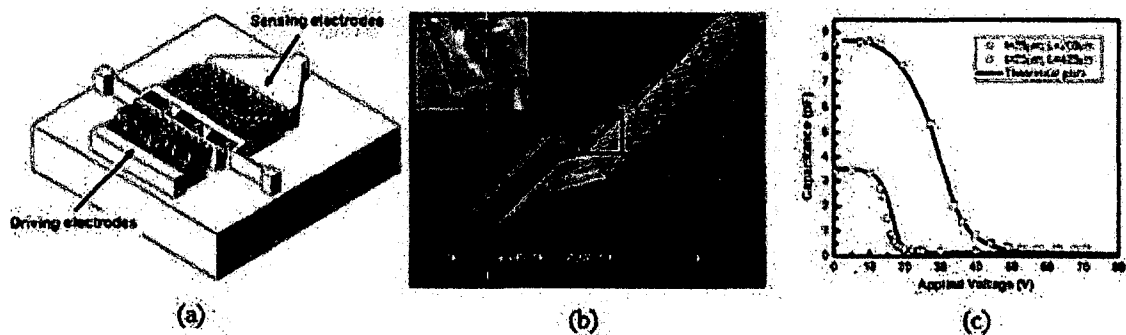


Figure 2-34: (a) Schematic, (b) SEM image, and (c) C - V characteristics of the rotational area-tuned varactor device with different finger lengths [118].

Wilson *et al.* developed a varactor device that utilizes in-plane rotation to change the area of overlap between the stationary and dynamic electrodes [120, 121]. Seen in **Figure 2-35**, the device is actuated by an electrostatically-driven micromachined gear assembly. As the gears turn, the bow-tie-shaped electrode rotates and causes the device capacitance to vary as the area of overlap changes. The device achieved a *CTR* of 1005% with no Q_e data provided.

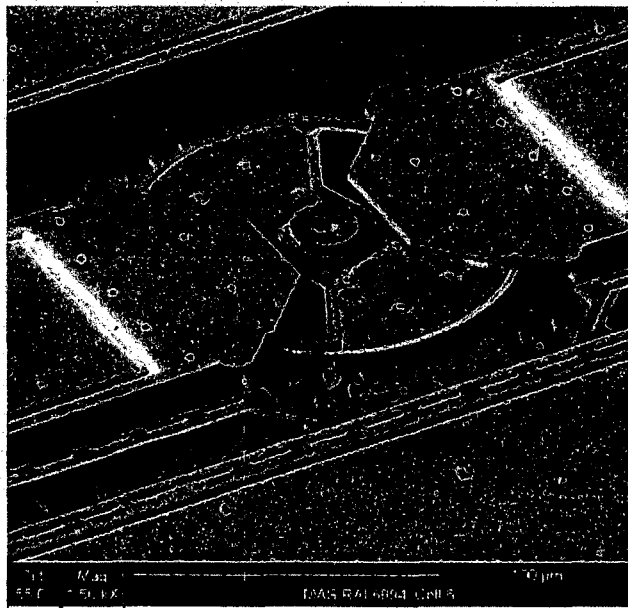


Figure 2-35: SEM image of gear-driven varactor with a bow-tie electrode turned to approximately 10° off of perpendicular where C_{\min} occurs at 0° and C_{\max} occurs at 90° of rotation [121].

Gu and Li also developed a varactor device that uses in-plane rotation of the device structure to vary the overlap of capacitive comb-structures fabricated with a CMOS-compatible process [122]. The suspension, shown in **Figure 2-36**, was designed to have increased stiffness radially outward from the central anchor, minimizing sensitivity to low frequency mechanical vibrations. The comb electrodes are composed of nickel and gold layers, yielding a *CTR* of 108% and a Q_e value of 51.3 at 1 GHz, where

the relatively low Q_e value was attributed to high parasitic inductances caused by the folded-beam suspension.

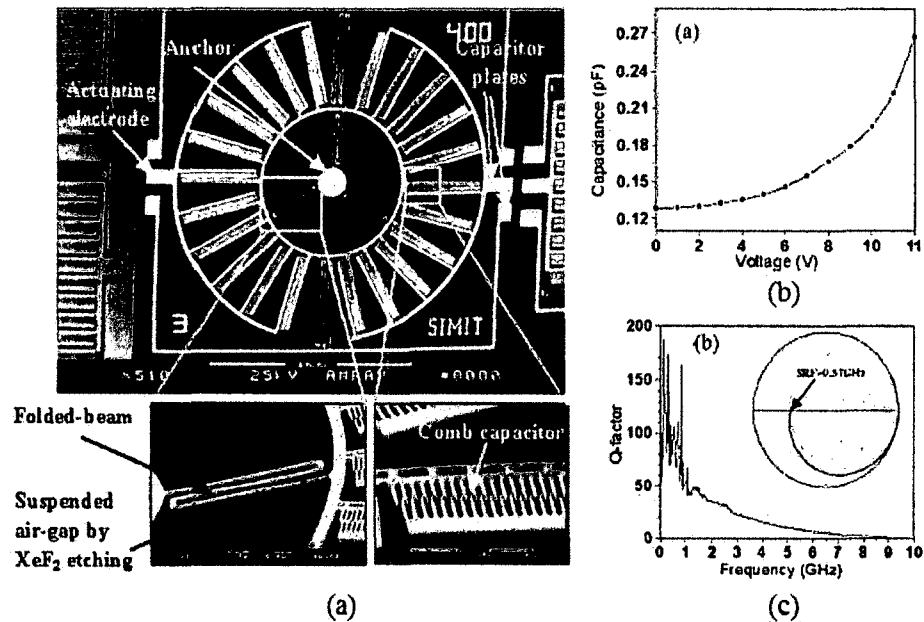


Figure 2-36: (a) SEM image of rotational comb-drive variable capacitor with insets depicting folded-beam suspension and variable capacitor structure; (b) C - V response and (c) Q_e vs. frequency plots [122].

2.2.2.2.2 Non-Electrostatically Actuated Area-Tuned Varactors

Electrothermal and piezoelectric actuation have also been explored in area-tuned devices. Oz and Fedder fabricated multiple area-tuned varactor designs which use electrothermal actuators to vary the overlap area of capacitive comb-drives [123–125]. Two of the designs are depicted in **Figure 2-37**. The device shown on the left was designed to operate as a gap-tuned device which utilizes an electrothermal actuator. Due to fabrication errors, the inner frame and comb-fingers had an initial upward curl. When heated, the curvature relaxed which caused an increase in the area of overlap between the comb-fingers, yielding a CTR of 35.7% and a Q_e of 38 at 1 GHz. The device depicted at

the right was designed to operate as an area tuned varactor. The top and bottom thermal actuators enable lateral displacement of the dynamic comb-electrodes, yielding a CTR of 252% with a Q_e of 52 at 1.5 GHz.

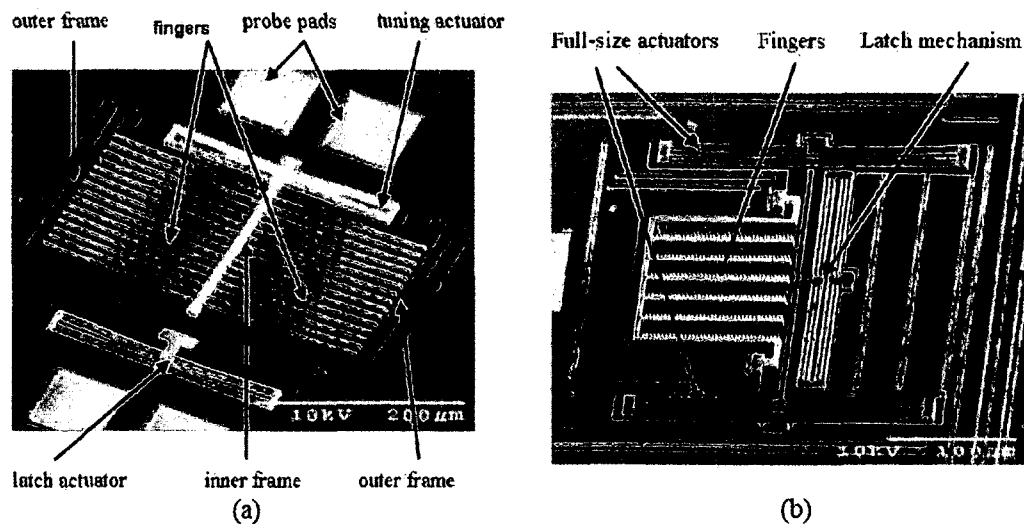


Figure 2-37: Electrothermally actuated area-tuned comb-drives [125].

Liu developed a varactor device that used electrothermal actuators to generate lateral displacement of a rigid segmented electrode with respect to a stationary electrode, yielding a change in the overlap area of the capacitor [126]. The device, shown in **Figure 2-38**, was constructed using polysilicon layers surface micromachined with a CMOS-compatible process. The device achieved a CTR of 550%, with Q_e measurements still under investigation at the time of reporting. Barzegar *et al.* developed a similar design that also included a latching mechanism which achieved a CTR of 17% and a Q_e of 43.4 at 1 GHz [127].

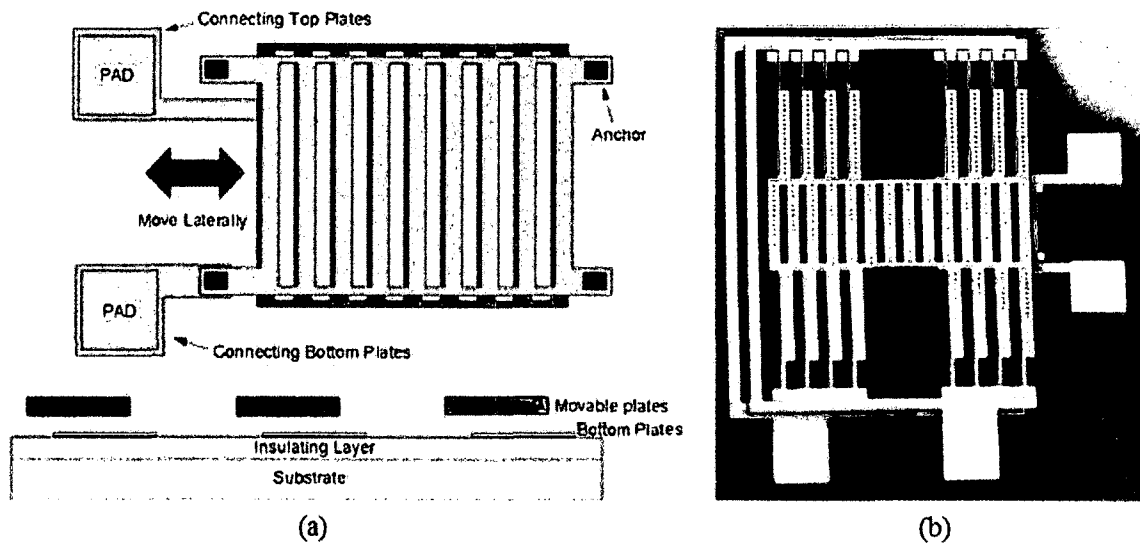


Figure 2-38: (a) Device schematic and (b) SEM image of laterally-actuated area-tuned capacitor [126].

Mehdaoui *et al.* developed an electrothermally-actuated area-tuned rotational varactor [128]. Shown in **Figure 2-39**, the device uses the offset expansions of linear electrothermal actuators to generate torque at the central hub which in turn rotates the upper fragmented bow-tie electrode and changes the effective capacitance area. A 1.2 V control voltage was used to generate a 7° rotation in the dynamic structure, yielding a *CTR* of 30%.

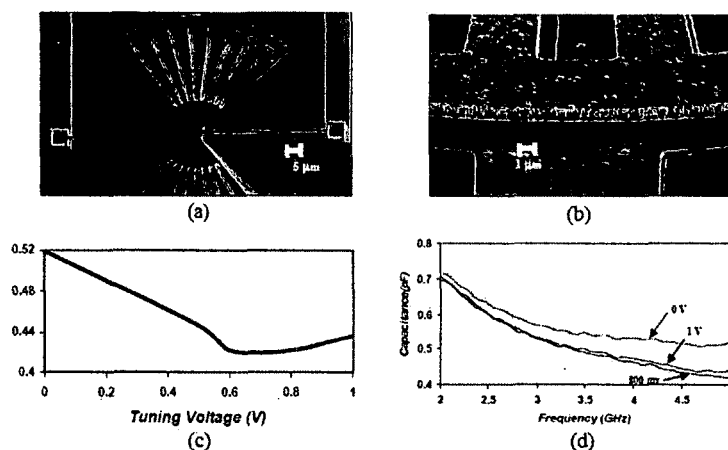


Figure 2-39: (a) SEM image of rotational electrothermally-actuated varactor, (b) close-up view of fragmented electrodes, (c) C - V characteristics of the device, and (d) capacitance vs. frequency plot for varying control voltages [128].

Pulskamp *et al.* created a piezoelectrically-actuated capacitive comb-drive area-tuned capacitor [129]. The PZT unimorph piezoelectric actuators seen in **Figure 2-40** generate an out-of-plane displacement which increases the effective capacitance area of the device. The large, high-aspect-ratio electrodes and cascaded actuator scheme enabled a large CTR of 1060% with a Q_e of 100 at a frequency of 8.7 GHz. This design achieved the highest frequency for $Q_e > 100$ amongst devices having a CTR greater than 1000% at the time of publication.

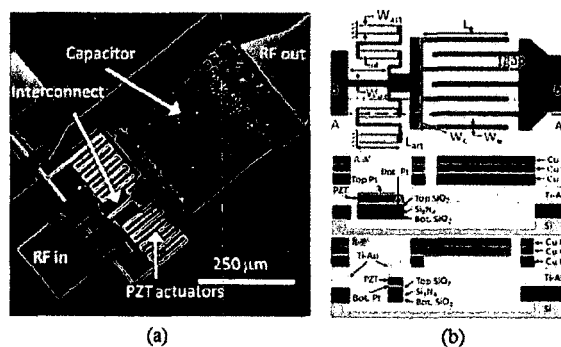


Figure 2-40: (a) SEM image and (b) device schematic of a piezoelectrically-actuated varactor device [129].

2.2.2.3 Digital Variable Capacitors

A digital variable capacitor is a microscale device which uses combinations of MEMS capacitive switches and fixed-value (static) capacitances to achieve varying discrete capacitance states, as shown in **Figure 2-41**.

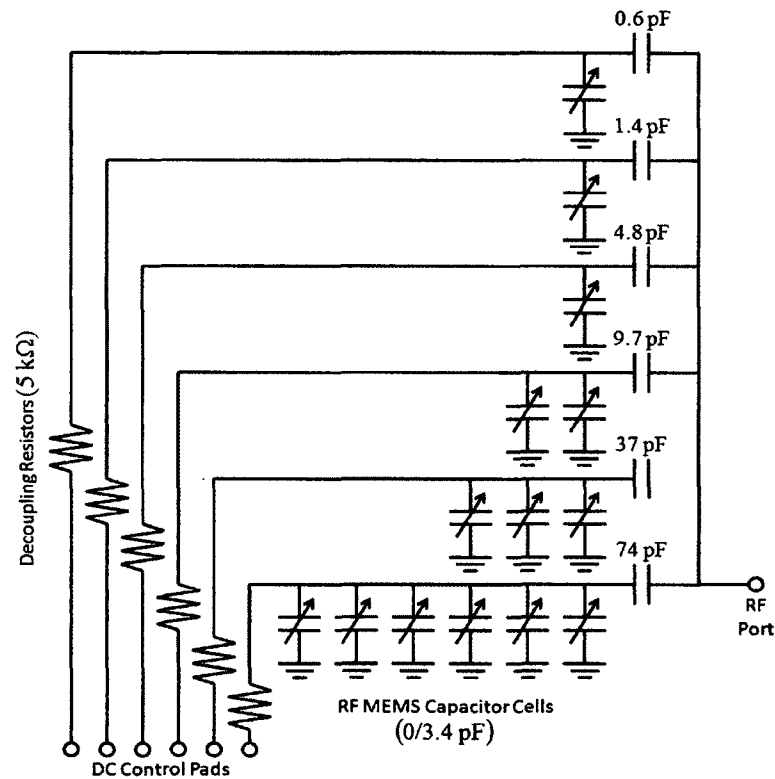


Figure 2-41: A 6-bit RF-MEMS digital variable capacitor utilizing weighted capacitance selection of bits composed of bistable MEMS capacitive switches. Adapted from [130].

Each capacitive switch contributes a discrete capacitance value to the device depending on the logic state of the switch: if the switch is open, C_{switch} is small and thus dominates the series combination resulting in a small equivalent capacitance; if the switch is closed, C_{switch} is large and both the fixed-value and switch capacitances contribute to the equivalent capacitance of the branch. The MEMS capacitive switches (shown in **Figure 2-42**) used to vary the capacitance in these devices are a subclass of

gap-tuned MEMS varactors in which the pull-in effect is used to mechanically close the switch. Similar bistable MEMS capacitive switches have been utilized by numerous researchers to create digital MEMS varactor devices [53, 59, 131–136], with variations used for applications in flexible circuit technology [137], high-power systems [138–139], and high-temperature operation [140]. Tristable switches have also been used for varactor designs [59, 141].

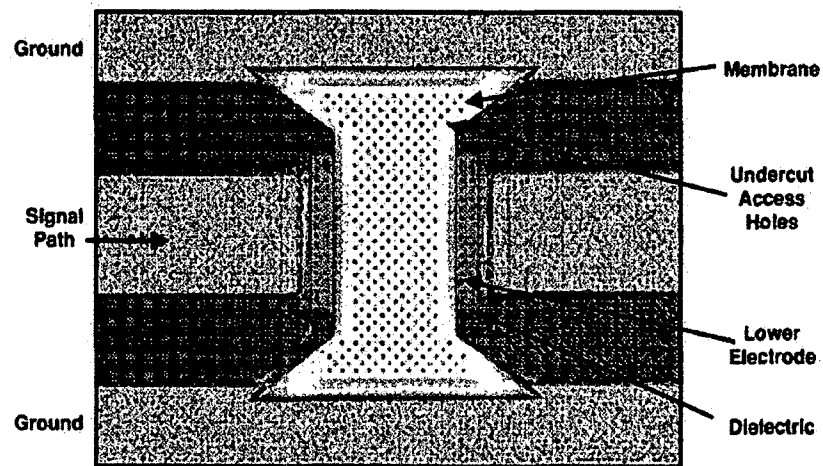


Figure 2-42: MEMS capacitive switch mounted in a shunt configuration over a coplanar waveguide [130].

Digital RF MEMS variable capacitors have also been implemented using ohmic switches like the one illustrated in **Figure 2-43**. These devices utilize cantilevers with varied mechanical spring constants (different lengths or thicknesses) to enable cascade pull-down effects [143] or voltage-controlled selection of individual fixed capacitor bits [144, 145] yielding discrete device capacitances as a function of actuation voltage.

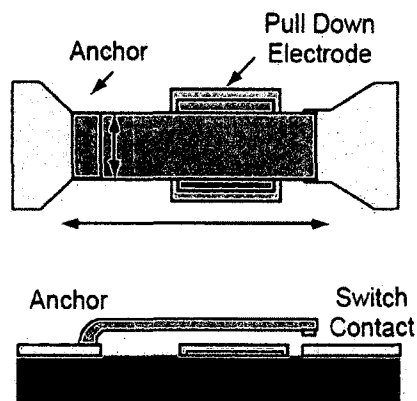


Figure 2-43: Schematic of an RF MEMS ohmic switch [142].

2.2.2.4 Other MEMS Variable Capacitors

Many researchers have developed MEMS varactors that do not fall into the categories previously discussed. These devices utilize novel concepts that may be useful in future varactor implementations.

Chiao *et al.* developed the scratch-drive-actuated gap-tuned varactor shown in **Figure 2-44** [146, 147]. The scratch-drive actuation mechanism and associated hinges enables the long-range in-plane movement of the actuator to enable dynamic electrode displacements of 1–100 μm in 20 nm steps, yielding a theoretical *CTR* of 9900%. In practice, parasitic capacitances limited tuning to 6900% with no information provided about electronic quality factor. The wide tuning range achieved by this design comes at the expense of the large voltages necessary to achieve actuation, typically greater than 100 V.

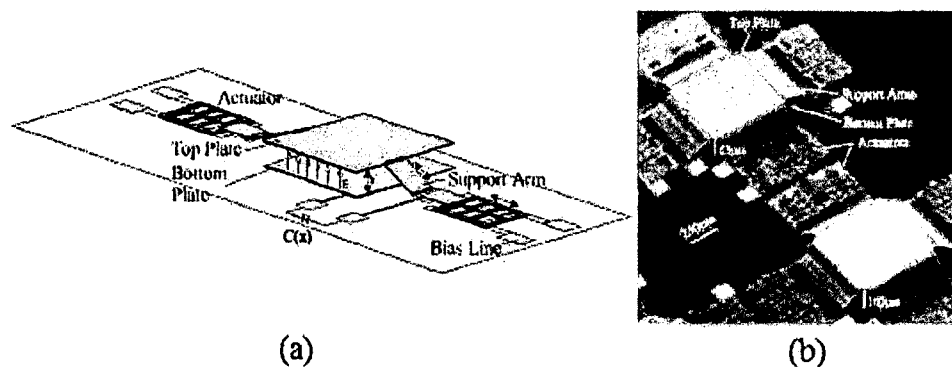


Figure 2-44: (a) Operational diagram and (b) SEM image of a scratch-drive-actuated variable capacitor [147].

Yoon and Nguyen demonstrated the first varactor to utilize dielectric tuning in 2000 [148], as shown in **Figure 2-45**. The device uses electrostatic actuation to move a patterned nitride dielectric layer attached to a MEMS spring between the capacitor electrodes. As the nitride layer is pulled further in between the capacitor electrodes, the effective dielectric constant between the plates increases yielding a larger capacitance. The device's structure uses thick copper layers to achieve a high Q -factor of 291 at 1 GHz, however tuning was limited to 7.7% due to the series combination of capacitances formed by the air gaps and nitride layer between the capacitor plates.

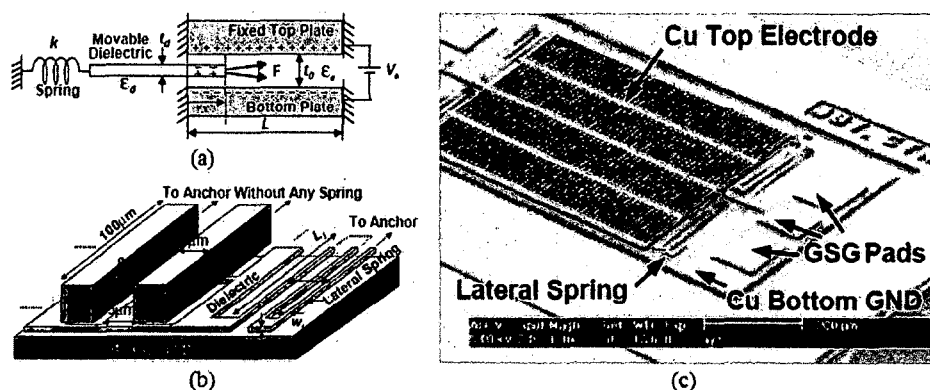


Figure 2-45: (a) Conceptual schematic, (b) operational schematic, and (c) SEM image of a dielectrically-tuned MEMS varactor device [148].

A varactor design utilizing a torsional MEMS spring and multiple was developed by De Coster, *et al.* as shown in **Figure 2-46** [149]. The device has actuation electrodes on each side of the torsion spring, allowing vertical displacement both towards and away from the planar substrate through superposition of the RF and actuation signals. This dual-actuation mechanism was used to extend the tuning range beyond the limitations of pull-in effects in conventional parallel-plate MEMS varactors. The device achieved a *CTR* of 61% however no information on electronic *Q*-factor was provided.

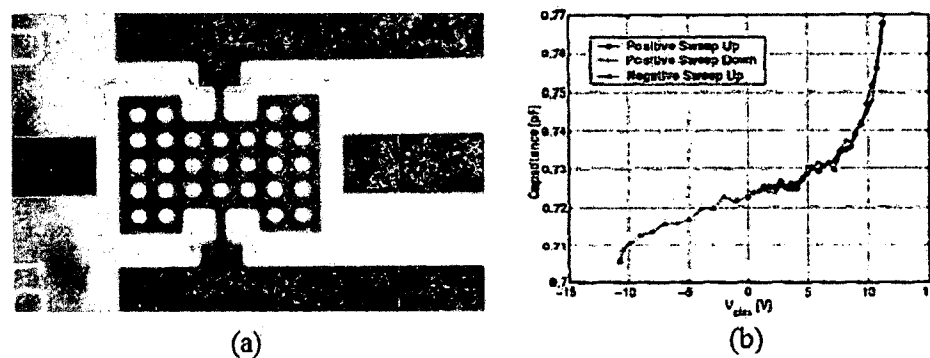


Figure 2-46: (a) SEM image and (b) C - V characteristics of a torsion beam MEMS varactor [149].

The design illustrated in **Figure 2-46** was expanded on by Farinelli *et al.* to create toggle varactors which use multiple actuation electrodes in conjunction with torsional springs to achieve large vertical displacements of the dynamic electrode of a parallel-plate capacitor, as seen in **Figure 2-47** [150]. The torsional springs serve as fulcrums which enable pull-out electrodes to raise the dynamic electrode, lowering device capacitance, and pull-in electrodes to lower the dynamic electrode, increasing device capacitance. The device achieved a *CTR* of 147% with near identical performance in DC and RF measurements. Similar designs were implemented by Han *et al.* [151] and Ling *et al.* [152], achieving *CTR*s of 134% and 160%, respectively.

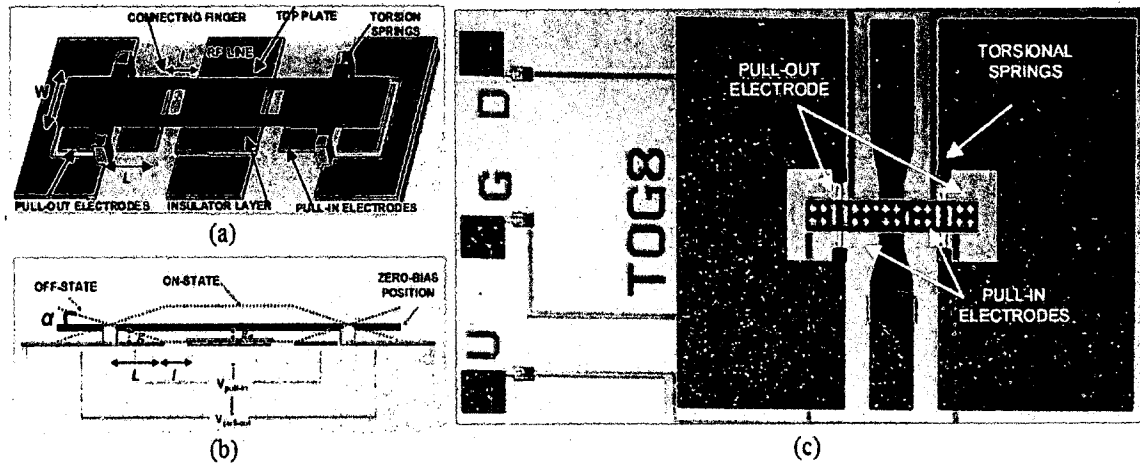


Figure 2-47: (a) Perspective view and (b) side view of operational schematic of MEMS toggle varactor. (c) Photograph of a completed device [150].

Cruau *et al.* developed a 3D-varactor that utilizes a central mobile conductor to vary device capacitance, as shown in **Figure 2-48** [153]. The device uses two RF electrodes with comb fingers and a V-shaped mobile conductor to vary the area of overlap seen at the RF electrodes, thereby varying the overall device capacitance. The use of comb structures limits the need for a large dynamic range of the mobile electrode, yielding a smaller device footprint.

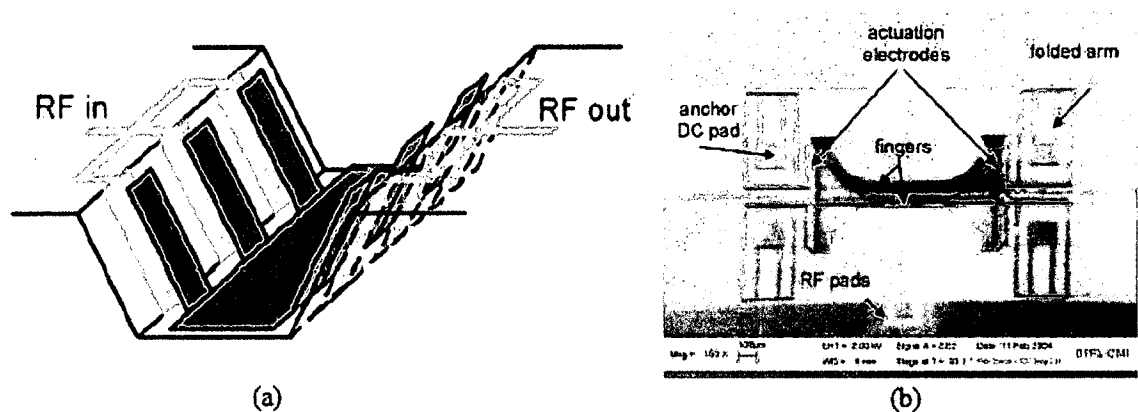


Figure 2-48: (a) Operational schematic and (b) SEM image of a V-shaped area-tuned varactor [153].

Klymyshyn *et al.* created a vertically-oriented gap-tuned varactor with in-plane movement using high aspect ratio electroplated nickel structures [154, 155]. The device, shown in **Figure 2-49**, uses electrostatic actuation to cause deflection of X-ray lithographically-patterned cantilevers, resulting in a variable capacitance. The thick metal structures that form the device yield a high Q -factor of 51.8 at 4 GHz, however the tuning range is limited to 24%. A subsequent design iteration that includes the use of leveraged bending increased the CTR to 90% [156].

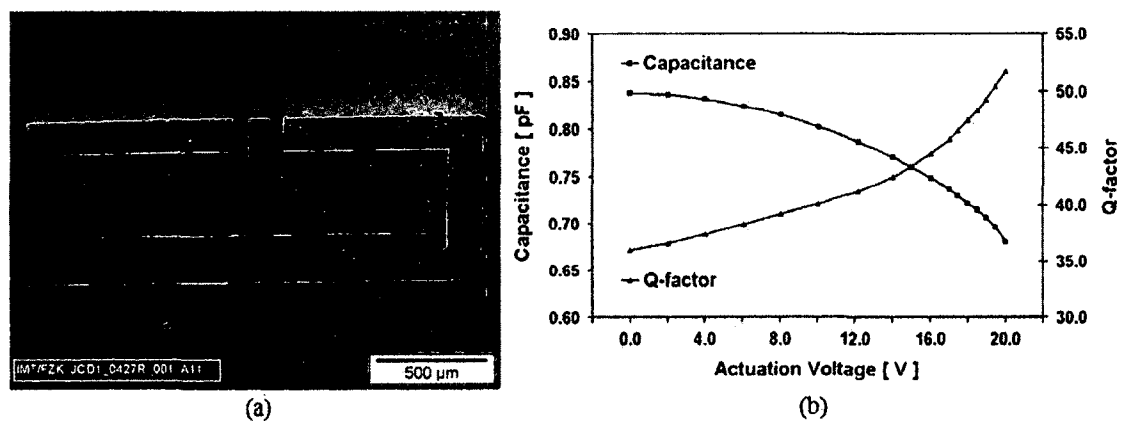


Figure 2-49: (a) SEM image and (b) C - V characteristic curve of vertically-oriented gap-tuned varactor [154].

Yoon *et al.* developed an electrostatically-actuated gap-tuned varactor that uses an electrically floating plate as the dynamic electrode [157, 158]. The tuning structure, shown in **Figure 2-50**, enables the actuation electrode to electrically polarize a suspended electrically floating plate which is then attracted down towards an RF signal electrode. Since no spring structures are directly connected to the RF signal path as is the case in most gap- and area-tuned devices, the device has a decreased series resistance which increases overall Q -factor. The device achieved a capacitive tuning ratio of 41% with a Q of 26.7 at 5 GHz. Zhu *et al.* adopted a similar design which utilized an electrically

floating dielectric material which caused device capacitance to vary through electrostatic attraction [159]. Khan *et al.* adopted a similar actuation scheme using comb-drives and achieved a CTR of 631% and a Q of 24.4 at 1 GHz [160].

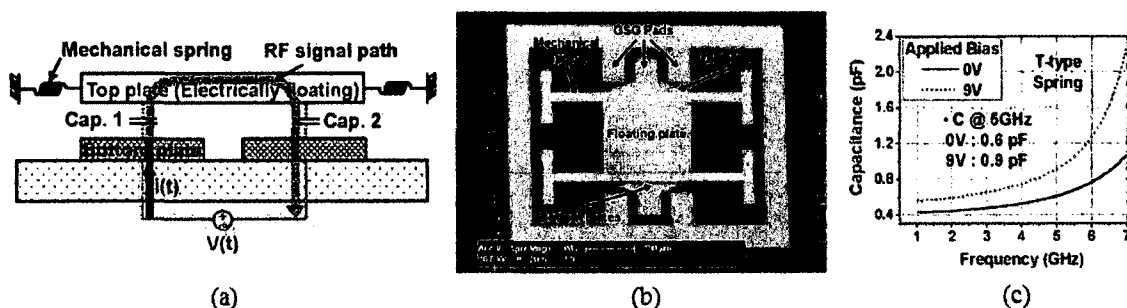


Figure 2-50: (a) Operational schematic, (b) SEM image, and (c) C - V characteristic curve of a gap-tuned varactor with an electrically floating plate [158].

Pottigari and Kwon developed a unique varactor that uses the thermal expansion of liquid mercury to electrically connect a number of parallel fixed capacitances, as seen in **Figure 2-51** [161]. The device consists of a microfluidic channel, a reservoir for containing the liquid mercury, and several parallel plate capacitors. As the temperature of the device increases, the liquid metal expands through the microchannel and connects the parallel-plate capacitors yielding a linear actuation method. A CTR of 2050% was reported for this device with no Q -factor information provided.

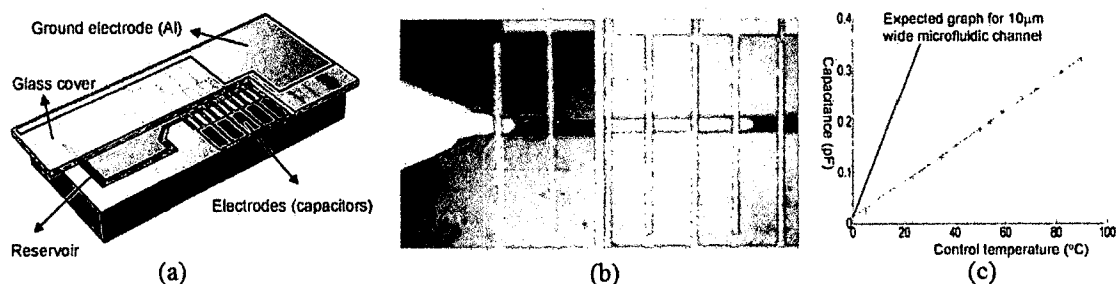


Figure 2-51: (a) CAD drawing of liquid-metal varactor, (b) pictures illustrating thermal expansion of mercury within the microchannel, and (c) C - V response of the device [161].

Ghavanini *et al.* developed the first nanoscale varactor with moving parts, shown in **Figure 2-52** [162]. The device uses plasma-enhanced chemical-vapor deposition-synthesized carbon nanofibers as vertically-aligned cantilevers which deflect under an electrical bias. Electrostatic attraction causes the carbon nanofibers to deflect toward each other, causing an increase in device capacitance. CTR s of 18% were reported with no Q -factor data available.

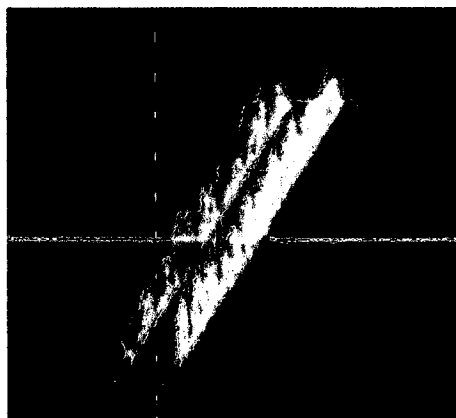


Figure 2-52: Vertically-aligned carbon nanofibers forming a parallel-plate capacitor [162].

Baek *et al.* developed a hybrid varactor device which uses thermal actuation and latching mechanisms to electrically connect different sets of electrostatically-actuated

comb drive varactors [163, 164]. The device uses a thermally-actuated four-position switching/latching mechanism increase the total number of comb fingers that contribute to the device capacitance which enables coarse tuning of the device. The electrostatically-actuated comb-drive mechanism provides fine tuning. The latching mechanism, seen in **Figure 2-53**, enables the connection between comb-drives to be maintained without consuming additional DC power. The device achieved a CTR of 471% with no Q -factor information reported.

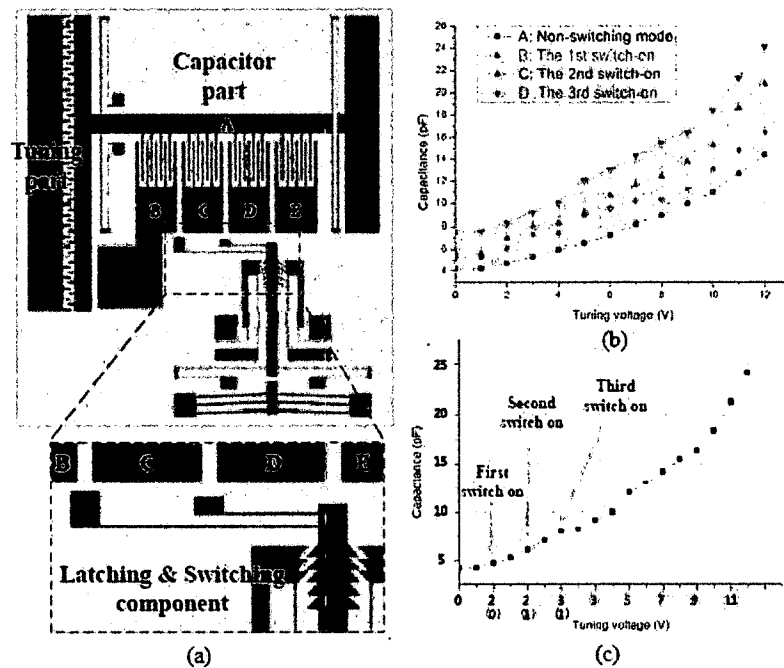


Figure 2-53: (a) Schematic view of the variable capacitor and its switching components, (b) C - V relationship as a function of switch position and voltage, and (c) continuous tuning capabilities of the device [163].

2.3 Microfluidic Variable Capacitor

While MEMS variable capacitors that use gap- and area-tuning schemes are common, varactors which utilize dielectric tuning are few and far between. The principal reason for this lack of implementation stems from design problems seen in [148]—the

dynamic movement of solid dielectric materials requires a) springs which increases series resistance and lowers electronic quality factor and b) air-gaps (and their associated parasitic capacitances) to eliminate friction between the moving dielectric and device electrodes which greatly decreases tunability. One method to achieve dielectric tuning that eliminates both of these drawbacks is the use of liquid dielectric materials.

2.3.1 Operational Theory

Tuning through manipulating the displacement of a liquid dielectric interface is achieved by using the charged (biased) capacitor electrodes to attract molecular dipoles of the primary liquid dielectric material towards the fringing electric field at the electrode edge, as illustrated in **Figure 2-54**.

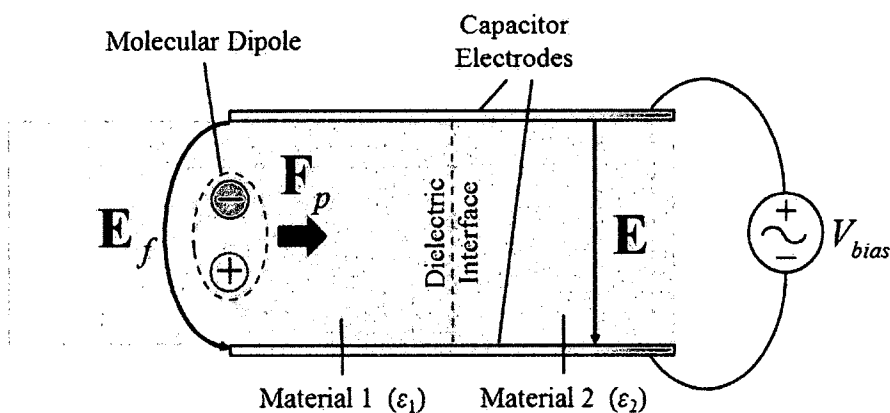


Figure 2-54: Conceptual illustration of microfluidic variable capacitor operation. The fringing electric field at the capacitor edge generates a polarization force that pushes the molecular dipoles of the liquid dielectric material further into the area of electrode overlap.

The fringing field provides a spatially-varying electric field which generates a polarization force density

$$\mathbf{F}_p = \mathbf{P} \cdot \nabla E \quad \text{Eq. 2-21}$$

where the force on the individual molecular dipoles is translated to the neutral medium, driving the higher permittivity liquid between the parallel capacitor electrodes while pushing the secondary dielectric material out. This action causes an increase in device capacitance as the high permittivity material replaces the lower permittivity material until the device is completely filled. The requirements for such an action to occur are that the dielectric fluids are immiscible and that the high-permittivity dielectric material is electrically polarizable.

If these conditions are met, the method of varying device capacitance using a movable liquid interface can be modeled as a parallel plate capacitor with two partially inserted dielectric materials, illustrated in **Figure 2-55**.

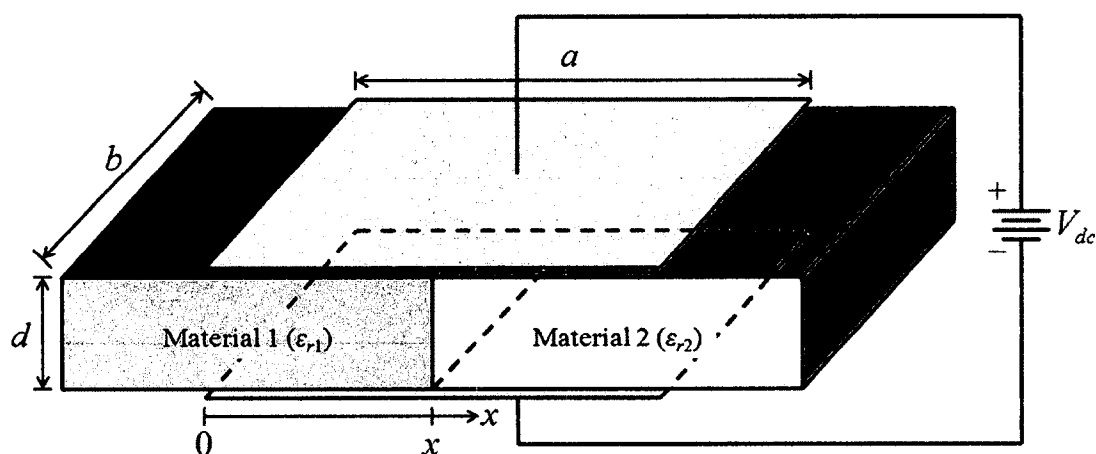


Figure 2-55: Schematic representation of a parallel plate capacitor filled with partially inserted dielectric materials. This configuration yields parallel capacitances with differing permittivities.

The equivalent capacitance of the capacitor architecture shown above is

$$C_{eq} = \epsilon_{r1} \epsilon_0 \frac{bx}{d} + \epsilon_{r2} \epsilon_0 \frac{b(a-x)}{d} \quad \text{Eq. 2-22}$$

where a , b , and d are defined in **Figure 2-22** and x is the dielectric interface displacement measured from the left edge of the capacitor. Substituting **Eq. 2-22** into **Eq. 2-11** yields a system energy of

$$W = \frac{1}{2} C_{eq} V_{dc}^2 = \frac{V_{dc}^2}{2} \left[\epsilon_{r1} \epsilon_0 \frac{bx}{d} + \epsilon_{r2} \epsilon_0 \frac{b(a-x)}{d} \right] \quad \text{Eq. 2-23}$$

where V_{DC} is the DC bias voltage used to set the operating point of the device.

Differentiating **Eq. 2-23** with respect to the dielectric interface displacement x yields the electrostatic force acting on the dielectric materials due to an applied bias:

$$F_x = \frac{dW}{dx} = \frac{V^2}{2} \frac{d}{dx} \left[\epsilon_{r1} \epsilon_0 \frac{bx}{d} + \epsilon_{r2} \epsilon_0 \frac{b(a-x)}{d} \right] = \frac{V^2 b \epsilon_0}{2d} (\epsilon_{r1} - \epsilon_{r2}). \quad \text{Eq. 2-24}$$

Analysis of **Eq. 2-24** reveals an interesting phenomenon: for any materials where $\epsilon_{r1} > \epsilon_{r2}$, the electrostatic force exerted on the dielectrics by the fringing electric fields of the biased capacitor is always in the positive x -direction, regardless of the polarity of the biasing voltage. This suggests that the electrostatic force always acts in such a way to pull the material with a larger dielectric constant further in between the plates. In doing so, the effective plate area seen by the high permittivity material increases as the dielectric interface moves further between the plates which causes the equivalent capacitance of the device to increase. In this way, the microfluidic variable capacitor behaves like the area-tuned capacitor from [148] without utilizing any moving parts or placing any mechanical suspension in the RF signal path.

Another interesting revelation can be obtained by looking at the theoretical minimum and maximum capacitance values for the device. Assuming $\epsilon_{r1} > \epsilon_{r2}$, C_{min} occurs when the space between the electrodes is completely filled by dielectric with relative permittivity ϵ_{r2} ($x = 0$), or

$$C_{\min} = \epsilon_{r2} \epsilon_0 \frac{ba}{d}. \quad \text{Eq. 2-25}$$

Similarly, C_{\max} occurs when the space between the electrodes is completely filled by the dielectric with ϵ_{r1} ($x = a$), or

$$C_{\max} = \epsilon_{r1} \epsilon_0 \frac{ba}{d}. \quad \text{Eq. 2-26}$$

Substituting these expressions into the definition of CTR established in Eq. 2-3 yields

$$CTR = \frac{\epsilon_{r1} \epsilon_0 \frac{ba}{d} - \epsilon_{r2} \epsilon_0 \frac{ba}{d}}{\epsilon_{r2} \epsilon_0 \frac{ba}{d}} = \frac{\epsilon_{r1} - \epsilon_{r2}}{\epsilon_{r2}} \quad \text{Eq. 2-27}$$

which illustrates that the theoretical tuning range of such a device depends only on the permittivities of the dielectric materials and not on the size or geometry of the device. By utilizing materials with large differences in permittivity, extremely large (>50) CTR s are achievable.

2.3.2 Modeling

The microfluidic varactor device described above was modeled using COMSOL's AC/DC Module with an electrostatic study to include the effects of fringing fields on the overall device capacitance, as well as with MATLAB using Eq. 2-23 to characterize the device's varying capacitance as a function of dielectric interface displacement. Four different devices were modeled utilizing different electrode sizes to determine the effects, if any, of electrode geometry on the fringing fields at the electrode edges. Capacitance calculations were performed using a parametric sweep of the dielectric interface displacement at 1% of electrode length intervals. Additionally, the electric field distribution of the devices was also simulated.

In order to develop a valid comparison between the different computational models, materials must be chosen for the liquid dielectrics and used throughout the simulations. De-ionized (DI) water was chosen as the high-permittivity material for its excellent insulating characteristics—at room temperature, DI water has a dielectric constant of $\epsilon_r = 80$ with a loss tangent of $\epsilon''/\epsilon' = 0.04$ for frequencies less than 1 GHz [165] and a dielectric breakdown voltage of 65–70 MV/m [166]. These properties make DI water a widely-used, high permittivity dielectric for pulse power systems where rapid discharge is necessary like the PBFA-Z (Z Machine) and its predecessors at Sandia National Laboratories [167]. The speed at which the dielectric can effectively discharge will aid in the use of the device in high frequency circuits. Another advantage of using DI water is that H₂O molecules naturally exhibit weak dipole moments due to the electronegativity imbalance of constituent hydrogen and oxygen atoms [168]. This phenomenon will allow the fringe electric field generated at the capacitor electrode edge to polarize the H₂O molecules in a single direction yielding a net force directed into the device which will assist in driving the fluid between the plates of the capacitor and lower the voltage necessary to achieve electrostatic actuation of the dielectric material.

Air was chosen as the second dielectric material principally due to the large permittivity mismatch with DI water. As air has a dielectric constant of $\epsilon_r \approx 1$, the electrostatic force generated for a particular bias voltage will be greater than if a second liquid dielectric like kerosene or oil were used. Additionally, gaseous contaminants like CO₂ leeching from the air into the DI water should have a limited effect on the electrical properties of the water [169] whereas fluid mixing could cause extreme changes in the dielectric properties of the medium. Finally, air is effectively non-polarizable so the

application of the bias voltage will not generate a force opposed to the DI water movement.

Shown in **Figure 2-56** are the results of the capacitance modeling for a device utilizing a 20 mm x 2mm x 25 μm microchannel. From the simulations, the fringing fields increase device capacitance by approximately 10% over the entire tuning range of the device (seen in the inset). As suggested in **Eq. 2-22**, the total device capacitance increases linearly with the displacement of the dielectric interface. The simulations also show a *CTR* of 6398% (COMSOL) and 8000% (MATLAB), illustrating the phenomenal potential tuning performance of the device versus virtually all other MEMS-based varactor designs. If a thin (2 μm) insulating layer of SU-8 is used to ensure against current leakage, the device performance decreases drastically due to the inclusion of the series capacitance formed via the additional dielectric. In this case, the simulations show a *CTR* of 2475% (COMSOL) and 3100% (MATLAB), illustrating performance comparable to the state-of-the-art MEMS devices reported in literature.

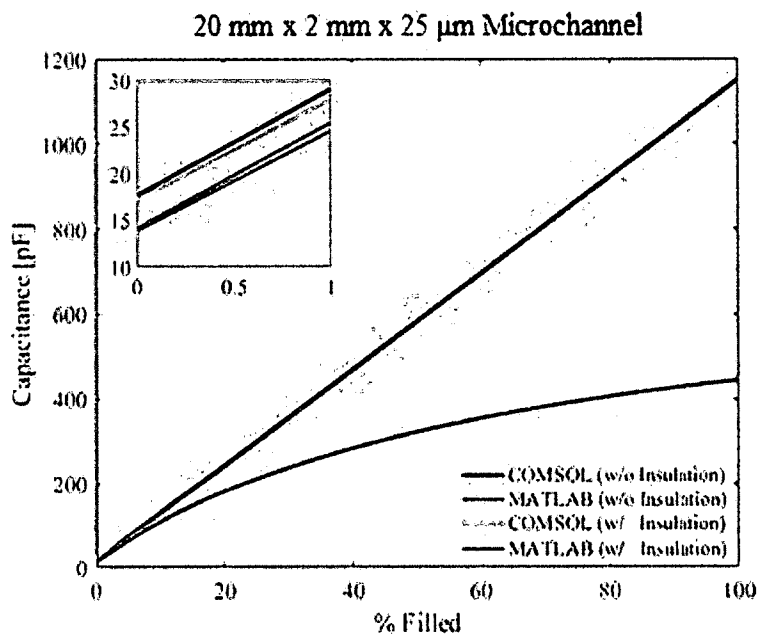


Figure 2-56: Simulations for device capacitance as a function of fill percentage for a microfluidic variable capacitor with a 20 mm x 2 mm x 25 μ m microchannel.

Figure 2-57 shows the results of the capacitance modeling for a device utilizing a 20 mm x 4 mm x 25 μ m microchannel. Again, the fringing fields increase device capacitance by approximately 10% over the entire tuning range of the device, resulting in a *CTR* of 6722% (COMSOL) and 8000% (MATLAB). The addition of the insulating layer into the model lowers device performance to a *CTR* of 2601% (COMSOL) and 3100% (MATLAB). The additional electrode area obtained by doubling the width of the microchannel yielded a 5.09% increase in simulated *CTR* due to the additional fringing fields generated.

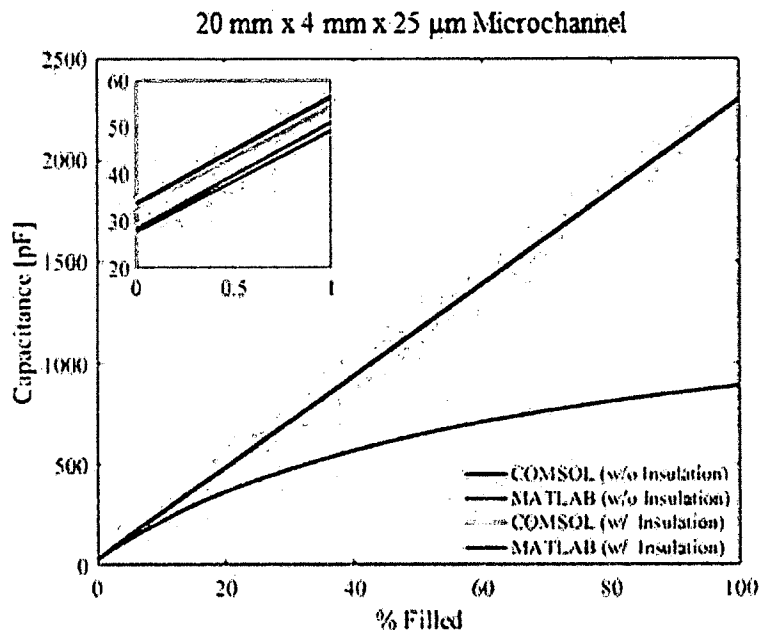


Figure 2-57: Simulations for device capacitance as a function of fill percentage for a microfluidic variable capacitor with a 20 mm x 4 mm x 25 μm microchannel.

Figure 2-58 shows the results of the capacitance modeling for a device utilizing a 40 mm x 2 mm x 25 μm microchannel. Again, the fringing fields increase device capacitance by approximately 10% over the entire tuning range of the device, resulting in a *CTR* of 6685% (COMSOL) and 8000% (MATLAB). The addition of the insulating layer into the model lowers device performance to a *CTR* of 2587% (COMSOL) and 3100% (MATLAB). The additional electrode area obtained by doubling the length of the microchannel yielded a 4.45% increase in simulated *CTR* due to the additional fringing fields generated, showing that wider electrodes have a greater influence on the tuning characteristics governed by fringing electric fields.

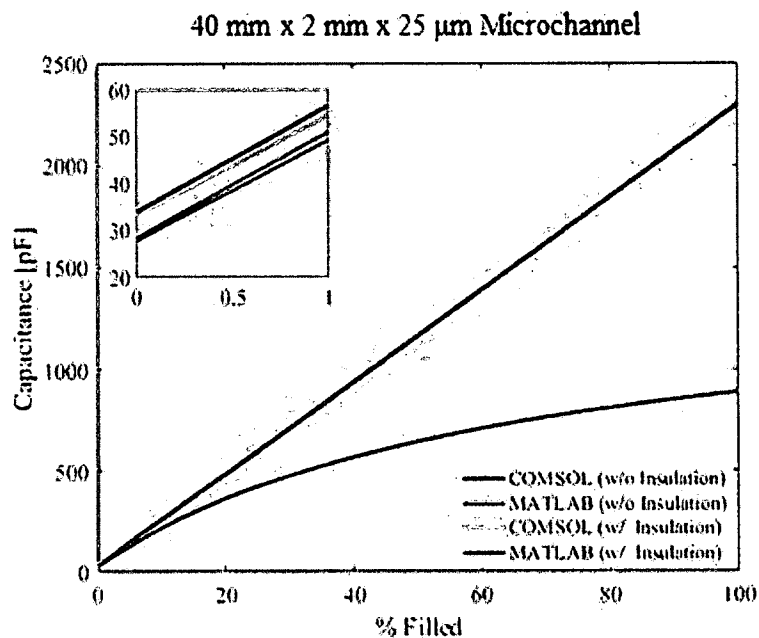


Figure 2-58: Simulations for device capacitance as a function of fill percentage for a microfluidic variable capacitor with a 40 mm x 2 mm x 25 μ m microchannel.

Figure 2-59 shows the results of the capacitance modeling for a device utilizing a 40 mm x 2 mm x 25 μ m microchannel. Again, the fringing fields increase device capacitance by approximately 10% over the entire tuning range of the device, resulting in a *CTR* of 7071% (COMSOL) and 8000% (MATLAB). The addition of the insulating layer into the model lowers device performance to a *CTR* of 2738% (COMSOL) and 3100% (MATLAB). By doubling both the electrode width and length, an increase in simulated *CTR* of 10.5% was observed. This illustrates that larger electrodes are less influenced by the presence of fringing fields as the overall tuning range is closer to the theoretical maximum given by the MATLAB simulation.

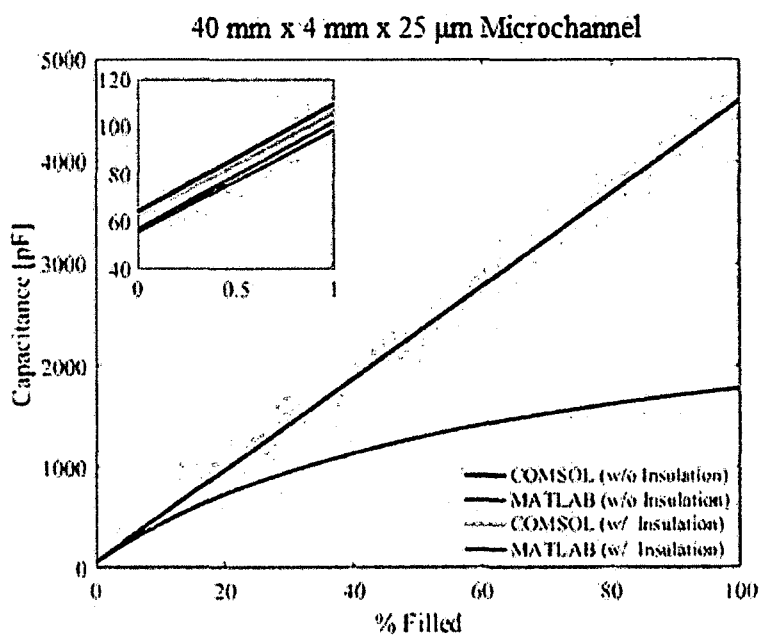


Figure 2-59: Simulations for device capacitance as a function of fill percentage for a microfluidic variable capacitor with a 40 mm x 4 mm x 25 μ m microchannel.

These results of the COMSOL simulations are summarized in **Table 2-1**.

Table 2-1: Simulation Results: Finite-Element Modeling of Microfluidic Variable Capacitors.

μ -channel length [mm]	μ -channel width [mm]	Cmin [pF]	Cmax [pF]	CTR
20	2	17.715	115.1	6398%
40	2	33.905	2300.6	6685%
20	4	33.720	2300.4	6722%
40	4	64.111	4597.5	7071%

Figure 2-60 shows the results of the COMSOL simulations on electric field distribution within a varactor device with a 40 mm x 4 mm x 25 μ m microchannel. The figure illustrates that the electric field intensity is greatest at the transmission line for

bias application and reduces as distance towards the electrode edge increases. At the electrode edges, the field circulates which enables the formation of a polarization force density which acts on the dielectric material.

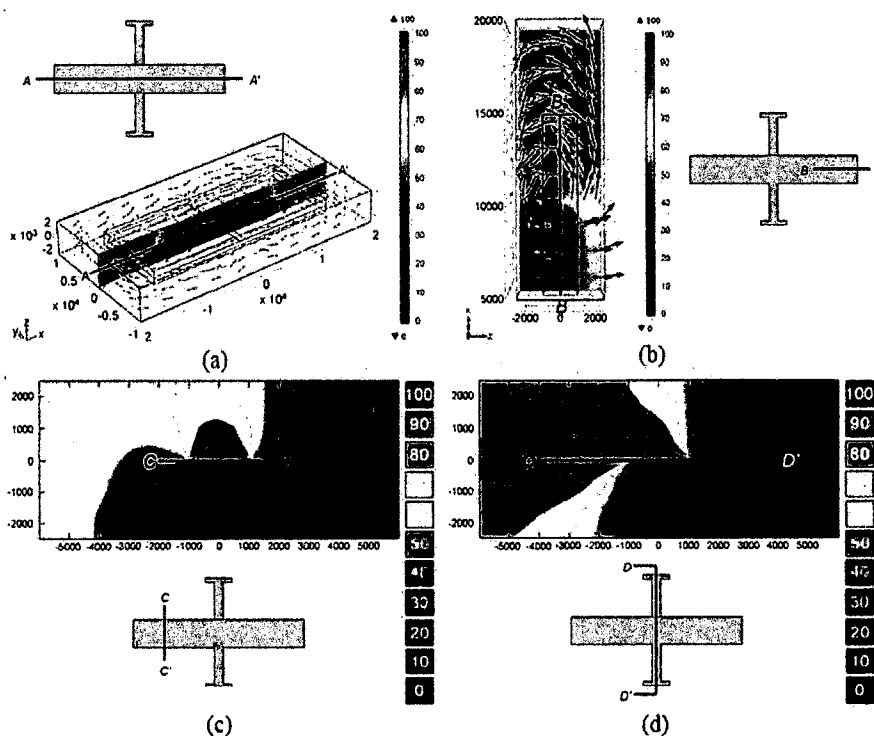


Figure 2-60: 3D plots of electric field lines and distribution for a biased microfluidic varactor over (a) the entire varactor length and (b) focused on the electrode edge. The arrows are normalized to illustrate field direction and their length is not indicative of field strength. Surface plots of transverse electric field distributions (c) at the electrode edge and (d) at the electrode feed point.

2.3.3 Device Design and Fabrication

Shown in **Figure 2-61** is an exploded diagrammatic view of a microfluidic variable capacitor. The device consists of two glass substrates, each with a patterned chromium electrode, and a polymer microchannel layer with attached microfluidic reservoirs. Water will be supplied to the device using the affixed Upchurch Scientific Nanoport assembly which provide tubing access to the etched inlet/outlet holes.

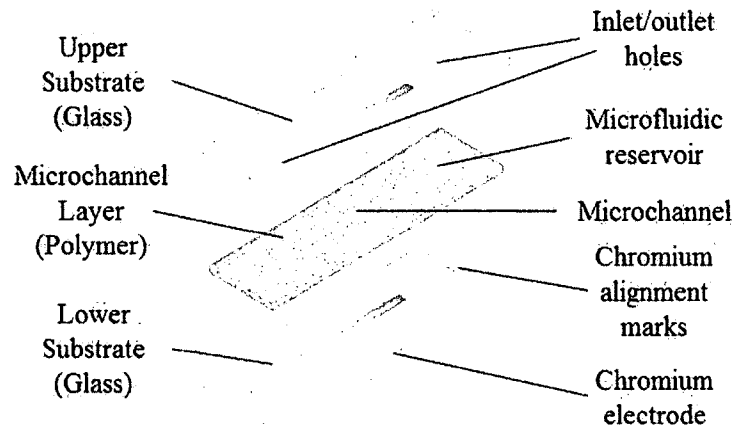


Figure 2-61: Exploded view of a microfluidic variable capacitor device detailing each portion of the assembly.

2.3.3.1 Electrodes and Alignment Marks

To enable simple device operation, “T”-shaped electrodes were employed where the stem serves as a feedline to the varactor device. The branches of the “T” are varied to conform to microchannel dimensions of different devices. The electrodes were fabricated by photolithographically patterning borosilicate glass slides which had been coated with a 50 nm layer of chromium. Alignment marks to aid assembly of the completed device were also including on the photolithography mask. A single photolithography mask was designed to accommodate all used variations of the microchannel dimensions and is shown in **Figure 2-62**.

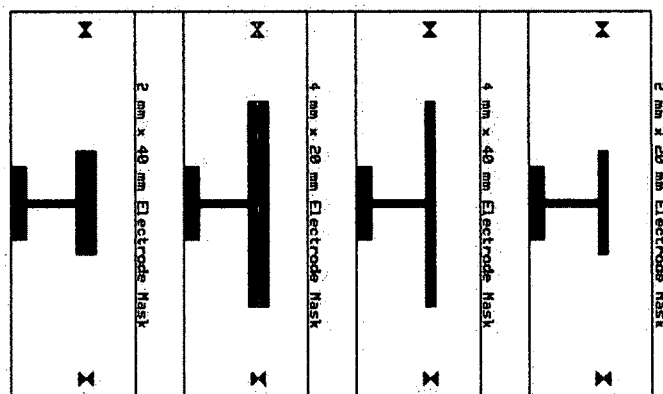


Figure 2-62: Photolithography mask design for patterning microfluidic varactor electrodes. The hourglass shapes on each side are alignment marks to ensure a maximum area of electrode overlap.

To pattern the electrodes, the chromium-coated substrates were first affixed to the spin chuck of an MTI VTC-50A Spin Coater and deposited with 2 mL of Shipley Microposit S1811 photoresist. The substrates were then spun at 3000 RPM for 60 seconds to achieve a 1 μm layer of photoresist over the substrate surface which, after processing, will serve as a mask for chemical removal of unwanted chromium features. After a 5 minute rest period to reduce the photoresist solvent concentration through evaporation, the substrates were placed on the photolithography mask and visually aligned before a five minute exposure to ultraviolet radiation which makes unmasked areas soluble to the resist developed. Next, the substrates were placed on a 60 $^{\circ}\text{C}$ hotplate for 5 minutes for a post-exposure bake. After a brief cooling period, the substrates were immersed in a bath of Microposit MF-319 Developer and agitate for 30 seconds to remove any soluble regions of photoresist. The substrates were then rinsed in DI water and placed into a bath of Transene Type 1020 Chromium Etchant for one minute which removes the unwanted chromium features not protected by the developed photoresist mask. Finally, the substrates are then rinsed with acetone and isopropyl alcohol to

remove the remaining photoresist, exposing the chromium layer underneath. The electrode and alignment mark patterning process flow is summarized in **Figure 2-63** and the results of this patterning process are shown in **Figure 2-64**.

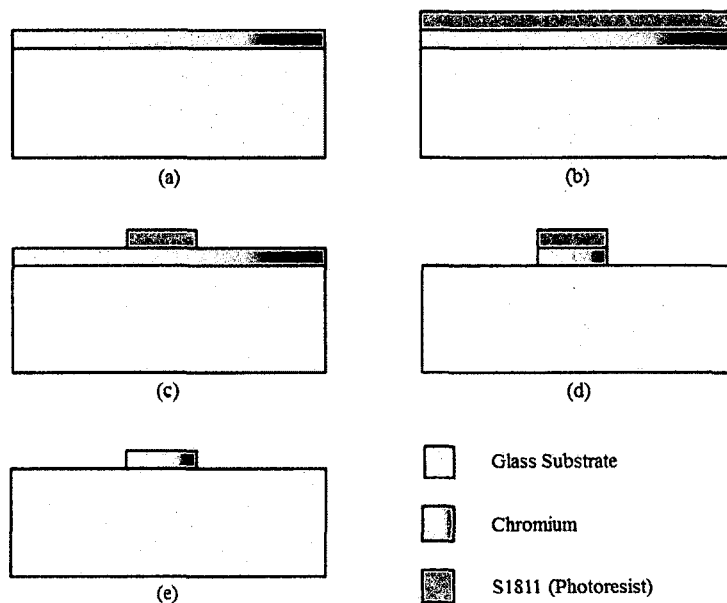


Figure 2-63: Process flow diagram for patterning electrodes and alignment marks. (a) Substrate is coated with 50 nm of chromium. (b) A 1 μm layer of S1811 photoresist is deposited on top of the chromium and exposed to UV radiation. (c) The photoresist layer is developed, removing unwanted photoresist features. (d) The exposed chromium is etched, leaving behind the patterned features topped with photoresist. (e) The photoresist is moved, revealing the patterned chromium layer underneath.

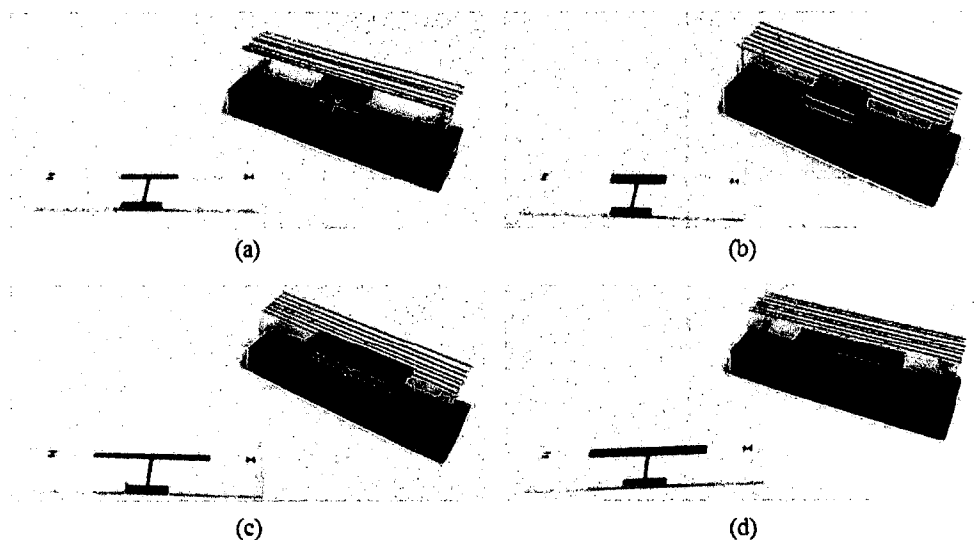


Figure 2-64: Glass substrates with photolithographically-patterned alignment marks and electrodes designed for microfluidic varactors with microchannel dimensions (a) 2 mm x 20 mm x 25 μm , (b) 4 mm x 20 mm x 25 μm , (c) 2 mm x 40 mm x 25 μm , and (d) 4 mm x 40 mm x 25 μm .

2.3.3.2 Microchannel and Microfluidic Reservoir

The fabrication method used to realize the microfluidic varactor devices relies on the xurographic patterning of thin adhesive layers to form the microchannel. Xurography is a micromanufacturing process commonly used in biomedical engineering for creating microstructures in which a computer-controlled knife-plotter is used to cut patterns into a polymer sheet. Once the outline of the design has been carved into the polymer, the unwanted portions of the design are discarded and the remaining portion is then affixed to a substrate for usage. The polymer chosen for use in the microfluidic variable capacitors is 3M #9019 adhesive polymer. This polymer has a thickness of 25 μm including the adhesive layers and been used in previous experiments to fabricate microchannels for DNA melting analysis and DNA polymerase chain reaction experiments [170]. The use of a double-sided adhesive polymer has numerous benefits for the device fabrication process: the xurographic technique for creating microchannels does not require the use of

cleanroom or photolithography equipment, the speed at which the channels can be designed and fabricated is reduced from several hours for conventional 3-D microstructure processing to a few minutes, the material cost per device is significantly reduced, and bonding between processed substrates to complete the fabrication process is rapid and guaranteed.

The microchannels include a xurographically-patterned stop valve which is designed to prohibit fluid flow into the microchannel due to capillary action. The stop valve as implemented is a simple passive gating system that exploits pressure barriers which arise from changes in the microchannel cross-section. A schematic diagram of the stop valve is shown in **Figure 2-65**.

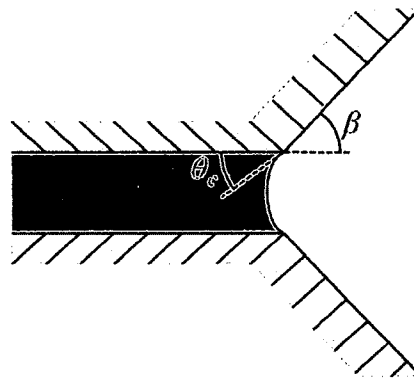


Figure 2-65: A top-down view of a microfluidic stop valve including angle definitions. Adapted from [171].

The pressure of the fluid flowing in the microchannel is a function of system energy W and liquid volume, V_l , given by

$$P = -\frac{dW}{dV_l} = \gamma_{la} \left(\cos \theta_c \frac{dA_{sl}}{dV_l} - \frac{dA_{la}}{dV_l} \right) \quad \text{Eq. 2-28}$$

where γ_{la} is the surface energy at the liquid-air interface area, θ_c is the equilibrium contact angle, A_{sl} is the solid-liquid interface area, and A_{la} is the liquid-air interface area [171]. In

the area of the stop valve, the sudden increase in A_{1a} causes the fluid pressure P to be negative, resulting in a pressure barrier which impedes fluid flow. After this point, external forces must be applied to induce the fluid into the expansion region and resume flow. **Figure 2-66** shows the microchannel patterns used to define the microchannel, stop valves, and microfluidic reservoirs for each device.

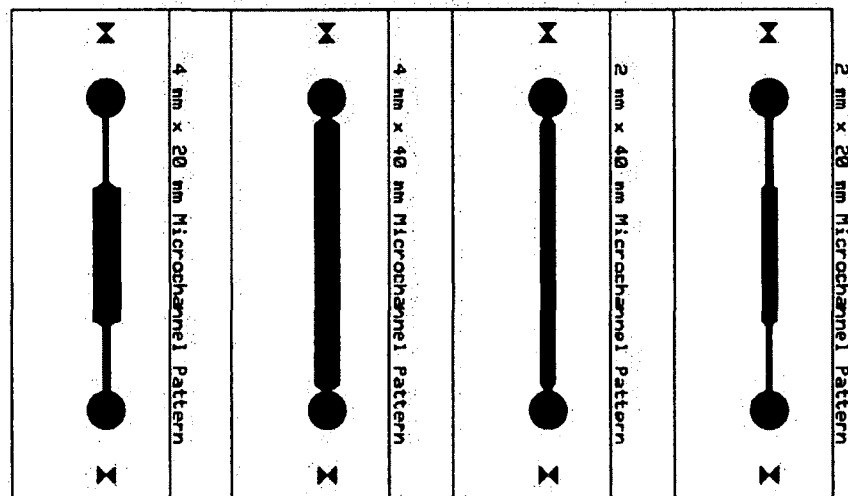


Figure 2-66: Microchannel pattern used to define the microchannel, stop valves, and microfluidic reservoirs for microfluidic variable capacitor devices.

To fabricate a microchannel layer, a sample of 3M #9019 adhesive polymer is loaded into the Graphitic CraftROBO Pro cutting plotter for xurographic patterning, as shown in **Figure 2-67**.

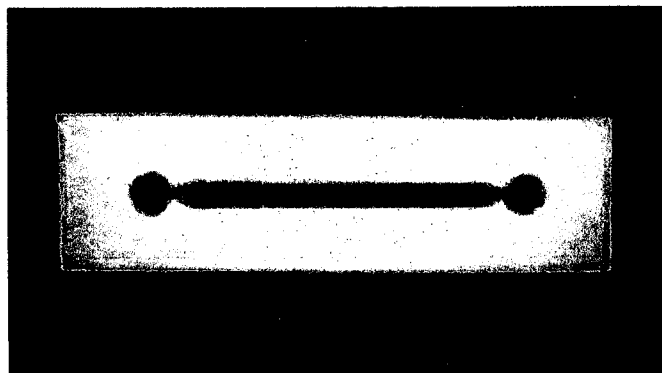


Figure 2-67: Xurographically-patterned microchannel layer for a 4 mm x 40 mm x 25 μm microfluidic variable capacitor device.

After completion of the patterning process, the exposed adhesive surface of the microchannel layer is used to adhesion bond the layer to a prepared glass substrate, as shown in **Figure 2-68**.

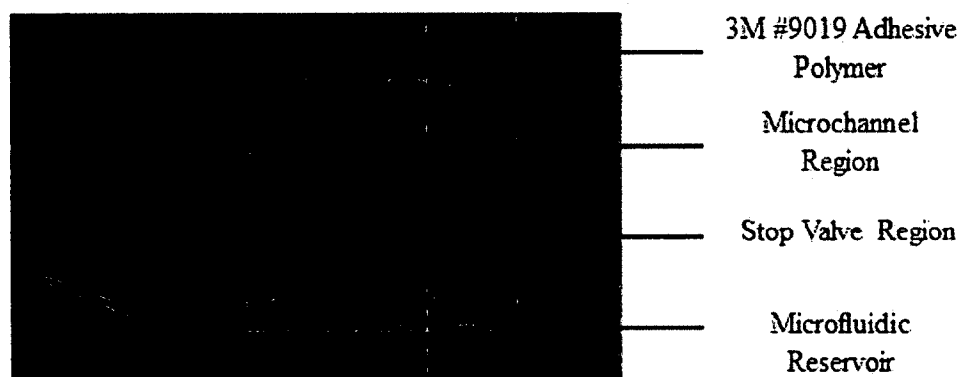


Figure 2-68: Photograph of a patterned microchannel layer affixed to a prepared substrate with key features illustrated.

2.3.3.3 Inlet/Outlet Hole

The inlet and outlet holes are fabricated by chemically etching the backside of a glass substrate with a patterned chromium electrode. A mechanical punch is used to remove a 1.5 mm diameter hole from a piece of chemically resistant Kapton tape. The Kapton tape is then affixed to the glass substrate while ensuring that the hole location

coincides with that of a microfluidic reservoir. A drop of 50% hydrofluoric acid is then deposited on the hole in the Kapton tape. The HF must be removed and the substrate cleaned after 15 minutes of etch time to remove calcium fluoride deposits generated by reactions between the HF and borosilicated glass substrate. Three etch cycles were necessary to leave only a thin membrane of glass on the front surface of the substrate. This membrane is removed with a silicon-carbide drill bit to complete the through-hole. A completed etched/drilled substrate is shown in **Figure 2-69**.

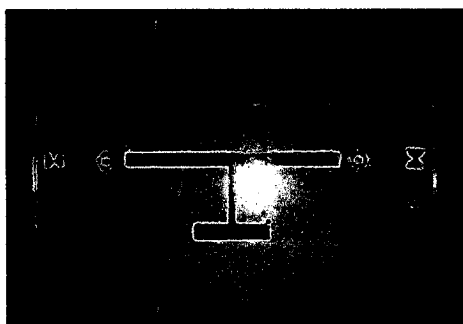


Figure 2-69: A 4 mm x 40 mm x 25 μm microfluidic variable capacitor electrode substrate with etched/drilled through-holes.

After the through-hole is completed, Upchurch Scientific Nanoport assemblies (shown in **Figure 2-70**) are baked onto the back surface of the glass substrate.

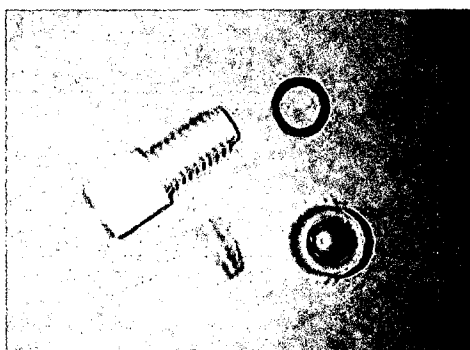


Figure 2-70: The components of an Upchurch Scientific Nanoport Assembly to be affixed to a glass substrate using thermal-set epoxy rings.

After the Nanoport assembly has been bonded, the inlet/outlet holes are fully fabricated (as shown in **Figure 2-71**) and the substrate is ready for final assembly.

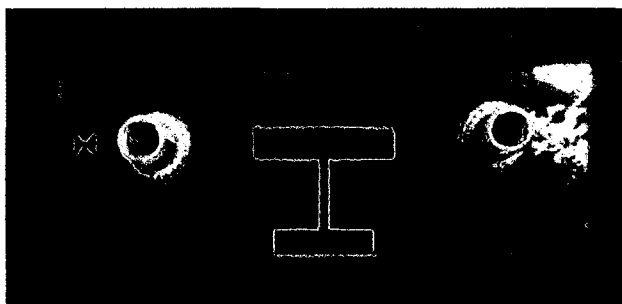


Figure 2-71: A 2 mm x 20 mm x 25 μm microfluidic variable capacitor electrode substrate with completed inlet/outlet hole assemblies.

2.3.3.4 *Final Assembly*

The xurographically-patterned microchannel layer is used to adhere the primary glass substrate with photolithographically-patterned chromium electrode and inlet/outlet holes to the secondary glass substrate with an additional photolithographically-patterned copper electrode, forming a parallel plate capacitor with a microchannel between the electrodes. The completed devices with varying electrode sizes are shown in **Figure 2-72**.

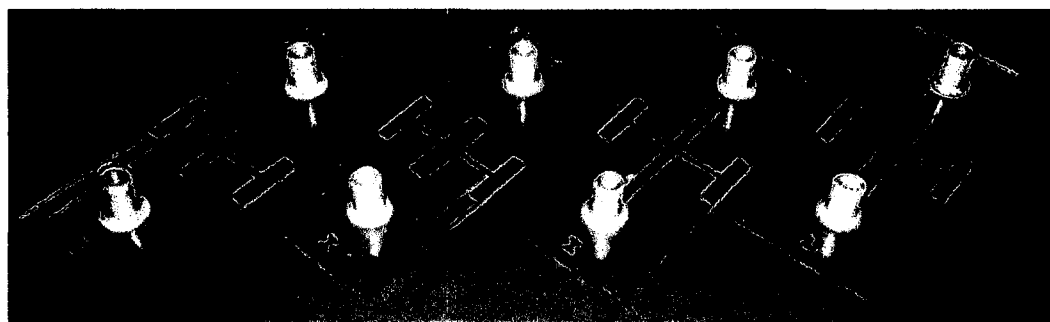


Figure 2-72: Completed microfluidic variable capacitors with varying microchannel dimensions.

2.3.4 Testing and Measurement

Testing of the microfluidic varactor devices was conducted using a Mastech 390-735 capacitance meter and a Stanford Research Systems PS350/5000V-25W High Voltage Power Supply. The initial capacitance (no liquid dielectric in the microchannel) was measured for each electrode configuration. This measurement was taken as a baseline to analyze the results of testing with a fluid dielectric; if the measured capacitance is less than the baseline, obviously current leakage between the conductors is present which will skew any collected data.

During testing with the liquid dielectric, the varactor device was oriented vertically such that any fluid movement would be against gravity. DI water was injected into the inlet reservoir and manually pumped such that the liquid-air interface occurred at the electrode edge once pressure equilibrium was established in the device. At this position, the capacitance of each device was again measured to serve as the unbiased capacitance C_0 .

An increasing DC voltage was applied to generate electrostatic forces necessary to overcome the equilibrium vacuum pressure holding the liquid-air interface stationary until visual observation of the fluid movement could be made. Unfortunately, the chromium electrode was not transparent enough to see the fluid movement through the microchannel even with the use of coloring agents to increase visibility. Instead, manual control of the liquid interface displacement was used via a syringe connected to the fluid inlet and capacitance measurements were taken. A linear relationship between the bias voltage and device capacitance was assumed as a result of the performed modeling, and

this relationship and the observed bias voltage necessary to achieve a maximum fill level were used to generate the following data sets.

Figure 2-73 shows the capacitance vs. fill percentage and actuation voltage data for a microfluidic varactor with 2 mm x 20 mm x 25 μm microchannel dimensions. The device has a minimum capacitance value of 15.1 pF at 0 V DC bias and a maximum capacitance value of 716 pF at 55.2 V DC bias, yielding a measured *CTR* of 4640%. The capacitance values deviate by an average of 26.5% from those predicted by the COMSOL simulations, and the measured *CTR* is 88.2% of the simulated value. These discrepancies can be attributed to variations in the thickness of the polymer and adhesive layers and dimensional inaccuracies introduced by the simple fabrication method, respectively.

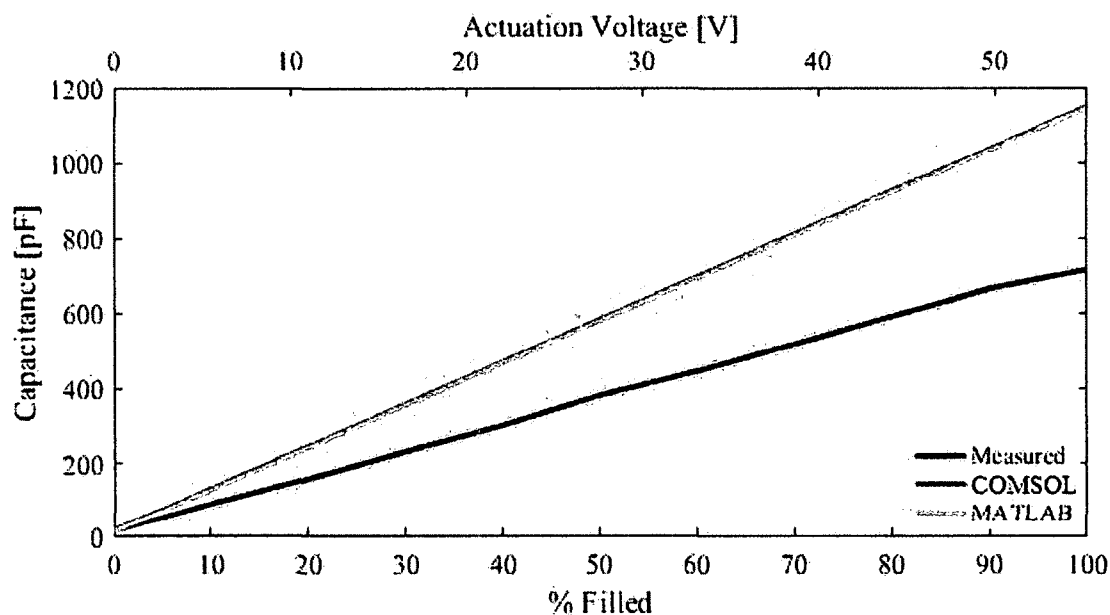


Figure 2-73: Device capacitance as a function of fill percentage and actuation voltage for a microfluidic varactor with 2 mm x 20 mm x 25 μm microchannel dimensions.

Figure 2-74 shows the capacitance vs. fill percentage and actuation voltage data for a microfluidic varactor with 4 mm x 20 mm x 25 μm microchannel dimensions. The device has a minimum capacitance value of 38.0 pF at 0 V DC bias and a maximum

capacitance value of 1880 pF at 98.5 V DC bias, yielding a measured *CTR* of 4850%. The capacitance values deviate by an average of 15.5% from those predicted by the COMSOL simulations, and the measured *CTR* is 72.3% of the simulated value. Again, these discrepancies can be attributed to variations in the thickness of the polymer and adhesive layers and dimensional inaccuracies introduced by the simple fabrication method, respectively.

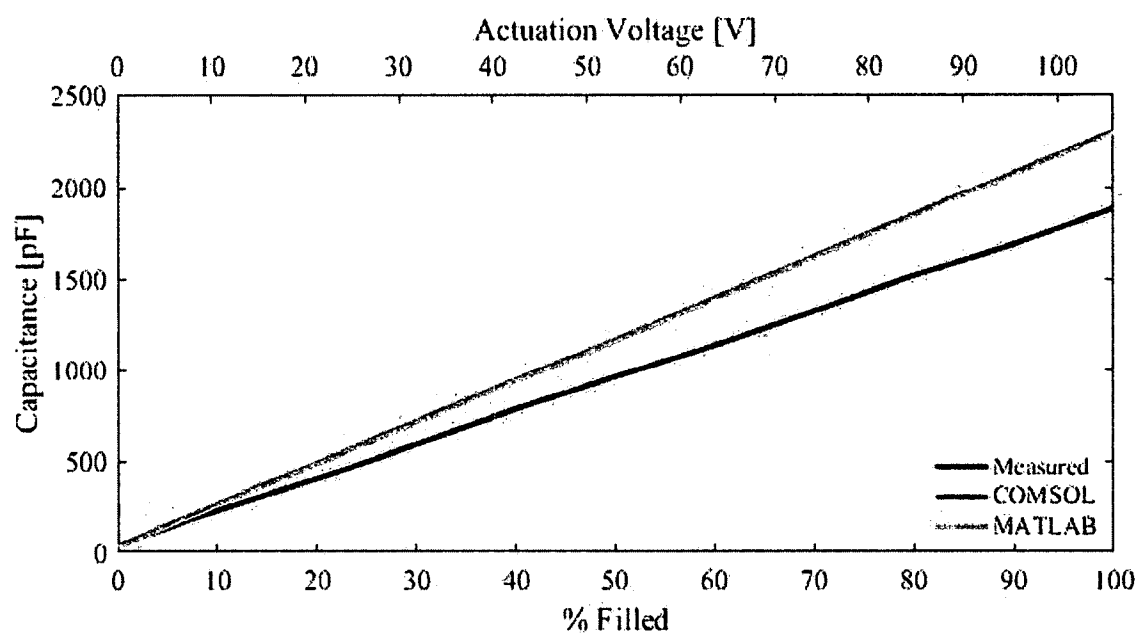


Figure 2-74: Device capacitance as a function of fill percentage and actuation voltage for a microfluidic varactor with 4 mm x 20 mm x 25 μ m microchannel dimensions.

Figure 2-75 shows the capacitance vs. fill percentage and actuation voltage data for a microfluidic varactor with 2 mm x 40 mm x 25 μ m microchannel dimensions. The device has a minimum capacitance value of 36.5 pF at 0 V DC bias and a maximum capacitance value of 1912 pF at 105.9 V DC bias, yielding a measured *CTR* of 5140%. The capacitance values deviate by an average of 12.3% from those predicted by the COMSOL simulations, and the measured *CTR* is 76.8% of the simulated value. Again,

these discrepancies can be attributed to variations in the thickness of the polymer and adhesive layers and dimensional inaccuracies introduced by the simple fabrication method, respectively.

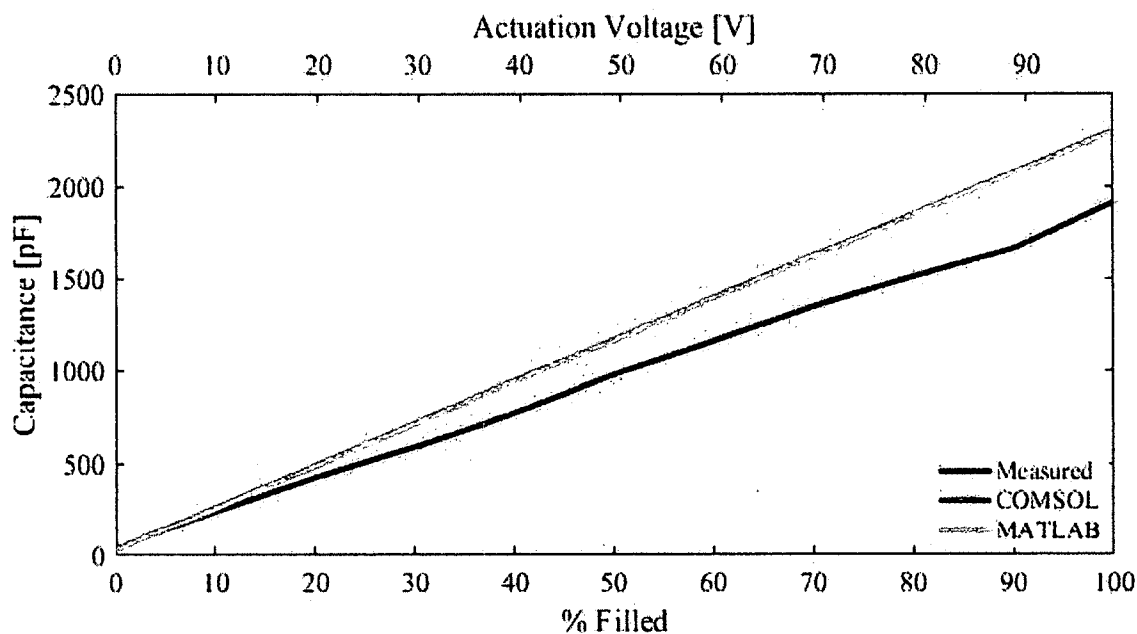


Figure 2-75: Device capacitance as a function of fill percentage and actuation voltage for a microfluidic varactor with 2 mm x 40 mm x 25 μm microchannel dimensions.

Finally, **Figure 2-76** shows the capacitance vs. fill percentage and actuation voltage data for a microfluidic varactor with 4 mm x 40 mm x 25 μm microchannel dimensions. The device has a minimum capacitance value of 68.6 pF at 0 V DC bias and a maximum capacitance value of 4351 pF at 183.2 V DC bias, yielding a measured *CTR* of 6240%. The capacitance values deviate by an average of 6.2% from those predicted by the COMSOL simulations, and the measured *CTR* is 88.2% of the simulated value. Again, these discrepancies can be attributed to variations in the thickness of the polymer and adhesive layers and dimensional inaccuracies introduced by the simple fabrication method, respectively.

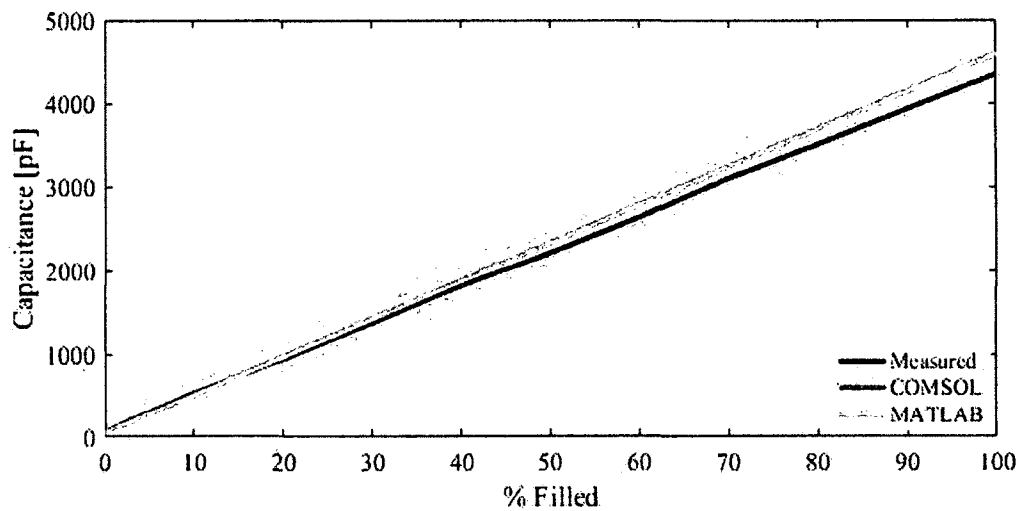


Figure 2-76: Device capacitance as a function of fill percentage and actuation voltage for a microfluidic varactor with 4 mm x 40 mm x 25 μm microchannel dimensions.

Figure 2-77 depicts the capacitance vs. fill percentage data for all four varactor designs. From **Figure 2-77**, we can see that an increase in electrode dimensions by a factor of 2 yields an approximately doubled device capacitance as is predicted by both the COMSOL and MATLAB models.

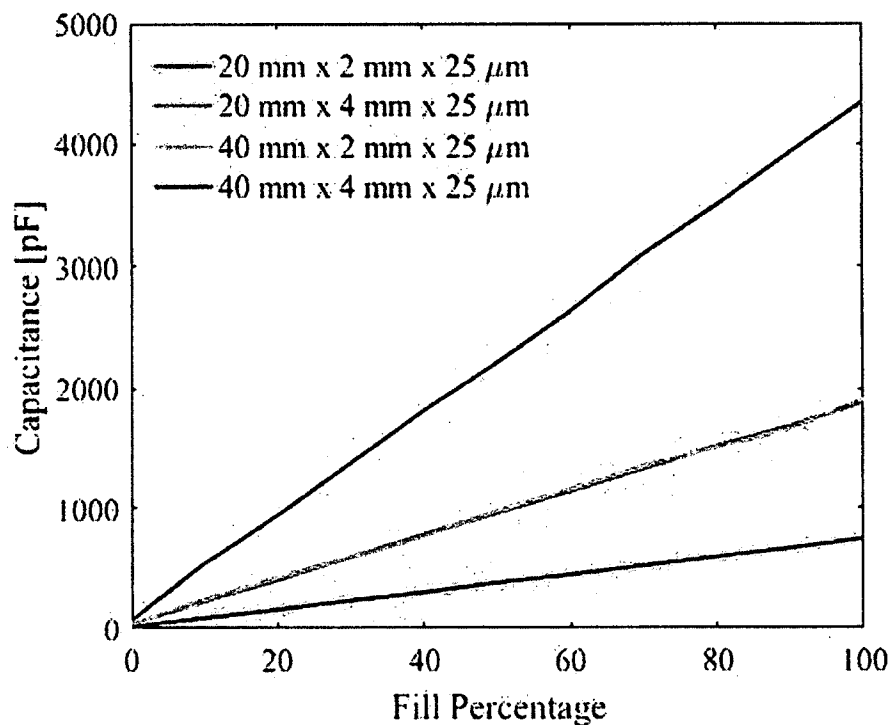


Figure 2-77: Capacitance vs. fill percentage data for different microchannel dimensions.

The results of the microfluidic varactor experiments and modeling are summarized in **Table 2-2**.

Table 2-2: Microfluidic Varactor Capacitive Tuning Range Performance.

Microchannel Dimensions	Actuation Voltage [V]	CTR - Measured	CTR - COMSOL	CTR - MATLAB
2 mm x 20 mm x 25 μm	0–55.2	4642%	6398%	8000%
4 mm x 20 mm x 25 μm	0–98.5	4847%	6722%	8000%
2 mm x 40 mm x 25 μm	0–105.9	5138%	6685%	8000%
4 mm x 40 mm x 25 μm	0–183.2	6243%	7071%	8000%

2.3.5 Conclusions and Future Work

The data presented in **Table 2-2** shows that a variable capacitor utilizing a partially inserted liquid dielectric is capable of achieving wide tuning ranges. The fabrication method used enabled simple device design and manufacture, however dimensional inaccuracies were introduced which caused the performance to deviate from the predictions of simulations. Use of conventional microfabrication techniques and materials would likely result in a device which achieves even better performance with enhanced reliability necessary for commercial applications.

To fully characterize the behavior of the device and its functionality, RF measurements must be made. Using a vector network analyzer, the device impedance as a function of frequency and resonance curves can be used to quantify the radio frequency performance of the device including electric quality factor and insertion loss.

CHAPTER 3

GRAPHENE-DOPED POLYMER FILMS FOR ELECTROMAGNETIC INTERFERENCE SHIELDING APPLICATIONS

3.1 Introduction

All electronic devices and many natural phenomena generate electromagnetic (EM) radiation in the form of propagating waves containing orthogonal electric and magnetic fields. Electromagnetic radiation can take many forms and is typically classified by the wavelength, λ , or linear frequency, ν , of the radiation as shown in **Figure 3-1**.

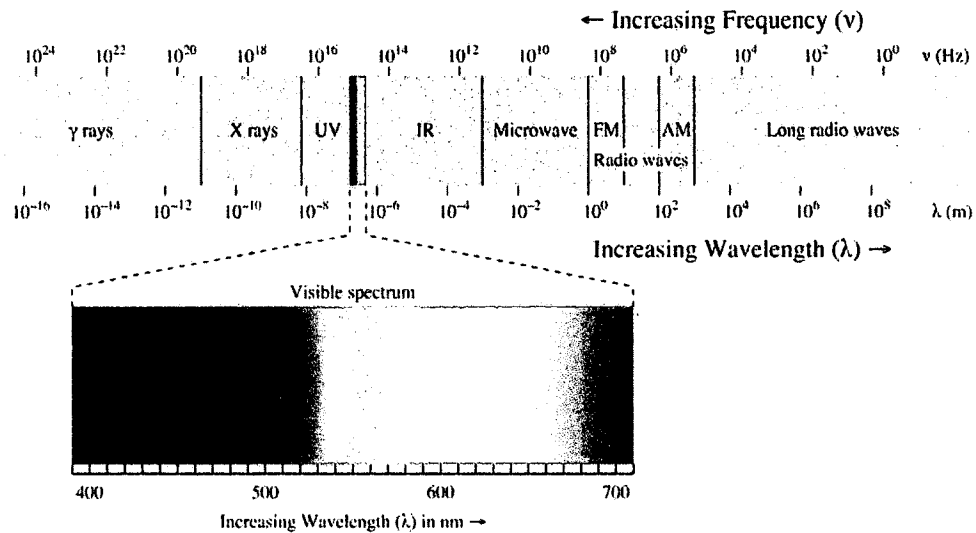


Figure 3-1: Classification of EM radiation as a portion of the electromagnetic spectrum [172].

Some forms of EM radiation are useful—radio waves, visible light, etc.—and some forms may be considered harmful— γ -rays, ultraviolet light, etc. The prevalent source of man-made EM radiation is the use of electronic devices which utilize some form of wireless communication technology and the proliferation of such devices has exacerbated issues with electromagnetic interference (EMI).

Electromagnetic interference is any spurious form of EM radiation that causes performance degradation or loss of information within an electronic component, system, or device through electromagnetic induction or coupling [173]. The effects of EMI may include temporary degradation effects like signal distortion and loss or permanent degradation like system or component failures. The principal method of combatting the effects of EMI is the use of EM shielding enclosures which hinder the propagation of EM fields through various mechanisms. An EM shielding enclosure may be used to house sensitive electronics which require isolation from external sources of EMI or conversely to confine the EM emissions of a device from interfering with external susceptible entities.

In the most basic sense an electromagnetic shielding enclosure is simply an electrically conductive housing which prohibits the transmission of EM radiation across its walls. The walls of a shielding enclosure may be constructed of mesh (perforated) sheets, in which case the enclosure acts like a sieve that prevents EM radiation with wavelengths larger than the holes of the mesh from passing through, or solid conductors which block EMI with both short and long wavelengths. The principal drawback of using solid conductors for shielding enclosures is the increased cost and weight of such an

enclosure. The performance of a EMI shielding enclosure is quantified by its shielding effectiveness

$$SE(\text{dB}) = 10 \log\left(\frac{P_i}{P_t}\right) = 20 \log\left(\frac{E_i}{E_t}\right) = 20 \log\left(\frac{H_i}{H_t}\right) \quad \text{Eq. 3-1}$$

where P_i is the EM power, E_i is the amplitude of the electric field, and H_i is the amplitude of the magnetic field intensity incident on the shielding enclosure and P_t is the EM power, E_t is the amplitude of the electric field, and H_t is the amplitude of the magnetic field intensity transmitted through the shielding enclosure.

3.2 Electromagnetic Shielding Theory

To quantify the behavior of an EM shielding enclosure, an understanding of how an EM wave interacts with the material that comprises the shielding enclosure is necessary. The following assumptions will be made throughout this section: the distance between the EMI source and the shielding enclosure, r , is sufficiently large such that far-field behavior is dominant ($r > 2\lambda$) as shown in **Figure 3-2** where λ is the wavelength of the EM radiation; the shielding material is homogeneous (permittivity ϵ_s and permeability μ_s are linear) and a good conductor ($\sigma_s \gg \omega\epsilon_s$) where σ_s is the electrical conductivity of the shielding material and ω is the angular frequency of the EM radiation; and the shielding enclosure consists of a planar slab of material with a finite thickness t to illustrate which material properties influence shielding effectiveness without considering geometric contributions due to the shape of the enclosure.

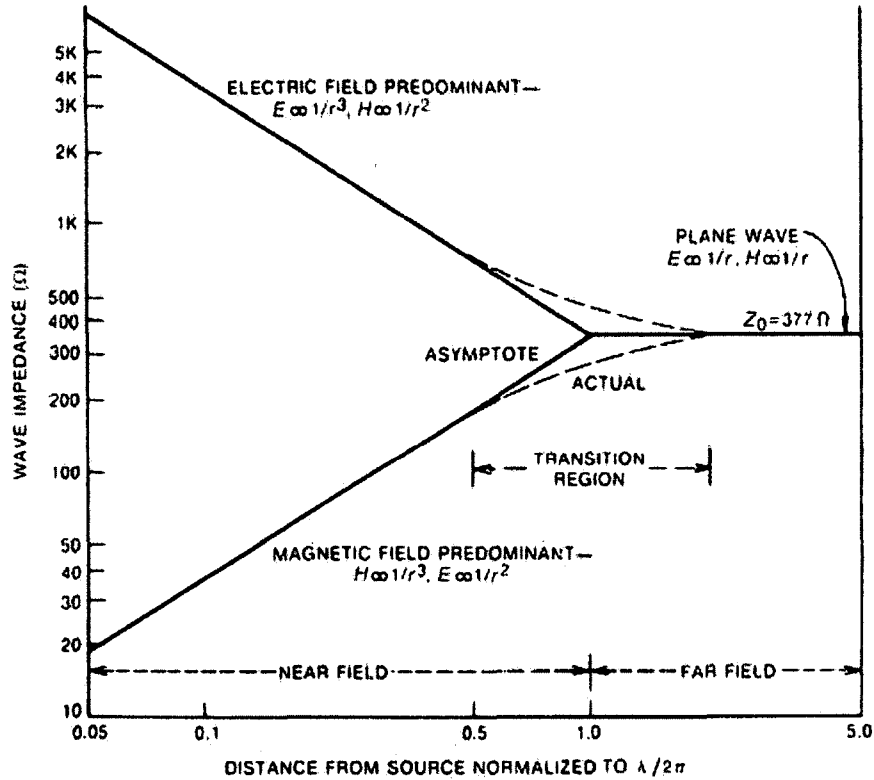


Figure 3-2: Characterization of electromagnetic waves as a function of distance from source [174].

In the far-field region, all EM fields can be considered as plane waves propagating in a direction normal to the wavefront, as seen in **Figure 3-3**.

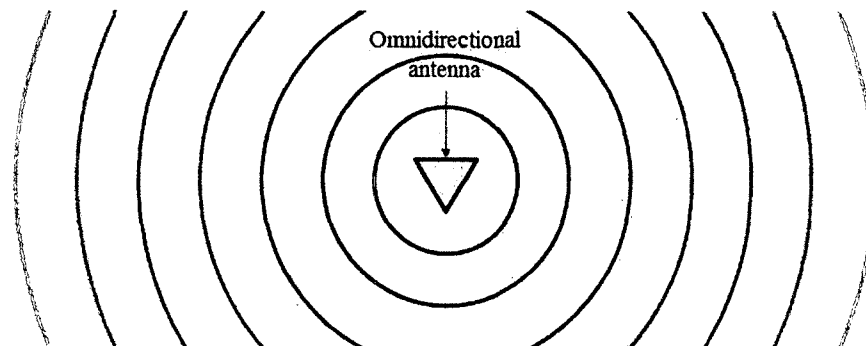


Figure 3-3: As distance between the radiating antenna and surface of incidence increases, the wavefront becomes increasingly planar.

These waves can be described in the frequency domain by the Helmholtz equations

$$\nabla^2 \mathbf{E} + \omega^2 \mu \epsilon \mathbf{E} = 0 \quad \text{Eq. 3-2}$$

and

$$\nabla^2 \mathbf{H} + \omega^2 \mu \epsilon \mathbf{H} = 0 \quad \text{Eq. 3-3}$$

whose solutions are travelling waves propagating in a direction orthogonal to \mathbf{E} and \mathbf{H} .

An EM wave has a characteristic impedance defined as

$$\eta = \frac{|\mathbf{E}|}{|\mathbf{H}|} = \sqrt{\frac{j\omega\mu}{\sigma + j\omega\epsilon}} \quad \text{Eq. 3-4}$$

where ϵ is the permittivity, μ is the permeability, and σ is the electrical conductivity of the material through which the wave is propagating. When an electromagnetic wave transitions between two materials (wave propagation across a material interface), its characteristic impedance changes. Consider the case of an electromagnetic plane wave incident normal to the surface of a slab of shielding (conductive) material of finite thickness, t , as shown in **Figure 3-4**.

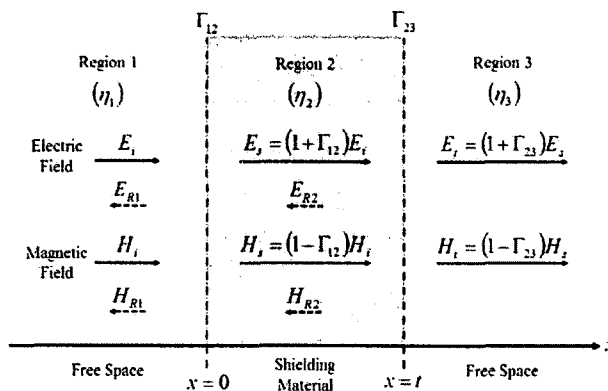


Figure 3-4: Behavior of normally-incident plane waves on a shielding medium. Adapted from [174].

When the incident waves in Region 1 reach the material interface at $x = 0$, some portion of the total wave power will be reflected at the interface (propagating in the $-x$ -direction) generating the reflected waves E_{R1} and H_{R1} , and the remainder will be transmitted into the shielding material (propagating in the $+x$ -direction) as waves E_s and H_s where a finite conductivity for the shielding material ($\sigma_s \neq \infty$) has been assumed, as illustrated in **Figure 3-4**. If the shielding material is electrically conductive, waves E_s and H_s will experience attenuation due to resistive losses while propagating through the bulk of the shielding material. When waves E_s and H_s reach the material interface at $x = t$, again some portion of the wave power will be reflected at the interface generating the reflected wave E_{R2} and H_{R2} , while the remainder will be transmitted into Region 3 as waves E_t and H_t . Reflected waves E_{R2} and H_{R2} may again reflect at the material interface at $x = 0$ or be transmitted into Region 1. From this, we can see that the shielding effectiveness defined in **Eq. 3-1** is thus due to a combination of reflection loss R , absorption loss A , and internal reflections B , as

$$SE \text{ (dB)} = R \text{ (dB)} + A \text{ (dB)} + B \text{ (dB)}. \quad \text{Eq. 3-5}$$

3.2.1 Reflection Loss

The generation of the reflected waves E_{R1} and H_{R1} seen in **Figure 3-4** occurs because of the change in wave impedance that occurs at the interface of Region 1 (free space) and Region 2 (the shielding material). The wave impedance in Region 1 ($\epsilon = \epsilon_0$, $\mu = \mu_0$, $\sigma = 0$) is

$$\eta_1 = \sqrt{\frac{\mu_0}{\epsilon_0}} = 377 \text{ } \Omega = \eta_0 \quad \text{Eq. 3-6}$$

and the wave impedance in Region 2 ($\sigma_s \gg \omega\epsilon_s$) is

$$\eta_2 = \sqrt{\frac{j\omega\mu_s}{\sigma_s + j\omega\epsilon_s}} \approx \sqrt{\frac{j\omega\mu_s}{\sigma_s}} = (1+j)\sqrt{\frac{j\omega\mu_s}{2\sigma_s}} = \eta_s. \quad \text{Eq. 3-7}$$

This change in wave impedance can be characterized by the reflection coefficient of the interface, given by

$$\Gamma_{12} = \frac{\eta_2 - \eta_1}{\eta_2 + \eta_1} = \frac{\eta_s - \eta_0}{\eta_s + \eta_0}. \quad \text{Eq. 3-8}$$

Satisfying boundary conditions requirements for the propagation of normally incident EM waves at the interface yields the relationships

$$E_s = (1 + \Gamma_{12})E_i = \frac{2\eta_s}{\eta_s + \eta_0} E_i \quad \text{Eq. 3-9}$$

and

$$H_s = (1 - \Gamma_{12})H_i = \frac{2\eta_0}{\eta_s + \eta_0} H_i \quad \text{Eq. 3-10}$$

where E_i (H_i) is the amplitude of the electric (magnetic) field incident on the surface of the shielding material ($x = 0^-$) and E_s (H_s) is the amplitude of the electric (magnetic) field as they begin to propagate through the shielding material ($x = 0^+$), as seen in **Figure 3-4**. The negative sign on the reflection coefficient of the magnetic field equation comes from the requirement that the reflected wave power is travelling opposite the direction of E_s (H_s).

The material interface at $x = t$ will also have an associated reflection coefficient

$$\Gamma_{23} = \frac{\eta_3 - \eta_2}{\eta_3 + \eta_2} = \frac{\eta_0 - \eta_s}{\eta_0 + \eta_s}. \quad \text{Eq. 3-11}$$

At the interface between Regions 2 and 3 (and neglecting any attenuation E_s and H_s may experience due to propagation within a lossy medium), the relationships between the propagating wave E_s (H_s) at $x = t^-$ and the transmitted wave E_t (H_t) at $x = t^+$ are

$$E_t = (1 + \Gamma_{23})E_s = \frac{2\eta_0}{\eta_0 + \eta_s} E_s \quad \text{Eq. 3-12}$$

and

$$H_t = (1 - \Gamma_{23})H_s = \frac{2\eta_s}{\eta_0 + \eta_s} H_s. \quad \text{Eq. 3-13}$$

Substituting Eq. 3-9 into Eq. 3-12 and Eq. 3-10 into Eq. 3-13, we can then see that the portions of E_i and H_i transmitted through the shielding material is given by

$$E_t = (1 + \Gamma_{12})(1 + \Gamma_{23})E_i = \frac{2\eta_s}{\eta_s + \eta_0} \frac{2\eta_0}{\eta_0 + \eta_s} E_i = \frac{4\eta_0\eta_s}{(\eta_0 + \eta_s)^2} E_i \quad \text{Eq. 3-14}$$

and

$$H_t = (1 - \Gamma_{12})(1 - \Gamma_{23})H_i = \frac{2\eta_0}{\eta_s + \eta_0} \frac{2\eta_s}{\eta_0 + \eta_s} H_i = \frac{4\eta_0\eta_s}{(\eta_0 + \eta_s)^2} H_i. \quad \text{Eq. 3-15}$$

For electrically conductive shielding materials, $\eta_0 \gg \eta_s$ and thus

$$E_t \approx \frac{4\eta_s}{\eta_0} E_i \quad \text{Eq. 3-16}$$

and

$$H_t \approx \frac{4\eta_s}{\eta_0} H_i \quad \text{Eq. 3-17}$$

yielding a reflection loss of

$$R(\text{dB}) = 20 \log\left(\frac{E_i}{E_t}\right) = 20 \log\left(\frac{H_i}{H_t}\right) = 20 \log\left(\frac{\eta_0}{4\eta_s}\right). \quad \text{Eq. 3-18}$$

3.2.2 Absorption Loss

When an electromagnetic wave propagates through a lossy medium like a conductive material, the majority of the fields are confined to propagate near the surface of the conductor due to a phenomenon known as the skin effect [175]. The skin effect occurs due to induced eddy currents generated by the non-reflected portions of the dynamic magnetic field. The eddy currents generate an induced magnetic field that opposes the propagating magnetic field H_s , causing joule heating (ohmic losses) through the bulk of the material and a reduction in field intensity as a function of propagation distance through the medium, given by

$$E_s(x) = E_0 e^{-x/\delta} \quad \text{Eq. 3-19}$$

and

$$H_s(x) = H_0 e^{-x/\delta} \quad \text{Eq. 3-20}$$

where E_0 (H_0) are the amplitudes of the electric (magnetic) fields at $x = 0^+$ and δ is known as the skin depth of the material, given by

$$\delta = \sqrt{\frac{2}{\omega\mu\sigma}}. \quad \text{Eq. 3-21}$$

At the material interface at $x = t$, the field intensities are given by

$$E_s(t) = E_0 e^{-t/\delta} \quad \text{Eq. 3-22}$$

and

$$H_s(t) = H_0 e^{-t/\delta}, \quad \text{Eq. 3-23}$$

yielding an absorption loss of

$$A(\text{dB}) = 20 \log \left(\frac{E_s(0)}{E_s(t)} \right) = 20 \log \left(\frac{H_s(0)}{H_s(t)} \right) = 20 \log(e^{t/\delta}). \quad \text{Eq. 3-24}$$

3.2.3 Losses Due to Multiple Internal Reflections

For electromagnetic waves incident on a conductive medium ($\eta_0 \gg \eta_s$), analysis of **Eq. 3-9** and **Eq. 3-10** shows that most of the incident electric field will be reflected by the shielding material and most of the incident magnetic field will be transmitted into the shielding material. If the slab of shielding material seen in **Figure 3-4** is sufficiently thin such that absorption losses are small, internal reflections may occur at the material interface between Regions 2 and 3 generating backwards-travelling waves E_{R2} and H_{R2} . A portion of these reflected waves can in turn reflect off the material interface between Regions 1 and 2, generating forward-travelling waves. This process can repeat indefinitely, however the intensity of the internally-reflected waves is typically negligible after a few reflections due to absorption losses from propagating through the shielding material multiple times [174].

For a slab of shielding material with thickness small enough to support multiple internal reflections for the propagating magnetic field wave, the intensity of the total magnetic field transmitted through the shielding material is given by

$$\begin{aligned} H_{t,\text{tot}} &= H_0(1-\Gamma_{12})e^{-t/\delta}(1-\Gamma_{23}) + H_0(1-\Gamma_{12})e^{-t/\delta}(\Gamma_{23})e^{-t/\delta}(\Gamma_{12})e^{-t/\delta}(1-\Gamma_{23}) + \dots \\ &= \frac{4H_0\eta_s}{\eta_0} \sum_{n=0}^{\infty} e^{-(2n+1)t/\delta} (\Gamma_{12})^n (\Gamma_{23})^n \\ &\approx \frac{4H_0\eta_s}{\eta_0} \left[\frac{1}{2\sinh(t/\delta)} \right] \end{aligned} \quad \text{Eq. 3-25}$$

where the phase-shift experienced by the propagating wave(s) has been neglected. This model includes reflection from the material interface between Regions 1 and 2,

attenuation losses, and multiple internal reflections for the magnetic field. The total losses experienced by magnetic fields propagating through the shielding material would then be

$$SE(\text{dB}) = 20 \log \left(\frac{H_0}{H_{t,\text{tot}}} \right) = 20 \log \left(\frac{\eta_0}{4\eta_s} \right) + 20 \log [2 \sinh(t/\delta)]. \quad \text{Eq. 3-26}$$

Equating this expression with **Eq. 3-5** and observing that the first term is $R(\text{dB})$ (**Eq. 3-18**), the second term must then be $A(\text{dB}) + B(\text{dB})$. Solving for $B(\text{dB})$ yields

$$B(\text{dB}) = 20 \log [2 \sinh(t/\delta)] - 20 \log(e^{t/\delta}) = 20 \log(1 - e^{-2t/\delta}). \quad \text{Eq. 3-27}$$

The term $B(\text{dB})$ is often referred to as the shielding effectiveness correction factor as its value is always negative and thus lowers the total shielding effectiveness in the case of thin shielding materials which support multiple internal reflections of the propagating electromagnetic fields.

3.3 Methods for Measuring Far-Field Shielding Effectiveness

There are four basic methods for measuring the far-field shielding effectiveness of material samples: the open field (or free space) method, the shielded room method, shielded box methods, and coaxial transmission line methods [176]. Each of these methods have specific advantages and disadvantages which will be discussed below.

3.3.1 Open Field Method

The open field or free space method of shielding effectiveness measurement is used to determine the amount of EM radiation that is transmitted through a shielding enclosure designed to house a specific electronic assembly where the shielding enclosure and internal electronics are treated as a single device. This method is used by manufacturers to ensure EMI compliance within established standards and serves as a test of the in-operation performance of a completed device and its associated EMI shielding.

The device-under-test is placed in an area with no metallic objects and receiving antennas are placed at various distances away ($d_{\min} = 30$ m). Any signals transmitted to the receiving antennas are processed by noise meters to ascertain the radiated field strength of the EM emissions. Simultaneously, conducted emissions transmitted through the power source are also measured [176], as shown in **Figure 3-5**.

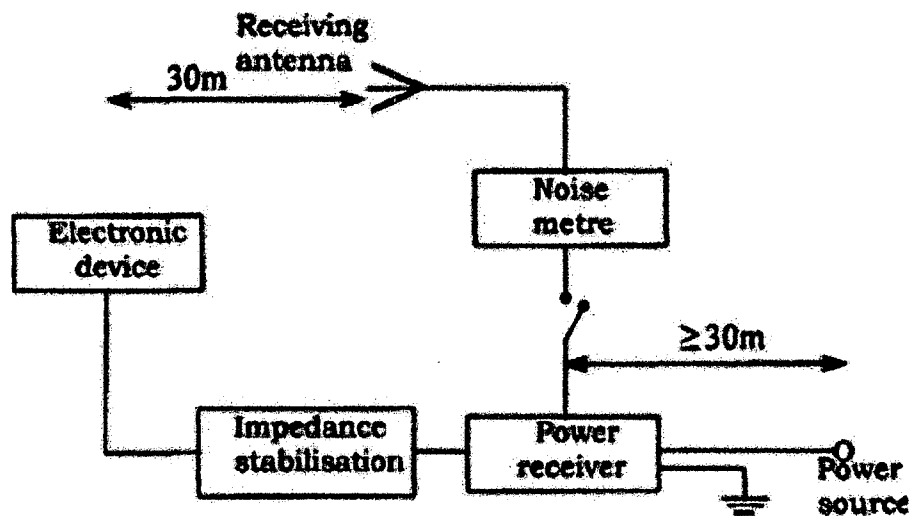


Figure 3-5: A block diagram describing the open field shielding effectiveness measurement [176].

3.3.2 Shielded Room Method

The shielded room method of measuring EM shielding effectiveness is used to determine the qualitative response of a planar sample of shielding material. In this method, a large anechoic chamber is divided into two regions by a metal partition containing an aperture to enable EM transmission between the two regions. A transmitting antenna is placed inside the chamber on one side of the aperture and a receiving antenna is placed inside the chamber on the other side of the aperture with the distance between the antennas remaining fixed. All signal generators, amplifiers,

and receivers are located outside the test chamber to minimize potential interference. A reference measurement is made by transmitting a signal through the aperture. Then a sample (with surface area typically larger than 2 m^2) is placed over the aperture with care to ensure that electrical contact is made between the sample and metal partition in order to electrically isolate the transmitting and receiving antennas. A signal is transmitted across the sample and picked up by the receiving antenna, as shown in **Figure 3-6**. The shielding effectiveness of the sample is determined by comparing the signal levels with and without the shielding material closing the aperture. This method is an adaptation of the MIL-STD-285 testing procedure for enclosures in the frequency range of 100 kHz – 10 GHz developed in 1956 [177].

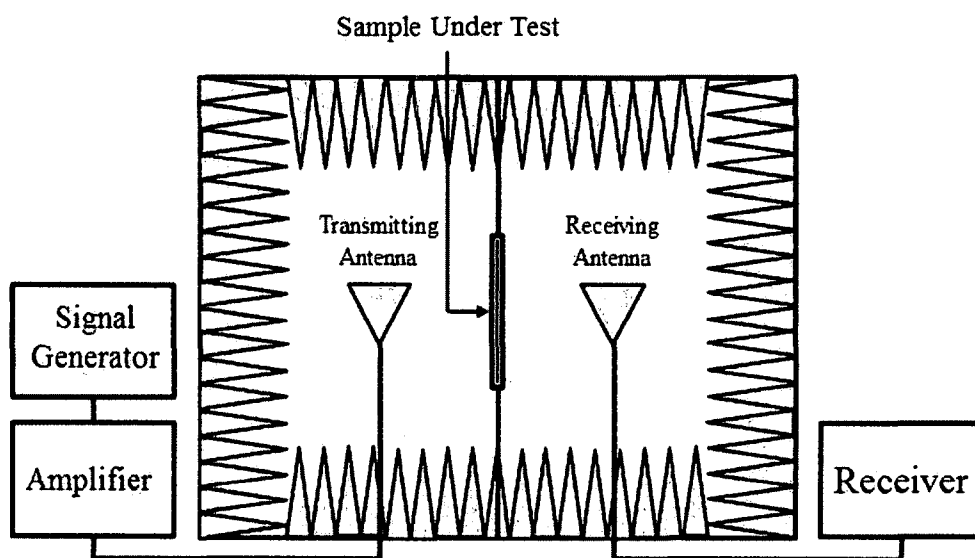


Figure 3-6: Schematic diagram of shielded room shielding effectiveness measurements. Adapted from [178].

The principal drawback of this method is the size of the test enclosure and the requirement for a large sample of shielding material to minimize diffraction effects. For

this reason, this method is typically restricted to solid and perforated metal samples generated via industrial processes as opposed to laboratory-generated samples.

3.3.3 Shielded Box Methods

The shielded box method is a scaled-down version of the shielded room method with a few fundamental changes: instead of an anechoic chamber which uses baffles to prevent reflections and simulate far-field conditions, a reverberation chamber is used to house the testing apparatus; a metal box with an aperture replaces the need to partition the reverberation chamber; and electromagnetic gaskets are used to prevent signal leakage between the reverberation chamber and interior of the shielding enclosure due to the smaller required sample size. A block diagram detailing the experimental set-up is shown in **Figure 3-7**.

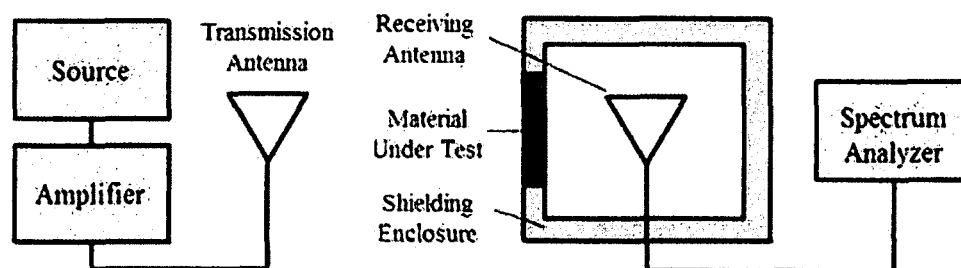


Figure 3-7: Block diagram of shielded box shielding effectiveness measurement. Adapted from [176].

The shielded box method is widely used for comparative measurements of test specimens of different shield materials [176] however the experimental set-up, as described above, has numerous drawbacks: the use of a reverberation chamber requires multiple measurements be made by placing the transmitting antenna at various points inside the reverberation chamber to determine an average for the shielding effectiveness of the sample resulting in difficulties with experimental repeatability; adequate electrical

contact between the test specimen and metal box is difficult to achieve, causing the results of the test to be highly dependent on operator skill as opposed to material properties; and the performance of the experimental set-up is only reliable for frequencies up to 500 MHz. To overcome these limitations, researchers have used adaptations of IEEE Std 299 [179–183] and ASTM E1851 [184–188] such as the use of anechoic chambers, frequency stirrers (both inside the reverberating chamber and metal box), and simultaneous excitation via multiple transmitting antennas to increase measurement accuracy and repeatability [189–191].

3.3.4 Coaxial Transmission Line Methods

Coaxial transmission line methods of measuring shielding effectiveness of planar samples are based on waveguide/transmission line theory and use electromagnetic coupling effects to measure the amount of power transmitted through a shielding sample. Coaxial transmission line test fixtures are the most commonly used means to measure shielding effectiveness of planar EMI shielding material samples as the results are easily repeatable and can be resolved into reflected, absorbed, and transmitted components by observing the scattering parameters of the multiport network, allowing an operator to determine the dominant shielding mechanism of a sample as well as the quantitative results of the experiment [176].

3.3.4.1 ASTM E57 Test Fixtures

The first coaxial transmission line test fixtures were developed in the early 1980s and utilized a two-part coaxial test fixture with a solid inner conductor as shown in **Figure 3-8**. These test fixtures used washer-shaped samples which were inserted between the inner- and outer-conductors of the test fixture which enabled the test apparatus to

support TEM₁₁ modes of electromagnetic radiation. The dimensions of both the sample and test fixture were standardized in ASTM ES7, yielding an operational frequency range of 1 MHz – 1.8 GHz [192]. At frequencies higher than 1.8 GHz the tapered section of the test fixture can support and reflect higher-order modes causing measurements to be unreliable.

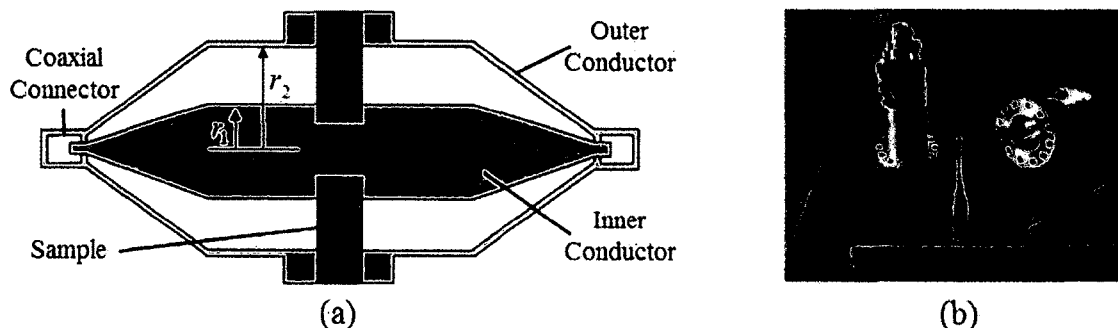


Figure 3-8: (a) Cross-sectional view (adapted from [176]) and (b) picture of ASTM ES7 test fixture [193].

To facilitate measurements at higher frequencies, researchers altered the dimensions of the test fixture to increase the cut-off frequency of the supported mode, given by

$$f_{\max} < \frac{c}{\pi(r_1 + r_2)} \quad \text{Eq. 3-28}$$

where c is the speed of light in a vacuum, and r_1 and r_2 are the radii of the inner and outer conductor, respectively while also maintaining the characteristic impedance of the test fixture at $Z_0 = 50 \Omega$ using the relationship

$$Z_0 = \sqrt{\frac{L}{C}} = \frac{\sqrt{\frac{\mu_0}{2\pi} \ln(r_2/r_1)}}{\sqrt{\frac{2\pi\epsilon_0}{\ln(r_2/r_1)}}} = \frac{377 \Omega}{2\pi} \ln\left(\frac{r_2}{r_1}\right). \quad \text{Eq. 3-29}$$

Modified versions of the ASTM ES7-83 design have achieved operating frequencies up to 5 GHz [193–195].

3.3.4.2 ASTM D4935 Test Fixtures

To improve measurement accuracy, coaxial test cells with interrupted conductors were developed. These cells utilize capacitive coupling between the sections of the inner conductor and flanges to determine the shielding effectiveness of conductive samples by measuring the difference in signal strength using load and reference samples, as shown in **Figure 3-9**.

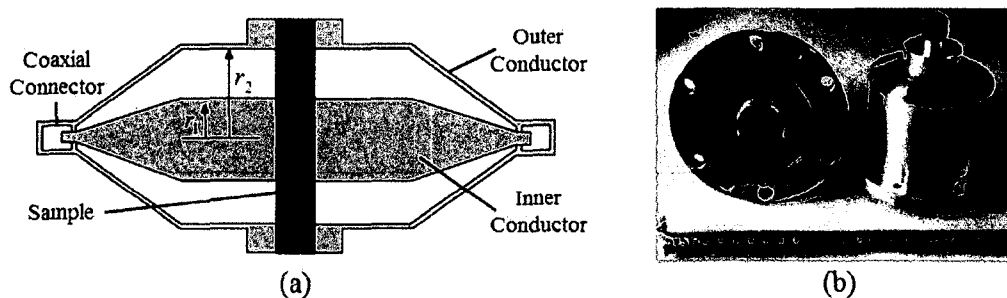


Figure 3-9: (a) Cross-sectional view (adapted from [176]) and (b) picture of ASTM D4935 test fixture [193].

The load sample consists of an insulating disc coated with shielding material with size equal to the external dimensions of the test apparatus. The reference sample consist of an insulating disc coated with shielding material with size equal to the dimensions of the inner conductor and a concentric ring of shielding material with dimensions matching the flange dimensions of the test apparatus, as shown in **Figure 3-10**. The reference and load samples must be made of the same material and have the same thickness to ensure accurate results. The dimensions of both the sample and test fixture were standardized in ASTM D4935, yielding an operational frequency range of 30 MHz – 1.5 GHz [196, 197].

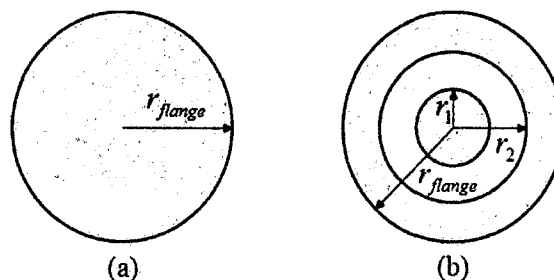


Figure 3-10: (a) Load and (b) reference samples for ASTM D4395-based test fixtures.

These test fixtures suffered similar problems as ASTM ES7 fixtures at high-frequencies of operation, causing researchers to again manipulate the dimensions of the fixture while maintaining a 50Ω characteristic impedance to increase the TE_{11} cut-off frequency to up to 18 GHz [193, 198, 199].

3.3.4.3 TEM-t Cell Test Fixtures

In ASTM D4395-based test fixtures, the inner conductor of the coaxial cell is in direct contact with the surface of the material under test. In cases where the sample surface is rough or has a high contact-resistance, accurate measurements are unable to be obtained. To combat this, Catrysse developed an adapted test fixture in which the inner conductor on each side of the flange assembly is shortened such that no contact is made between the test apparatus and material sample, known as the TEM-t cell [200, 201]. Illustrated in **Figure 3-11**, TEM-t test fixtures uses capacitive coupling to determine the shielding effectiveness for a variety of materials not supported by ASTM ES7- and ASTM D4395-based tools such as coated textiles and filled plastics.

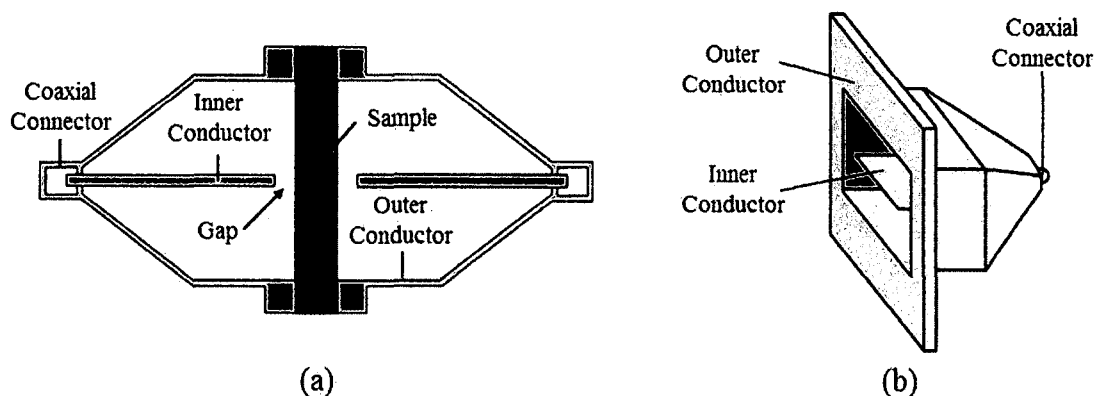


Figure 3-11: (a) Cross-sectional view (adapted from [176]) and (b) schematic diagram of the TEM-t cell (adapted from [200]).

3.4 A Brief Review of Composite Materials Used for EMI Shielding

Combining the results of Eq. 3-18, Eq. 3-24, and Eq. 3-27, the total shielding effectiveness of a planar sample of shielding material is given by

$$SE(\text{dB}) = 20 \log\left(\frac{\eta_0}{4\eta_s}\right) + 20 \log(e^{t/\delta}) + 20 \log(1 - e^{-2t/\delta}). \quad \text{Eq. 3-30}$$

Equation 3-30 illustrates that the shielding effectiveness of a planar slab of material depends primarily on the characteristic impedance of the material η_s and the skin depth of the material δ , both of which depend on the material's permeability μ_s and electrical conductivity σ_s . For materials with low conductivities ($\sigma_s \leq 10^4$ S/m), the material's permittivity ϵ_s also plays a significant role in its shielding effectiveness. Due to the high electrical conductivity requirement of an effective shielding material, metals have been the traditional material of choice for shielding enclosures. However, the performance requirements for certain aerospace and military applications have led to the investigation of composite materials which utilize insulating polymers and high-conductivity micro- and nanoparticles to provide EMI shielding.

The shielding properties of polymer films doped with conductive fillers have been shown to exhibit performance sufficient to replace many metal EMI shielding materials. In such a composite material, EMI shielding is achieved through sufficient doping to create an electrically-conductive network within the bulk. Continuous electronic pathways are not necessary to achieve EMI shielding, however shielding performance is increased when the conductive fillers are in electrical contact together [202]. While different polymers can be used to obtain specific mechanical, physical and chemical properties, the EMI properties are tuned by the electrically conductive dopant material. There are three types of conductive dopants commonly used for composite EMI shielding materials: metal, metal-coated fillers, and carbon.

Metal dopant materials used for composite EMI shielding can be in the form of fibers [203], filaments [204], or flakes [205]. Yanagisawa *et al.* developed a copper-fiber/ABS composite that achieved a 70 dB shielding effectiveness at 300 MHz by loading thermoplastic with 20% by volume Cu cylindrical fibers with approximate dimensions of 50 μm in diameter and 2.4 mm in length [203]. Shui and Chung achieved a shielding effectiveness of 87 dB at 1 GHz using a 7% by volume nickel filament doped polyethersulfone [204]. The nickel filaments used were 0.4 μm in diameter with lengths in excess of 100 μm .

When metal fibers with diameters less than 2 μm in diameter are required, carbon fibers (which are much easier to manufacture) are coated with thin layers of metal [206–208]. The EMI shielding composite developed by Huang and Wu achieved 47 dB of signal reduction, however oxidation of the nickel coating through phase separation of the polycarbonate and ABS polymers caused the shielding effectiveness to decrease with

increasing heat treatment time [206]. Further investigation eliminated the polycarbonate material while achieving similar values for shielding effectiveness, however problems with interfacial adhesion between the ABS and nickel-coated-fibers led to separation which lowered SE over time [207]. Tzeng and Chang used electroless deposition to coat carbon fibers with copper and nickel [208]. The coating process used resulted in poor bonding between the metal coating and carbon fibers, yielding low shielding effectiveness values.

To avoid potential issues with coating adhesion and metal oxidation, many researchers have begun to investigate carbon-based materials like carbon black [209], carbon fibers [210], carbon nanotubes [211], and graphene [212] as dopants in composite EMI shielding materials. While metals offer higher electrical conductivity, carbon offers significant oxidation resistance and thermal stability in comparison [202].

3.5 Graphene-Doped Polymer Films for Electromagnetic Interference Shielding Applications

Graphene is of particular interest among the EMI shielding community due to its extraordinarily unique characteristics. Graphene is a monolayer of carbon atoms arranged in a two-dimensional honeycomb lattice—the first experimentally discovered material of its kind [213]. The two-dimensional nature of graphene allows its massless Dirac fermion charge carriers to travel via ballistic transport over thousands of interatomic distances without scattering, yielding carrier mobilities of $\mu = 1.5 \times 10^4 \text{ cm}^2/\text{V}\cdot\text{s}$ at room temperature. The charge carrier concentration can also be tuned via electric potential, yielding concentrations of $n = 10^{13} \text{ cm}^{-2}$. These properties hold until the 3D limit of graphite is approached at a thickness of 10 atomic layers. Because of these electronic

properties, graphene makes an ideal additive to create composite EMI shielding materials.

3.5.1 Measurement and Testing

3.5.1.1 Shielded Box Testing

Preliminary testing of graphene as a dopant for composite electromagnetic shielding materials was performed using a variation on the shielded box method. In the performed experiments, an acrylic box was coated with 100 μm layers of 10% by weight graphene-doped resin. After each layer was cured, a HP Signal Generator was used to broadcast a 900 MHz using a Laird Technologies Phantom multiband antenna. This signal was received by a second Laird Technologies Phantom multiband antenna placed inside the coated box and the amount of signal transmission received was measured using an Agilent Spectrum Analyzer. Additional coatings were applied to the surface of the shielded box and further measurements were made. These experiments showed that each 100 μm coating added an average of 6 dB of shielding effectiveness, with a total of 64.975 dB of shielding effectiveness seen with a total coating thickness of 1.2 mm, as shown in **Figure 3-12**.

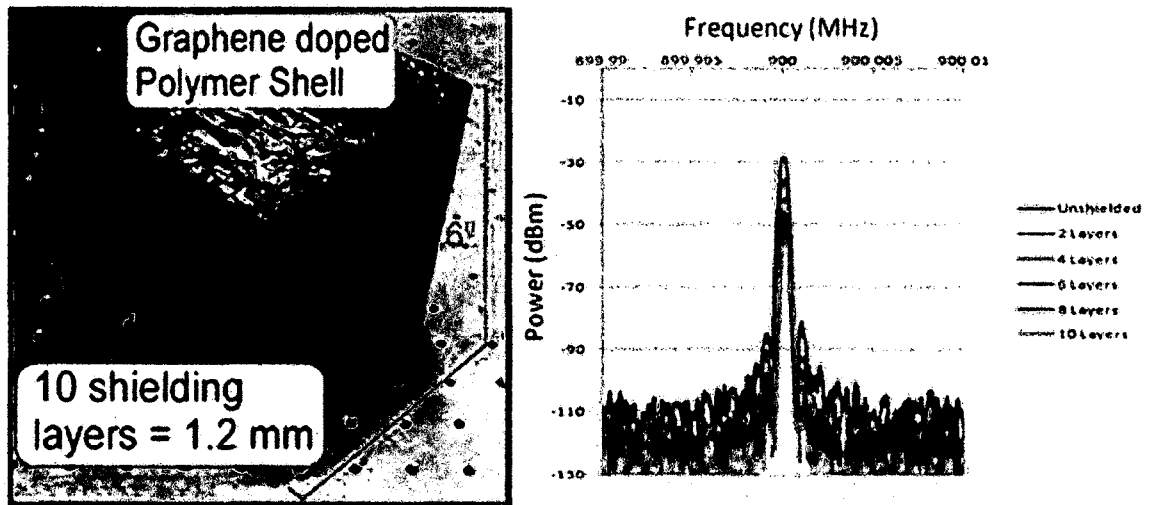


Figure 3-12: (a) Graphene-doped resin coated shielded box and (b) collected signal attenuation data.

3.5.1.2 DC 4-Point Probe Measurements

In order to quantify the electrical conductivity of our graphene-doped polymer shielding materials for future modeling and simulation efforts, a 4-point probe test set-up was employed. Circular acrylic disk substrates with a diameter of $D = 1$ in and thickness $t = 1.0$ mm were coated with an 80:20 acetone-ABS solution doped with varying weight percentages of electrolytically-exfoliated graphene nanoflakes. These coatings served to form an electrically-conducting thin film on the surface of the substrate after the volatile acetone was allowed to evaporate. Each different doping concentration of solution was used to create 10 samples, and each sample in turn was measured five times at varying locations across the surface to generate an average value of the DC sheet resistance. The four-point probe measurements were made using a Keithley 2400 SourceMeter with an attached Signatone SP4 Four-Point Probe Head as shown in **Figure 3-13**.

Table 3-2: Sheet Resistance [Ω/\square] Measurements for 5% Graphene-Nanoflake Doping.

	Sample 1	Sample 2	Sample 3	Sample 4	Sample 5	Sample 6	Sample 7	Sample 8	Sample 9	Sample 10
Avg.	1.4E6	1.8E6	2.1E6	9.1E5	8.6E5	2.3E5	5.9E5	1.5E5	3.1E5	3.3E5
Min.	1.4E5	2.3E5	1.4E5	4.5E4	9.1E4	1.7E5	7.7E4	1.1E5	7.9E4	9.1E4
Max.	5.4E6	7.7E6	6.8E6	3.6E6	3.6E6	3.3E5	2.5E6	2.1E5	6.4E5	6.2E5
t_c [mm]	0.41	0.24	0.30	0.39	0.19	0.32	0.21	0.14	0.15	0.22
σ_e [S/mm]	1.8E- 6	2.3E- 6	1.6E- 6	2.8E- 6	6.1E- 6	4.4E- 5	8.1E- 6	4.7E- 5	2.1E- 5	1.4E- 5

Table 3-3: Sheet Resistance [Ω/\square] Measurements for 10% Graphene-Nanoflake Doping.

	Sample 1	Sample 2	Sample 3	Sample 4	Sample 5	Sample 6	Sample 7	Sample 8	Sample 9	Sample 10
Avg.	2.6E4	1.3E4	3.6E3	4.8E4	8.3E3	1.1E4	1.3E4	2.8E4	6.0E3	1.0E4
Min.	5.3E3	7.1E3	1.5E3	9.2E3	3.4E3	5.5E3	4.0E3	1.7E4	3.6E3	4.7E3
Max.	4.4E4	2.0E4	9.0E3	9.1E4	1.6E4	2.4E4	3.6E4	9.3E4	9.1E3	2.8E4
t_c [mm]	0.11	0.10	0.33	0.33	0.07	0.34	0.33	0.49	0.22	0.30
σ_e [S/mm]	3.6E- 4	7.5E- 4	8.4E- 4	6.3E- 5	1.7E- 3	2.6E- 4	2.3E- 4	7.2E- 5	7.5E- 4	3.3E- 4

Table 3-4: Sheet Resistance [Ω/\square] Measurements for 15% Graphene-Nanoflake Doping.

	Sample 1	Sample 2	Sample 3	Sample 4	Sample 5	Sample 6	Sample 7	Sample 8	Sample 9	Sample 10
Avg.	6.9E2	1.3E3	1.2E2	6.3E2	7.5E2	9.3E2	3.1E3	7.2E2	3.7E4	3.4E3
Min.	2.2E2	5.2E2	6.8E1	7.7E1	3.8E2	8.9E2	9.2E2	3.1E2	6.1E2	3.1E2
Max.	1.5E3	2.5E3	1.5E2	1.7E3	1.1E3	9.5E2	6.8E3	9.2E2	1.8E5	9.0E3
t_c [mm]	0.07	0.06	0.36	0.10	0.26	0.27	0.26	0.28	0.23	0.41
σ_e [S/mm]	2.1E- 2	1.2E- 2	2.3E- 2	1.6E- 2	5.1E- 3	4.0E- 3	1.2E- 3	5.0E- 3	1.2E- 4	7.2E- 4

Table 3-5: Sheet Resistance [Ω/\square] Measurements for 20% Graphene-Nanoflake Doping.

	Sample 1	Sample 2	Sample 3	Sample 4	Sample 5	Sample 6	Sample 7	Sample 8	Sample 9	Sample 10
Avg.	6.7E2	1.9E2	6.2E2	1.0E2	2.9E2	1.4E2	2.2E2	1.7E2	1.6E2	1.6E2
Min.	2.3E2	1.2E2	1.9E2	8.4E1	1.2E2	1.2E2	9.2E1	1.3E2	1.0E2	9.2E1
Max.	9.2E2	3.2E2	1.3E3	1.3E2	4.4E2	1.7E2	3.2E2	2.1E2	2.4E2	2.8E2
t_c [mm]	0.34	0.39	0.45	0.46	0.42	0.42	0.39	0.39	0.45	0.31
σ_e [S/mm]	4.4E- 3	1.3E- 2	3.6E- 3	2.2E- 2	8.2E- 3	1.7E- 2	1.1E- 2	1.5E- 2	1.4E- 2	2.0E- 2

Table 3-6: Sheet Resistance [Ω/\square] Measurements for 25% Graphene-Nanoflake Doping.

	Sample 1	Sample 2	Sample 3	Sample 4	Sample 5	Sample 6	Sample 7	Sample 8	Sample 9	Sample 10
Avg.	2.4E2	2.0E2	6.6E2	4.8E2	1.9E2	1.8E2	2.3E2	2.5E2	2.2E2	2.0E2
Min.	1.5E2	1.2E2	3.7E2	1.8E2	1.4E2	1.3E2	1.5E2	1.6E2	1.2E2	1.1E2
Max.	3.6E2	2.6E2	1.3E3	6.6E2	2.5E2	2.0E2	3.1E2	4.5E2	3.5E2	2.8E2
t_c [mm]	0.66	0.71	0.71	0.57	0.87	0.78	0.37	0.46	0.43	0.27
σ_e [S/mm]	6.4E- 3	7.0E- 3	2.1E- 3	3.6E- 3	6.0E- 3	7.1E- 3	1.2E- 2	8.7E- 3	1.1E- 2	1.9E- 2

The 1% by weight carbon/ABS film did not achieve electrical conductivity high enough to register using the experimental set up. However, all further doping concentrations provided data that yielded the trend an increase in the doping concentration generally yields a lower sheet resistance and thus higher conductivity. Using the data collected above, an average value for sheet resistance as a function of doping concentration was determined. The results of these calculations are shown in **Table 3-7**.

Table 3-7: Average Electrical Properties for Graphene Nanoflake-Doped ABS Films.

Specimen	R_s (Ω/\square)	Thickness (mm)	σ_e (S/mm)
1% Doping	Overload	0.281	Overload
5% Doping	8.61×10^5	0.257	1.18×10^{-5}
10% Doping	1.68×10^4	0.262	5.37×10^{-4}
15% Doping	4.86×10^3	0.230	8.81×10^{-3}
20% Doping	2.73×10^2	0.402	1.28×10^{-2}
25% Doping	2.84×10^2	0.583	8.24×10^{-3}

The collected data shows that there is a practical limit to this approach—as the solution becomes super saturated with dopant nanoparticles, the flakes agglomerate which yields lower conductivity as the sample thickness increases while sheet resistance remains effectively constant. From this we can see that doping in the 15-20% by weight range yields the best results for the 80:20 acetone/ABS solution used.

Figure 3-14 shows the collected sheet resistance data and also includes error bars representing the highest and lowest measured value for a particular doping concentration. From the graph, we can see that a graphene nanoflake concentration of 20% by weight yields the most consistent data.

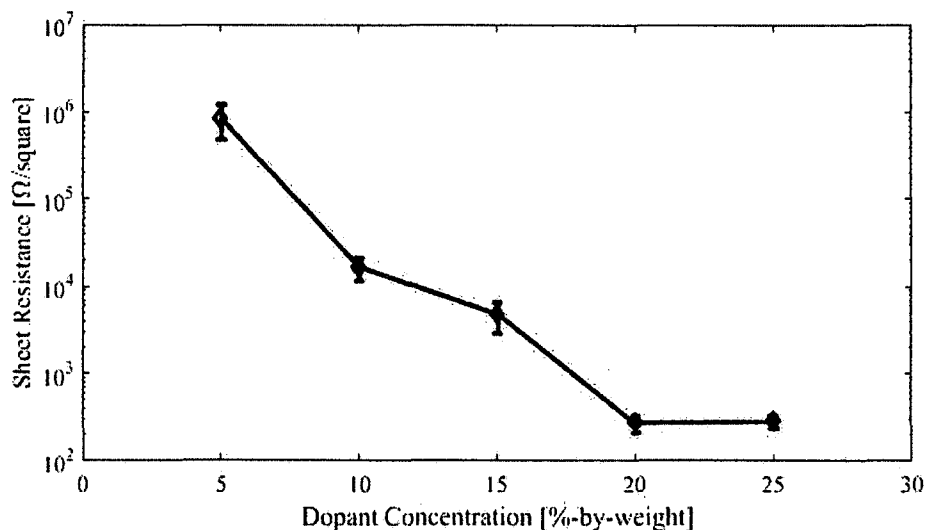


Figure 3-14: Sheet resistance as a function of doping concentration for graphene-doped ABS thin films. The error bars represent the standard deviation of each dopant concentration.

3.5.1.3 *Coaxial Transmission Line Testing*

The large amounts of shielding material needed to perform shielded box testing of graphene-doped polymer materials led to the development of a modified ASTM D4395 test fixture which would enable shielding effectiveness measurements using small material samples. The test fixture, shown in **Figure 3-15**, was designed to use the same-sized samples as those utilized in the DC 4-point probe sheet resistance and conductivity measurements. As designed, the test fixture has a TE_{11} cut-off frequency of 8.0 GHz.



Figure 3-15: Custom coaxial transmission line test fixture for measuring shielding effectiveness based on the ASTM D4395 method.

Shielding effectiveness measurements were carried out for each sample using an Agilent 4396B Network/Spectrum/Impedance analyzer in its vector network analyzer mode with an Agilent 87512A Transmission/Reflection Test Set attached. The vector network analyzer (VNA) was used to measure the amount of signal transmitted (S_{21}) to the output port of the custom coaxial transmission line test fixture, as shown in **Figure 3-16**, for load and reference samples as depicted in **Figure 3-10**.

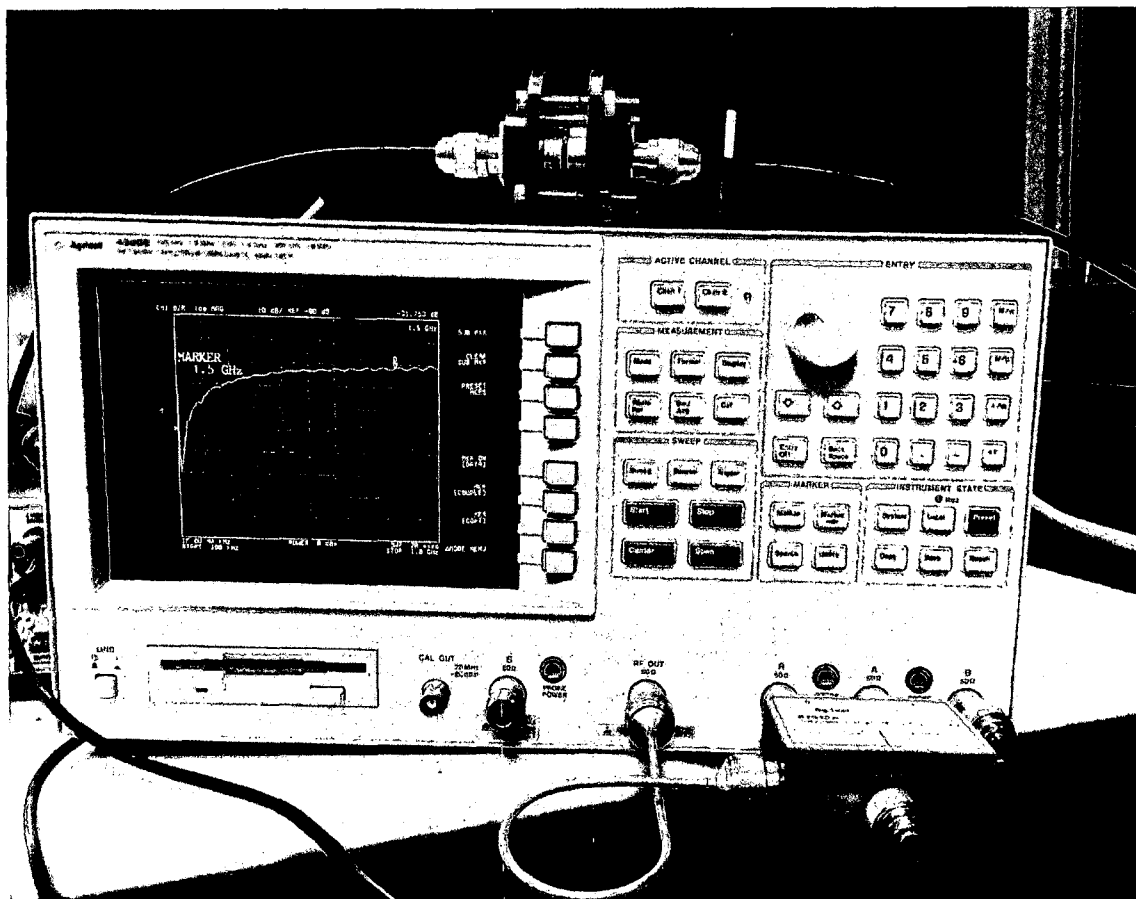


Figure 3-16: Shielding effectiveness measurement being made using the custom coaxial transmission line test fixture.

To ensure that sample thicknesses for the load and reference measurements were equal, load tests were performed first and then the sample was converted to the “donut” reference sample using a mechanical punch capable of removing concentric rings of the sample polymer film. The measurements were carried out over a frequency range of range of 0.1–1.8 GHz, the measurement bandwidth of the Agilent 4396B VNA and the difference between the collected load and reference S_{21} data for each sample was used to determine the shielding effectiveness of the sample. Shielding effectiveness measurements were performed for each of the 10 samples per doping concentration, with the results collected in **Tables 3.8–3.12**.

Table 3-8: Shielding Effectiveness [dB] Measurements for 1% Graphene-Nanoflake Doping.

Frequency [GHz]	Sample 1	Sample 2	Sample 3	Sample 4	Sample 5	Sample 6	Sample 7	Sample 8	Sample 9	Sample 10
0.25	0.2	0.1	0.2	0.3	0.1	0.1	0.1	0.3	0.2	0.2
0.50	0.1	0.4	0.2	0.2	0.0	0.1	0.1	0.1	0.1	0.1
0.75	0.1	0.0	0.2	0.1	0.0	0.1	0.0	0.2	0.1	0.1
1.00	2.3	0.3	0.3	0.2	0.2	0.1	0.1	0.4	0.2	0.2
1.25	0.0	0.0	0.3	0.0	0.0	0.1	0.1	0.1	0.1	0.1
1.50	0.8	1.9	0.3	0.1	0.0	0.0	0.1	0.2	0.0	0.0
1.75	0.2	0	0.2	0.0	0.0	0.0	0.0	0.1	0.0	0.1

Table 3-9: Shielding Effectiveness [dB] Measurements for 5% Graphene-Nanoflake Doping.

Frequency [GHz]	Sample 1	Sample 2	Sample 3	Sample 4	Sample 5	Sample 6	Sample 7	Sample 8	Sample 9	Sample 10
0.25	0.1	2.2	0.8	0.1	2.3	1.3	0.4	3.4	2.2	0.0
0.50	0.2	2.1	0.7	0.2	1.9	1.0	0.3	3.2	2.0	0.0
0.75	0.1	2.0	0.7	0.2	2.0	1.1	0.2	3.1	1.9	0.0
1.00	0.2	1.9	0.6	0.3	1.8	1.0	0.3	2.9	1.7	0.0
1.25	0.2	1.9	0.6	0.0	1.3	0.6	0.4	2.8	1.7	0.4
1.50	0.2	1.8	0.5	0.2	1.6	1.0	0.1	2.8	1.6	0.1
1.75	0.3	2.1	0.4	0.4	1.7	1.0	0.3	2.9	1.8	0.1

Table 3-10: Shielding Effectiveness [dB] Measurements for 10% Graphene-Nanoflake Doping.

Frequency [GHz]	Sample 1	Sample 2	Sample 3	Sample 4	Sample 5	Sample 6	Sample 7	Sample 8	Sample 9	Sample 10
0.25	1.1	2.4	10.6	12.0	1.5	14.6	5.5	8.4	1.1	4.7
0.50	0.8	1.7	7.6	9.1	1.1	10.4	3.4	5.4	1.1	2.9
0.75	0.8	1.5	6.2	7.2	1.1	8.2	2.5	4.0	1.0	2.1
1.00	0.8	1.4	5.7	6.6	1.0	7.3	2.2	3.3	0.9	1.7
1.25	0.6	1.1	5.2	6.0	1.1	6.5	2.2	2.8	1.4	1.2
1.50	0.7	1.1	4.8	5.5	1.0	5.9	1.8	2.5	0.9	1.0
1.75	0.8	1.2	4.9	5.4	1.1	5.9	1.8	2.3	1.1	1.1

Table 3-11: Shielding Effectiveness [dB] Measurements for 15% Graphene-Nanoflake Doping.

Frequency [GHz]	Sample 1	Sample 2	Sample 3	Sample 4	Sample 5	Sample 6	Sample 7	Sample 8	Sample 9	Sample 10
0.25	10.6	9.7	18.7	12.6	15.2	18.5	9.0	5.6	8.5	7.3
0.50	7.3	6.3	14.9	10.7	11.9	14.8	6.1	3.4	6.1	4.6
0.75	5.7	4.8	12.3	9.5	10.0	12.0	4.7	2.3	4.4	3.1
1.00	4.7	4.1	11.0	8.1	8.9	10.3	4.1	0.8	3.1	2.5
1.25	4.1	3.6	10.4	7.8	8.5	9.6	3.7	2.0	3.3	2.1
1.50	3.5	3.4	9.0	7.0	7.6	8.6	3.3	1.0	2.5	2.1
1.75	3.2	2.9	14.5	6.6	7.2	7.9	2.9	0.9	2.2	1.7

Table 3-12: Shielding Effectiveness [dB] Measurements for 20% Graphene-Nanoflake Doping.

Frequency [GHz]	Sample 1	Sample 2	Sample 3	Sample 4	Sample 5	Sample 6	Sample 7	Sample 8	Sample 9	Sample 10
0.25	11.7	19.5	16.8	20.4	23.3	28.0	15.9	12.4	29.6	31.9
0.50	7.8	14.7	12.8	18.5	21.2	24.4	11.9	10.8	26.4	25.9
0.75	4.9	10.7	9.9	13.8	17.9	19.8	9.0	6.5	19.2	22.2
1.00	3.7	9.7	8.7	13.5	16.7	18.4	8.0	6.3	17.5	20.5
1.25	3.3	9.3	7.7	11.6	15.0	16.6	6.6	4.7	17.3	8.6
1.50	2.3	7.7	6.7	10.4	14.6	15.6	5.7	4.8	14.7	7.2
1.75	1.5	6.8	6.4	9.6	14.0	14.4	5.0	4.4	13.5	6.5

Shielding effectiveness measurements were unable to be taken for the 25% by weight doped samples as the films were so brittle that the mechanical process used to convert the load sample to a reference sample destroyed the film. However, all other dopant concentrations provided data yielding a trend of increasing shielding effectiveness as dopant concentration increases. This behavior follows the trend seen in the 4-point probe measurements: an increase in the doping concentration generally yields a lower sheet resistance and thus higher conductivity. Using the data collected above, an average value for shielding effectiveness as a function of dopant concentration was determined. The results of these calculations are shown in **Figure 3-17**.

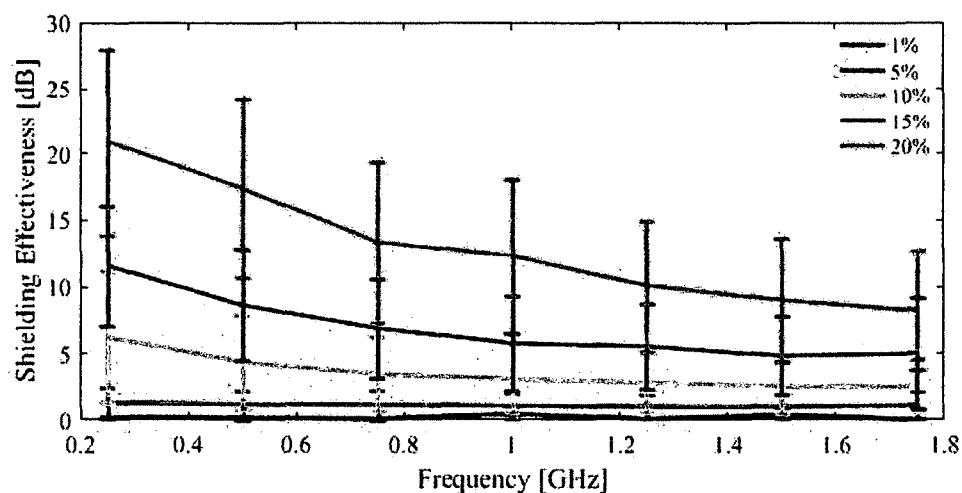


Figure 3-17: Shielding effectiveness of ABS/graphene samples as a function of dopant concentration and frequency. The error bars represent the standard deviation of the measured shielding effectiveness for a particular dopant concentration and frequency.

As expected, the 1% by weight doped samples offered almost no shielding at all as the samples were essentially purely insulating. As the doping concentration increases, the shielding effectiveness also increases with a maximum average value of 20.95 dB at 250 MHz for the 20% doped samples. The figure also shows that the shielding effectiveness decreases as the frequency increases. This is likely due to voids in the

conducting network formed by the dopant particles. Increasing homogeneity of the film should yield a slower “roll-off” in SE as the excitation frequency increases.

3.5.2 Conclusions

The shielding effectiveness measurements performed illustrate the potential of non-metallic shielding as a means to protect sensitive electronics from sources of electromagnetic interference. Low weight, non-reactive shielding methods are of paramount importance in military applications where hardening against EM attacks can help to establish strategic control of the electromagnetic spectrum. Consumer electronics applications like cellular telephones could also see significant benefits from the employment of non-rigid shielding enclosures created via film deposition at the IC scale.

CHAPTER 4

A 3D-PRINTED PRE-FRACTAL SIERPINSKI TETRAHEDRAL ANTENNA

4.1 Introduction

The rapid expansion of wireless communication usage from predominately industrial and military applications to consumer applications has created a demand for complex, multiband transmission and receiver systems which utilize a number of different antenna structures (often within a single device) to facilitate communication. As an example, a basic “smart” cellular telephone for use in North American markets allows for data transmission over four UMTS bands (850 MHz, 900 MHz, 1800 MHz, and 1900 MHz), GPS bands (1225 MHz and 1575 MHz), and an ISM band (2.4 GHz), requiring multiple antennas to enable the efficient detection and processing of telephony, GPS, and Wi-Fi/Bluetooth signals. Similarly, military radios for in-field communications transmit and received frequency-hopping spread-spectrum (FHSS) signals which can require a similar number of antennas to properly process wide-bandwidth encoded signals without loss of information. The development of dynamic antennas capable of true multiband operation is of paramount importance in creating compact communications systems in an era where wireless communication using multiple sections of the electromagnetic spectrum is quickly becoming the norm. The desire for multiband operation has led

investigators in several directions, one of which is the use of complex electromagnetically-radiating structures based on fractal geometries.

Fractals, as defined by French mathematician B. B. Mandelbrot, are a class of irregular shapes not contained within the realms of conventional Euclidian geometry that exhibit some degree of self-similarity and are formed through recursion of a geometric pattern [214]. Other properties associated with fractal geometries include scale-invariance wherein similar patterns appear upon magnification of a fractal which makes scale-determination difficult, space-filling wherein the area bounded by the general fractal shape tends to fill-in as the iteration of the self-similar pattern increases, and lacunarity wherein the hollow spaces inside the fractal pattern also exhibit fractal characteristics. While the study of such patterns began in the early 1900s through mathematicians like Koch, Hilbert, and Sierpinski, the use of fractals as anything more than a mathematical curiosity is a more recent development. After Mandelbrot's seminal work on the subject, fractals have found widespread use in geology, atmospheric sciences, forest sciences, physiology, and engineering [215].

The engineering applications of fractals are varied—fractal meshes are used to reduce memory requirements and computation time in finite-element modeling of vibrating structures [216], fractal image coding can be used to compress images which greatly decrease rendering time [217, 218], fractal geometries are used in the creation of frequency-selective surfaces used in applications as varied as microwave ovens and metamaterials [219, 220], and fractal geometries are used in the synthesis of both antenna arrays and radiating elements for individual devices in the field of antenna engineering.

4.2 Application of Fractals in Antenna Engineering

Fractal patterns are used in the field of antenna design to expand the boundaries of synthesis beyond those available using only Euclidean geometry [221]. To this end, the use of fractals has been investigated in both the formulation of antenna arrays and the development of patch and monopole antenna radiating elements.

4.2.1 Fractal Antenna Arrays

Fractal antenna arrays were created to achieve the scale-invariance requirement of frequency-independent (wideband) antenna arrays. The first research into fractal antenna arrays was performed by Kim and Jaggard in 1986 [222]. Their work used random fractal tree arrays to bridge the performance gap between completely ordered (periodic) and completely disordered (random) array configurations which led to both robust and small sidelobe characteristics within a single configuration.

This work was expanded on using recursively generated deterministic fractal arrays by Lakhtakia *et al.* [223]. This research involved placing Hertzian dipoles at the node-points of a Sierpinski carpet fractal pattern, resulting in the observation that while the time-harmonic far-field response of a bifractal array of dipoles is also bifractal its time-dependent far-field response is unifractal. The use of recursively generated fractal arrays was expanded to Weierstrass arrays [224], Koch arrays [225, 226], Cantor arrays [225, 227] and Peano-Gosper arrays [228] by various researchers.

Antenna arrays have also been used to generate fractal-based radiation patterns via controlled element spacing. Werner and Werner achieved self-similar radiation patterns using iterated function systems based on Weierstrass arrays [224, 229], while Puente-Balaridia *et al.* achieved similar results using Koch arrays [225].

4.2.2 Fractal Shaped Antenna Elements

The use of fractals to form the radiating elements of an antenna is a widely-investigated topic in antenna engineering. The self-similarity of an iterative pre-fractal pattern has been shown to enable multiple distinct current modes to exist within the radiating element(s) of the antenna which yields wideband multi-frequency response [230] and the geometric scaling used in the iterative fractal-generation process yields a reduction in size when compared to classical monopole antennas based on Euclidean geometries operating at similar frequencies [231]. These modifications to classic antenna architectures generate high-performance devices with increased bandwidth and reduced size which have potential applications in the miniaturization of space vehicles, drones, and UAVs; wireless energy harvesting; and cellular telephony systems.

Antennas which use fractal radiating elements have been demonstrated based on the Sierpinski gasket [232, 233], Sierpinski carpet [234], Koch curve [235], Hilbert curve [236], Peano curve [237], and Minkowski island [238] fractal patterns shown in **Figure 4-1**.

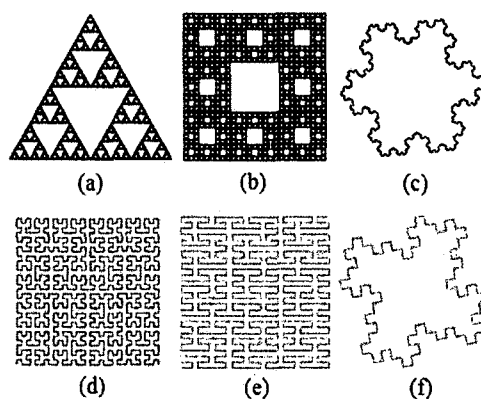


Figure 4-1: Fractal patterns used in antenna radiating elements. (a) Sierpinski gasket; (b) Sierpinski carpet; (c) Koch curve; (d) Hilbert curve, (e) Peano curve, (f) Minkowski island.

The “curve”-based fractal antennas are typically used to reduce the overall size of conventional dipole and meander line antennas, yielding antennas with low resonant frequencies that do not exhibit increased size as would be expected with Euclidean geometries [239]. This behavior occurs because as the fractal iteration increases, the effective length of such an antenna also increases while keeping the same relative dimensions. The large number of bends and corners in such an antenna has been shown to increase radiation efficiency as well [215].

Self-similar scale-invariant designs like the Sierpinski gasket and carpet have been explored for their multiband characteristics. The Sierpinski gasket is perhaps the most researched fractal antenna, due in part to its similarity to the widely-used bow-tie antenna [215]. Monopole, dipole, and patch configurations of the Sierpinski gasket have been widely investigated, yielding the observation that the self-similar current distribution that occurs on the individual triangles forming the Sierpinski gasket pattern give rise to the multiband characteristics of the antennas [240]. Perturbation of the geometry using irregular triangles [241, 242] and rectangular slots [243] has been used to control the multiband nature of the devices. Additionally, research has shown that bandwidth of a Sierpinski gasket antenna can be varied by changing the flare angle of the pattern [244].

While planar realization of the Sierpinski gasket has been extensively researched, very few attempts have been made to realize its three-dimensional counterpart, the Sierpinski tetrahedron (shown in **Figure 4-2**), in the field of fractal antenna engineering. This is due primarily to difficulties in fabricating the complex geometric structure through conventional metal casting techniques.

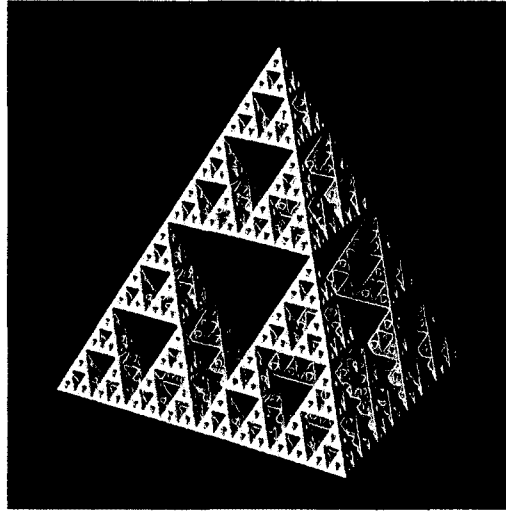


Figure 4-2: A computer-generated rendering of a 5th-order Sierpinski tetrahedron.

The first attempt at a three-dimensional fractal antenna was by Best in 2003 [245]. Best used a perturbed Sierpinski gasket with truncated central gaps to approximate the fractal geometry, then turned the planar structure in on itself to create a conical monopole antenna as depicted in **Figure 4-3**. The increased volume of the conical structure was shown to increase radiation pattern symmetry and omnidirectionality while maintaining the multiband characteristics of a planar Sierpinski gasket antenna.

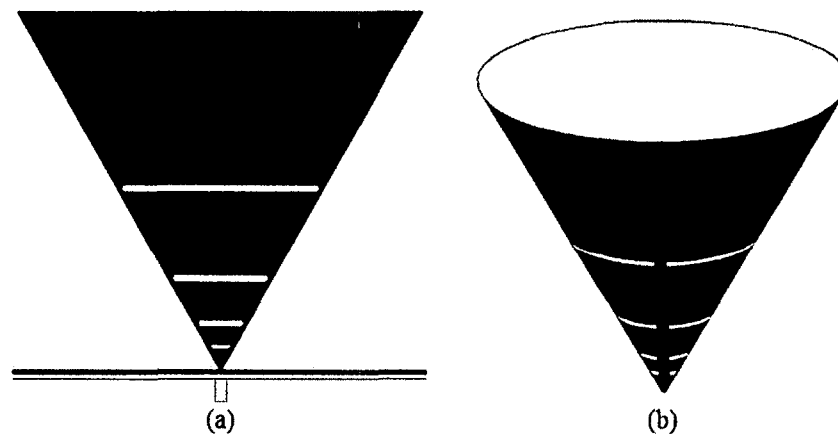


Figure 4-3: (a) Perturbed Sierpinski gasket monopole antenna with truncated central gaps and (b) a diagram of the three-dimensional conical monopole antenna [245].

Hebib *et al.* developed a pyramidal antenna using four perturbed Sierpinski gaskets loaded with a circular waveguide [246]. The device, shown in **Figure 4-4**, forms a simple array to enhance radial directivity of the output signal. The radiating elements of the antenna structure are planar in nature; the pyramidal base-structure used to influence antenna directivity enables the three-dimensional structure to be obtained.

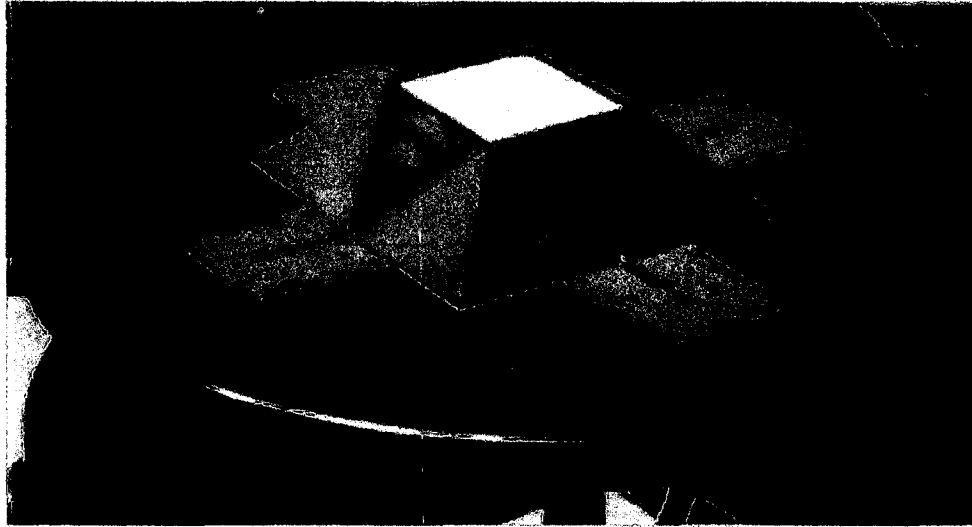


Figure 4-4: Pyramidal antenna utilizing four perturbed planar Sierpinski gasket antennas [246].

Alaydrus reported on the first truly three-dimensional Sierpinski tetrahedral antenna in [247]. The device, shown in **Figure 4-5**, utilized small brass tetrahedrons welded together to form a 2rd-order Sierpinski tetrahedron atop a 16 cm x 16 cm ground plane. The fabrication method yielded low dimensional accuracy which caused a significant deviation in device input return loss as compared to the expected results generated by surface integral modeling, however the general characteristics associated with fractal antennas (multiband behavior, high bandwidth) were achieved.

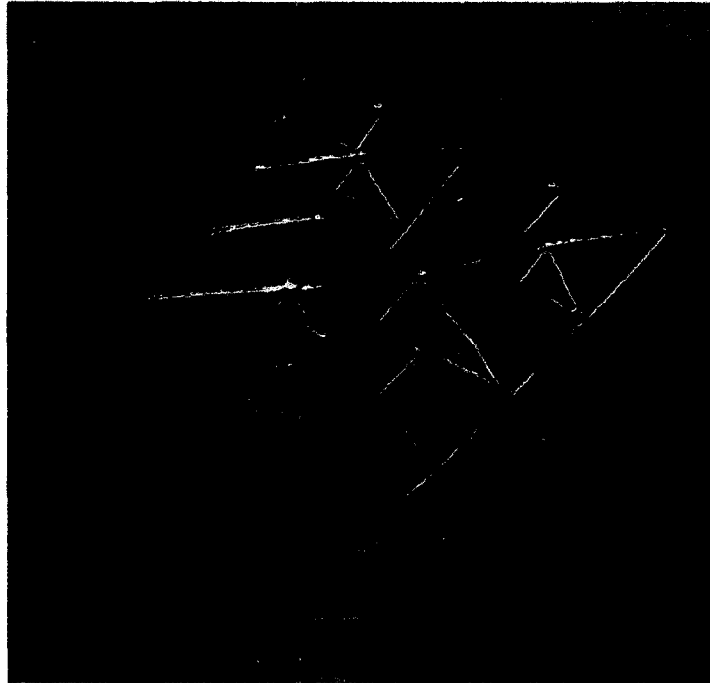


Figure 4-5: Brass Sierpinski tetrahedral antenna fabricated by Alaydrus [247].

4.3 A 3D-Printed Pre-Fractal Sierpinski Tetrahedral Antenna

The results reported by Alaydrus in [247] illustrate that three-dimensional realization of a planar fractal antenna can yield enhanced electromagnetic properties, however the need for an accurate fabrication process is of paramount importance to ensure the expected frequency response. Recent advances in additive manufacturing techniques have enabled the creation of geometrically complex structures which can achieve high dimensional accuracy. Using stereolithography and/or fused-layer deposition 3D-printing, the generation of higher-order pre-fractal structures for use as antenna radiating elements through the use of conductive coatings and inherently conductive filaments and photopolymers is now possible. Additionally, the ability to quickly prototype devices will allow for a more thorough investigation of antenna structures based on the variations of classical fractal geometries.

4.3.1 Antenna Design

Previous research on Sierpinski gasket antennas have shown that the antenna should exhibit multiband resonances at specific frequencies determined by the relationship

$$f_n \approx 0.26 \frac{c}{h_0} \delta^n \quad \text{Eq. 4-1}$$

where c is the speed of light in a vacuum, h_0 is the height of the 0th-order triangular iteration (as shown in **Figure 4-6**), δ is the scaling factor between subsequent triangular iterations, and n is the iteration number [232]. Since a Sierpinski tetrahedron is a three-dimensional structure in which each triangle of a Sierpinski gasket is replaced with an equivalent tetrahedron having the face dimensions of the replaced triangle, the electrical resonance of a tetrahedral antenna should coincide with that of a planar antenna.

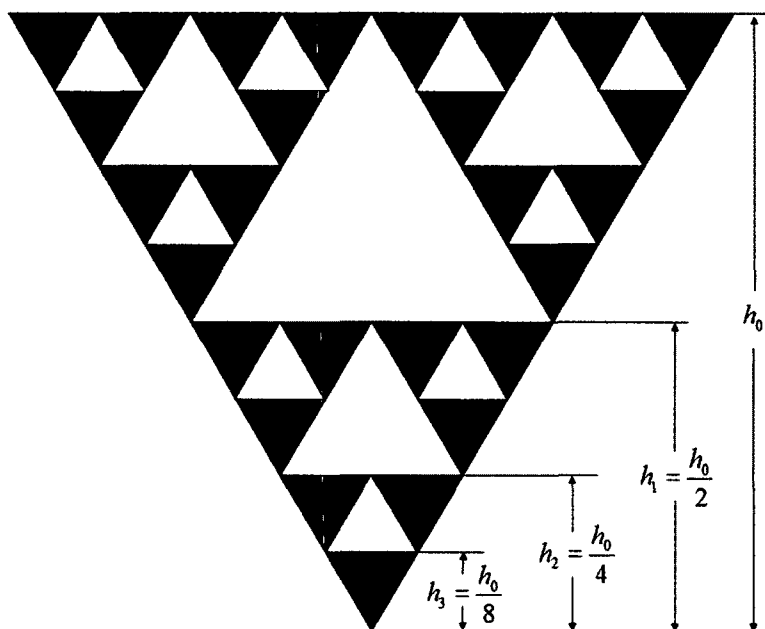


Figure 4-6: Sierpinski gasket pre-fractal structure illustrating 3rd-order self-similarity with a scaling factor of $\delta = 2$.

The dimensions of the antenna and the number of iterative patterns to include in the device architecture were chosen such that the first resonance of the antenna structure should occur at approximately 1.5 GHz, the middle of the *L*-band, with additional resonances occurring near the middle of the *C*- and *S*-frequency bands if the frequency response behavior follows that of a Sierpinski gasket antenna. These characteristics could eliminate the need for multiple antennas in multiband communications systems.

The resulting antenna structure is an equilateral tetrahedron with face length 128.0 cm and a height of 104.5 mm. This height corresponds to an h_0 value of 110.8 mm for the Sierpinski gasket created on each tetrahedral face. The radiating structure is fed with a 50 Ω coaxial transmission line and placed on a finite ground plane with a radius of 90 mm to form a monopole antenna, as shown in **Figure 4-7**.

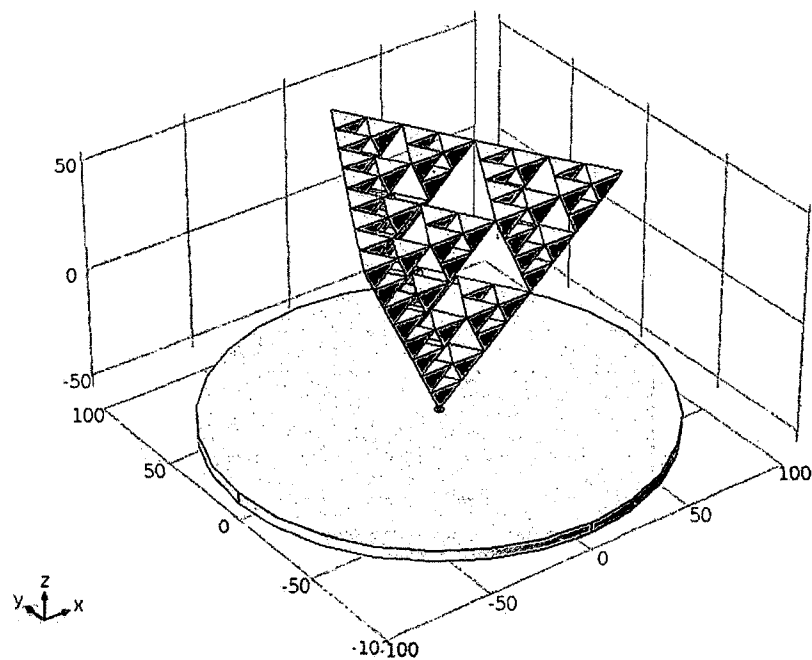


Figure 4-7: Three-dimensional model of the proposed 3rd-order Sierpinski tetrahedral antenna.

4.3.2 Finite Element Modeling of the Antenna Structure

The radiating element(s) of antennas are traditionally fabricated from materials with high electrical conductivities like copper or brass for most applications. Because of this, modelling was necessary to determine if the use of a significantly less conductive material like carbon black impregnated polylactic acid (PLA) thermoplastic or coated acrylonitrile butadiene styrene (ABS) thermoplastic would still deliver the expected electromagnetic performance of a fractal antenna structure. Finite element modeling of the antenna structure was performed using COMSOL's RF Module over a frequency range of 0.1–3.0 GHz with a 50 MHz step-size in the frequency sweep for various conductivities. The simulations employed an adaptive mesh that limits the maximum element size to 20% of the wavelength of the excitation frequency being simulated. Modeling was carried out for 0th-, 1st-, 2nd-, and 3rd-order pre-fractal structures to analyze the changes in input return loss as a function of both material and geometric complexity. A spherical ($r = 180$ mm) perfectly matched layer with a thickness of 35 mm was used to simulate far-field conditions for the antenna.

Figure 4-8 shows the results of these simulations. Using electrical conductivities of $\sigma_e = \infty$ (perfect electrical conductor), $\sigma_e = 6.17 \times 10^7$ S/m (silver), $\sigma_e = 5.80 \times 10^7$ S/m (copper), and $\sigma_e = 7.00 \times 10^4$ S/m (graphite), a decrease in electrical conductivity by three orders of magnitude yields at most a 2.116-dB change in the input return loss of the simulated pre-fractal antenna structure regardless of its geometric complexity over the simulated frequency range. From these results, we can see that the use of lower-conductivity materials can still produce electromagnetic radiation with minimal change in radiation efficiency.

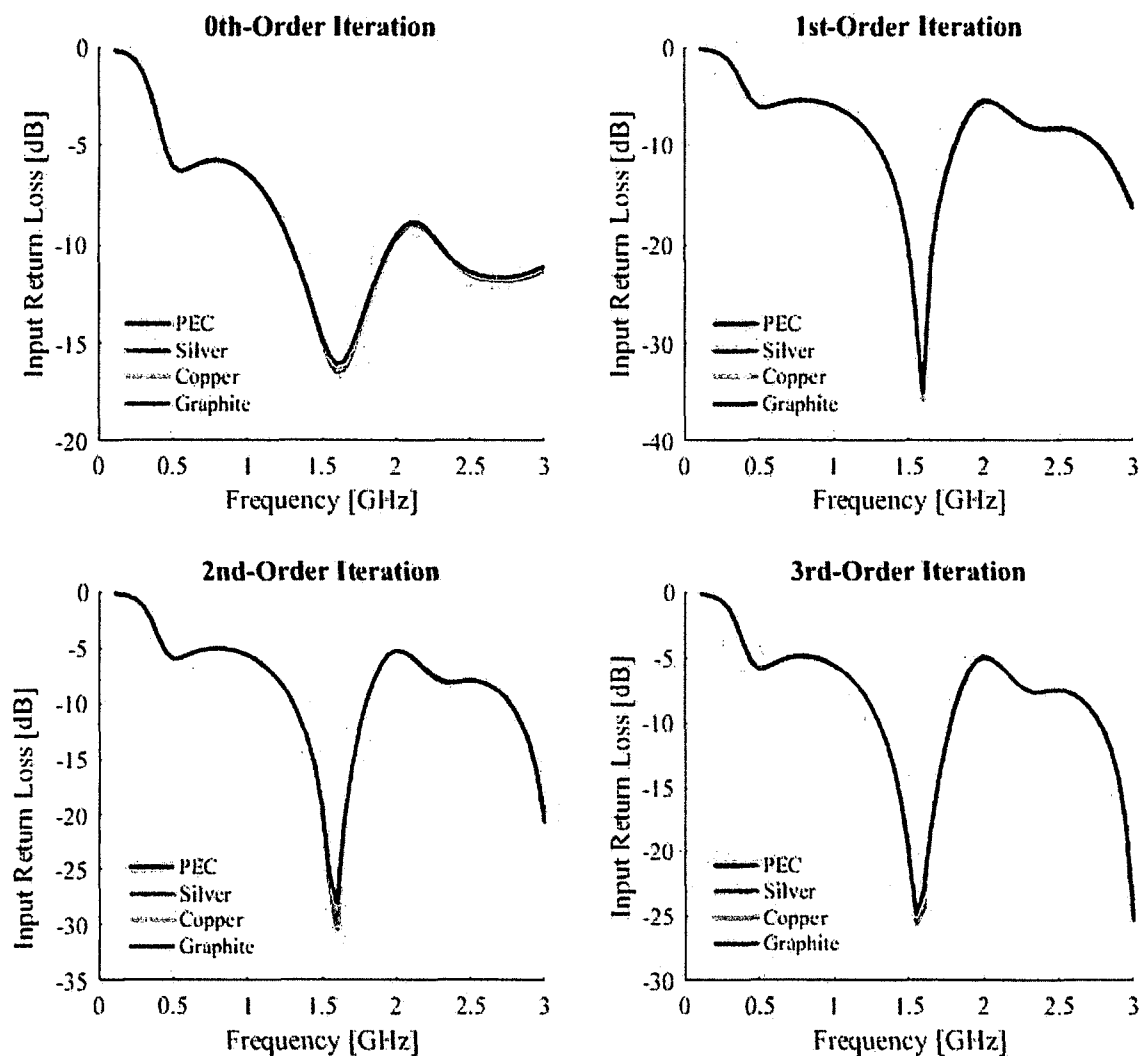


Figure 4-8: Simulated input return loss as a function of material and pre-fractal iteration over a frequency range of 0.1–3.0 GHz for a Sierpinski tetrahedral antenna.

The multiband frequency responses of a 3rd-order Sierpinski tetrahedral antenna and a 3rd-order Sierpinski gasket antenna were also simulated to determine if any advantages arise from three-dimensional realization of the radiating element. Again, finite element modeling of the antenna structure was performed using COMSOL's RF Module, however the simulated frequency range was extended to 0.1–6.75 GHz with a 50 MHz step-size in the frequency sweep. A spherical ($r = 180$ mm) perfectly matched layer with a thickness of 35 mm was used to simulate far-field conditions for the antenna. The

simulated antennas were designed with identical face dimensions and employed identical feed structures and ground planes so that any difference in simulated input return loss could only be attributed to the additional dimension added to the antenna geometry.

Figure 4-9 shows that the tetrahedral antenna structure has significantly increased radiative properties than its planar counterpart at higher-order resonant modes with a minimum $|S_{11}|$ increase of 3.3 dB occurring at $f_3 = 6.3$ GHz. The 0th- and 1st-order resonant peaks of the 3D antenna exhibit significantly increased bandwidth as compared to the 2D implementation. This phenomenon was observed experimentally by Alaydrus in [246]. From this we can see that the 3D realization of the Sierpinski pre-fractal as a radiative element offers distinct advantages over conventional gasket-based antenna designs for *S*-band applications.

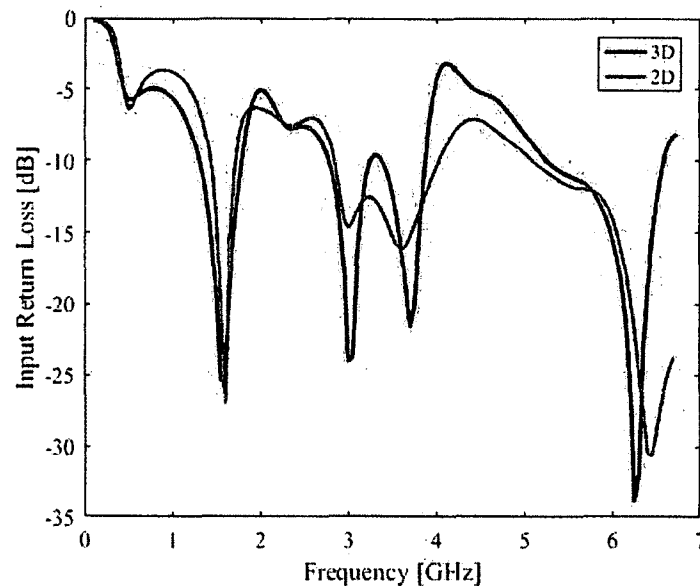


Figure 4-9: Simulated input return loss for 3rd-order tetrahedral (3D) and planar (2D) Sierpinski pre-fractal antennas. The 3D antenna exhibits increased power dissipation at higher-order resonant frequencies as well as increased bandwidth at lower-order resonant frequencies.

Finally, the antenna structure was modeled to determine the electric field distribution, expected frequency response, and radiation pattern as a function of frequency and pre-fractal iteration. Finite element modeling of the antenna structure was performed using COMSOL's RF Module over a frequency range of 0.1–6.75 GHz with a 50 MHz step-size in the frequency sweep. The simulation software was used to solve the equation

$$\nabla \times \frac{1}{\mu_r} (\nabla \times \mathbf{E}) - k_0^2 \left(\epsilon_r - \frac{j\sigma_e}{\omega\epsilon_0} \right) \mathbf{E} = 0 \quad \text{Eq. 4-2}$$

for the electric field intensity at each node point generated by the mesh. In **Eq. 4-2**, μ_r and ϵ_r are the relative permeability and permittivity of the antenna medium, k_0 is the wavenumber for free-space (dependent on angular excitation frequency ω), and ϵ_0 is the permittivity of free-space.

Figure 4-10 illustrates the spatial characteristics of the electric field distribution at each resonance for a 3rd-order pre-fractal tetrahedral antenna. At each frequency, the electric field distribution is effectively the same over each vertical face of the tetrahedral structure. As the frequency increases, different regions of the antenna activate and the electric field is confined to a smaller area which causes the radiation pattern of the antenna to change drastically as a function of increasing frequency.

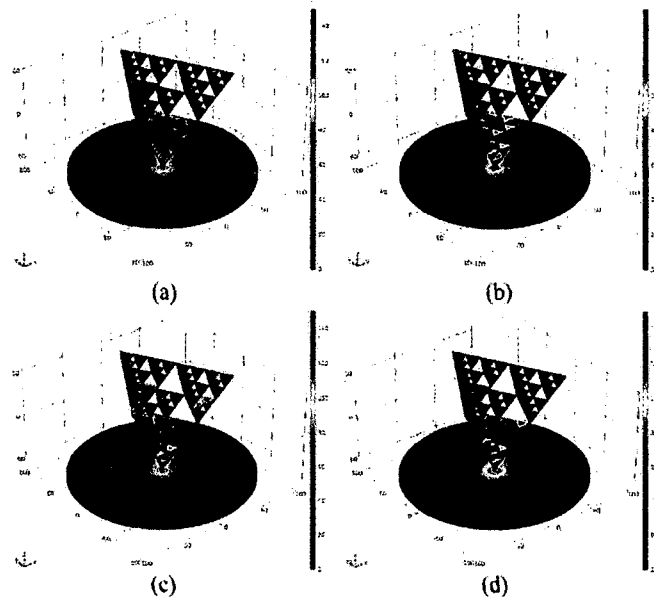


Figure 4-10: Spatial variance of the simulated electric field distribution over a 3rd-order Sierpinski tetrahedral antenna's surface at (a) 1.55 GHz, (b) 3.00 GHz, (c) 3.70 GHz, and (d) 6.25 GHz. As the excitation frequency increases, the electric field intensifies over an increasingly smaller surface area of the radiating element.

Figure 4-11 depicts the simulated radiation pattern of a 3rd-order pre-fractal tetrahedral antenna at different resonant frequencies. As the frequency increases, the changing electric field distribution causes the lobes of the radiation pattern to become less distinct and thus the directionality of the antenna decreases as a function of frequency. This is best illustrated by looking at the XY-plane radiation characteristics: as the excitation frequency increases the radiation direction alternates between the faces and edges of the tetrahedral structure with small perturbations occurring at 60° intervals between the directional lobes. At a frequency of 6.25 GHz, the antenna approaches omnidirectional radiation in the XY-plane as the magnitude of the perturbations are of similar scale to the directional lobes.

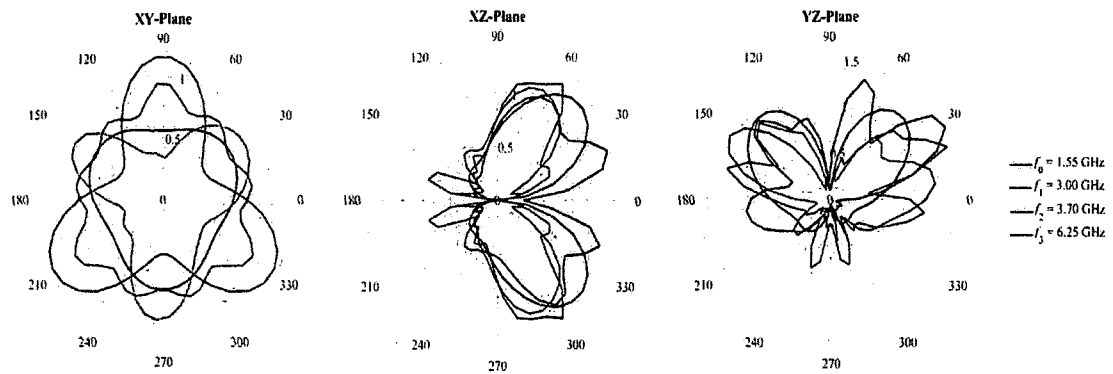


Figure 4-11: Simulated radiation characteristics of a 3rd-order Sierpinski tetrahedral pre-fractal antenna. As the frequency increases, the directivity of the antenna changes with more omnidirectional behavior observed at higher frequency resonances.

A three-dimensional representation of the simulated radiation pattern data is shown in **Figure 4-12**.

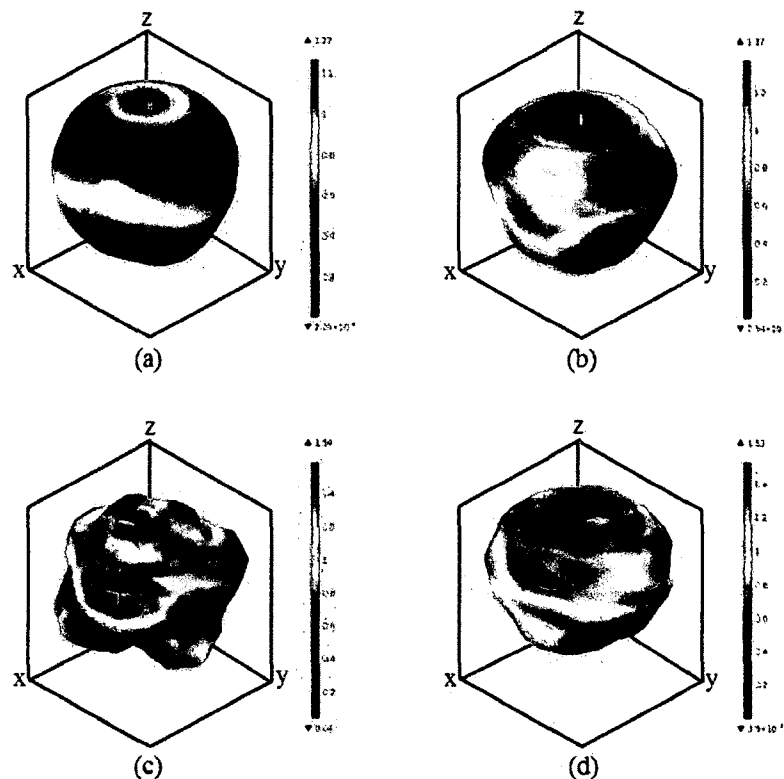


Figure 4-12: Simulated 3D radiation pattern data for a 3rd-order Sierpinski tetrahedral antenna at (a) 1.55 GHz, (b) 3.00 GHz, (c) 3.70 GHz, and (d) 6.25 GHz.

Figure 4-13 shows the input return loss of the simulated Sierpinski tetrahedron monopole antennas for varying pre-fractal iteration numbers. Resonances are observed at 1.6 GHz, 3.0 GHz, 3.6 GHz, and 6.3 GHz, with each pre-fractal iteration generating an additional resonance as was observed in both simulated and practical Sierpinski gasket monopole antennas. The data provided through these simulations show that even-ordered resonances experience a slight frequency shift to the right as the number of iterations increase while odd-ordered resonances experience a similar frequency shift to the left. The simulated antennas demonstrate high radiation efficiencies ($|S_{11}| > 20$ dB) at all resonances for 2nd- and 3rd-order designs, showing potential for true multiband transmission of signals at these frequencies.

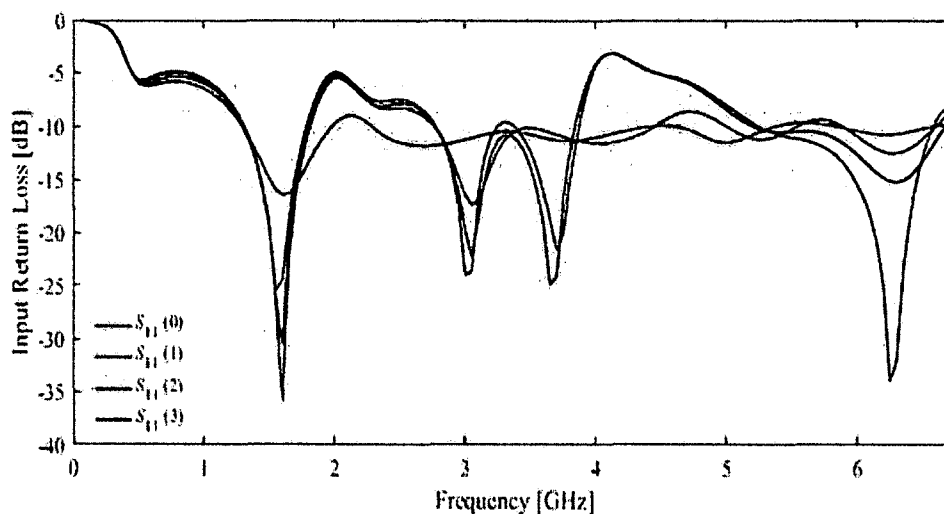


Figure 4-13: Simulated input return loss of pre-fractal Sierpinski tetrahedral antennas on a finite ground plane. The numbers in parentheses represent the order of the pre-fractal iteration.

These simulations are the first to illustrate the performance potential of 3D antenna based on a 3rd-order Sierpinski fractal geometry. The extension of the Sierpinski gasket pre-fractal pattern into three-dimensions results in an increase in S_{11} response at

higher-order resonant frequencies, demonstrating usefulness as a true multiband antenna. Expansion beyond the constraints of planar implementation increased efficiency, bandwidth, and directional gain versus a Sierpinski gasket antenna with equivalent face dimension, characteristics which can be exploited for any application within the field of wireless communication.

4.3.3 Antenna Fabrication

To physically realize the modeled Sierpinski tetrahedral antennas, the radiative antenna element structures were fabricated using fused-layer-deposition (FLD) 3D-printing techniques. Two methods were employed to create the radiative elements: coating 3D-printed insulating structures with conductive materials and directly printing 3D-printed electrically-conductive structures using commercially available carbon-doped filaments.

An XYZprinting da Vinci 1.0 Pro 3D-printer was used to generate multiple pre-fractal Sierpinski tetrahedron substrates, shown in **Figure 4-14**, using XYZprinting ABS filament.

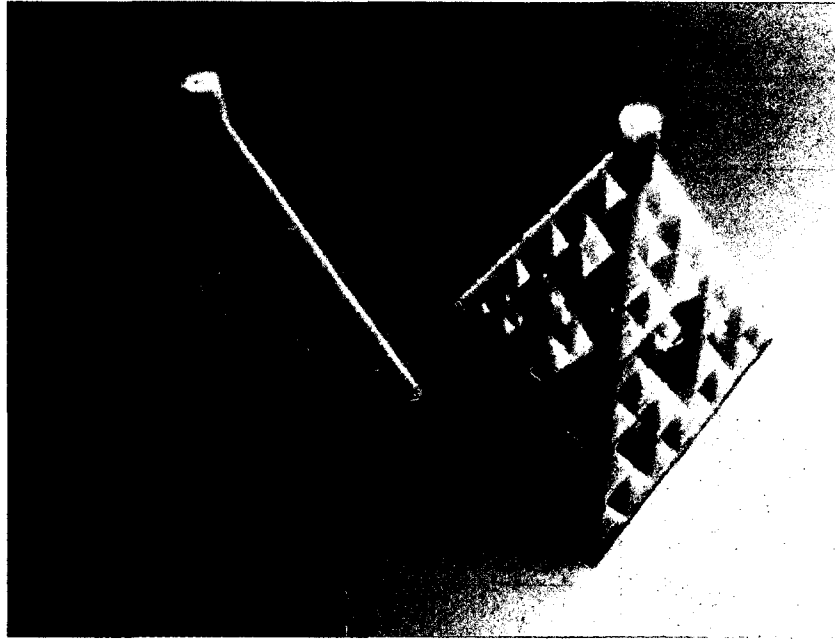


Figure 4-14: Third-order Sierpinski tetrahedron substrates fabricated by FLD 3D-printing ABS filament. These substrates are to be coated with conductive carbon films and will serve as the radiating element for a monopole antenna.

These electrically-insulating substrates were then coated with an 80:20 acetone-ABS solution doped with varying weight percentages of electrolytically-exfoliated graphene nanoflakes or carbon nanoparticles. These coatings served to form a thin electrically-conducting layer on the surface of the tetrahedral structure which should enable the tetrahedral structure to serve as the radiating element for a monopole antenna. The coated substrates were affixed to the inner conductor of a 50 Ω N-type Amphenol RF connector. The outer conductor of the RF connector was electrically connected to a copper-clad piece of FR-4 circuit board material using silver conductive epoxy. The copper-clad FR-4 serves as a ground plane for the monopole antenna structure. When fully assembled, the ground planes and radiating elements form 3rd-order pre-fractal antennas as shown in **Figure 4-15**.

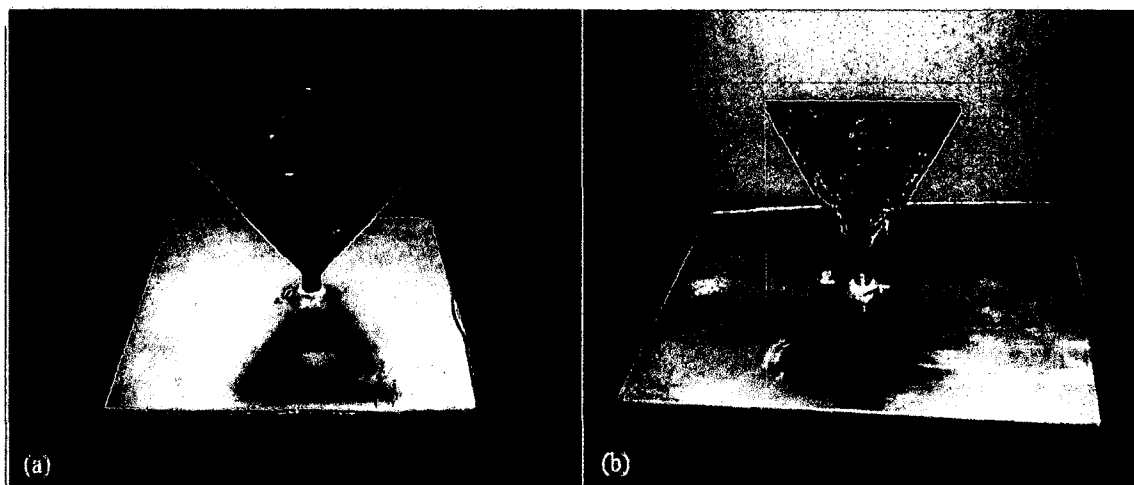


Figure 4-15: A 3D-printed Sierpinski antenna coated with (a) an electrolytically-exfoliated-graphene-doped acetone-ABS solution and (b) a carbon nanoparticle-doped acetone-ABS solution.

An XYZprinting da Vinci Jr. 2.0 Mix 3D-printer was used to directly print conducting tetrahedral radiating element using carbon-impregnated PLA filaments manufactured by Proto-Pasta and Graphene 3D Lab Inc. The manufacturer specifications regarding the electrical resistivity performance of these conductive filaments are given in **Table 4-1**. In both cases, the volume resistivity of printed parts should be sufficient for similar EM performance as compared to the antennas fabricated using the conductive coating method.

Table 4-1: Composite PLA filament volume resistivity specifications.

Filament	Dopant	$\rho_{vol} (\Omega \cdot \text{cm})$ [unprinted]	$\rho_{vol} (\Omega \cdot \text{cm})$ [in-plane]	$\rho_{vol} (\Omega \cdot \text{cm})$ [out-of-plane]
Proto-Pasta	Conductive Graphite	15	30	115
Graphene 3D Lab	Conductive Graphene	1	n/a	n/a

For both commercially available electrically-conductive filaments, the manufacturers claim that the addition of carbon to the PLA thermoplastic should increase the mechanical strength of both the filament and printed structures. This behavior was not observed—instead, prints which used the composite filaments suffered a significantly higher rate of shear stresses causing filament fracture and layer separation within a print job. Scanning electron microscope (SEM) images were taken of printed samples of both filaments and are presented in **Figure 4-16**.

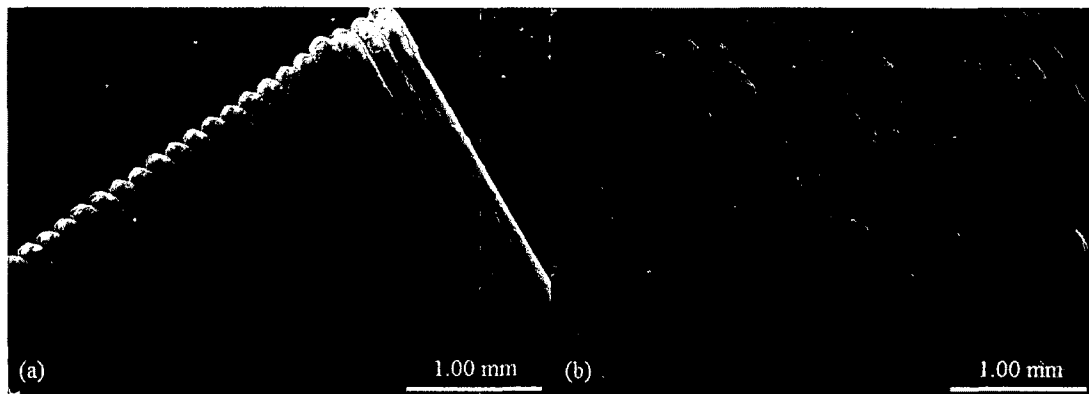


Figure 4-16: SEM images of printed samples of (a) graphite-doped-PLA filament and (b) graphene-doped-PLA filament. The additional carbon-content of the graphene-doped-PLA filament resulted in decreased bonding between subsequent layers of the printed material.

As seen in **Figure 4-16**, printed samples of the Graphene 3D Labs Inc. filament featured irregular nodules of dopant materials which resulted in small fissures occurring between layers of the printed object. These fissures affect the rigidity of the printed object and increase its electrical resistance.

As before, the tetrahedral radiating elements were affixed to the inner conductors of 50 Ω N-type Amphenol RF connectors while copper-clad pieces of FR-4 circuit board material were connected to the outer conductor of the RF connectors to serve as ground planes, forming the 3rd-order pre-fractal antennas shown in **Figure 4-17**.

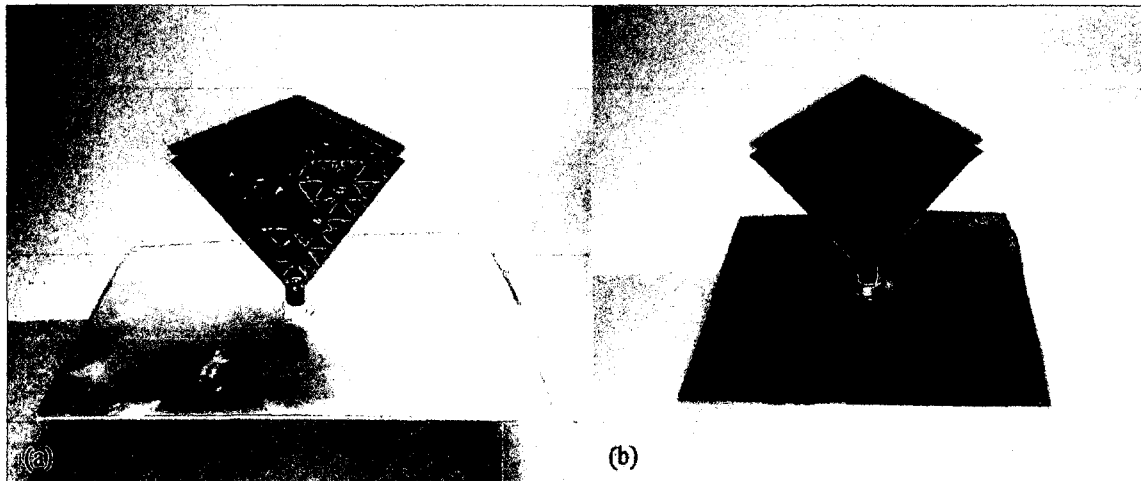


Figure 4-17: A 3D-printed Sierpinski tetrahedral antenna with radiating element made from (a) graphite-doped-PLA filament and (b) graphene-doped-PLA filament.

4.3.4 Antenna Measurement and Testing

The radiative capabilities of the various 3D-printed Sierpinski tetrahedral antennas that were fabricated were measured using an Agilent 4396B Network/Spectrum/Impedance analyzer in its vector network analyzer mode with a Agilent 87512A Transmission/Reflection Test Set attached. The vector network analyzer (VNA) measures both the amplitude and phase of signals simultaneously, enabling measurements over a broad spectrum of frequencies in a single measurement. A Laird Technologies Phantom multiband antenna was used as a reference antenna for the various antenna measurements.

A comparative method (as described in [197]) was used to determine the S_{21} transmission coefficient for the fabricated antennas. This method assumes that the return loss of the antenna under test is comparable to that of a standard antenna. First, the VNA is calibrated using an Agilent calibration kit containing a short circuit, an open circuit, and a matched (50Ω) load. These loads are affixed to the signal cables as prescribed in

the calibration protocol to minimize the effects of the cables during experimental measurements. Next, a matched pair of reference antennas are used to establish a baseline S_{21} (transmission) measurement using the network analyzer. This data is used to normalize the collected test data and identify the noise-bandwidth of the measurement system. Next, the reference antenna at the receiver port of the VNA is replaced with the test antenna without disturbing the rest of the experimental set-up and the S_{21} parameter is measured for the test antenna. The difference in these S_{21} measurements beyond the noise-bandwidth of the measurement systems enables the determination of a S_{21} transmission parameter for each test antenna measured. A picture of the experimental set-up is shown in **Figure 4-18**. The experimental configuration described above was used to collect S_{21} data on fourteen different 3D-printed antennas over a frequency range of 0.1–1.8 GHz, the measurement bandwidth of the Agilent 4396B VNA.

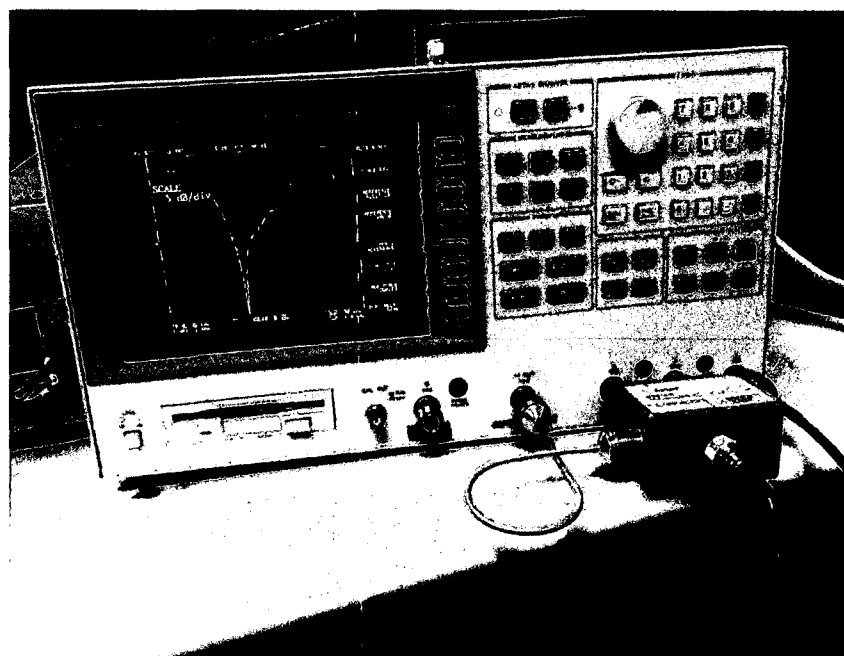


Figure 4-18: Photograph of the VNA and Reflection/Transmission test module during an antenna transmission parameter measurement.

4.3.5 Experimental Data

4.3.5.1 Sierpinski Gasket Antenna on Copper-Clad FR4

To validate the performance of the 3D-printed antenna designs, a Sierpinski gasket radiating element with identical face dimensions as the 3D-printed antennas was produced via photolithographically patterning a piece of copper-clad circuit board as shown in **Figure 4-19**. The patterned radiating element was then affixed to a copper ground plane via an Amphenol RF edge mount connector. This Sierpinski gasket antenna was tested identically to the 3D-printed antennas in an effort to define the expected behaviors of the antennas under test. The measured resonant frequency was observed to be $f = 1.31$ GHz with a 42.70 dB peak ($S_{21,max} - S_{21,min}$).

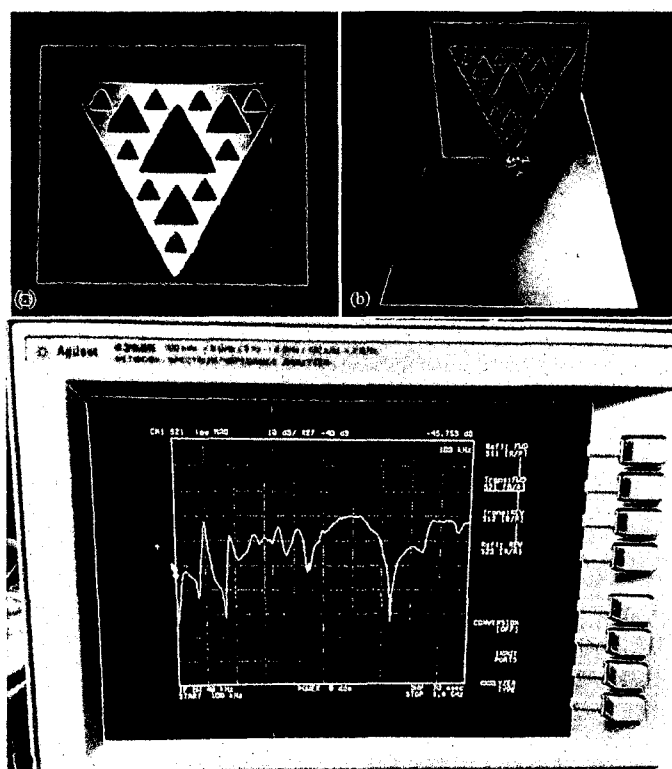


Figure 4-19: Photographs of (a) a lithographically-patterned Sierpinski gasket antenna radiating element and (b) an assembled gasket antenna. (c) Measured S_{21} data taken for the antenna shown in (b).

4.3.5.2 Electrolytically-Exfoliated Graphene Nanoflake-Doped Antennas

Figure 4-20 shows the collected S_{21} data for a radiating element coated with a 1%-by-weight carbon-doped 80:20 acetone/ABS solution. Section (c) of the figure depicts a region of low-frequency noise over the frequency range of 100 MHz to 800 MHz with an average signal intensity of -66.54 dB. Beyond this frequency range the noise is minimized and a 43.33 dB ($S_{21,max} - S_{21,min}$) peak occurs at 1.31 GHz, indicating signal transmission between the reference antenna and antenna under test. This frequency closely matches the observed operational frequency of the planar Sierpinski gasket antenna with similar face characteristics.

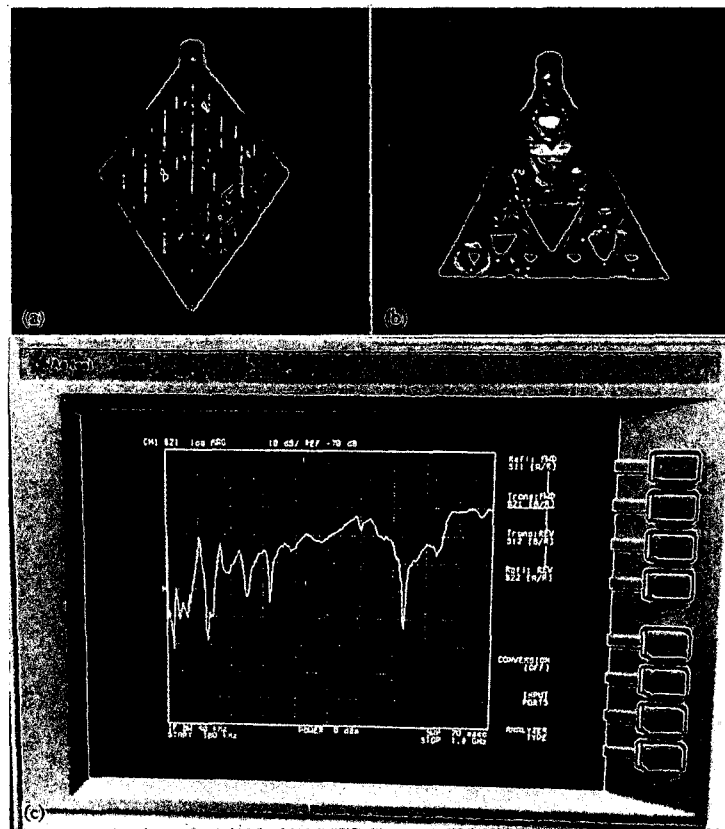


Figure 4-20: (a, b) Photographs of a 3D-printed ABS substrate coated with a 1%-by-weight doped solution of 80:20 acetone/ABS. (c) Measured S_{21} data taken for the antenna shown in (a) and (b).

Figure 4-21 shows the collected S_{21} data for a radiating element coated with a 5%-by-weight carbon-doped 80:20 acetone/ABS solution. Section (c) of the figure depicts a region of low-frequency noise over the frequency range of 100 MHz to 800 MHz with an average signal intensity of -69.10 dB. Beyond this frequency range the noise is minimized and a 39.96 dB ($S_{21,max} - S_{21,min}$) peak occurs at 1.32 GHz, indicating signal transmission between the reference antenna and antenna under test. This frequency closely matches the observed operational frequency of the planar Sierpinski gasket antenna with similar face characteristics.

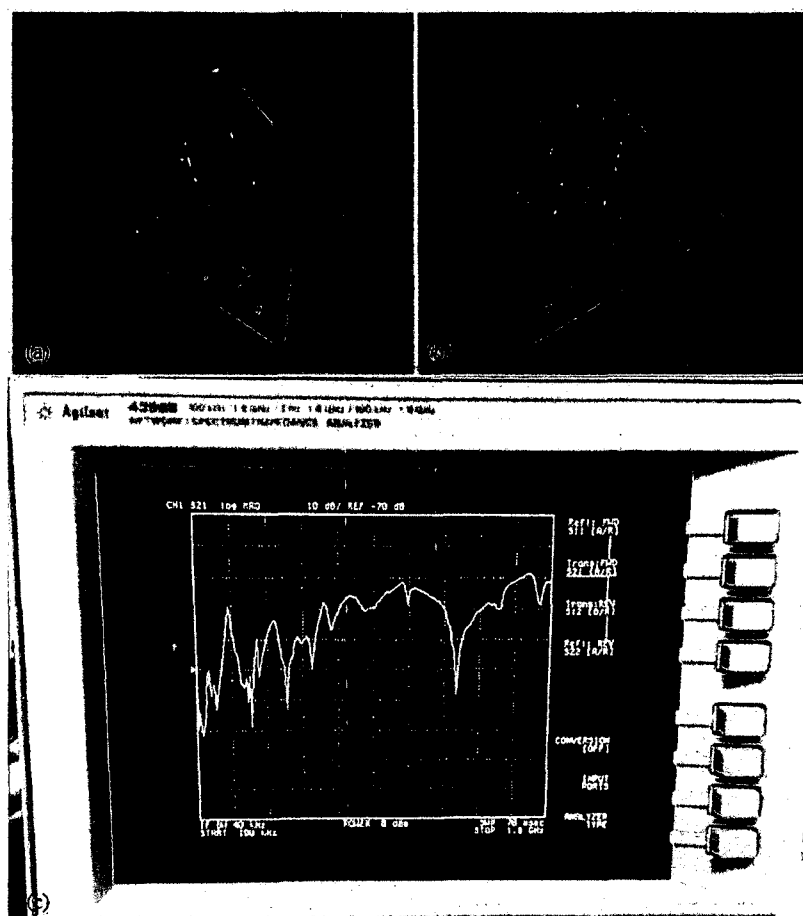


Figure 4-21: (a, b) Photographs of a 3D-printed ABS substrate coated with a 5%-by-weight doped solution of 80:20 acetone/ABS. (c) Measured S_{21} data taken for the antenna shown in (a) and (b).

Figure 4-22 shows the collected S_{21} data for a radiating element coated with a 10%-by-weight carbon-doped 80:20 acetone/ABS solution. Section (c) of the figure depicts a region of low-frequency noise over the frequency range of 100 MHz to 800 MHz with an average signal intensity of -69.10 dB. Beyond this frequency range the noise is minimized and a 39.96 dB ($S_{21,max} - S_{21,min}$) peak occurs at 1.32 GHz, indicating signal transmission between the reference antenna and antenna under test. This frequency closely matches the observed operational frequency of the planar Sierpinski gasket antenna with similar face characteristics.

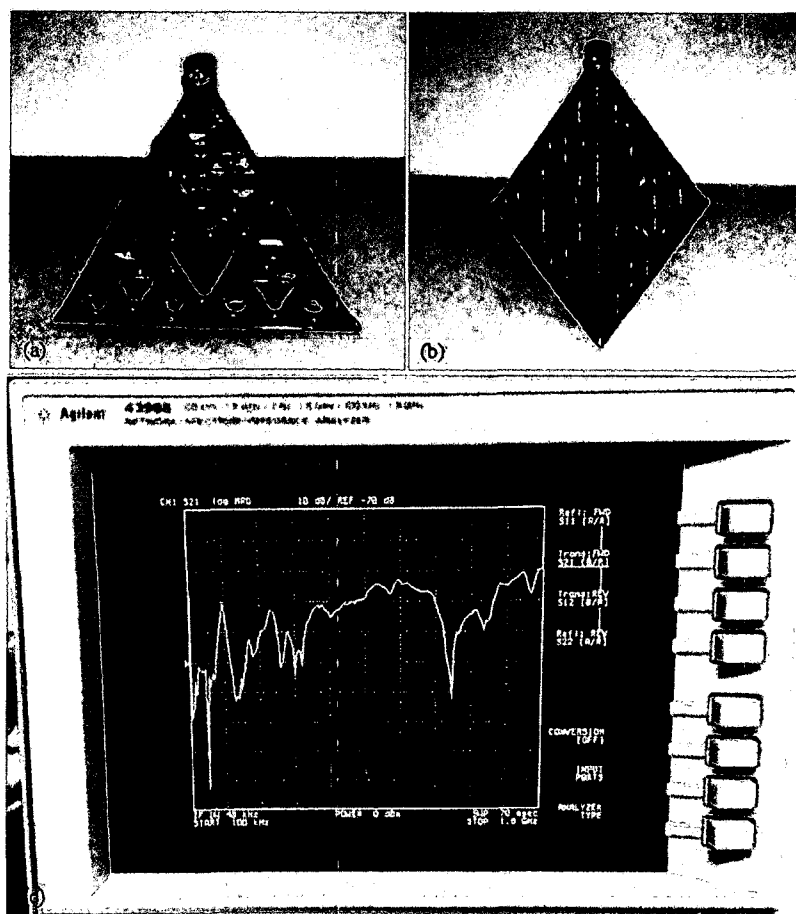


Figure 4-22: (a, b) Photographs of a 3D-printed ABS substrate coated with a 10%-by-weight doped solution of 80:20 acetone/ABS. (c) Measured S_{21} data taken for the antenna shown in (a) and (b).

Figure 4-23 shows the collected S_{21} data for a radiating element coated with a 15%-by-weight carbon-doped 80:20 acetone/ABS solution. Section (c) of the figure depicts a region of low-frequency noise over the frequency range of 100 MHz to 800 MHz with an average signal intensity of -55.97 dB. Beyond this frequency range the noise is minimized and a 51.76 dB ($S_{21,max} - S_{21,min}$) peak occurs at 1.31 GHz, indicating signal transmission between the reference antenna and antenna under test. This frequency closely matches the observed operational frequency of the planar Sierpinski gasket antenna with similar face characteristics.

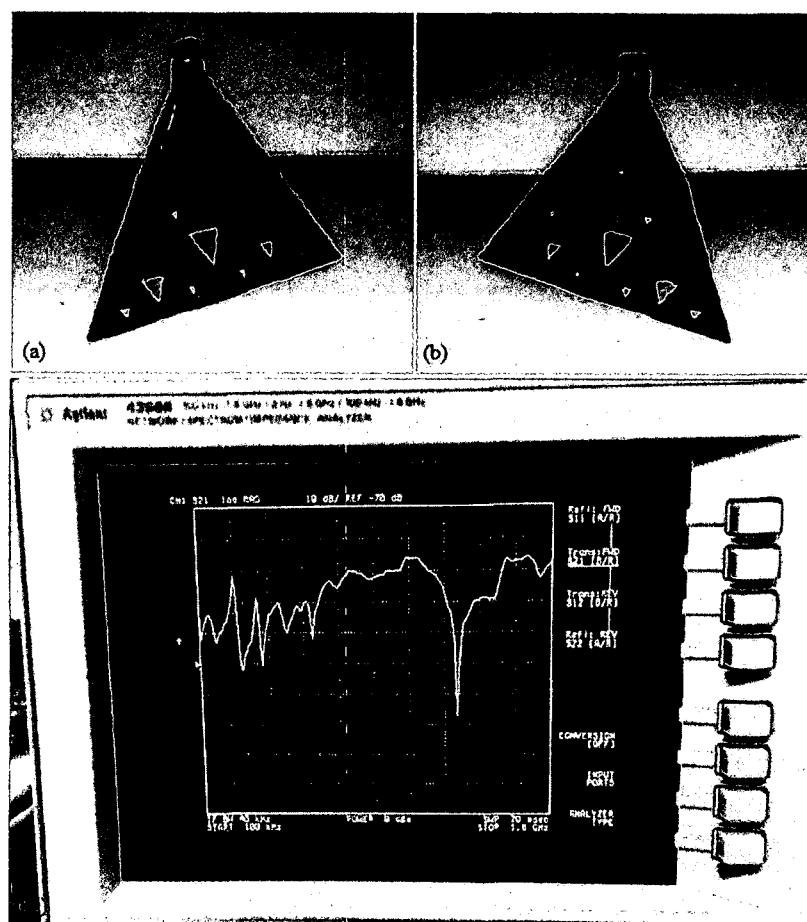


Figure 4-23: (a, b) Photographs of a 3D-printed ABS substrate coated with a 15%-by-weight doped solution of 80:20 acetone/ABS. (c) Measured S_{21} data taken for the antenna shown in (a) and (b).

Figure 4-24 shows the collected S_{21} data for a radiating element coated with a 20%-by-weight carbon-doped 80:20 acetone/ABS solution. Section (c) of the figure depicts a region of low-frequency noise over the frequency range of 100 MHz to 800 MHz with an average signal intensity of -45.74 dB. Beyond this frequency range the noise is minimized and a 52.28 dB ($S_{21,max} - S_{21,min}$) peak occurs at 1.32 GHz, indicating signal transmission between the reference antenna and antenna under test. This frequency closely matches the observed operational frequency of the planar Sierpinski gasket antenna with similar face characteristics.

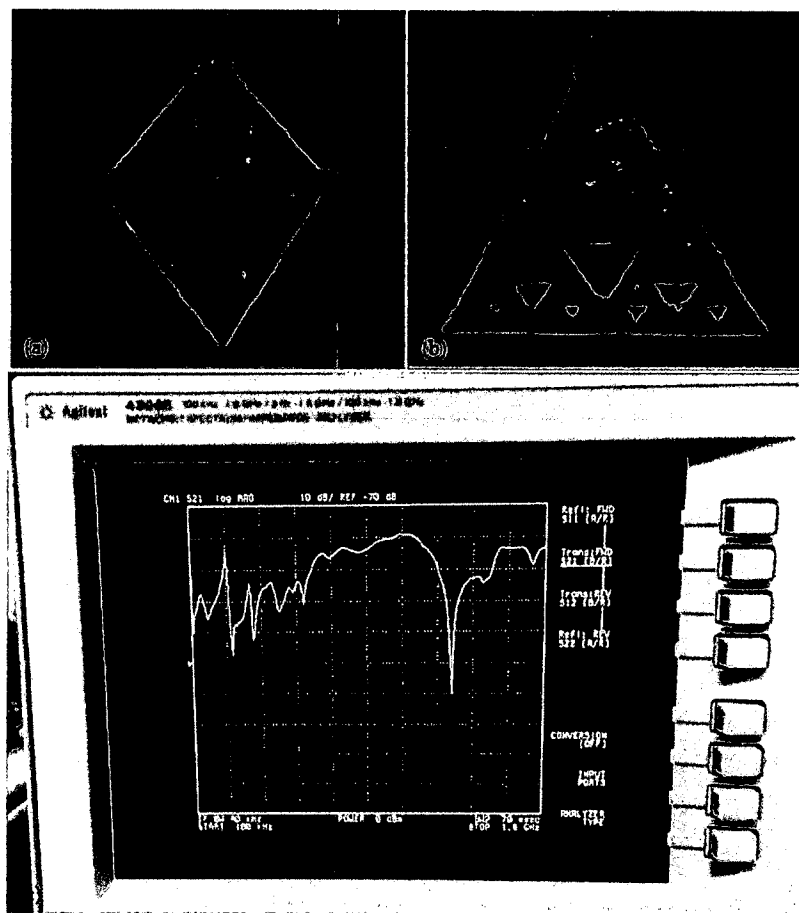


Figure 4-24: (a, b) Photographs of a 3D-printed ABS substrate coated with a 20%-by-weight doped solution of 80:20 acetone/ABS. (c) Measured S_{21} data taken for the antenna shown in (a) and (b).

Figure 4-25 shows the collected S_{21} data for a radiating element coated with a 25%-by-weight carbon-doped 80:20 acetone/ABS solution. Section (c) of the figure depicts a region of low-frequency noise over the frequency range of 100 MHz to 800 MHz with an average signal intensity of -48.26 dB. Beyond this frequency range the noise is minimized and a 43.89 dB ($S_{21,\max} - S_{21,\min}$) peak occurs at 1.32 GHz, indicating signal transmission between the reference antenna and antenna under test. This frequency closely matches the observed operational frequency of the planar Sierpinski gasket antenna with similar face characteristics.

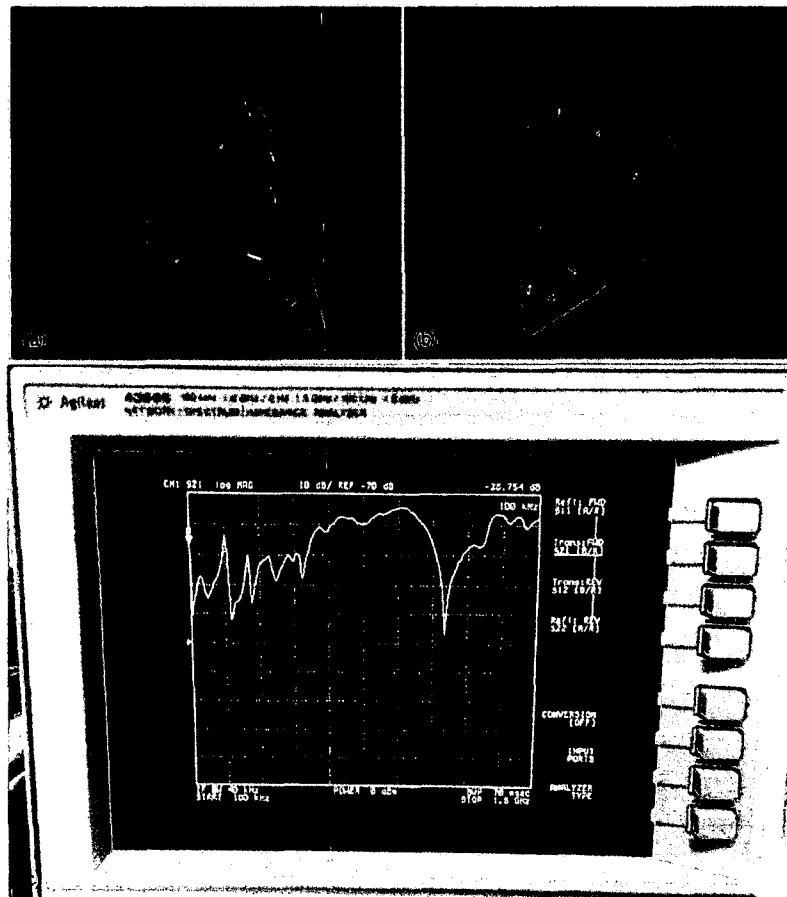


Figure 4-25: (a, b) Photographs of a 3D-printed ABS substrate coated with a 25%-by-weight doped solution of 80:20 acetone/ABS. (c) Measured S_{21} data taken for the antenna shown in (a) and (b).

Figure 4-26 illustrates the S_{21} response of the electrolytically-exfoliated graphene-nanoflake-doped antennas as compared to the copper Sierpinski gasket reference antenna.

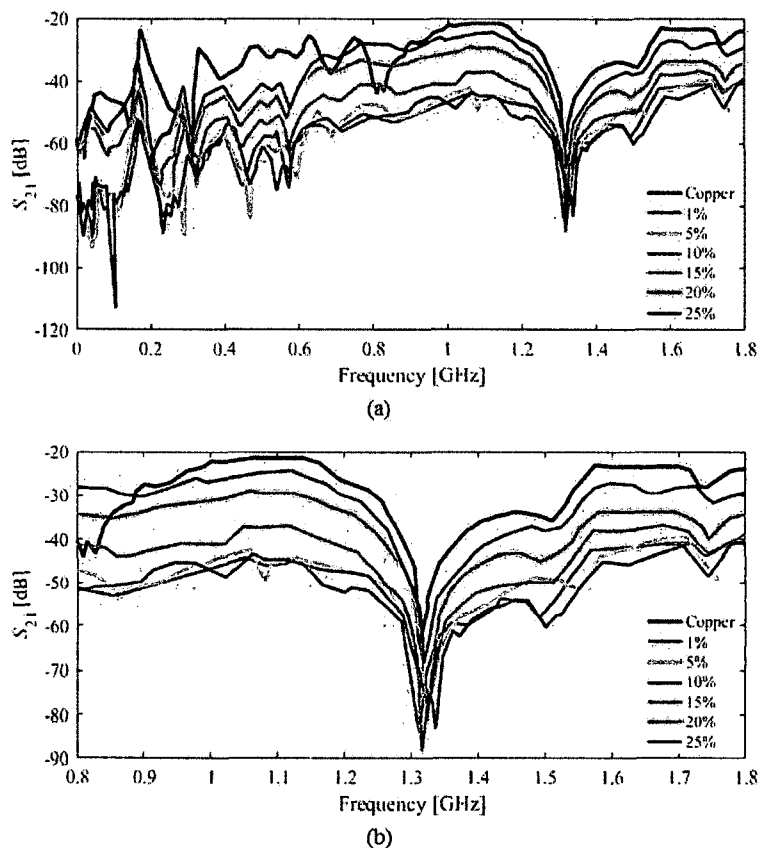


Figure 4-26: S_{21} response of the copper reference antenna and electrolytically-exfoliated graphene-nanoparticle-doped antennas (a) over the measurement bandwidth of the test set-up and (b) over a frequency range of 0.8–1.8 GHz to eliminate noise contributions.

From **Figure 4-26**, we can see that dopant concentrations of 1%, 5%, and 10% have similar noise-floors and peak values of S_{21} response. At dopant concentrations of 15% and greater, the increased conductivity of the coating yields a reduced noise floor for the antenna under test which is indicative of a decrease in the occurrence of resistive losses and thus provides an increase in antenna efficiency. The figure also illustrates small deviations in the location of the antenna resonant frequency. These deviations can

be attributed to variations in coating thickness as well as the x - y -resolution of the 3D-printer used.

4.3.5.3 Graphene Nanoparticle-Doped Antennas

Figure 4-27 shows the collected S_{21} data for a radiating element coated with a 1%-by-weight carbon-doped 80:20 acetone/ABS solution. Section (c) of the figure depicts a region of low-frequency noise over the frequency range of 100 MHz to 800 MHz with an average signal intensity of -64.54 dB. Beyond this frequency range the noise is minimized and a 42.04 dB ($S_{21,max} - S_{21,min}$) peak occurs at 1.33 GHz, indicating signal transmission between the reference antenna and antenna under test. This frequency closely matches the observed operational frequency of the planar Sierpinski gasket antenna with similar face characteristics.

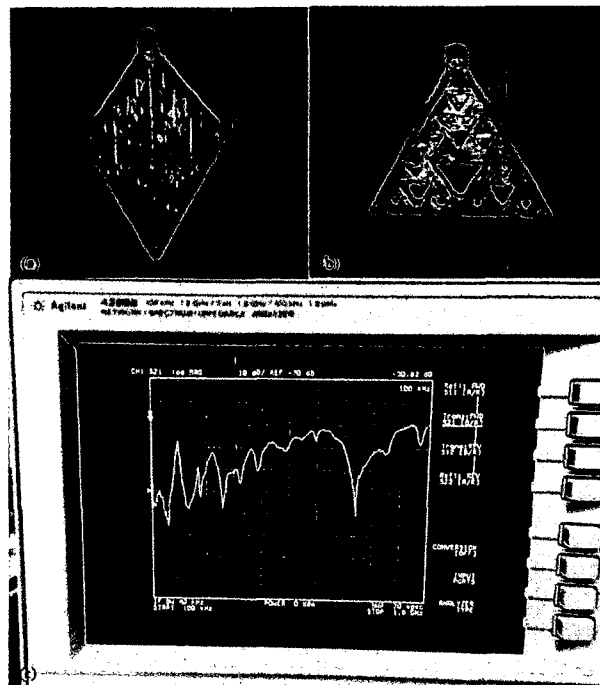


Figure 4-27: (a, b) Photographs of a 3D-printed ABS substrate coated with a 1%-by-weight doped solution of 80:20 acetone/ABS. (c) Measured S_{21} data taken for the antenna shown in (a) and (b).

Figure 4-28 shows the collected S_{21} data for a radiating element coated with a 5%-by-weight carbon-doped 80:20 acetone/ABS solution. Section (c) of the figure depicts a region of low-frequency noise over the frequency range of 100 MHz to 800 MHz with an average signal intensity of -66.21 dB. Beyond this frequency range the noise is minimized and a 43.72 dB ($S_{21,max} - S_{21,min}$) peak occurs at 1.34 GHz, indicating signal transmission between the reference antenna and antenna under test. This frequency closely matches the observed operational frequency of the planar Sierpinski gasket antenna with similar face characteristics.

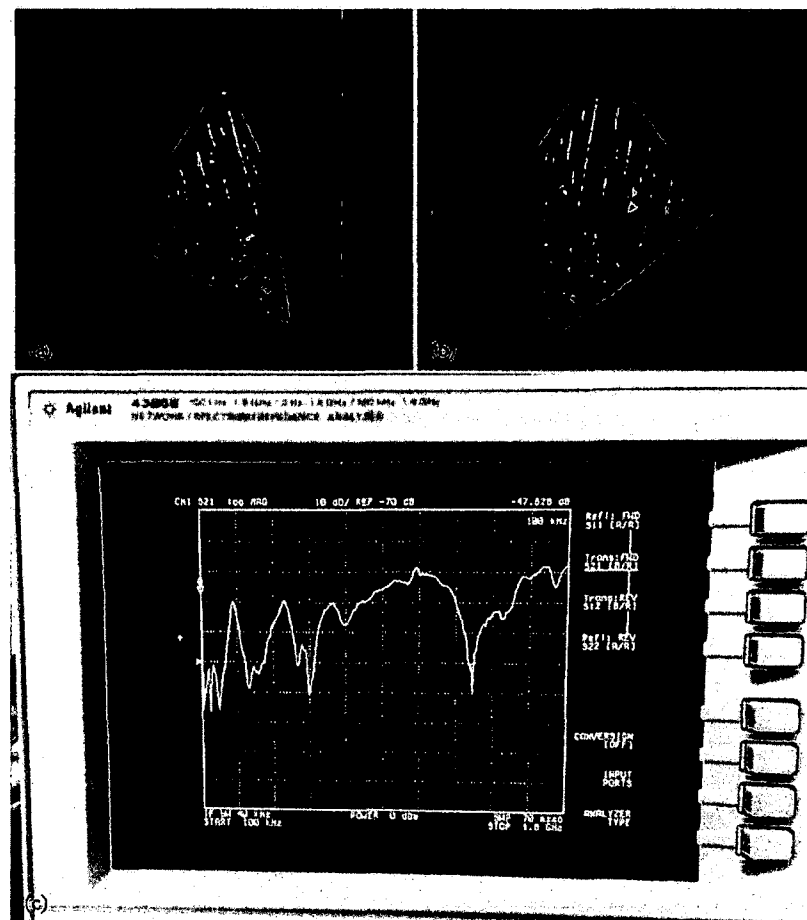


Figure 4-28: (a, b) Photographs of a 3D-printed ABS substrate coated with a 5%-by-weight doped solution of 80:20 acetone/ABS. (c) Measured S_{21} data taken for the antenna shown in (a) and (b).

Figure 4-29 shows the collected S_{21} data for a radiating element coated with a 10%-by-weight carbon-doped 80:20 acetone/ABS solution. Section (c) of the figure depicts a region of low-frequency noise over the frequency range of 100 MHz to 800 MHz with an average signal intensity of -65.01 dB. Beyond this frequency range the noise is minimized and a 44.49 dB ($S_{21,max} - S_{21,min}$) peak occurs at 1.33 GHz, indicating signal transmission between the reference antenna and antenna under test. This frequency closely matches the observed operational frequency of the planar Sierpinski gasket antenna with similar face characteristics.

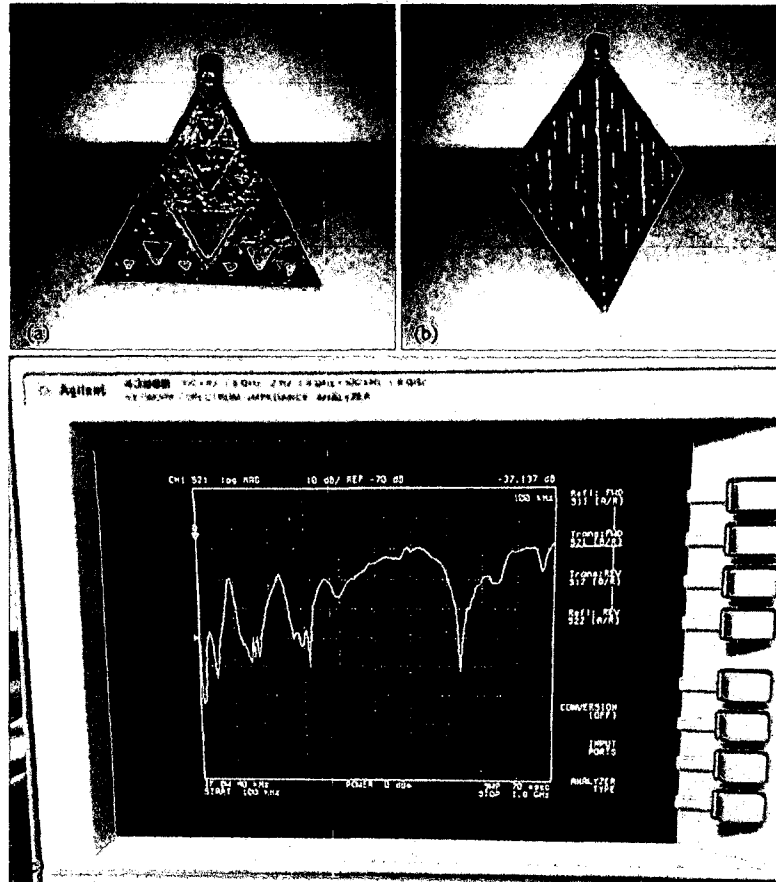


Figure 4-29: (a, b) Photographs of a 3D-printed ABS substrate coated with a 10%-by-weight doped solution of 80:20 acetone/ABS. (c) Measured S_{21} data taken for the antenna shown in (a) and (b).

Figure 4-30 shows the collected S_{21} data for a radiating element coated with a 15%-by-weight carbon-doped 80:20 acetone/ABS solution. Section (c) of the figure depicts a region of low-frequency noise over the frequency range of 100 MHz to 800 MHz with an average signal intensity of -63.04 dB. Beyond this frequency range the noise is minimized and a 50.24 dB ($S_{21,max} - S_{21,min}$) peak occurs at 1.33 GHz, indicating signal transmission between the reference antenna and antenna under test. This frequency closely matches the observed operational frequency of the planar Sierpinski gasket antenna with similar face characteristics.

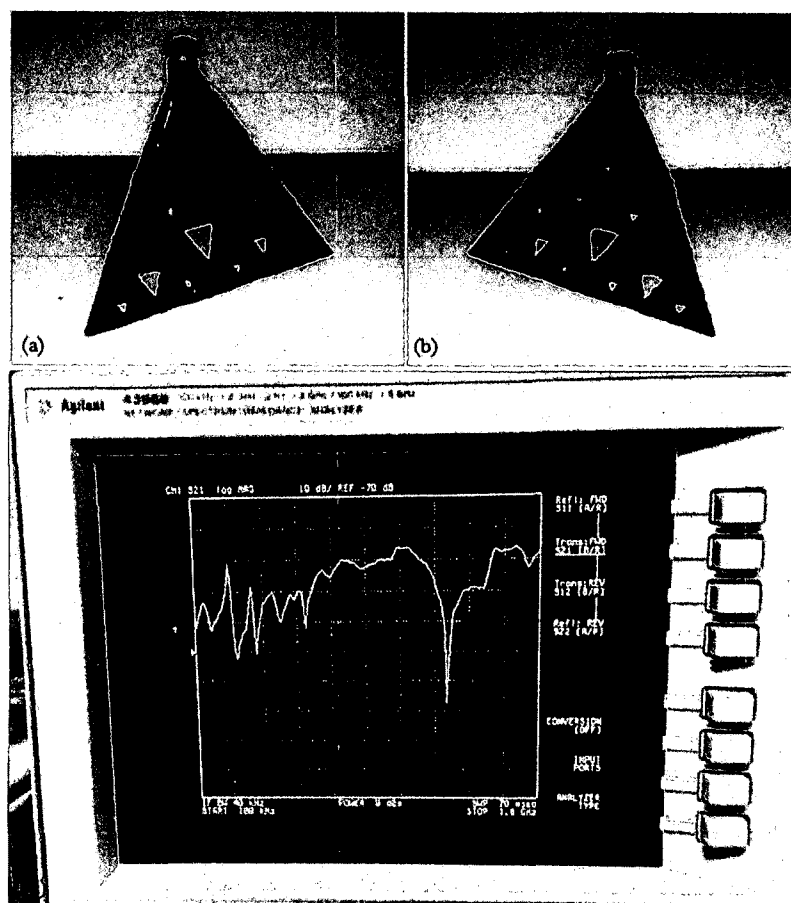


Figure 4-30: (a, b) Photographs of a 3D-printed ABS substrate coated with a 15%-by-weight doped solution of 80:20 acetone/ABS. (c) Measured S_{21} data taken for the antenna shown in (a) and (b).

Figure 4-31 shows the collected S_{21} data for a radiating element coated with a 20%-by-weight carbon-doped 80:20 acetone/ABS solution. Section (c) of the figure depicts a region of low-frequency noise over the frequency range of 100 MHz to 800 MHz with an average signal intensity of -54.33 dB. Beyond this frequency range the noise is minimized and a 49.85 dB ($S_{21,max} - S_{21,min}$) peak occurs at 1.31 GHz, indicating signal transmission between the reference antenna and antenna under test. This frequency closely matches the observed operational frequency of the planar Sierpinski gasket antenna with similar face characteristics.

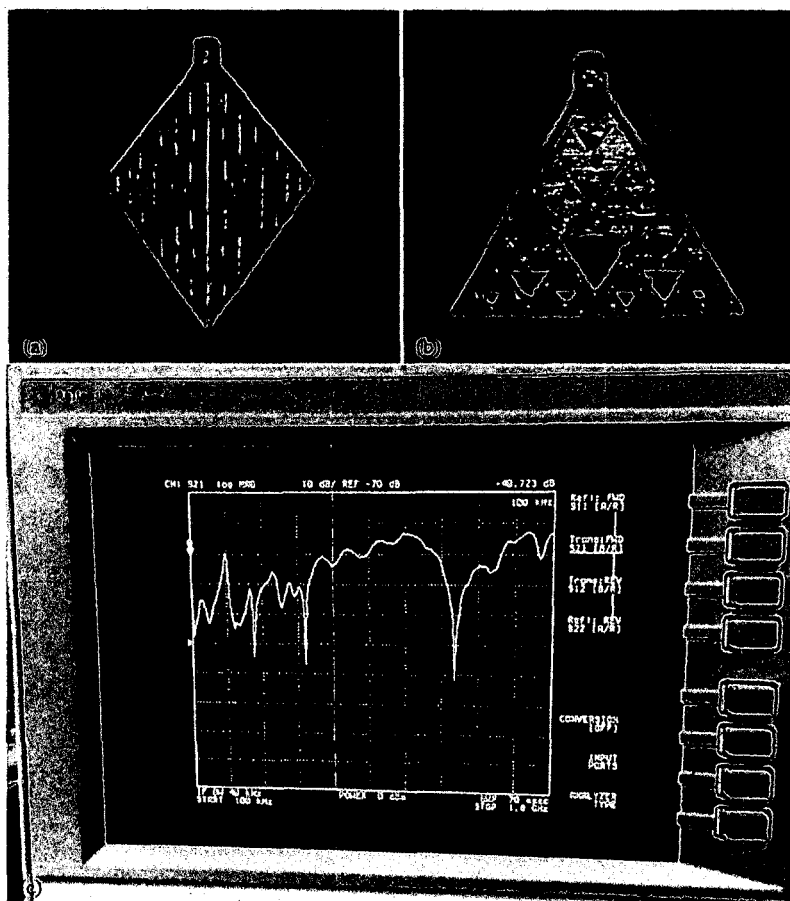


Figure 4-31: (a, b) Photographs of a 3D-printed ABS substrate coated with a 20%-by-weight doped solution of 80:20 acetone/ABS. (c) Measured S_{21} data taken for the antenna shown in (a) and (b).

Figure 4-32 shows the collected S_{21} data for a radiating element coated with a 25%-by-weight carbon-doped 80:20 acetone/ABS solution. Section (c) of the figure depicts a region of low-frequency noise over the frequency range of 100 MHz to 800 MHz with an average signal intensity of -53.03 dB. Beyond this frequency range the noise is minimized and a 49.73 dB ($S_{21,max} - S_{21,min}$) peak occurs at 1.31 GHz, indicating signal transmission between the reference antenna and antenna under test. This frequency closely matches the observed operational frequency of the planar Sierpinski gasket antenna with similar face characteristics.

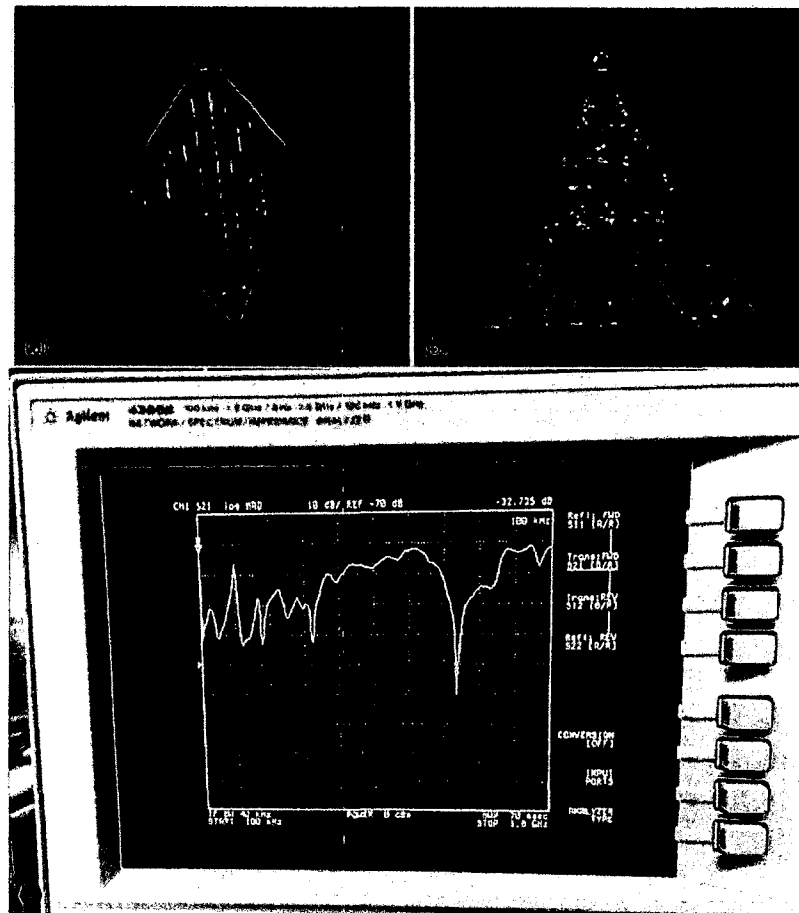


Figure 4-32: (a, b) Photographs of a 3D-printed ABS substrate coated with a 25%-by-weight doped solution of 80:20 acetone/ABS. (c) Measured S_{21} data taken for the antenna shown in (a) and (b).

Figure 4-33 illustrates the S_{21} response of the graphene nanoparticle-doped antennas as compared to the copper Sierpinski gasket reference antenna.

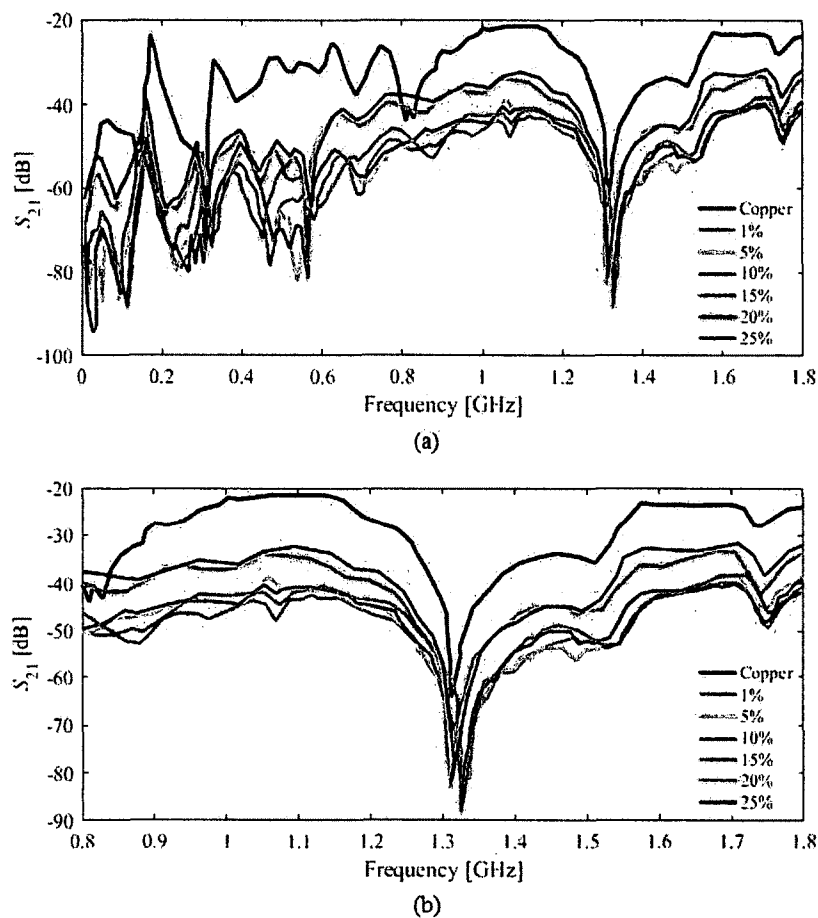


Figure 4-33: S_{21} response of the copper reference antenna and electrolytically-exfoliated graphene-nanoparticle-doped antennas (a) over the measurement bandwidth of the test set-up and (b) over a frequency range of 0.8–1.8 GHz to eliminate noise contributions.

From **Figure 4-33**, we can see that 20%, increasing the dopant concentration of the conductive coating yield effectively no change in the noise-floor or peak values of the S_{21} response for the antennas under test. At dopant concentrations of 20% and 25%, the noise floor is reduced however the change is much smaller than that observed using the electrolytically-exfoliated graphene-nanoflake coating. This phenomenon can be attributed to the size of the nanoparticles used to dope the acetone/ABS solution: the

nanoparticles (as opposed to the electrically-exfoliated nanoflakes) have small lateral dimensions which limit particle-to-particle overlap and prohibit the formation of a conductive network within the polymer matrix. The figure also illustrates small deviations in the location of the antenna resonant frequency, with all values experiencing a small positive shift in the frequency regime. These deviations (on the order of <150 MHz) can also be attributed to variations in coating thickness as well as the x - y -resolution of the 3D-printer used.

4.3.5.4 Conductive Filament Antennas

Figure 4-34 shows the collected S_{21} data for a 3D-printed radiating element fabricated using carbon black-doped PLA filament purchased from Proto-Pasta. Section (c) of the figure depicts a region of low-frequency noise over the frequency range of 100 MHz to 800 MHz with an average signal intensity of -42.25 dB. Beyond this frequency range the noise is minimized and a 43.17 dB ($S_{21,\max} - S_{21,\min}$) peak occurs at 1.32 GHz, indicating signal transmission between the reference antenna and antenna under test. This frequency closely matches the observed operational frequency of the planar Sierpinski gasket antenna with similar face characteristics.

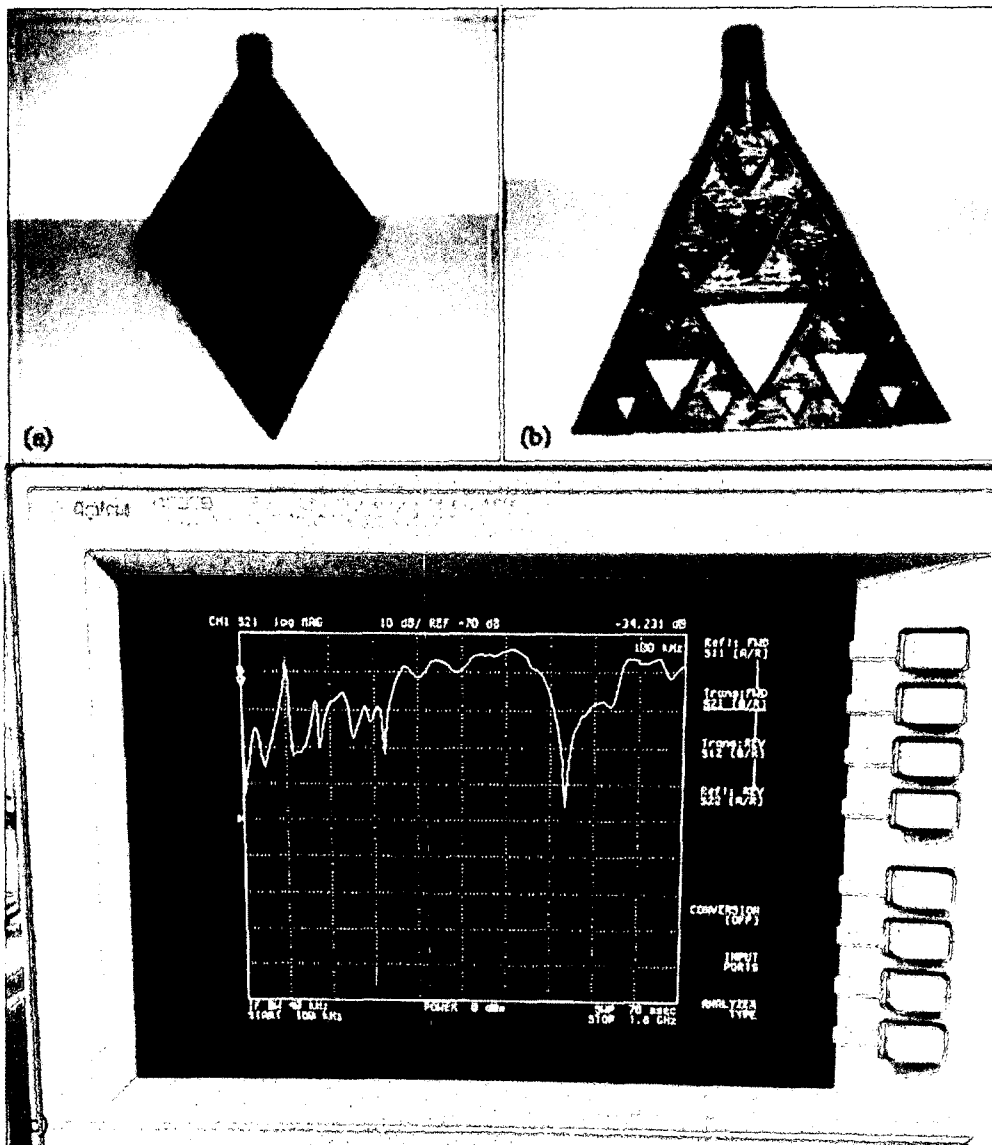


Figure 4-34: (a, b) Photographs of a 3D-printed carbon-doped PLA tetrahedral antenna radiating element. (c) Measured S_{21} data taken for the antenna shown in (a) and (b).

Figure 4-35 shows the collected S_{21} data for a 3D-printed radiating element fabricated using graphene-doped PLA filament purchased from BlackMagic3D. Section (c) of the figure depicts a region of low-frequency noise over the frequency range of 100 MHz to 800 MHz with an average signal intensity of -43.25 dB. Beyond this frequency range the noise is minimized and a 48.99 dB ($S_{21,max} - S_{21,min}$) peak occurs at 1.32 GHz, indicating signal transmission between the reference antenna and antenna under test. This

frequency closely matches the observed operational frequency of the planar Sierpinski gasket antenna with similar face characteristics.

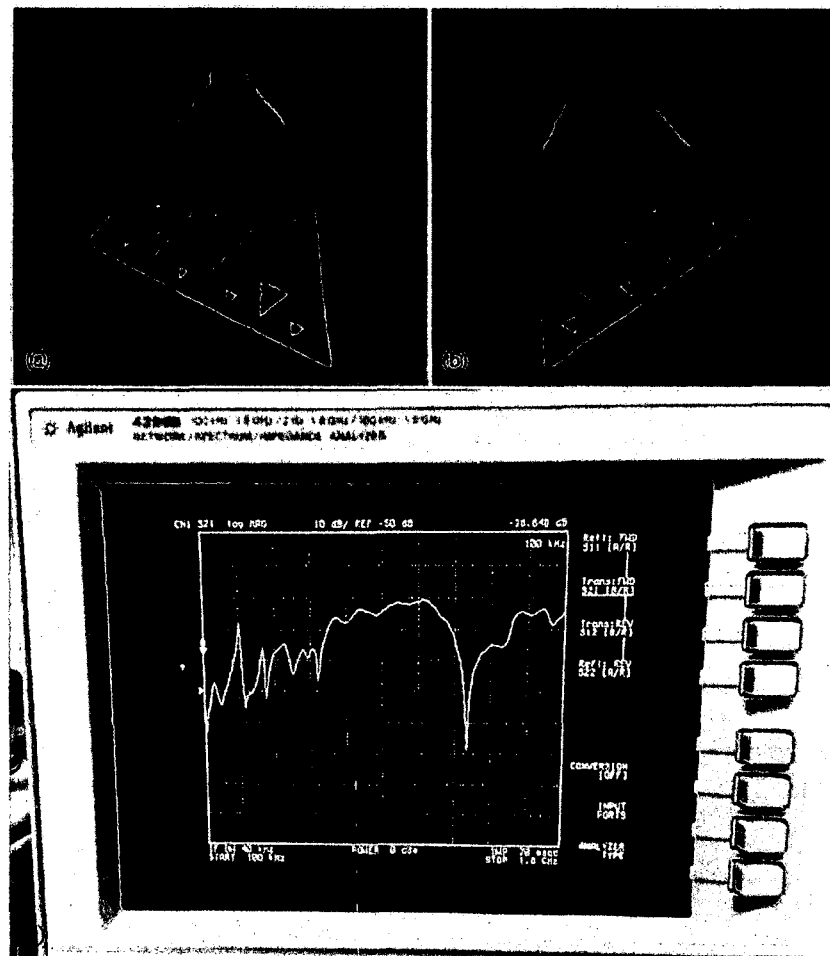


Figure 4-35: (a, b) Photographs of a 3D-printed graphene-doped PLA tetrahedral antenna radiating element. (c) Measured S_{21} data taken for the antenna shown in (a) and (b).

Figure 4-36 illustrates the S_{21} response of the graphene nanoparticle-doped antennas as compared to the copper Sierpinski gasket reference antenna. The data presented illustrates that the use of conductively-doped filaments yields a similar noise-floor and peak value as compared to the planar copper reference antenna. In both instances of using a conductively-doped filament, the antenna performance is nearly

identical with the graphene-doped filament, exhibiting an additional 5.82 dB of signal transmission at resonance.

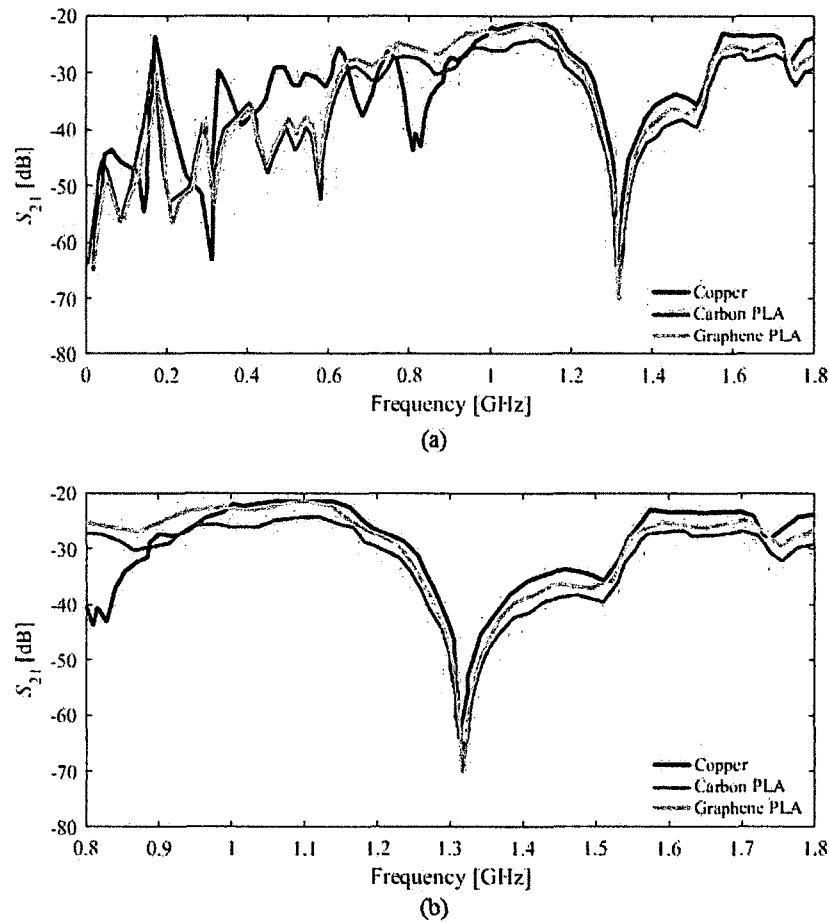


Figure 4-36: S_{21} response of the copper reference antenna and 3D-printed antennas utilizing conductive PLA filaments (a) over the measurement bandwidth of the test set-up and (b) over a frequency range of 0.8–1.8 GHz to eliminate low-frequency noise contributions.

4.3.6 Comparative Analysis of the Collected Data

The collected data shown in the previous section illustrates the potential of using 3D-printed antenna radiating elements which achieve transmission through both bulk conductivity of the element and conductive coatings applied to the element. This section will provide a comparison between the different methods used to generate radiating elements using normalized data sets obtained by setting the relative maximum of each

measurement to an intensity of 0 dB. Analysis of the normalized data will enable determinations of transmission intensities at resonance among the sixteen devices fabricated.

Figure 4-37 depicts the normalized transmission coefficient data for the antennas which received an electrolytically-exfoliated graphene-nanoflake-doped conductive coating. The transmission intensity ($-S_{21,\min}$) values are similar for dopant concentrations of 1%, 5%, and 10% with values of ranging from 39.96–43.33 dB, while further increases in the dopant concentration begin to increase this value with a maximum of 52.28 dB for the 20% dopant concentration. An interesting observation is that the transmission intensity decreases as the dopant concentration increases from 20% to 25%. The physical characteristics yielded by this change in dopant concentration may explain this anomaly: at a 25% doping concentration, there is more carbon than ABS in the coating solution. At this concentration, the acetone-based conductive coating dries extremely quickly, yielding a brittle, flaky coating containing cracks and fissures as seen in **Figure 4-25**. These cracks may interfere with the formation of the conductive network which enables signal transmission across the coating.

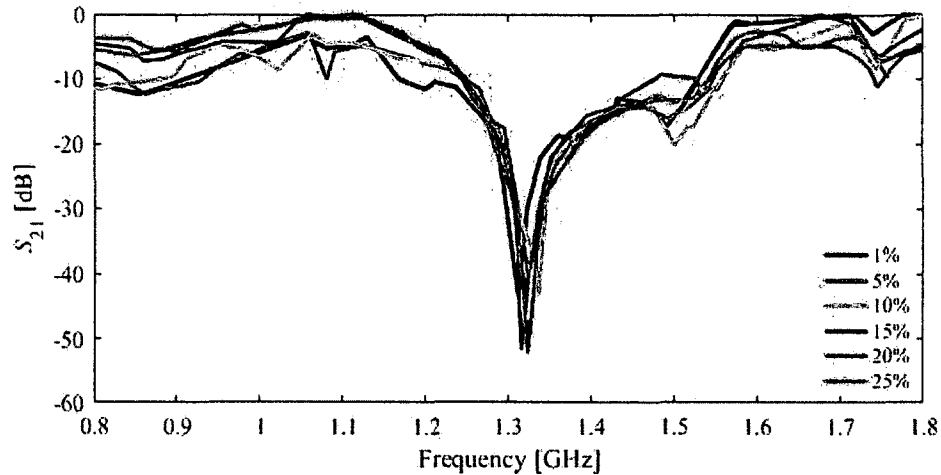


Figure 4-37: Normalized transmission coefficient data for antenna radiating elements which received an electrolytically-exfoliated graphene-nanoflake-doped conductive coating.

Figure 4-38 depicts the normalized transmission coefficient data for the antennas which received an electrolytically-exfoliated graphene-nanoflake-doped conductive coating. The transmission intensity ($-S_{21,\min}$) values are similar for dopant concentrations of 1%, 5%, and 10% with values of ranging from 42.04–44.49 dB, while further increases in the dopant concentration increase this value to between 49.73–50.24 dB with the maximum corresponding to a 15% dopant concentration. As compared to the antennas with an electrolytically-exfoliated graphene-doped coating, the carbon nanoparticle coating appears to produce less signal power transmission due to the decreased surface area of the dopant material.

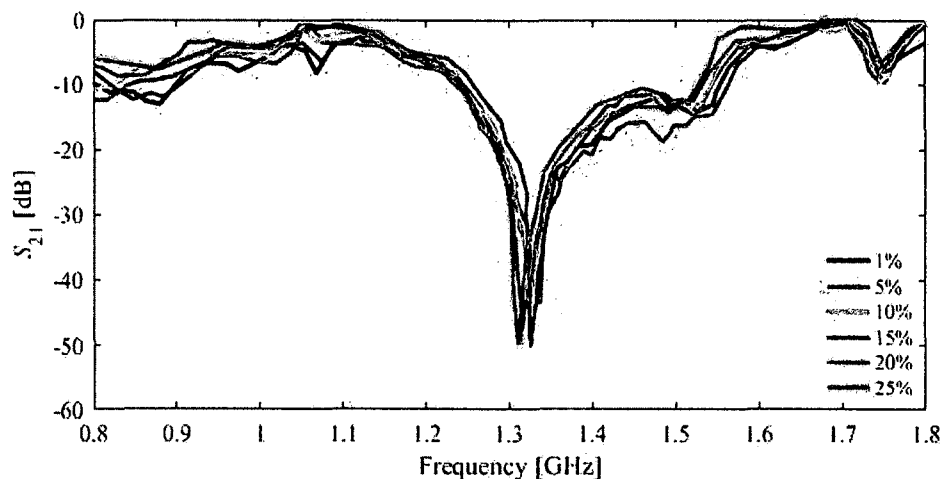


Figure 4-38: Normalized transmission coefficient data for antenna radiating elements which received a graphene-nanoparticle-doped conductive coating.

Figure 4-39 depicts the normalized transmission coefficient data for the best-performing coated antennas, as well as the conductive filament and copper antennas. The transmission intensity ($-S_{21,\min}$) values for all of the 3D-printed antennas utilizing some form of graphene are very similar, falling within a range of 48.99–52.28 dB with the maximum corresponding to the 20% electrolytically-exfoliated graphene-doped sample. From the figure above, we can also determine the bandwidth of each antenna using -30 dB as the reference for signal transmission. Using this criterion, the planar copper antenna has a bandwidth of 15.8 MHz, the 20% electrolytically-exfoliated graphene-doped sample has a bandwidth of 18.6 MHz, the 15% graphene-nanoparticle-doped sample has a bandwidth of 21.6 MHz, and both conductive filament antennas have a bandwidth of 20.1 MHz. This observation validates the increased bandwidth observed for 3D Sierpinski antennas during the radio frequency simulations.

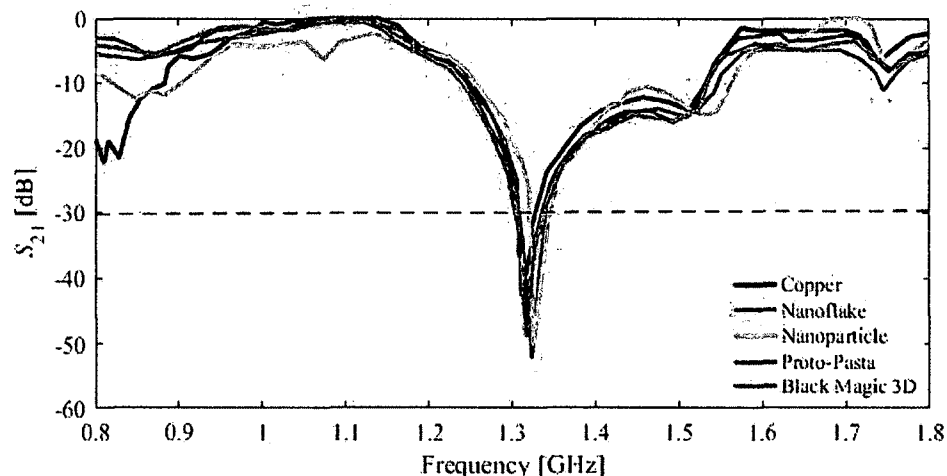


Figure 4-39: Normalized transmission coefficient data for the best-performing coated antennas, conductive filament antennas, and copper antenna.

4.3.7 Conclusions and Future Work

As illustrated above in **Figure 4-39**, the four materials used to create an electrically conductive radiating element via 3D-printing have all achieved promising results that illustrate the potential of additive manufacturing as a means to generate antennas for specific frequency applications. The use of 3D-printing techniques has enabled the fabrication of a complex antenna geometry that is unrealizable using conventional metal-casting techniques, yielding results comparable to a planar fractal antenna using conventional manufacturing technology. In the future, the advantages gained by using plastic as a structural material has many advantages that outweigh these limitations in applications requiring low weight, exposure to corrosion, or rapid fabrication.

The next step in increasing the performance of these devices is to evaluate different metallization techniques. Future research will include coating the devices with thin metal films via sputtering and electroplating to achieve uniform coating and higher

conductivities which should enhance performance towards the limits established by pure-metal devices.

BIBLIOGRAPHY

- [1] H. A. C. Tilmans, W. D. Raedt and E. Beyne, "MEMS for Wireless Communications: 'From RF-MEMS Components to RF-MEMS-SiP'," *Journal of Micromechanics and Microengineering*, vol. 13, no. 4, p. S139–S163, July 2003.
- [2] G. M. Rebeiz, K. Entesari, I. C. Reines, S.-J. Park, M. A. El-Tanani, A. Grichener and A. R. Brown, "Tuning in to RF MEMS," *IEEE Microwave Magazine*, vol. 10, no. 6, p. 55–72, October 2009.
- [3] Q. Zu and J. R. D. Luis, "RF MEMS Tunable Capacitor Applications in Mobile Phones," in *2010 10th IEEE International Conference on Solid-State and Integrated Circuit Technology*, Shanghai, CHN, 1–4 November 2010.
- [4] V. Kaajakari, "RF MEMS," in *Practical MEMS*, Las Vegas, NV: Small Gear Publishing, 2009, p. 285–305.
- [5] J. J. Yao, "RF MEMS from a Device Perspective," *Journal of Micromechanics and Microengineering*, vol. 10, no. 4, p. R9–R38, December 2000.
- [6] M/A-COM, "High Tuning Ratio Silicon Hyperabrupt Varactor Diode," MA4ST1103-1141T datasheet. [Online] Available: <http://www.macom.com>
- [7] Aeroflex, "Silicon Hyperabrupt Tuning Varactor," MHV500-18-1 datasheet. [Online] Available: <http://www.aeroflex.com>
- [8] L. E. Larson, R. H. Hackett, M. A. Melendes and R. F. Lohr, "Micromachined Microwave Actuator (MIMAC) Technology - A New Tuning Approach for Microwave Integrated Circuits," in *Digest of Papers from the Microwave and Millimeter-Wave Monolithic Circuits Symposium*, Boston, MA, USA, 10–11 June 1991.

- [9] L. E. Larson, R. H. Hackett and R. F. Lohr, "Microactuators for GaAs-Based Microwave Integrated Circuits," in *Digest of Technical Papers from the 1991 International Conference on Solid-State Sensors and Actuators*, San Francisco, CA, USA, 24–27 June 1991.
- [10] D. J. Young and B. E. Boser, "A Micromachined Variable Capacitor for Monolithic Low-Noise VCOs," in *Proceedings of the Solid-State Sensor and Actuator Workshop*, Hilton Head Island, SC, USA, 3–6 June 1996.
- [11] D. J. Young and B. E. Boser, "A Micromachine-Based RF Low-Noise Voltage-Controlled Oscillator," in *Proceedings of the IEEE Custom Integrated Circuits Conference, 1997*, Santa Clara, CA, USA, 5–8 May 1997.
- [12] D. J. Young, V. Malba, J.-J. Ou, A. F. Bernhardt and B. E. Boser, "A Low-Noise RF Voltage-Controlled Oscillator Using On-Chip High-Q Three-Dimensional Coil Inductor and Micromachined Variable Capacitor," in *Solid-State Sensor and Actuator Workshop*, Hilton Head Island, SC, USA, 8–11 June 1998.
- [13] D. J. Young, B. E. Boser, V. Malba and A. F. Bernhardt, "A Micromachined RF Low Phase Noise Voltage-Controlled Oscillator for Wireless Communication," *Journal of RF and Microwave Computer-Aided Engineering*, vol. 11, no. 5, p. 285–300, September 2001.
- [14] A. Dec and K. Suyama, "A 2.4 GHz CMOS LC VCO Using Micromachined Variable Capacitors for Frequency Tuning," in *1999 IEEE MTT-S International Microwave Symposium Digest*, Anaheim, CA, USA, 13–19 June 1999.
- [15] A. Dec and K. Suyama, "A 1.9-GHz CMOS VCO with Micromachined Electromechanically Tunable Capacitors," *IEEE Journal of Solid-State Circuits*, vol. 35, no. 8, p. 1231–1237, August 2000.
- [16] A. Dec and K. Suyama, "Microwave MEMS-Based Voltage-Controlled Oscillators," *IEEE Transactions of Microwave Theory and Techniques*, vol. 48, no. 11, p. 1943–1949, November 2000.
- [17] A. Malczewski, S. Eshelman, B. Pillans, J. Ehmke and C. L. Goldsmith, "X-Band RF MEMS Phase Shifters for Phased Array Applications," *IEEE Microwave and Guided Wave Letters*, vol. 9, no. 12, p. 517–519, December 1999.

- [18] B. Pillans, S. Eshelman, A. Malczewski, J. Ehmke and C. Goldsmith, "Ka-Band RF MEMS Phase Shifters," *IEEE Microwave and Guided Wave Letters*, vol. 9, no. 12, p. 520–522, December 1999.
- [19] A. Borgioli, Y. Liu, A. S. Nagra and a. R. A. York, "Low-Loss Distributed MEMS Phase Shifter," *IEEE Microwave and Guided Wave Letters*, vol. 10, no. 1, p. 7–9, January 2000.
- [20] J. S. Hayden and G. M. Rebeiz, "Low-Loss Cascadable MEMS Distributed X-Band Phase Shifters," *IEEE Microwave and Guided Wave Letters*, vol. 10, no. 4, p. 142–144, April 2000.
- [21] Y. Liu, A. Borgioli, A. S. Nagra and R. A. York, "K-Band 3-Bit Low-Loss Distributed MEMS Phase Shifter," *IEEE Microwave and Guided Wave Letters*, vol. 10, no. 10, p. 415–417, October 2000.
- [22] M. Kim, J. B. Hacker, R. E. Mihailovich and J. F. DeNatale, "A DC-to-40 GHz Four-Bit RF MEMS True-Time Delay Network," *IEEE Microwave and Wireless Components Letters*, vol. 11, no. 2, p. 56–58, February 2001.
- [23] J. B. Hacker, R. E. Mihailovich, M. Kim and J. F. DeNatale, "A Ka-Band 3-bit RF MEMS True-Time-Delay Network," *IEEE Transactions on Microwave Theory and Techniques*, vol. 51, no. 1, p. 305–308, January 2003.
- [24] G.-L. Tan, R. E. Mihailovich, J. B. Hacker, J. F. DeNatale and G. M. Rebeiz, "Low-Loss 2- and 4-bit TTD MEMS Phase Shifters Based on SP4T Switches," *IEEE Transactions on Microwave Theory and Techniques*, vol. 51, no. 1, p. 297–304, January 2003.
- [25] J. Brank, J. Yao, M. Eberly, A. Malczewski, K. Varian and C. Goldsmith, "RF MEMS-Based Tunable Filters," *International Journal of RF and Microwave Computer-Aided Engineering*, vol. 11, no. 5, p. 276–284, September 2001.
- [26] R. L. Borwick, P. A. Stupar, J. DeNatale, R. Anderson and R. Erlandson, "Variable MEMS Capacitors Implemented into RF Filter Systems," *IEEE Transactions on Microwave Theory and Techniques*, vol. 54, no. 1, p. 315–319, January 2003.
- [27] C. A. Hall, R. C. Leutzelschwab, R. D. Streeter and J. H. VanPatten, "A 25 Watt RF MEMS-Tune VHF Bandpass Filter," in *2003 IEEE MTT-S International Microwave Symposium Digest*, Philadelphia, PA, USA, 8–13 June 2003.

- [28] A. Abbaspour-Tamijani, L. Dussopt and G. M. Rebeiz, "Miniature and Tunable Filters Using MEMS Capacitors," *IEEE Transactions on Microwave Theory and Techniques*, vol. 51, no. 7, p. 1878–1885, July 2003.
- [29] G. M. Kraus, C. L. Goldsmith, C. D. Nordquist, C. W. Dyck, P. S. Finnegan, F. A. IV, A. Muyschondt and C. T. Sullivan, "A Widely Tunable RF MEMS End-Coupled Filter," in *2004 IEEE MTT-S International Microwave Symposium Digest*, Dallas, TX, USA, 6–11 June 2004.
- [30] J.-C. Chiao, Y. Fu, M. DeLisio and L.-Y. Lin, "MEMS Reconfigurable Vee Antenna," in *1999 IEEE MTT-S International Microwave Symposium Digest*, Anaheim, CA, USA, 13–19 June 1999.
- [31] W. H. Weedon, W. J. Payne and G. M. Rebeiz, "MEMS-Switched Reconfigurable Antennas," in *IEEE Antennas and Propagation Society International Symposium*, Boston, MA, USA, 8–13 July 2001.
- [32] C.-W. Baek, S. Song, J.-H. Park, S. Lee, J.-M. K. W. Choi, C. Cheon, Y.-K. Kim and Y. Kwon, "A V-Band Micromachined 2-D Beam-Steering Antenna Driven by Magnetic Force with Polymer-Based Hinges," *IEEE Transactions on Microwave Theory and Techniques*, vol. 51, no. 1, p. 325–331, January 2003.
- [33] R. Jackson and R. Ramadoss, "A MEMS-Based Electrostatically Tunable Circular Microstrip Patch Antenna," *Journal of Micromechanics and Microengineering*, vol. 17, no. 1, p. 1–8, January 2007.
- [34] N. Kingsley, D. E. Anagnostou, M. Tentzeris and J. Papapolymerou, "RF MEMS Sequentially Reconfigurable Sierpinski Antenna on a Flexible Organic Substrate with Novel DC-Biasing Technique," *Journal of Microelectromechanical Systems*, vol. 16, no. 5, p. 1185–1192, October 2007.
- [35] H.-T. Kim, S. Jung, K. Kang, J.-H. Park, Y.-K. Kim and Y. Kwon, "Low-Loss Analog and Digital Micromachined Impedance Tuners at the Ka-Band," *IEEE Transactions on Microwave Theory and Techniques*, vol. 49, no. 12, p. 2397–2400, December 2001.
- [36] M. Unlu, K. Topalli, H. Sagkol, S. Demir, O. A. Civi, S. S. Koc and T. Akin, "RF MEMS Adjustable Impedance Matching Network and Adjustable Power Divider," in *IEEE Antennas and Propagation Society International Symposium*, San Antonio, TX, USA, 16–21 June 2002.

- [37] Q. Shen and N. S. Barker, "RF-MEMS Based Tunable Matching Network," in *Proceedings of the Radio and Wireless Conference*, Boston, MA, USA, 10–13 August 2003.
- [38] Y. Lu, D. Peroulis, S. Mohammadi and L. P. B. Katehi, "A MEMS Reconfigurable Matching Network for a Class AB Amplifier," *IEEE Microwave and Wireless Components Letters*, vol. 13, no. 10, p. 437–439, October 2003.
- [39] A. v. Bezooijen, M. A. d. Jongh, C. Chanlo, L. C. H. Ruijs, F. v. Straten, R. Mahmoudi and A. H. M. v. Roermund, "A GSM/EDGE/WCDMA Adaptive Series-LC Matching Network Using RF-MEMS Switches," *IEEE Journal of Solid-State Circuits*, vol. 43, no. 10, p. 2259–2268, October 2008.
- [40] V. Kaajakari, "Damping," in *Practical MEMS*, Las Vegas, NV, USA, Small Gear Publishing, 2009, p. 178–198.
- [41] C. Liu, "Electrostatic Sensing and Actuation," in *Foundations of MEMS*, 2nd ed., Upper Saddle River, NJ: Prentice Hall, 2012, p. 127–175.
- [42] V. Kaajarkai, "Capacitive Actuation," in *Practical MEMS*, Las Vegas, NV: Small Gear Publishing, 2009, p. 223–240.
- [43] A. Dec and K. Suyama, "Micromachined Electro-Mechanically Tunable Capacitors and Their Applications to RF IC's," *IEEE Transactions on Microwave Theory and Techniques*, vol. 46, no. 12, p. 2587–2596, December 1998.
- [44] M. Bakri-Kassem and R. R. Mansour, "A High-Tuning-Range MEMS Variable Capacitor Using Carrier Beams," *Canadian Journal of Electrical and Computer Engineering*, vol. 31, no. 2, p. 89–95, Spring 2006.
- [45] M. Shavezipur, S. M. Hashemi, P. Nieva and A. Khajepour, "Development of a Triangular-Plate MEMS Tunable Capacitor with Linear Capacitance-Voltage Reponse," *Microelectronic Engineering*, vol. 87, no. 9, p. 1721–1727, November 2010.
- [46] M. K. Yoon, J. H. Park and J. Y. Park, "Actively Formed Gold Dual Anchor Structures-Based RF MEMS Tunable Capacitor," *Microwave and Optical Technology Letters*, vol. 57, no. 6, p. 1451–1454, June 2015.
- [47] A. Dec and K. Suyama, "Micromachined Varactor with Wide Tuning Range," *Electronics Letters*, vol. 33, no. 11, p. 922–924, May 1997.

- [48] D. A. Koester, R. Mahadevan, A. Shishkoff and K. W. Markus, "SmartMUMPs Design Handbook Including MUMPs Introduction and Design Rules, Revision 4," MEMS Technology Application Center, 1996.
- [49] H. Konishi, M. Nishiyama, J. Suzuki, Y. Tezuka, A. Komai, Y. Suzuki and K. Suzuki, "Built-In Upwards-Bending Electrostatic Actuator Capable of Three-Level-Structural Variable Capacitor," in *International Solid-State Sensors, Actuators and Microsystems Conference Digest*, Lyon, FRA, 10–14 June 2007.
- [50] F. Barrière, D. Passerieux, D. Mardivirin, A. Pothier and P. Blondy, "An Inverted-Gap Analog Tuning RF-MEMS Capacitor with 250 Milliwatts Power Handling Capability," in *2012 IEEE 25th International Conference on Micro Electro Mechanical Systems*, Paris, FRA, 29 January – 2 February 2012.
- [51] J. Zou, C. Liu, J. Schutt-Aine, J. Chen and S.-M. Kang, "Development of a Wide Tuning Range MEMS Tunable Capacitor for Wireless Communication Systems," in *International Electron Devices Meeting Technical Digest*, San Francisco, CA, USA, 10–13 December 2000.
- [52] J. Chen, J. Zou, C. Liu, J. E. Schutt-Ainé and S. M. Kang, "Design and Modeling of a Micromachined High-Q Tunable Capacitor with Large Tuning Range and a Vertical Planar Spiral Inductor," *IEEE Transactions on Electron Devices*, vol. 50, no. 3, p. 730–739, March 2003.
- [53] L. Dussopt and G. M. Rebeiz, "High-Q Millimeter-Wave MEMS Varactors: Extended Tuning Range and Discrete-Position Designs," in *2002 IEEE MTT-S International Microwave Symposium Digest*, Seattle, WA, USA, 2–7 June 2002.
- [54] D. Peroulis and L. P. B. Katehi, "Electrostatically-Tunable Analog RF MEMS Varactors with Measured Capacitance Range of 300%," in *2003 IEEE MTT-S International Microwave Symposium*, Philadelphia, PA, USA, 8–13 June 2003.
- [55] T. G. S. M. Rijks, P. G. Steeneken, J. T. M. v. Beek, M. J. E. Ulenaers, A. Jourdain, H. A. C. Tilmans, J. D. Coster and R. Puers, "Microelectromechanical Tunable Capacitors for Reconfigurable RF Architectures," *Journal of Micromechanics and Microengineering*, vol. 16, no. 3, p. 601–611, February 2006.

- [56] G. McFeetors and M. Okoniewski, "Performance and Operation of Stressed Dual-Gap RF MEMS Varactors," in *Proceedings of the 36th European Microwave Conference*, Manchester, GBR, 10–15 September 2006.
- [57] I.-Y. Huang, C.-H. Sun, H.-C. Tasi, C.-Y. Chou and C.-S. Huang, "Development of a Wide-Tuning Range and High Q Variable Capacitor Using Metal-Based Surface Micromachining Process," *Sensors and Actuators A: Physical*, vol. 149, no. 2, p. 193–200, February 2009.
- [58] Y. Shim, Z. Wu and M. Rais-Zadeh, "A High-Performance, Temperature-Stable, Continuously Tuned MEMS Capacitor," in *IEEE 24th International Conference on Micro Electro Mechanical Systems*, Cancun, QR, MEX, 23–27 January 2011.
- [59] H. Nieminen, V. Ermolov, K. Nybergh, S. Silanto and T. Ryhänen, "Microelectromechanical Capacitors for RF Applications," *Journal of Micromechanics and Microengineering*, vol. 12, no. 2, p. 177–186, February 2002.
- [60] J.-M. Kim, S. Lee, J.-M. Kim, C.-W. Baek, Y. Kwon and Y.-K. Kim, "A Mechanically Reliable Digital-Type Single Crystalline Silicon (SCS) RF MEMS Variable Capacitor," *Journal of Micromechanics and Microengineering*, vol. 15, no. 10, p. 1854–1863, August 2005.
- [61] C.-L. Dai, S.-C. Lin and M.-W. Chang, "Fabrication and Characterization of a Microelectromechanical Tunable Capacitor," *Microelectronics Journal*, vol. 38, no. 12, p. 1257–1262, December 2007.
- [62] G. Kahmen, M. Kaynak, M. Wietstruck, B. Tillack and H. Schumacher, "MEMS Varactor with High RF Power Handling Capability for Tuning of Wideband Low Noise RF VCOs," in *Proceedings of the 44th European Microwave Conference*, Rome, ITA, 6–9 October 2014.
- [63] A. Cazzorla, M. Kaynak, P. Farinelli and R. Sorrentino, "A Novel Dual Gap MEMS Varactor Manufactured in a Fully Integrated BiCMOS-MEMS Process," in *2015 Asia-Pacific Microwave Conference*, Nanjing, CHN, 6–9 December 2015.
- [64] E. S. Hung and S. D. Senturia, "Tunable Capacitors with Programmable Capacitance-Voltage Characteristic," in *Proceedings of the Solid-State Sensor and Actuator Workshop*, Hilton Head Island, SC, USA, 8–11 June 1998.

- [65] J. M. Bueno-Barrachina, C. S. Cañas-Peñuelas and S. Catalan-Izquierdo, "Capacitance Evaluation on Non-Parallel Thick-Plate Capacitors by Means of Finite Element Analysis," *Journal of Energy and Power Engineering*, vol. 5, no. 4, p. 373–378, April 2011.
- [66] E. S. Hung, "Positioning, Control, and Dynamics of Electrostatic Actuators for Use in Optical and RF Systems," Cambridge, MA, USA, 1998.
- [67] T. Ketterl, T. Weller and D. Fries, "A Micromachined Tunable CPW Resonator," in *2001 IEEE MTT-S International Microwave Symposium Digest*, Phoenix, AZ, USA, 20–25 May 2001.
- [68] G. V. Ionis, A. Dec and K. Suyama, "A Zipper-Action Differential Micro-Mechanical Tunable Capacitor," in *2001 Microelectromechanical Systems Conference*, Interlaken, BE, CHE, 24–26 August 2001.
- [69] G. V. Ionis, A. Dec and K. Suyama, "Differential Multi-Finger MEMS Tunable Capacitors for RF Integrated Circuits," in *2002 IEEE MTT-S International Microwave Symposium Digest*, Seattle, WA, USA, 2–7 June 2002.
- [70] C. D. Nordquist, A. Muyshondt, M. V. Pack, P. S. Finnegan, C. W. Dyck, I. C. Reines, G. M. Kraus, G. R. Sloan and C. T. Sullivan, "A MEMS High-Q Tunable Capacitor for Reconfigurable Microwave Integrated Circuits," in *Proceedings of SPIE 4981: MEMS Components and Applications for Industry, Automobiles, Aerospace, and Communications II*, San Jose, CA, USA, 25 January 2003.
- [71] J. K. Luo, M. Lin, Y. Q. Fu, L. Wang, A. J. Flewitt, S. M. Spearing, N. A. Fleck and W. I. Milne, "MEMS Based Digital Variable Capacitors with a High-k Dielectric Insulator," *Sensors and Actuators A: Physical*, vol. 132, no. 1, p. 139–146, November 2006.
- [72] L. Rederus, "A MEMS Multi-Cantilever Variable Capacitor on Metamaterial," Wright-Patterson Air Force Base, OH, USA, 2009.
- [73] M. Shavezipur, P. Nieva, S. M. Hashemi and A. Khajepour, "A Parallel-Plate-Based Fishbone-Shape MEMS Tunable Capacitor with Linear Capacitance-Voltage Response," *Sensors & Transducers Journal*, vol. 7, p. 15–24, October 2009.

- [74] R. Mahameed, M. A. El-Tanani and G. M. Rebeiz, "A Zipper RF MEMS Tunable Capacitor with Interdigitated RF and Actuation Electrodes," *Journal of Micromechanics and Microengineering*, vol. 20, no. 3, p. 1–6, February 2010.
- [75] R. Mahameed and G. M. Rebeiz, "Electrostatic RF MEMS Tunable Capacitors with Analog Tunability and Low Temperature Sensitivity," in *2010 IEEE MTT-S International Microwave Symposium Digest*, Anaheim, CA, USA, 23–28 May 2010.
- [76] J. Muldavin, C. Bozler, S. Rabe and a. C. Keast, "Large Tuning Range Analog and Multi-bit MEMS Varactors," in *2004 IEEE MTT-S International Microwave Symposium Digest*, Fort Worth, TX, USA, 6–11 June 2004.
- [77] S. H. Pu, A. S. Holmes, E. M. Yeatman, C. Papavassiliou and S. Lucyszyn, "Stable Zipping RF MEMS Varactors," *Journal of Micromechanics and Microengineering*, vol. 20, no. 3, p. 1–8, March 2010.
- [78] S. H. Pu, "A Micromachined Zipping Variable Capacitor," London, GBR, 2010.
- [79] S. H. Pu, D. A. Darbyshire, R. V. Wright, P. B. Kirthy, M. D. Rotaru, A. S. Holmes and E. M. Yeatman, "RF MEMS Zipping Varactor with High Quality Factor and Very Large Tuning Range," *IEEE Electron Device Letters*, unpublished.
- [80] M. Bakri-Kassem and R. R. Mansour, "Two Movable-Plate Nitride-Loaded MEMS Variable Capacitor," *IEEE Transactions on Microwave Theory and Techniques*, vol. 52, no. 3, p. 831–837, March 2004.
- [81] M. Bakri-Kassem, S. Fouladi and R. R. Mansour, "Novel High-Q MEMS Curled-Plate Variable Capacitors Fabricated in 0.35-um CMOS Technology," *IEEE Transactions on Microwave Theory and Techniques*, vol. 56, no. 2, p. 530–541, February 2008.
- [82] M. Bakri-Kassem and R. R. Mansour, "Linear Bilayer ALD Coated MEMS Varactor with High Tuning Capacitance Ratio," *Journal of Microelectromechanical Systems*, vol. 18, no. 1, p. 147–153, February 2009.
- [83] M. Shakhray, "Design and Investigation of Microelectromechanical (MEMS) Varactors," Kiel, DEU, 2005.

- [84] X. Yang, "A Circular Electrostatic Zipping Actuator for the Application of a MEMS Tunable Capacitor," Cambridge, MA, USA, 2005.
- [85] D.-M. Fang, S. Fu, Y. Cao, Y. Zhou and X.-L. Zhao, "Surface Micromachined RF MEMS Variable Capacitor," *Microelectronics Journal*, vol. 38, no. 8–9, p. 855–859, August–September 2007.
- [86] M. Shavezipur, A. Khajepour and S. M. Hashemi, "Development of Novel Segmented-Plate Linearly Tunable MEMS Capacitors," *Journal of Micromechanics and Microengineering*, vol. 18, no. 3, p. 1–8, February 2008.
- [87] M. Shavezipur, A. Khajepour and S. M. Hashemi, "A Novel Linearly Tunable Butterfly-Shape MEMS Capacitor," *Microelectronics Journal*, vol. 39, no. 5, p. 756–762, May 2008.
- [88] X. Li, Y. Xia, J. Liu, L. Yin, Y. Liu, D. Fang and H. Zhang, "Tunable RF MEMS Capacitor for Wireless Communication," in *SPIE 7510: 2009 International Conference on Optical Instruments and Technology: MEMS/NEMS Technology and Applications*, Shanghai, CHN, 19–21 October 2009.
- [89] A. M. Elshurafa and E. I. El-Masry, "MEMS Variable Capacitance Devices Utilizing the Substrate: II. Zipping Varactors," *Journal of Micromechanics and Microengineering*, vol. 20, no. 4, p. 1–7, April 2010.
- [90] Z. Li and N. C. Tien, "A High Tuning-Ratio Silicon-Micromachined Variable Capacitor with Low Driving Voltage," in *Solid-State Sensor, Actuator, and Microsystems Workshop*, Hilton Head Island, SC, USA, 2–6 June 2002.
- [91] Z. Xiao, W. Peng, R. F. Wolfenbuttel and K. R. Farmer, "Micromachined Variable Capacitors with Wide Tuning Range," *Sensors and Actuators A: Physical*, vol. 104, no. 3, p. 299–305, May 2003.
- [92] P. Monajemi and F. Ayazi, "A High-Q Low-Voltage HARPSS Tunable Capacitor," in *2005 IEEE MTT-S International Microwave Symposium Digest*, Long Beach, CA, USA, 12–17 June 2005.

- [93] M. Rais-Zadeh, A. K. Samarao, P. Monajemi and F. Ayazi, "Low-Voltage Large-Value Tunable Capacitors Using Self-Aligned HARPSS," in *IEEE 21st International Conference on Micro Electro Mechanical Systems*, Tuscon, AZ, USA, 13–17 January 2008.
- [94] M. Rais-Zadeh and F. Ayazi, "High-Q Tunable Silver Capacitors for RFIC's," in *2007 Topical Meeting on Silicon Monolithic Integrated Circuits in RF Systems*, Long Beach, CA, USA, 10–12 January 2007.
- [95] W. Han and Y.-H. Cho, "High-Precision Micromechanical Tunable Capacitors Using Parallel-Interconnected Digital Actuators," in *IEEE 20th International Conference on Micro Electro Mechanical Systems*, Kobe, JPN, 21–25 January 2007.
- [96] W. Han and Y.-H. Cho, "High-Precision Digital-to-Analog Tunable Capacitors with Improved Quality Factor Using a Parallel Digital Actuator Array," *Journal of Microelectromechanical Systems*, vol. 18, no. 4, p. 773–783, August 2009.
- [97] H. D. Wu, K. F. Harsh, R. S. Irwin, W. Zhang, A. R. Mickelson, Y. C. Lee and J. B. Dobson, "MEMS Designed for Tunable Capacitors," in *1998 IEEE MTT-S International Microwave Symposium Digest*, Baltimore, MD, USA, 7–12 June 1998.
- [98] K. F. Harsh, B. Su, W. Zhang, V. M. Bright and Y. C. Lee, "The Realization and Design Considerations of a Flip-Chip Integrated MEMS Tunable Capacitor," *Sensors and Actuators A: Physical*, vol. 80, no. 2, p. 108–118, March 2000.
- [99] Z. Feng, H. Zhang, K. C. Gupta, W. Zhang, V. M. Bright and Y. C. Lee, "MEMS-Based Series and Shunt Variable Capacitors for Microwave and Millimeter-Wave Frequencies," *Sensors and Actuators A: Physical*, vol. 91, no. 3, p. 256–265, July 2001.
- [100] J. Mireles, H. Ochoa and V. Hinostroza, "Design and Analysis of a MEMS Variable Capacitor using Thermal Actuators," *Computación y Sisternas*, vol. 10, no. 1, p. 1–15, 2006.
- [101] B. R. Jackson and C. E. Saavedra, "Variable MEMS Capacitors for Millimeter-Wave Integrated Circuit Filtering Applications," in *XV Workshop Iberchip*, Buenos Aires, ARG, 25–27 March 2009.

- [102] J. Reinke, G. K. Fedder and T. Mukherjee, "CMOS-MEMS Variable Capacitors Using Electrothermal Actuators," *Journal of Microelectromechanical Systems*, vol. 19, no. 5, p. 1105–1115, October 2012.
- [103] J. Y. Park, Y. J. Yee, H. J. Nam and J. U. Bu, "Micromachined RF MEMS Tunable Capacitors Using Piezoelectric Actuators," in *2001 IEEE MTT-S International Microwave Symposium Digest*, Phoenix, AZ, USA, 20–24 May 2001.
- [104] C.-Y. Lee and E. S. Kim, "Piezoelectrically Actuated Tunable Capacitor," *Journal of Microelectromechanical Systems*, vol. 15, no. 4, p. 745–755, August 2006.
- [105] C.-Y. Lee, S.-J. Chen, D. Chi, H. Yu and E. S. Kim, "Surface Micromachined GHz Tunable Capacitor with 14:1 Continuous Tuning Range," in *IEEE 21st International Conference on Micro Electro Mechanical Systems*, Tuscon, AZ, USA, 13–17 January 2008.
- [106] C.-Y. Lee, W. Pang, S.-J. Chen, D. Chi, H. Yu and E. S. Kim, "Surface Micromachined Complementary-Metal-Oxide-Semiconductor Compatible Tunable Capacitor with 14:1 Continuous Tuning Range," *Applied Physics Letters*, vol. 92, p. 1–3, January 2008.
- [107] T. Nagano, M. Nishigaki, K. Abe, K. Itaya and T. Kawabuko, "Fabrication and Performance of Piezoelectric MEMS Tunable Capacitors Constructed with AlN Bimorph Structure," in *2006 IEEE MTT-S International Microwave Symposium Digest*, San Francisco, CA, USA, 11–16 June 2006.
- [108] T. Kawakubo, T. Nagano, M. Nishigaki, K. Abe and K. Itaya, "RF-MEMS Tunable Capacitor with 3 V Operation Using Folded Beam Piezoelectric Bimorph Actuator," *Journal of Microelectromechanical Systems*, vol. 15, no. 6, p. 1759–1765, December 2006.
- [109] J. J. Yao, S. T. Park and J. DeNatale, "High Tuning-Ratio MEMS-Based Tunable Capacitors for RF Communications Applications," in *Solid-State Sensor and Actuator Workshop*, Hilton Head Island, SC, USA, 8–11 June 1998.
- [110] R. L. Borwick, P. A. Stupar, J. DeNatale, R. Anderson, C. Tsai and K. Garrett, "A High Q, Large Tuning Range, Tunable Capacitor for RF Applications," in *The Fifteenth IEEE International Conference on Micro Electro Mechanical Systems*, Las Vegas, NV, USA, 20–24 January 2002.

- [111] R. L. Borwick, P. A. Stupar, J. DeNatale, R. Anderson, C. Tsai, K. Garrett and R. Erlandson, "A High Q, Large Tuning Range MEMS Capacitor for RF Filter Systems," *Sensors and Actuators A: Physical*, vol. 103, no. 1–2, p. 33–41, January 2003.
- [112] C. Tsai, P. A. Stupar, R. L. Borwick, M. Pai and J. DeNatale, "An Isolated Tunable Capacitor with a Linear Capacitance-Voltage Behavior," in *12th International Conference on Solid-State Sensors, Actuators, and Microsystems*, Boston, MA, USA, 8–12 June 2003.
- [113] R. L. Borwick, P. A. Stupar and J. DeNatale, "Liquid Packaged MEMS Tunable Capacitors with Fast Response Times and Reduced Vibration Sensitivity," in *AMSE 2005 2005 Pacific Rim Technical Conference and Exhibition on Integration and Packaging of MEMS, NEMS, and Electronic Systems*, San Francisco, CA, USA, 17–22 July 2005.
- [114] A. D. Yalçinkaya, S. Jensen and O. Hansen, "Low Voltage, High-Q SOI MEMS Varactors for RF Applications," in *Proceedings of the 29th European Solid-State Circuits Conference*, Estoril, PRT, 16–18 September 2003.
- [115] S. Seok, W. Choi and K. Chun, "A Novel Linearly Tunable MEMS Variable Capacitor," *Journal of Micromechanics and Microengineering*, vol. 12, no. 1, p. 82–86, December 2001.
- [116] C.-L. Dai, M.-C. Liu and Y.-R. Li, "A Linearly Tunable Capacitor Fabricated by the Post-CMOS Process," in *SPIE 5386: Smart Sensors, Actuators, and MEMS II*, Sevilla, ESP, 9–11 May 2005.
- [117] H. Nguyen, D. Hah, P. R. Patterson, W. Piywattanametha and M. C. Wu, "A Novel MEMS Tunable Capacitor Based on Angular Vertical Comb Drive Actuators," in *Proceedings of the Solid-State Sensor, Actuator, and Microsystems Workshop*, Hilton Head Island, SC, USA, 2–6 June 2002.
- [118] H. D. Nguyen, D. Hah, P. R. Patterson, R. Chao, W. Piyawattanametha, E. L. Lau and M. C. Wu, "Angular Vertical Comb-Driven Tunable Capacitor with High-Tuning Capabilities," *Journal of Microelectromechanical Engineering*, vol. 13, no. 4, p. 406–413, June 2004.
- [119] J. Kim and L. Lin, "A MEMS Tunable Capacitor Based on Plastically Deformed Vertical Comb Sets," in *Proceedings of the 2004 ASME International Mechanical Engineering Congress and Exposition*, Anaheim, CA, USA, 13–20 November 2004.

- [120] J. Wilson, R. Bashirullah, D. Nackashi, D. Winick, B. Duewer and P. D. Franzon, "Design of Rotating MEMS Tunable Capacitors for Use at RF and Microwave Frequencies," in *SPIE 4593: Design, Characterization, and Packaging for MEMS and Microelectronics II*, Adelaide, SA, AUS, 17–19 December 2001.
- [121] J. M. Wilson, "Linearly Tunable RF-MEMS Capacitors Implemented Using an Integrated Removable Self-Masking Technique," Raleigh, NC, USA, 2003.
- [122] L. Gu and X. Li, "Rotational Driven RF Variable Capacitors with Post-CMOS Processes," *IEEE Electron Device Letters*, vol. 29, no. 2, p. 195–197, February 2008.
- [123] A. Oz and G. K. Fedder, "RF CMOS-MEMS Capacitor Having Large Tuning Range," in *12th International Conference on Solid-State Sensors, Actuators, and Microsystems*, Boston, MA, USA, 8–12 June 2003.
- [124] A. Oz and G. K. Fedder, "CMOS-Compatible RF-MEMS Tunable Capacitors," in *2003 IEEE Radio Frequency Integrated Circuits Symposium*, Philadelphia, PA, USA, 9–10 June 2003.
- [125] A. Oz, "CMOS/BICMOS Self-Assembling and Electrothermal Microactuators for Tunable Capacitors," Pittsburgh, PA, USA, 2003.
- [126] Q. Liu, "Laterally Driven Tunable Capacitors Fabricated by a Surface Micromachining Process for RF Circuits," in *2010 Second Pacific-Asia Conference on Circuits*, Beijing, CHN, 1–2 August 2010.
- [127] S. Barzegar, H. Mirzajani and H. B. Ghavifekr, "A New Linearly Tunable RF MEMS Varactor with Latching Mechanism for Low Voltage and Low Power Reconfigurable Networks," *Wireless Personal Communications*, vol. 83, no. 3, p. 2249–2265, August 2015.
- [128] A. Mehdaoui, M. B. Pisani, D. Tsamados, F. Casset, P. Ancey and A. M. Ionescu, "MEMS Tunable Capacitors with Fragmented Electrodes and Rotational Electro-Thermal Drive," *Microsystems Technologies*, vol. 13, no. 11, p. 1589–1594, July 2007.
- [129] J. S. Pulskamp, S. S. Bedair, R. G. Polcawich, C. D. Meyer, I. Kierzewski and B. Maack, "High-Q and Capacitance Ratio Multilayer Metal-on-Piezoelectric RF MEMS Varactors," *IEEE Electron Device Letters*, vol. 35, no. 8, p. 871–873, August 2014.

- [130] C. L. Goldsmith, A. Malczewski, Z. J. Yao, S. Chen, J. Ehmke and D. H. Hinzl, "RF MEMS Variable Capacitors for Tunable Filters," *International Journal of RF and Microwave Computer-Aided Engineering*, vol. 9, no. 4, p. 362–374, July 1999.
- [131] J. B. Rizk and G. M. Rebeiz, "Digital-Type RF MEMS Switched Capacitors," in *2002 IEE MTT-S International Microwave Symposium Digest*, Seattle, WA, USA, 2–7 June 2002.
- [132] L. Dussopt and G. M. Rebeiz, "An X- to Ku-Band 3-Bit Digital MEMS Varactor," *IEEE Microwave and Wireless Components Letter*, vol. 13, no. 9, p. 361–363, September 2003.
- [133] A. Grichener, D. Mercier and G. M. Rebeiz, "High-Power High-Reliability High-Q Switched RF MEMS Capacitors," in *2006 IEEE MTT-S International Microwave Symposium Digest*, San Francisco, CA, USA, 11–16 June 2006.
- [134] M. Nishiyama, H. Konishi, J. Suzuki, Y. Tezuka, Y. Suzuki and K. Suzuki, "Extremely High Capacitance Ratio (C/R) RF MEMS Variable Capacitor with Chameleon Actuators," in *2007 International Solid-State Sensors, Actuators, and Microsystems Conference*, Lyon, FRA, 10–14 June 2007.
- [135] S. P. Natarajan, S. J. Cunningham, A. S. M. III and D. R. Dereus, "CMOS Integrated Digital RF MEMS Capacitors," in *2011 IEEE 11th Topical Meeting on Silicon Monolithic Integrated Circuits in RF Systems*, Phoenix, AZ, USA, 16–19 January 2011.
- [136] J. Reinke, G. K. Fedder and T. Mukherjee, "CMOS-MEMS 3-bit Digital Capacitors with Tuning Ratios Greater Than 60:1," *IEEE Transactions on Microwave Theory and Techniques*, vol. 59, no. 5, p. 1238–1248, May 2011.
- [137] R. Ramadoss, S. Lee, Y. C. Lee, V. M. Bright and K. C. Gupta, "Fabrication, Assembly, and Testing of RF MEMS Capacitive Switches Using Flexible Printed Circuit Technology," *IEEE Transactions on Advanced Packaging*, vol. 26, no. 3, p. 248–254, August 2003.
- [138] J. A. Etxeberria and F. J. Garcia, "High Q Factor RF MEMS Tunable Metallic Parallel Plate Capacitor," in *2007 Spanish Conference on Electron Devices*, Madrid, ESP, 31 January – 2 February 2007.

- [139] J. A. Etxeberria and F. J. Garcia, "Tunable MEMS Volume Capacitors for High Voltage Applications," *Microelectronic Engineering*, vol. 84, no. 5–8, p. 1393–1397, May-August 2007.
- [140] H. Nieminen, V. Ermolov, S. Silanto, K. Nybergh and T. Rhyänen, "Design of a Temperature-Stable RF MEM Capacitor," *Journal of Microelectromechanical Systems*, vol. 13, no. 5, p. 705–714, October 2004.
- [141] A. Cazzorla, R. Sorrentino and P. Farinelli, "Double-Actuation Extended Tuning Range RF MEMS Varactor," in *2015 European Microwave Conference*, Paris, FRA, 7–10 September 2015.
- [142] G. M. Rebeiz and J. B. Muldavin, "RF MEMS Switches and Switch Circuits," *IEEE Microwave Magazine*, vol. 2, no. 4, p. 59–71, December 2001.
- [143] N. Høivik, M. A. Michalíček, Y. C. Lee, K. C. Gupta and V. M. Bright, "Digitally Controllable High-Q MEMS Capacitors for RF Applications," in *2001 IEEE MTT-S International Microwave Symposium Digest*, Phoenix, AZ, USA, 20–25 May 2001.
- [144] H. Kannan and B. Lakshminarayanan, "Multi-Finger RF MEMS Variable Capacitors for RF Applications," in *34th European Microwave Conference*, Amsterdam, NLD, 11–15 October 2004.
- [145] Y. Q. Fu, J. K. Luo, S. Milne, A. J. Flewitt and W. I. Milne, "Smart Digital Micro-Capacitor Based on Doped Nanocrystalline Silicon with HFO₂ High K Insulator," in *2016 IEEE 29th International Conference on Micro Electro Mechanical Systems*, Shanghai, CHN, 24–28 January 2016.
- [146] J.-C. Chiao, Y. Fu, D. Choudhury and L.-Y. Lin, "MEMS Millimeterwave Components," in *1999 IEEE MTT-S International Microwave Symposium*, Anaheim, CA, USA, 13–19 June 1999.
- [147] V. M. Lubecke and J.-C. Chiao, "MEMS Technologies for Enabling High Frequency Communications Circuits," in *4th International Conference on Telecommunications in Modern Satellite, Cable and BroadCasting Services*, Niš, MKD, 13–15 October 1999.
- [148] J. B. Yoon and C. T.-C. Nguyen, "A High-Q Tunable Micromechanical Capacitor with Movable Dielectric for RF Applications," in *Technical Digest of the International Electron Devices Meeting*, San Francisco, CA, USA, 10–13 December 2000.

- [149] J. D. Coster, R. Puers, H. A. C. Tilmans, J. T. M. V. Beek and T. G. S. M. Rijks, "Variable RF MEMS Capacitors with Extended Tuning Range," in *12th International Conference on Solid-State Sensors, Actuators, and Microsystems*, Boston, MA, USA, 8–12 June 2003.
- [150] P. Farinelli, F. Solazzi, C. Calaza, B. Margesin and R. Sorrentino, "A Wide Tuning Range MEMS Varactor Based on a Toggle Push-Pull Mechanism," in *38th European Microwave Conference*, Amsterdam, NDL, 27–31 October 2008.
- [151] C.-H. Han, D.-H. Choi and J.-B. Yoon, "Parallel-Plate MEMS Variable Capacitor with Superior Linearity and Large Tuning Ratio Using a Levering Structure," *Journal of Microelectromechanical Systems*, vol. 20, no. 6, p. 1345–1354, December 2011.
- [152] L. Ling, C. Zhao, M. Li and Z. Liu, "Symmetric Toggle Structured MEMS Linear Variable Capacitor with Large Tuning Ratio," in *2013 8th IEEE International Conference on Nano/Micro Engineering and Molecular Systems*, Suzhou, CHN, 7–10 April 2013.
- [153] A. Cruau, G. Lissorgues, P. Nicole, D. Placko and A. M. Ionescu, "V-Shaped Micromechanical Tunable Capacitors for RF Applications," *Microsystem Technologies*, vol. 12, no. 1, p. 15–20, December 2005.
- [154] D. M. Klymyshyn, D. T. Haluzan, M. Börner, S. Achenbach, J. Mohr and T. Mappes, "High Aspect Ratio Vertical Cantilever RF-MEMS Variable Capacitor," *IEEE Microwave and Wireless Components Letters*, vol. 17, no. 2, p. 127–129, February 2007.
- [155] S. Achenbach, D. Klymyshyn, D. Haluzan, T. Mappes, G. Welles and J. Mohr, "Fabrication of RF MEMS Variable Capacitors by Deep X-Ray Lithography and Electroplating," *Microsystems Technologies*, vol. 13, no. 3, p. 343–347, February 2007.
- [156] S. Achenbach, D. T. Haluzan, D. M. Klymyshyn, M. Börner and J. Mohr, "Large Tuning Ratio High Aspect Ratio Variable Capacitors Using Leveraged Bending," *Microsystems Technologies*, vol. 20, no. 10, p. 1807–1813, October 2014.
- [157] Y. J. Yoon, H. S. Lee and J.-B. Yoon, "MEMS Variable Capacitor Actuated with an Electrically Floating Plate," in *2007 IEEE International Electron Devices Meeting*, Washington, D.C., USA, 10–12 December 2007.

- [158] H. S. Lee, Y. J. Yoon, D.-H. Choi and J.-B. Yoon, "High-Q, Tunable-Gap MEMS Variable Capacitor Actuated with an Electrically Floating Plate," in *IEEE 21st International Conference on Microelectromechanical Systems*, Tuscon, AZ, USA, 13–17 January 2008.
- [159] Y. Zhu, M. R. Yuce and S. O. R. Moheimani, "A Low-Loss MEMS Tunable Capacitor with Moveable Dielectric," in *THE 8th IEEE Conference on Sensors*, Christchurch, NZL, 25–28 October 2009.
- [160] F. Khan, Y. Zhu, J. Lu, J. Pal and D. V. Dao, "A Single-Layer Micromachined Tunable Capacitor with an Electrically Floating Plate," *Smart Materials and Structures*, vol. 25, no. 4, p. 1–6, March 2016.
- [161] S. S. Pottigari and J. W. Kwon, "An Ultra Wide Range MEMS Variable Capacitor with a Liquid Metal," in *2008 Device Research Conference*, Santa Barbara, CA, USA, 23–25 June 2008.
- [162] F. A. Ghavanini, P. Enoksson, S. Bengtsson and P. Lundgren, "Vertically Aligned Carbon Based Varactors," *Journal of Applied Physics*, vol. 110, no. 2, p. 1–14, July 2011.
- [163] D.-H. Baek, Y. Eun, D.-S. Kwon, M.-O. Kim, T. Chung and J. Kim, "Variable Capacitor with Switching Mechanism for Wide Tuning Range," in *IEEE 27th International Conference on Micro Electro Mechanical Systems*, San Francisco, CA, USA, 26–30 January 2014.
- [164] D.-H. Baek, Y. Eun, D.-S. Kwon, M.-O. Kim, T. Chung and J. Kim, "Widely Tunable Variable Capacitor with Switching and Latching Mechanisms," *IEEE Electron Device Letters*, vol. 36, no. 2, p. 186–188, February 2015.
- [165] W. H. Hayt and J. A. Buck, "Appendix C: Material Constants," in *Engineering Electromagnetics*, 8th ed., New York, NY: McGraw-Hill, 2010, p. 562–564.
- [166] "Dielectric Strength of Insulating Materials," in *Handbook of Chemistry and Physics, 93rd Ed.*, Boca Raton, FL: CRC, 2013, pp. 15-43–15-47.
- [167] M. Zahn, Y. Ohki, D. Fenneman, R. Gripshover and V. Gehman, "Dielectric Properties of Water and Water/Ethylene Glycol Mixtures for Use in Pulsed Power Systems," *Proceedings of the IEEE*, vol. 74, no. 9, p. 1182–1221, September 1986.

- [168] "Electronegativity," in *Handbook of Chemistry and Physics, 93rd Ed.*, Boca Raton, FL: CRC, 2013, pp. 9-97.
- [169] R. M. Pashley, M. Rzechowicz, L. R. Pashley and M. J. Francis, "De-gassed Water is a Better Cleaning Agent," *The Journal of Physical Chemistry B*, vol. 109, no. 3, p. 1231–1238, 2005.
- [170] I. Pješčić, C. Tranter, P. L. Hindmarsh and N. D. Crews, "Glass composite prototyping for flow PCR with in situ DNA analysis," *Biomedical Microdevices*, vol. 12, no. 2, p. 333–343, 2010.
- [171] P. F. Man, C. H. Mastrangelo, M. A. Burns and D. T. Burke, "Microfabricated Capillarity-Driven Stop Valve and Sample Injector," in *Proceedings of the Eleventh Annual Workshop on Micro Electro Mechanical Systems*, Heidelberg, DEU, 25–29 January 1998.
- [172] LeaderTech, "The Basics of the Electromagnetic Spectrum," August 2016. [Online]. Available: <https://leadertechinc.com/blog/basics-electromagnetic-spectrum/>. [Accessed 1 February 2017].
- [173] International Telecommunication Union, "Radio Regulations Articles," 2012.
- [174] H. W. Ott, "Shielding," in *Electromagnetic Compatibility Engineering*, Hoboken, NJ, USA, John Wiley & Sons, Inc., 2009, p. 238–301.
- [175] D. M. Pozar, "Electromagnetic Theory," in *Microwave Engineering*, Hoboken, NJ, USA, John Wiley & Sons, Inc., 2005, p. 1–48.
- [176] S. Geetha, K. K. Satheesh-Kumar, C. R. K. Rao, M. Vijayan and D. C. Trivedi, "EMI Shielding: Methods and Materials—A Review," *Journal of Applied Polymer Science*, vol. 112, no. 4, p. 2073–2086, May 2009.
- [177] "MIL-STD-285: Method of Attenuation Measurements for Enclosures, Electromagnetic Shielding, for Electronic Test Purposes," Government Printing Office, Washington, DC, USA, 1956.
- [178] C. Morari and I. Bălan, "Methods for Determining the Shielding Effectiveness of Materials," *Electrotehnică, Electronică, Automatică*, vol. 63, no. 2, p. 126–136, April–June 2015.

- [179] "IEEE Std 299-1969: Recommended Practice for Measurement of Shielding Effectiveness of High-Performance Shielding Enclosures," The Institute of Electrical and Electronics Engineers, Inc., New York, NY, USA, 1969.
- [180] "IEEE Std 299-1991: Standard Method for Measuring the Effectiveness of Electromagnetic Shielding Enclosures," The Institute of Electrical and Electronics Engineers, Inc., New York, NY, USA, 1991.
- [181] "IEEE Std 299-1997: Standard Method for Measuring the Effectiveness of Electromagnetic Shielding Enclosures," The Institute of Electrical and Electronics Engineers, Inc., New York, NY, USA, 1997.
- [182] "IEEE Std 299-2006: Standard Method for Measuring the Effectiveness of Electromagnetic Shielding Enclosures," The Institute for Electrical and Electronics Engineers, Inc., New York, NY, USA, 2006.
- [183] "IEEE Std 299.1-2013: Standard Method for Measuring the Shielding Effectiveness of Enclosures and Boxes Having All Dimensions Between 0.1 m and 2 m," The Institute for Electrical and Electronics Engineers, Inc., New York, NY, 2013.
- [184] "ASTM E1851-97: Standard Test Method for Electromagnetic Shielding Effectiveness of Durable Rigid Wall Relocatable Structures," ASTM International, West Conshohocken, PA, USA, 1997.
- [185] "ASTM E1851-02: Standard Test Method for Electromagnetic Shielding Effectiveness of Durable Rigid Wall Relocatable Structures," ASTM International, West Conshohocken, PA, 2002, 2002.
- [186] "ASTM E1851-04: Standard Test Method for Electromagnetic Shielding Effectiveness of Durable Rigid Wall Relocatable Structures," ASTM International, West Conshohocken, PA, USA, 2004.
- [187] "ASTM 1851-09: Standard Test Method for Electromagnetic Shielding Effectiveness of Durable Rigid Wall Relocatable Structures," ASTM International, West Conshohocken, PA, USA, 2009.
- [188] "ASTM 1851-15: Standard Test Method for Electromagnetic Shielding Effectiveness of Durable Rigid Wall Relocatable Structures," ASTM International, West Conshohocken, PA, USA, 2015.

- [189] R. Perumalraj and B. S. Dasaradan, "Electromagnetic Shielding Effectiveness of Doubled Copper-Cotton Yarn Woven Materials," *Fibres and Textiles in Eastern Europe*, vol. 18, no. 3, p. 14–80, July–September 2010.
- [190] C. Morari, I. Balan, J. Pintea, E. Chitanu and I. Iordache, "Electrical Conductivity and Electromagnetic Shielding Effectiveness of Silicone Rubber Filled with Ferrite and Graphite Powders," *Progress in Electromagnetics Research M*, vol. 21, p. 93–104, 2011.
- [191] L. L. Hatfield and B. Schilder, "Microwave Shielding Measurement Method," in *2009 IEEE Pulsed Power Conference*, Washington, DC, USA, 28 June–2 July 2009.
- [192] "ASTM ES7-83: Test Method for Electromagnetic Shielding Effectiveness of Planar Materials," ASTM International, West Conshohocken, PA, USA, 1983.
- [193] A. Tamburrano, D. Desideri, A. Maschio and M. S. Sarto, "Coaxial Waveguide Methods for Shielding Effectiveness Measurement of Planar Materials Up to 18 GHz," *IEEE Transactions on Electromagnetic Compatibility*, vol. 56, no. 6, p. 1386–1395, Decemeber 2014.
- [194] J. Dřinovský and Z. Kejík, "Electromagnetic Shielding Efficiency Measurement of Composite Materials," *Measurement Science Review*, vol. 9, no. 4, p. 109–112, January 2009.
- [195] D. Desideri and A. Maschio, "A New Version of Coaxial Holder with Continuous Conductor for Tests on Planar Films," *International Journal of Applied Electromagnetics and Mechanics*, vol. 39, no. 4, p. 189–194, 2012.
- [196] "ASTM D4935-99: Standard Test Method for Measuring the Electromagnetic Shielding Effectiveness of Planar Materials," ASTM International, West Conshohocken, PA, USA, 1999.
- [197] "ASTM D4935-10: Standard Test Method for Measuring the Electromagnetic Shielding Effectiveness of Planar Materials," ASTM International, West Conshohocken, PA, USA, 2010.
- [198] M. S. Sarto and A. Tamburrano, "Innovative Test Method for the Shielding Effectiveness Measurement of Conductive Thin Films in a Wide Frequency Range," *IEEE Transactions on Electromagnetic Compatibility*, vol. 48, no. 2, p. 331–341, May 2006.

- [199] D. A. Lampasi, A. Tamburrano, S. Bellini, M. Tului, A. Albolino and M. S. Sarto, "Effect of Grain Size and Distribution on the Shielding Effectiveness of Transparent Conducting Thin Films," *IEEE Transactions on Electromagnetic Compatibility*, vol. 56, no. 2, p. 352–359, April 2014.
- [200] J. Catrysse, "A New Test-Cell for the Characterisation of Shielding Materials in the Far Field," in *Seventh International Conference on Electromagnetic Compatibility*, York, GBR, 28–31 August 1990.
- [201] J. Catrysse, M. Delesie and W. Steenbakkers, "The Influence of the Test Fixture on Shielding Effectiveness Measurements," *IEEE Transactions on Electromagnetic Compatibility*, vol. 34, no. 3, p. 348–351, August 1992.
- [202] D. D. L. Chung, "Electromagnetic Interference Shielding Effectiveness of Carbon Materials," *Carbon*, vol. 39, no. 2, p. 279–285, February 2001.
- [203] A. Yanagisawa, H. Koyama, K. Suzuki and T. Nakagawa, "Recent Advancement in the EMI Shielding Technique with Conductive Plastics Mixed with Metal Fibers," in *Proceedings of the 31st International SAMPE Symposium and Exhibition*, Seattle, WA, USA, 1986.
- [204] X. P. Shui and D. D. L. Chung, "Nickel Filament Polymer-Matrix Composites with Low Surface Impedance and High Electromagnetic Interference Shielding Effectiveness," *Journal of Electronic Materials*, vol. 26, no. 8, p. 928–934, August 1997.
- [205] L. Li and D. D. L. Chung, "Thin-Lead Flake, Polyether Sulfone Composite Formed by In-Situ Melt Processing of Tin-Lead Particles," in *Proceedings of the 6th International SAMPE Electronics Conference*, Baltimore, MD, USA, 1992.
- [206] C.-Y. Huang and C.-C. Wu, "The EMI Shielding Effectiveness of PC/ABS/Nickel-Coated-Carbon-Fiber Composites," *European Polymer Journal*, vol. 36, no. 12, p. 2729–2737, December 2000.
- [207] C.-Y. Huang and T.-W. Chiou, "The Effect of Reprocessing on the EMI Shielding Effectiveness of Conductive Fibre Reinforced ABS Composites," *European Polymer Journal*, vol. 34, no. 1, p. 37–43, January 1998.
- [208] S.-S. Tzeng and F.-Y. Chang, "EMI Shielding Effectiveness of Metal-Coated Carbon-Fiber Reinforced ABS Composites," *Materials Science and Engineering: A*, vol. 302, no. 2, p. 258–267, April 2001.

- [209] D. A. Oliver and D. W. Radford, "A Multiple Percolation Approach to EMI Shielding Composites Incorporating Conductive Fillers," *Journal of Reinforced Plastics and Composites*, vol. 17, no. 8, p. 674–690, August 1998.
- [210] P. B. Jana and A. K. Mallick, "Studies on Effectiveness of Electromagnetic Interference Shielding in Carbon Fiber Filled Polychloroprene Composites," *Journal of Elastomers and Plastics*, vol. 26, no. 1, p. 58–73, January 1994.
- [211] R. Ramasubramaniam and J. Chen, "Homogeneous Carbon Nanotube/Polymer Composites for Electrical Applications," *Applied Physics Letters*, vol. 83, no. 14, p. 2928–2930, October 2003.
- [212] J. Liang, Y. Wang, Y. Huang, Y. Ma, Z. Liu, J. Cai, C. Zhang, H. Gao and Y. Chen, "Electromagnetic Interference Shielding of Graphene/Epoxy Composites," *Carbon*, vol. 47, no. 3, p. 922–925, March 2009.
- [213] A. K. Geim and K. S. Novoselov, "The Rise of Graphene," *Nature Materials*, vol. 6, p. 183–191, March 2007.
- [214] B. B. Mandelbrot, *The Fractal Geometry of Nature*, New York, New York: W. H. Freeman, 1983.
- [215] K. J. Vinoy, "Fractal Shaped Antenna Elements for Wide- and Multiband Wireless Applications," State College, PA, USA, 2002.
- [216] J. H. Jeng, V. V. Varadan and V. K. Varadan, "Fractal Finite Element Mesh Generation for Vibration Problems," *The Journal of the Acoustical Society of America*, vol. 82, no. 5, p. 1451–1465, November 1987.
- [217] A. E. Jacquin, "Fractal Image Coding: A Review," *Proceedings of the IEEE*, vol. 81, no. 10, p. 1451–1465, October 1993.
- [218] B. Wohlberg and G. D. Jager, "A Review of the Fractal Image Coding Literature," *IEEE Transactions on Image Processing*, vol. 8, no. 12, p. 1716–1729, December 1999.
- [219] J. Romeu and Y. Rahmat-Samii, "Dual Band FSS with Fractal Elements," *Electronics Letters*, vol. 35, no. 9, p. 702–703, April 1999.

- [220] D. H. Werner and D. Lee, "Design of Dual-Polarised Multiband Frequency Selective Surfaces Using Fractal Elements," *Electronics Letters*, vol. 36, no. 6, p. 487–488, March 2000.
- [221] D. H. Werner, R. L. Haupt and P. L. Werner, "Fractal Antenna Engineering: The Theory and Design of Fractal Antenna Arrays," *IEEE Antennas and Propagation Magazine*, vol. 41, no. 5, p. 37–58, October 1999.
- [222] Y. Kim and D. L. Jaggard, "The Fractal Random Array," *Proceedings of the IEEE*, vol. 74, no. 9, p. 1278–1280, September 1986.
- [223] A. Lakhtakia, V. K. Varadan and V. V. Varadan, "Time-Harmonic and Time-Dependent Radiation by Bifractal Dipole Arrays," *International Journal of Electronics*, vol. 63, no. 6, p. 819–824, June 1987.
- [224] D. H. Werner and P. L. Werner, "Frequency-Independent Features of Self-Similar Fractal Antennas," *Radio Science*, vol. 31, no. 6, p. 1331–1343, November–December 1996.
- [225] C. Puente-Baliarda and R. Pous, "Fractal Design of Multiband and Low Side-Lobe Arrays," *IEEE Transactions on Antennas and Propagation*, vol. 44, no. 5, p. 730–739, May 1996.
- [226] S. E. El-Khamy, M. A. Abaul-Dahab and M. J. Elkaslan, "A Simplified Koch Multiband Fractal Array Using Windowing and Quantization Techniques," in *Proceedings of the IEEE Antennas and Propagation Society International Symposium*, Salt Lake City, UT, USA, 16–21 July 2000.
- [227] C. Puente-Baliarda, "Fractal Antennas," Catalonia, ESP, 1997.
- [228] D. H. Werner, W. Kuhirun and P. L. Werner, "The Peano-Gosper Fractal Array," *IEEE Transactions on Antennas and Propagation*, vol. 51, no. 8, p. 2063–2072, August 2003.
- [229] D. H. Werner and P. L. Werner, "On the Synthesis of Fractal Radiation Patterns," *Radio Science*, vol. 30, no. 1, p. 29–45, January 1995.
- [230] C. Puente, J. Romeu and A. C. R. Pous, "Multiband Fractal Antennas and Arrays," in *Fractals in Engineering*, J. L. Véhel, E. Lutton and C. Tricot, Eds., London, Springer, 1997, p. 222–236.

- [231] N. Cohen and R. G. Hohlfeld, "Fractal Loops and the Small Loop Approximation," *Communications Quarterly*, p. 77–78, Winter 1996.
- [232] C. Puente, J. Romeu, R. Pous, X. Garcia and F. Benitez, "Fractal Multiband Antenna Based on the Sierpinski Gasket," *Electronics Letters*, vol. 32, no. 1, p. 1–2, January 1996.
- [233] C. Puente-Baliarda, J. Romeu, R. Pous and A. Cardama, "On the Behavior of the Sierpinski Multiband Fractal Antenna," *IEEE Transactions on Antennas and Propagation*, vol. 46, no. 4, p. 517–524, April 1998.
- [234] C. T. P. Song, P. S. Hall, H. Ghafouri-Shiraz and D. Wake, "Fractal Stacked Monopole with Very Wide Bandwidth," *Electronics Letters*, vol. 35, no. 12, p. 945–946, June 1999.
- [235] C. Puente-Baliarda, J. Romeu and A. Cardama, "The Koch Monopole: A Small Fractal Antenna," *IEEE Transactions on Antennas and Propagation*, vol. 48, no. 11, p. 1773–1781, November 2000.
- [236] K. J. Vinoy, K. A. Jose, V. K. Varadan and V. V. Varadan, "Hilbert Curve Fractal Antenna: A Small Resonant Antenna for VHF/UHF Applications," *Microwave and Optical Technology Letters*, vol. 29, no. 4, p. 215–219, May 2001.
- [237] J. Zhu, A. Hoorfar and N. Engheta, "Peano Antennas," *IEEE Antennas and Wireless Propagation Letters*, vol. 3, no. 1, p. 71–74, December 2004.
- [238] N. Cohen, "Fractal Antenna Applications in Wireless Telecommunications," in *Professional Program Proceedings of the Electronics Industries Forum of New England*, Boston, MA, USA, 6–8 May 1997.
- [239] C. Puente, J. Romeu, R. Pous, J. Ramis and A. Hijazo, "Small but Long Koch Fractal Monopole," *Electronics Letters*, vol. 34, no. 1, p. 9–10, January 1998.
- [240] M. Navarro, J. M. Gonzalez, C. Puente, J. Romen and A. Aguasca, "Self-Similar Surface Current Distribution on Fractal Sierpinski Antenna Verified with Infrared Thermograms," in *Digest of the 1999 IEEE Antennas and Propagation Society International Symposium*, Orlando, FL, USA, 11–16 July 1999.

- [241] C. Puente, J. Romeu, R. Bartolemé and R. Pous, "Perturbation of the Sierpinski Antenna to Allocate Operating Bands," *Electronics Letters*, vol. 32, no. 24, p. 2186–2188, November 1996.
- [242] C. T. P. Song, P. S. Hall, H. Ghafouri-Shiraz and D. Wake, "Sierpinski Monopole Antenna with Controlled Band Spacing and Input Impedance," *Electronics Letters*, vol. 35, no. 13, p. 1036–1037, June 1999.
- [243] S. R. Best, "On the Significance of Self-Similar Fractal Geometry in Determining the Multiband Behavior of the Sierpinski Gasket Antenna," *IEEE Antennas and Wireless Propagation Letters*, vol. 1, no. 1, p. 23–25, December 2002.
- [244] C. Puente, M. Navarro, J. Romeu and R. Pous, "Variations on the Fractal Sierpinski Antenna Flare Angle," in *Digest of the 1998 IEEE Antenna and Propagation Society International Symposium*, Atlanta, GA, USA, 21–26 June 1998.
- [245] S. R. Best, "A Multiband Conical Monopole Antenna Derived from a Modified Sierpinski Gasket," *IEEE Antennas and Wireless Propagation Letters*, vol. 2, no. 1, p. 205–207, December 2003.
- [246] S. Hebib, H. Aubert, O. Pascal, N. J. G. Fonseca, L. Ries and J.-M. E. Lopez, "Sierpinski Pyramidal Antenna Loaded with a Cutoff Open-Ended Waveguide," *IEEE Antennas and Wireless Propagation Letters*, vol. 8, no. 1, p. 352–355, December 2009.
- [247] M. Alaydrus, "Analysis of Sierpinski Gasket Tetrahedron Antennas," *Journal of Telecommunications*, vol. 5, no. 2, p. 6–10, November 2010.